Ultrafast Dynamics in Nanomaterials: From Gold Clusters to Dye-Sensitized Semiconductors

Stephen Andrew Miller

A dissertation submitted to the faculty of the University of North Carolina at Chapel Hill in partial fulfillment of the requirements for the degree of Doctor of Philosophy in the Department of Chemistry

Chapel Hill
2012

Approved by:

Dr. James Cahoon

Dr. Andrew Moran

Dr. Wei You

Dr. Yosuke Kanai

Dr. Jillian Dempsey

ABSTRACT

STEPHEN ANDREW MILLER: Ultrafast Dynamics in Nanomaterials: From Gold Clusters
to Dye-Sensitized Semiconductors
(Under the direction of Andrew M. Moran)

Femtosecond resolved "pump-probe" spectroscopic experiments are utilized to probe

energy and charge transport mechanisms in a variety of synthetic nanomaterials systems.

These systems range from applied materials synthesized for use in solar energy conversion

devices (π-conjugated polymers and dye sensitized semiconductors) to materials prepared for

more fundamental research ("quantum-sized" gold nanoclusters). Because all quantum

mechanical rate models are effectively derivatives of Fermi's Golden Rule, the observed

energy and charge transfer dynamics in all systems are discussed in various contexts of this

famous rate law. In addition, reduced descriptions of the rate law that are more suitable to

the condensed phase systems studied herein are introduced.

Marcus theory of electron transfer is used extensively in the study of both

intramolecular and intermolecular electron transfer mechanisms in osmium and ruthenium

polypyridyl dye complexes both in neat solution and complexed with TiO_2 semiconductor

nanoparticles. These electron transfer events were observed to occur on the femtosecond to

picosecond timescale in all systems. Picosecond energy transfer events observed in a newly

synthesized π-conjugated polymer in the form of exciton "hopping" are discussed in the

framework of Förster theory. In addition, sub-picosecond electron transfer from the pure

polymer to electron accepting dopants (PCBM) is observed, where the quantum yield is

strongly dependent on the microscopic structure of the system. Finally, femtosecond and picosecond energy transfer events in the form of interval conversion between core and semiring ligand localized excited states are observed in two novel gold nanocluster systems, whose < 2 nm size allows them to exhibit molecule-like electronic properties.

For all systems, energy and charge transport dynamics/mechanisms are experimentally investigated using the specialized "pump-probe" spectroscopic technique known as transient grating. Although providing equivalent information to more conventional techniques such as transient absorption, the transient grating technique has many advantages over the former including background free signals and the ability to use extremely low laser fluences. In addition, the use of multiple laser beams to excite and probe samples allows for direct experimental control over all field matter interactions with the samples, which allows one to probe dynamics that would otherwise be unobservable.

To my family and friends

ACKNOWLEDGEMENTS

TABLE OF CONTENTS

LIST OF TABLES

LIST OF FIGURES

LIST OF ABBREVIATIONS AND SYMBOLS

A   acceptor molecule

A^{-} reduced acceptor molecule

Å   angstrom

$A_A(\omega)$ acceptor molecule absorption spectrum

$\alpha(\omega)$ polarizability

Au   gold

b Kuhn monomer length

BBO   β-barium borate

BHJ   bulk heterojunction

c   speed of light

CB   conduction band

CCD   charge coupled device

$c_n^{(1)}$ first order coefficient of state "b"

CS   quartz coverslip

$C(T)$ correlation function

$\chi^{(n)}(\omega)$ susceptibility at n^{th} order

D   dye or donor molecule

D^*	photoexcited dye or photoexcited donor molecule
D^+	oxidized dye or donor molecule
DFT	density functional theory
DSPEC	dye sensitized photoelectrochemical cell
$\underset{\sim}{d}_{\alpha}^{A}$	specific vibrational nuclear coordinate
Δ	fluctuation in energy gap due to interactions with surroundings
E(t)	electric field
e^-	electron
EET	electronic energy transfer
ESA	excited state absorption
ESE	excited state emission
ET	electron transfer
eV	electron volt
$\Delta E^{\dagger}$	energy activation barrier
ε	extinction coefficient
$F_D(\omega)$	donor molecule fluorescence spectrum
F	fluence
$f(s)$	oscillator strength
Φ	fraction of monomers photoexcited

FRET	fluorescence resonance energy transfer
FROG	frequency resolved optical gating
fs	femtosecond
FWHM	full width half maximum
ΔG	free energy change
$G(s)$	log normal distribution
$g(t)$	line broadening function
$G(t';w)$	Gaussian instrument response function
$\mathcal{G}(t_n)$	Green Function
GSB	ground state bleach
GVD	group velocity dispersion
Γ	damping constant for line broadening function
h	Planck's constant
$\hbar$	reduced Planck's constant ($=h/2\pi$)
H^{Coul}	coulombic coupling
H_{DA}	energy gap Hamiltonian ($=H_A-H_D$)
H^{el-ph}	electron-phonon coupling
HOMO	highest occupied molecular orbital
ITO	indium tin oxide

η (%)	photovoltaic power conversion efficiency
J_{DA}	dipole-dipole coupling between donor and acceptor molecules
J_{sc}	short circuit current
k	rate
k_B	Boltzmann's constant
k_n	wavevector of pulse "n"
κ	orientational factor
$L(\omega)$	absorption lineshape
LO	local oscillator
LUMO	lowest unoccupied molecular orbital
Λ^{-1}	correlation time of solvent fluctuations
λ	reorganization energy or wavelength
M	number of stabilizing ligands
MPC	monolayer protected cluster
MLCT	metal to ligand charge transfer
$M(t)$	solvation correlation function
μm	micrometer
N	number of metallic atoms in a nanocluster or number of monomers
N_A	Avogadro's constant

ND	neutral density
nm	nanometer
NOPA	noncollinear optical parametric amplifier
n^*	number of electrons available in a nanocluster
OHD	optical heterodyne signal detection
OPA	optical parametric amplifier
OPG	optical parametric generation
OPV	organic photovoltaic
ω	angular frequency
ω_0	carrier frequency
ω_{vib}	vibrational frequency
$P_n(t)$	probability of residing in state "n" at time t.
$P_n(kT)$	thermal population of state "n"
$P^{(n)}$	polarization of nth order
PCBM	phenyl-C_{61}-butyric acid methyl ester
ps	picosecond
q	collective nuclear coordinate
r_{DA}	intermolecular distance between donor and acceptor molecules
$r(T)$	polarization anisotropy

$\hat{\rho}(t)$	time dependent density operator
Q_C	fluorescence quantum yield
$R(t)$	response function term
R	mean end to end distance in a polymer chain
$S_{\parallel}(T)$	signals measured with parallel pump and probe polarizations
$S_{\perp}(T)$	signals measured with orthogonal pump and probe polarizations
$S^{(n)}(t)$	response function of nth order
SM	spherical mirror
$\psi(t)$	wavefunction
σ	absorption cross section
T	temperature (or time interval)
TA	transient absorption
TAA	transient absorption anisotropy
TDPT	time dependent perturbation theory
TG	transient grating
$t_{group}(\omega)$	group velocity
TOD	third order dispersion
$\theta(t)$	Heaviside step function or temporal phase

$\theta(\omega)$	spectral phase
μ	transition dipole
$\hat{\mu}(t)$	dipole operator
$\hat{V}_I(t)$	time dependent interactive perturbation
V_{ba}	coupling between states "a" and "b"
V_{oc}	open circuit voltage
ν	frequency
ν_A	number of valence electrons
wp	wave plate
$\xi(t)$	Gaussian envelope function
z	charge
ZINDO	Zerner's intermediate neglect of differential overlap

CHAPTER 1 . INTRODUCTION

1.1. MOTIVATION

On the smallest length scales the world is a very complicated place. Even in seemingly simple macroscopic systems, the underlying physical processes occurring can be quite complex and difficult to ascertain. For example, although water is one of the simplest chemicals and probably has been studied more than any other, we still do not have a complete understanding of some of its most basic properties.[1,2] For more complex systems with many degrees of freedom (e.g., macromolecules, synthetic devices, etc.) obtaining an exact picture of what occurs on the molecular scale is a monumental challenge. In most cases, we will probably never obtain an exact understanding and must therefore content ourselves with a partial understanding through the use of models.

One of the most important things to understand about a given system is how energy and or charge is transported at the molecular level. Often vaguely defined, the term "energy transfer" in the context of this dissertation refers to the nonradiative transfer of neutral electronic excitations between spatially separate molecules/atoms. Analogously, "charge transfer" refers to the spatial transfer of charge (i.e., unbound electrons/holes) throughout a system. Knowledge of these processes not only tells one the rate at which energy/charge is conveyed but also provides deeper insights into such things as the electronic structures or spatial arrangement of the atoms/molecules.

This dissertation is concerned with probing the mechanisms of energy and charge transfer following photoexcitation in a variety of synthetic systems. These systems range from applied materials synthesized for use in solar energy conversion (conjugated polymers and transition metal polypyridyl complexes) to materials synthesized for more fundamental research ("quantum-sized" gold nanoclusters). With the solar energy materials, it is absolutely essential to obtain a deep understanding of the energy and charge transfer mechanisms as these processes are strongly linked to the overall efficiency of a working device. On the other hand, knowledge of energy and charge transfer mechanisms in less applied systems such as gold nanoclusters is equally as important due to the fact that on a fundamental level, all mechanistic models are related. Consequently, furthering the understanding of energy and charge transport in one system helps one understand these processes in all systems.

All quantum mechanical mechanistic energy and charge transfer rate models are in effect derivatives of the famous rate equation developed by Dirac and Fermi in the first half of the 20th Century.[3,4] This rate equation, now known as "Fermi's Golden Rule," calculates the transition rate between two or more coupled states following some external perturbation (e.g., interaction with an electromagnetic field). Fermi's Golden Rule is extremely powerful because it describes the rates of change for essentially all possible situations and mechanisms. This flexibility is possible because one needs only to change the coupling parameter in the equation (i.e., the perturbative Hamiltonian) to match the specifics of the system/mechanism being modeled.

As aforementioned, the systems studied in this dissertation vary widely, and thus necessitate the use of multiple derivatives of Fermi's Golden Rule. Of most prominent use

herein are the Marcus theory of electron transfer[5] and the Förster Resonance Energy Transfer theory.[6] The former is used extensively in the study of both intramolecular and intermolecular electron transfer mechanisms in osmium and ruthenium polypyridyl complexes both bound and unbound to TiO_2 semiconductor nanoparticles. Discussions of these studies are included in Chapters 7 and 8 along with a derivation of Marcus theory shown in Chapter 2.2.3. Förster theory is used prominently in the study of energy transfer mechanisms in the form of "hopping" of photoexcitations between chains of a newly synthesized π-conjugated polymer for use in solar energy collection. This study is discussed in Chapter 6 and a derivation of Förster theory is shown in Chapter 2.2.2. Studies of energy transfer mechanisms in gold nanoclusters are included in Chapters 4 and 5. In these systems the primary mechanism of energy transfer observed is internal conversion between spatially localized excited states. Although the laws governing internal conversion can also be shown to be a derivative of Fermi's Golden Rule where the coupling parameter is described by the nuclear kinetic energy operator,[7-9] the mathematics are considerably more complicated than in the other examples and a derivation is not included in this dissertation.

For all systems, energy and charge transport dynamics/mechanisms are experimentally investigated using a specialized femtosecond resolved "pump-probe" spectroscopic technique known as transient grating. "Pump-probe" spectroscopy is one of the most widely used techniques for studying energy/charge transfer processes.[10,11] The main advantage of the technique is its unparalleled time resolution afforded by the use of ultrashort laser pulses to both excite the systems and probe the subsequent relaxation processes. Although experiments were originally limited to millisecond time resolutions,[12] modern experiments can probe processes on the femtosecond timescale for visible spectroscopy[13] and

attoseconds for more energetic spectroscopies (e.g., X-Rays).[14] Although providing equivalent information to more conventional "pump-probe" techniques such as transient absorption, the transient grating technique utilized in this dissertation has several advantages over the former including background free signals and the ability to use extremely low laser fluences. In addition, the use of multiple laser beams to excite and probe the samples allows for direct control over all field matter interactions with the sample (e.g., control of polarizations). As will be demonstrated in Chapter 8, this is an extremely valuable advantage, which allows one to probe charge transfer dynamics that would otherwise be unobservable.

1.2. GOLD NANOCLUSTERS

1.2.1. Bulk and Quantum-Sized Regimes

Throughout all of recorded history gold has been a material of great interest and value to humankind. Its properties such as its malleability, ductility, chemical inertness, and beauty have long made it a prime candidate for such applications as currency, jewelry, and art.[15] Since the inception of modern science, however, many other interesting properties/applications of gold have been discovered. In particular, during recent decades a great deal of research has been focused on the properties of gold nanoparticles rather than the bulk material.[16,17] As applied materials, gold nanoparticles are intriguing in that they exhibit properties suitable for a variety of applications including but not limited to: catalysis,[18,19] chemical sensing,[20-22] and biomedicine.[23,24]

Perhaps the most interesting aspect of gold nanoparticles, however, is the fascinating dependence exhibited by the electronic and optical properties on the size and shape of the nanoparticle. In general, there are two main size regimes to consider. For "large" gold nanoparticles in the 3-100 nm size range, the absorption spectra are broad and featureless; consisting primarily of a surface plasmon band.[16,17,25,26] That is, light absorption is the result of interactions between photons and the 6s conduction band electrons of the surface gold atoms. This is analogous to the interactions that occur in the bulk material with one important exception being that the bandgap between the valence and conduction bands is considerably larger in nanoparticles than in the bulk material. As the size of the nanoparticle increases, the bandgap decreases; eventually matching the electronic structure of bulk gold.

For smaller nanoparticles the situation is considerably more interesting. When the size of the nanoparticles is near or less than the de Broglie wavelength of the electron (i.e., ~1.5 nm) quantization effects begin to occur due to the spatial confinement of the valence electrons.[17,27-39] These nanoparticles consist of only a few 10's or 100's of atoms and are thus generally referred to as gold nanoclusters. For gold nanoclusters, it is more accurate to describe the electronic structure and optical transitions as occurring between "molecule-like" electronic orbitals whose spatial locations and dipole orientations are strongly dependent on the bond structure of the nanocluster.[30-32,35,39-42] As a result, the absorption spectra of gold nanoclusters are analogous to the absorption spectra of molecules and will generally exhibit "fine" structure corresponding to transitions between states that are spatially localized throughout the nanocluster structure. An excellent example of this can be seen in Figure 1.1(B), which exhibits the absorption spectrum of the well known 25 gold atom monolayer protected nanocluster, $Au_{25}(SR)_{18}^{-}$. For this particular cluster, the "R" groups represent

5

CH$_2$CH$_2$Ph moieties not included in Figure 1.1(A) for clarity. Full spectroscopic studies of this particular cluster and the analogous cluster, Au$_{24}$Pd(SR)$_{18}^-$ are described in detail in Chapters 4 and 5, respectively. Here it is sufficient to say that the peaks observed in the absorption spectrum correspond to the lowest energy electronic transitions between states localized to the Au$_{13}$ core structure.
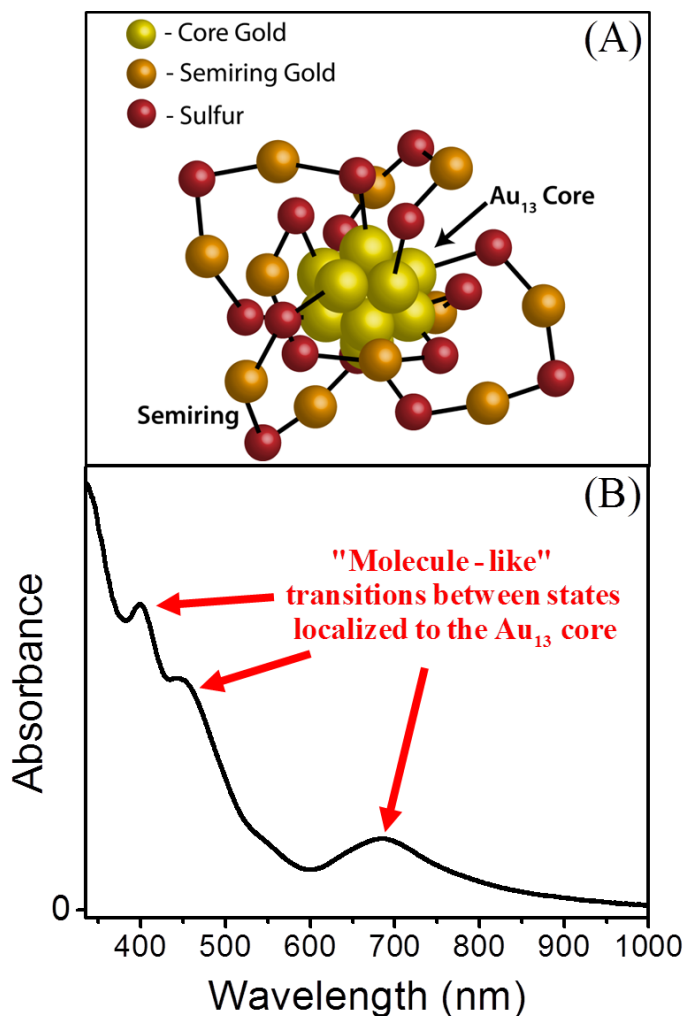
Figure 1.1: (A) Crystal structure of the gold nanocluster, Au$_{25}$(SR)$_{18}^-$ where the R groups, CH$_2$CH$_2$Ph, are not shown for clarity. The icosahedral Au$_{13}$ core structure is stabilized by the presence of six "floppy" semiring moieties, -SR-Au-SR-Au-SR-. (B) Linear absorption spectrum of the nanocluster exhibiting "molecule-like" electronic transitions between spatially localized states.

1.2.2. Superatom Model

If the concepts governing the absorption spectra of gold nanoclusters are comparable to that of molecules, then the rules that govern the stability of gold nanoclusters can be said to atomistic in nature. As taught in general chemistry courses, the electronic configuration of an atom is determined by the Aufbau principle in which an atom's atomic orbitals are filled up successively with electrons according to the most stable configuration. Filled and half filled angular momentum "shells" are especially stable, which leads to a specific order in which the "shells" are filled (i.e., $1s^2 2s^2 2p^6 3s^2 3p^6 ...$).

In an analogous manner, the Superatom model predicts the stability of metallic nanoclusters by modeling their electronic structures as a building up of electrons in a sequence of angular momentum "shells" of a "jellium sphere."[33,36,43-45] The sequence of angular momentum "shells" resembles that of individual atoms and is given as

$$\left[1S^2\right]\left[1P^6\right]\left[1D^{10}\right]\left[2S^2 1F^{14}\right]\left[2P^6\right]\left[1G^{18}\right]\left[2D^{10} 3S^2 1H^{22}\right]... \tag{1.1}$$

where each set of brackets encloses a single "shell," the letters represent the character of the angular momentum of a "sub-shell", the superscripts refer to the maximum number of electrons that can be contained in each "sub-shell", and the numbers in front of the letters represent the principle quantum number.[36] According to the Superatom model, filled shells correspond to maximum stability; therefore a given nanocluster will be stable if the total number of available electrons in the nanocluster, n^*, is equal to the following[36]

$$n^* = 2, 8, 18, 34, 58, 92, 138, ... \tag{1.2}$$

The number of electrons available is proportional to the number of metal atoms included in the nanocluster and is given by the following expression

$$n^* = Nv_A - M - z \qquad (1.3)$$

where N is the number of metal atoms included in the nanocluster, v_A is the number of valence electrons in each atom, M is the number of stabilizing ligands attached to the nanocluster, and z is the net charge of the nanocluster.[36]

The Superatom model has been very successful at predicting and explaining the stability of nanoclusters.[44-49] In the context of this dissertation, it can readily explain the stability of the gold nanocluster, $Au_{25}(SR)_{18}^-$. For this nanocluster, twelve of the twenty five gold atoms are located in the semiring moieties, and thus should not be included in Equation 1.3. The Au_{13} core of the nanocluster contains the remaining gold atoms, therefore $N = 13$. Each gold atom contributes a single valence electron (i.e., $6s^1$), thus $v_A = 1$. Each semiring moiety is considered to be a single ligand, therefore making $M = 6$. Finally, as the charge of the nanocluster is negative, $z = -1$. If one inserts these parameters into Equation 1.3, the number of electrons available, n^* is equal to 8, which corresponds to a stable filled $\left[1S^2\right]\left[1P^6\right]$ electronic configuration.

1.3. ORGANIC PHOTOVOLTAIC MATERIALS

1.3.1. Organic Semiconducting Polymers

Currently, solar energy collection technologies are on the brink of but not quite efficient/cheap enough compete commercially with terrestrial energy sources. There is a great deal of emphasis being put on this problem in the scientific community, however, and new advances in concepts and technology are constantly closing the gap. One promising avenue of solar energy technology research deals with the use of organic photovoltaic devices (OPV) whose functionality is based on the semiconducting properties of π-conjugated polymers. Although currently yielding device efficiencies ($\leq 10\%$) notably lower than "conventional" inorganic solid state junction semiconductor photovoltaics, OPVs have several advantages over the former including: significantly lower manufacturing costs, molecular-level customization, and thin film flexibility.[50,51]

The backbone of a π-conjugated polymer chain consists of an uninterrupted progression of unsaturated carbon atoms. Each carbon atom is in a sp^2 hybridized state and contains a single p_z orbital extending orthogonal to the chain direction. Adjacent p_z orbitals undergo π-overlap with their nearest neighbors resulting in a delocalization of π-states along the chain.[50,52,53] The semiconducting properties of these polymers arise from the fact that the energy spacing between individual HOMO and LUMO π-states becomes narrow as the delocalization length of the backbone increases; a process that is analogous to the classic particle in the box quantum illustration. Eventually, as the delocalization length increases enough, the groups of HOMO and LUMO levels "contract" together so that one can describe their aggregates as electronic bands.[50,52,53] As in inorganic semiconductors, these bands are

referred to as the valence and conduction bands for the HOMO and LUMO states, respectively. The bandgap of π-conjugated polymers is typically low (~1-4 eV), making the corresponding optical transition in the visible-NIR spectral region.[53] Furthermore, because functionalization of the polymer chain strongly affects the delocalization properties of the polymer, one has the ability to fine-tune the bandgap to optimally match the solar spectrum by "simply" altering the chemical structure of the chains.[52-54]

Many materials have the ability to absorb sunlight; however, most do not make effective photovoltaic materials. This is primarily due to the fact that they have poor electrical conductivity over the distances required to create a working device. This is not the case for π-conjugated polymers. Due to the aforementioned delocalization along the chain backbone, the charge conductivity along the backbone of π-conjugated polymers can rival that of metallic systems. The discovery of these remarkable properties in the latter half of the 20th century ultimately led to the Chemistry Nobel prize in 2000.[52] Unfortunately, visible-NIR photoexcitations in π-conjugated polymers are excitonic in nature. That is, they consist of Coulombically bound electron-hole pairs and do not contain free charge carriers.[55] As a photovoltaic material, this is a significant problem as free charge carriers are essential for devices to function. For example, the very first OPV devices were comprised of pristine π-conjugated polymers and exhibited very poor efficiencies ($\ll 1\%$).[56,57] Since then, significant effort has gone into developing ways to dissociate photoexcited excitons into free charge carriers in order to increase device efficiency.[58,59] One of the simplest and most efficient solutions consists of a random microscopically interpenetrating mixture of π-conjugated polymer and an electron accepting material which aids in the dissociation of the

exciton into free charges.[51,59] This type of device is referred to as a bulk heterojunction and will be discussed in the next section.

1.3.2. Bulk Heterojunction Films

As discussed in the previous section, low energy photoexcitations in π-conjugated polymers consist of excitons and not free charge carriers. In order to generate the free charges required for photovoltaic devices to function, one must introduce an electron accepting material to the system in order to dissociate excitons into unbound electrons and holes. Since the observation of sub-picosecond electron transfer from π-conjugated polymers to fullerenes in the 1990's,[60,61] fullerenes and their functionalized derivatives (e.g., PCBM) have become the most widely used electron accepting materials in OPV devices. The simplest manner in which to contact the two materials together in a device is in a bilayer configuration, where there are simply two layers of pristine π-conjugated polymer and fullerene in contact with one another.[62] As excitons in π-conjugated polymers typically exhibit a diffusion length of only ~10 nm before undergoing radiative/nonradiative relaxation, polymer film thicknesses in bilayer devices cannot exceed this length.[50,63-70] Unfortunately, this thickness is considerably less than the average optical absorption depth of π-conjugated polymers (~100 nm), which severely limits the amount of sunlight that can be absorbed.[50]

A considerably more efficient device design is the bulk heterojunction (BHJ) thin film. A bulk heterojunction is simply a random microscopically interpenetrating mixture of π-conjugated polymer and fullerene phases formed by self-organized phase separation.[51,59] The main advantage of BHJ films is that the average phase separation distance of the two

materials is considerably less than in bilayer devices, therefore increasing the number of excitons that are able to diffuse to a polymer/fullerene interface and undergo electron transfer. Additionally, the thickness of BHJ films is not limited by the exciton diffusion length and thicker films can be prepared that maximize light absorption. As of today, BHJs are the state of the art for OPV devices, and photo conversion efficiencies in the range of 3-10% have been reported.[71-80]

A schematic representation of the processes occurring in a BHJ device is shown in Figure 1.2 and can be summarized as follows. First, a photon is absorbed by the π-conjugated polymer creating an exciton in the polymer phase. This exciton then diffuses by "hopping" across/along different polymer chains until it reaches an interface between the polymer and fullerene phases. At the interface, electron injection into the excited state of the fullerene occurs leaving behind a hole in the polymer HOMO. Injection overcomes the Coulombic attraction between the electron and hole, which are free to diffuse to the device cathode and anode, respectively.
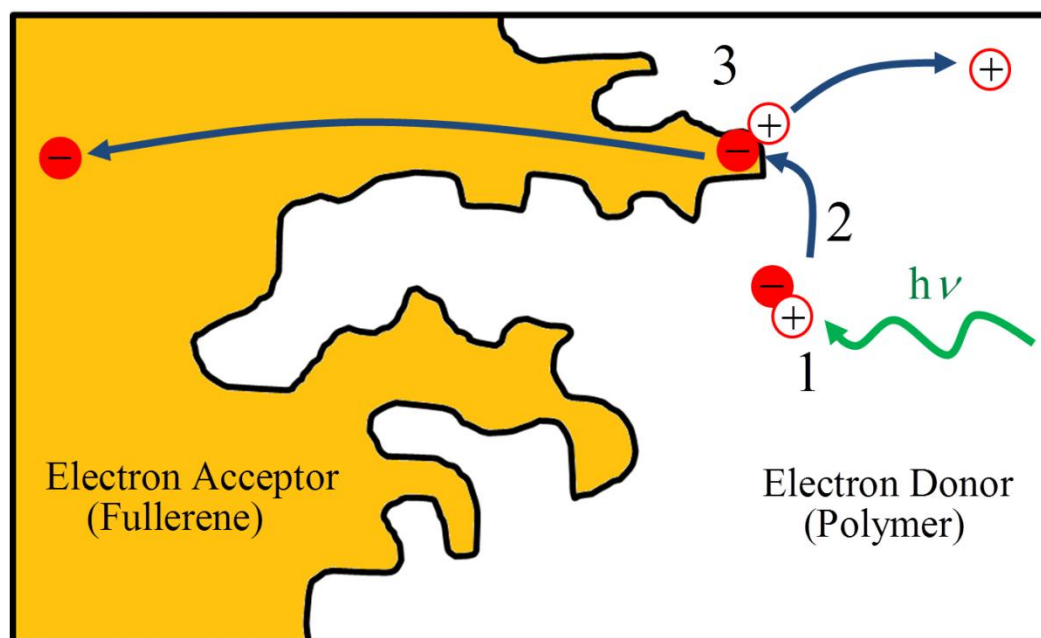
Figure 1.2: Schematic of a bulk-heterojunction thin film. 1. Light absorption by the π-conjugated polymer creates an exciton in the polymer phase. 2. Exciton diffusion occurs until an interface between the polymer and fullerene is reached. 3. At the interface, electron injection occurs into the fullerene excited state leaving behind a hole in the polymer HOMO. No longer bound to one another, the electron and hole are now free to migrate to their respective electrodes.

1.4. DYE–SENSITIZED PHOTOELECTROCHEMICAL CELL

1.4.1. Introduction

Another exciting alternative to "conventional" inorganic solid state junction solar cell technologies is the photoelectrochemical solar cell. Although the foundations for this technology were originally laid out by photographic science in the 1800's to early 1900's,[81] detailed studies of the photoelectrochemical process were not performed until the pioneering work of by Brattain and Gerret,[82] and Gerischer[83] in the mid 20th century. Broadly defined, photoelectrochemical cells consist of two spatially separate electrodes divided by some electrolyte (liquid, gel, or organic solid), where the type of electrolyte utilized depends on the

type and purpose of the photoelectrochemical cell. The photo-anode, (typically an n-type inorganic semiconductor) absorbs any photons whose energy exceeds the semiconductor's bandgap to create unbound electron-hole pairs.[81] The electrons diffuse through the semiconductor and into an external circuit connected to the cathode. The holes diffuse to the semiconductor-electrolyte interface, where one of two things will happen depending on the type of photoelectrochemical cell. In a regenerative cell, the hole oxidizes an electrolyte molecule which then migrates to the cathode. Upon arriving at the cathode, the oxidized electrolyte molecule is reduced back to its original state by an electron which has traveled through the external circuit. This process is constantly repeated thus creating an external current which can be used to perform useful work.[81] The other type of photoelectrochemical cell is referred to a photosynthetic cell. Photosynthetic cells are identical to regenerative cells in all respects except for the fact that the electrolyte consists of more than one redox system that do not regenerate. One redox system is reduced by interaction with the photoelectrons at the cathode, thus creating a useful chemical product (e.g., $H_2O + e^- \rightarrow H_2$) which can be collected and stored for further use. The other redox system is oxidized at the semiconductor anode by the holes to again create a useful product (e.g., $H_2O \rightarrow O_2 + e^-$).

Following the demonstration by Fujishima and Honda of using titanium dioxide to perform water photolysis,[84] TiO_2 has become the most utilized semiconducting material in photoelectrochemical cells. Unfortunately, TiO_2 has a large bandgap (3-3.2 eV)[85] which limits its absorption to only the ultraviolet region of the solar spectrum. Use of lower bandgap semiconductors that more effectively match the solar spectrum is unfortunately hindered by the fact that low bandgap semiconductors are generally conducive to photocorrosion.[81] A solution to this dilemma is obtained by separating the light absorption

14

and charge carrier generation processes. This is accomplished by sensitizing the semiconductor anode with a chemical dye whose absorption spectrum better matches the solar spectrum.[81,86-88] Although dye sensitization is certainly not a new concept, original designs were limited by low light harvesting efficiencies due to the belief that only flat semiconductor surfaces should be used.[89,90] The invention of the "Grätzel Cell" by Michael Grätzel and coworkers in 1991 was a revolution in dye sensitized photoelectrochemical cell design and now represents the most famous and one of the more efficient (7-8%) and cost-effective designs.[88] In the Grätzel Cell, in order to maximize light absorption, the flat semiconductor anode was replaced with a mesoscopic thin film (~10 μm thick) of crystalline TiO_2 semiconductor nanoparticles. This ultimately increased the surface area available for dye adsorption by orders of magnitude relative to a flat surface, while surprisingly still retaining a large charge carrier mobility in the TiO_2.[86,88] Nearly all subsequent dye sensitized photoelectrochemical (DSPEC) cells designs are based on this concept.

With the exception of charge carrier generation, the physical processes occurring in DSPEC cells are equivalent to those of non dye sensitized cells. Charge carrier generation is accomplished as follows. Following light absorption by the dye, an electron is injected on an ultrafast timescale from the excited state of the dye into the conduction band of the semiconductor.[91,92] As in the non dye sensitized cells, the electron diffuses through the semiconductor to the external circuit. At the same time, the now oxidized dye (or dye-catalyst assembly[93]) is reduced by the electrolyte in either a regenerative or photosynthetic manner depending on the electrolyte(s) present.[81] These processes are outlined schematically in Figure 1.3 for a regenerative DSPEC cell.
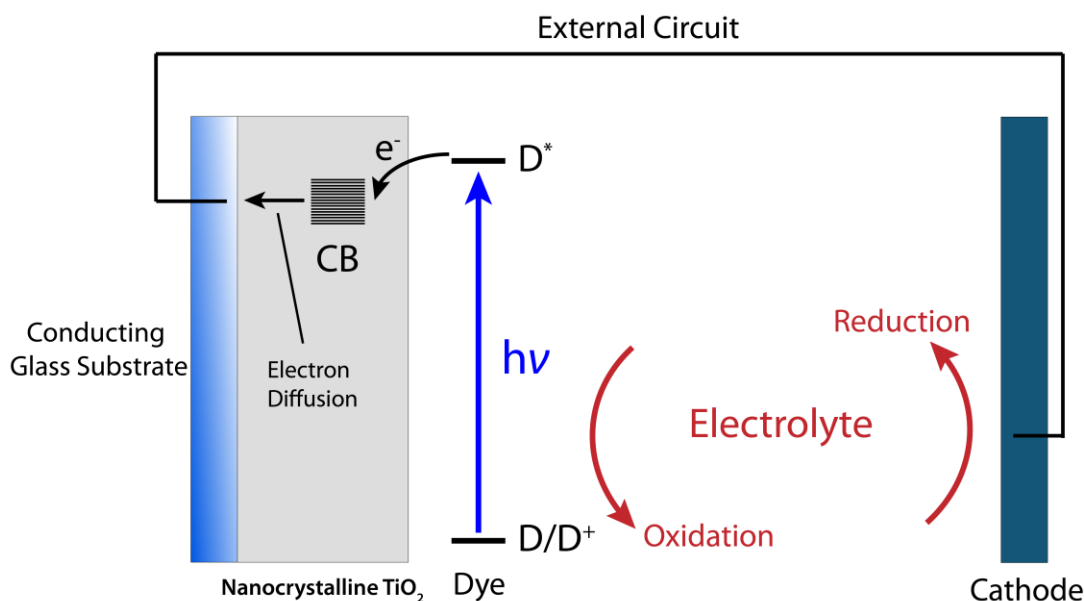
Figure 1.3: Schematic of a regenerative DSPEC cell. Photoexcitations in the dye (D^*) undergo electron transfer on an ultrafast timescale into the conduction band (CB) of a nanocrystalline TiO_2 particle. This electron is then free to diffuse through the nanocrystalline film until the external circuit is reached where reduction of the electrolyte subsequently occurs at the cathode. Electron injection by the dye results in an oxidized state of the dye (D^+) which then causes oxidation of the electrolyte.

1.4.2. Ruthenium Polypyridyl Complexes

By far, the most common types of dyes used as molecular sensitizers in dye sensitized photoelectrochemical cells have been ruthenium polypyridyl complexes (e.g., $Ru[(bpy)_3]^{2+}$).[81,86,93-95] These complexes have proven to have excellent photovoltaic properties including, broad visible absorbance, good electrochemical and thermal stability, and long lived excited states.[86] Most importantly, the excited and ground state energy levels in these complexes are suitably located relative to the conduction band energies of common semiconductors (e.g., TiO_2) and the energy levels of electrolytes (e.g., I^-/I_3^-).[81] This allows for efficient fast electron injection into the semiconductor conduction bands and efficient oxidation of the electrolyte by the hole, respectively.

16

In ruthenium polypyridyl complexes the electronic transition responsible for the visible absorption is a metal to ligand charge transfer process (MLCT) from the central ruthenium atom to one of the ancillary ligands.[86] Functionalizing these ancillary ligands (typically bipyridine or terpyridines) allows one to alter the energy levels of the MLCT states therefore giving synthetic chemists the ability to "tune" the electronic properties of the complexes to suit one's specific requirements.[86] Complexes can be anchored to semiconductor nanoparticles by a variety of anchoring groups bonded to the ancillary ligand(s) including but not limited to: carboxylates, phosphonates, and hydroxyl groups.[86] Furthermore, the number and location of anchoring groups can be synthetically controlled, thus affecting the manner in which complexes are bonded to the surface. As will be discussed briefly in the next section, and more thoroughly in Chapter 8, the manner in which ruthenium polypyridyl complexes are attached to the semiconductor particles has a strong effect on the electronic structure at the interface and thus the mechanism of electron injection.[96,97] Specifically, the discussions in this dissertation will be on the ruthenium polypyridyl complex, $[(Ru(bpy)_2(4,4'-(PO_3H_2)_2bpy)]Cl_2$, whose structure is shown in Figure 1.4. For mechanistic studies on electron injection, the complex is adsorbed onto TiO_2 anatase nanoparticles through one or two phosphonate anchoring groups located on a single bipyridine ligand.
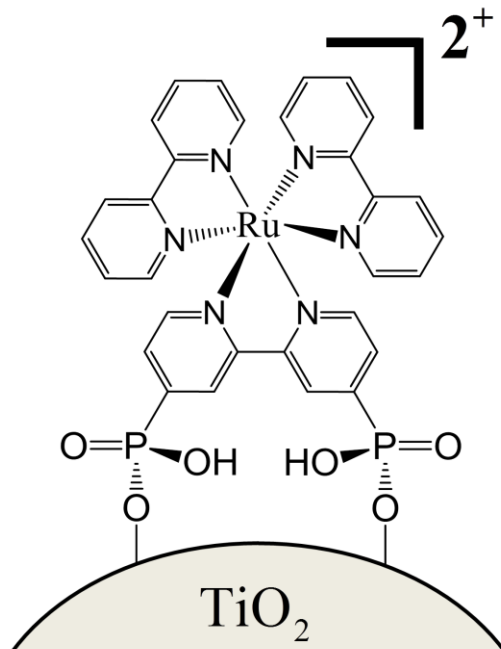
Figure 1.4: Chemical structure of the dye, $[(Ru(bpy)_2(4,4'-(PO_3H_2)_2bpy)]^{2+}$ bonded to a nanocrystalline TiO_2 particle.

1.4.3. Electronic Structure at Molecule-TiO₂ Interfaces

The first and arguably the most important step of any working DSPEC cell is the absorption of a photon by the dye molecule and subsequent electron injection into the conduction band of the semiconductor nanoparticle. While the ensuing steps are clearly also important, it is the efficiency of this electron injection process that directly governs the availability of free charge carriers in a device. For this reason, a great deal of research has been performed in order to further the understanding of the mechanism(s) of electron injection in molecule-sensitized semiconductor systems.

Pioneering work around the turn of the century has established that the injection process occurs extremely fast (< 100 fs) for many molecule-sensitized TiO_2 complexes, including ruthenium polypyridyl complexes.[91,92] These dynamics have traditionally been

18

explained by an electron injection model developed by Marcus and Gerischer in the 1960-70s in which the photon absorption and electron injection steps are described as sequential.[5,98,99] That is, light absorption by the sensitizing molecule yields photoexcitations in excited states that are spatially localized in the molecule. After some finite delay, an electron is then injected from the molecule into the TiO_2 conduction band. This process is illustrated schematically in Figure 1.5(A). The rate of injection in this model is described by Marcus theory and is determined primarily by the molecule-TiO_2 coupling strength and the density of states in the TiO_2 conduction band at the energy of the molecule's excited state.

For weakly coupled molecule-TiO_2 complexes this model has proved to be the best description of the electron injection process. In reality, however, the situation is not that simple. Recent quantum dynamics simulations have shown that the nature of the excited electronic structure depends strongly on the nuclear geometry of the complex at the "instant" of photoexcitation.[96] DSPEC cells consisting of inhomogeneous mesoscopic nanocrystalline films are inherently full of geometric heterogeneity; therefore making the local molecule-TiO_2 geometry variable throughout the system. Thus, although the excited electronic structure in a weakly coupled system is best described by the localized states model described above, it is possible for a large sub-ensemble in the system to contain an unusual local molecule-TiO_2 geometry with substantially increased coupling strength. In this sub-ensemble, the strong molecule-TiO_2 coupling results in photoexcitations being delocalized spatially over both the molecule and semiconductor surface.[96,97] Electron injection for this regime would therefore not be a sequential process. Instead, light absorption and electron injection should be viewed as one in the same processes (i.e., a charge transfer resonance), which is shown schematically in Figure 1.5(B). In Chapter 8, specialized transient grating

techniques will exhibit evidence for this surprising result even for the nominally weakly

coupled system, $[(Ru(bpy)_2(4,4'-(PO_3H_2)_2bpy)]^{2+}$ adsorbed on TiO_2.
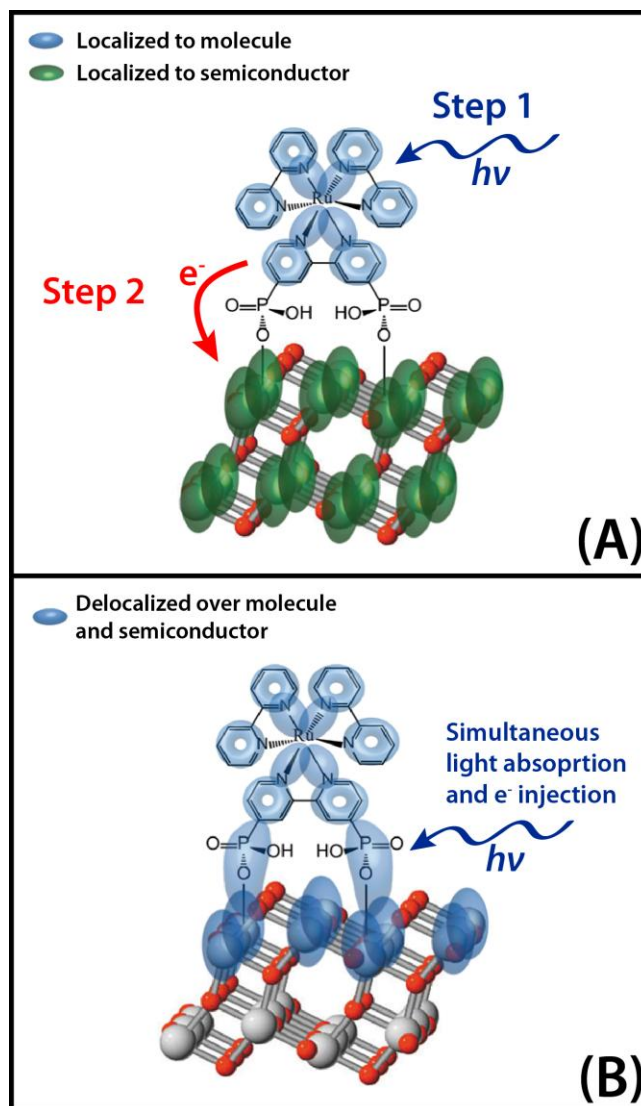
Figure 1.5: Schematic showing the two mechanisms of molecule-TiO_2 electron injection. Colored ovals represent the spatial locations of excited states in the system. Note that these are shown for illustrative purposes only and do not accurately represent the electronic structure. (A) For this weakly coupled molecule-TiO_2 geometry, excited states are independently localized onto the molecule and TiO_2 moieties. Therefore, light absorption creates photoexcitations that are spatially localized to the molecule. Subsequently, after some non zero delay an electron is injected from the molecule excited state to the TiO_2 excited state(s). (B) For this strongly coupled molecule-TiO_2 geometry, excited states are spatially delocalized over both the molecule and the TiO_2. Consequently, light absorption and electron injection should be considered to be the same process (charge transfer resonance).

1.5. STRUCTURE OF DISSERTATION

As aforementioned, this dissertation is concerned with examining mechanisms of energy and charge transport in a variety of synthetic systems. Chapter 2 reviews the theoretical framework needed to describe these mechanisms. Starting with the standard form of Fermi's golden rule, a reduced description of the rate law will be presented that is more suitable for the condensed phase systems studied herein. Derivations of Förster theory, Marcus theory, and absorption lineshapes from this reduced description are included to demonstrate its versatility. Finally, a discussion of optical response theory in the context of time dependent perturbation theory provides the groundwork for understanding spectroscopic experiments in this dissertation. Diagrammatic time dependent perturbation theory is introduced as well as four-wave mixing signal components.

Chapter 3 presents the technical experimental aspects of this dissertation. The principles of the generation of ultrashort light pulses are discussed as well as the management of pulse dispersion. Technical details of the interferometric transient grating spectroscopy utilized are also developed. Chapter 4 presents the transient grating study of the well known gold nanocluster, $Au_{25}(SCH_2CH_2Ph)_{18}^{-}$. Extremely fast internal conversion mechanisms are exhibited, which is discussed in the context of energy transfer between core and semiring localized excited states. Femtosecond resolved polarization anisotropy measurements also provide strong empirical support for the Superatom model. Chapter 5, presents a transient grating and steady state spectroscopic study on the analogous bimetallic nanocluster, $Au_{24}Pd(SCH_2CH_2Ph)_{18}^{-}$. The results substantiate the energy transfer mechanisms developed in Chapter 4 along with providing further strong evidence for the existence of the somewhat controversial semiring localized excited states in both of these nanocluster systems.

A primarily spectroscopic study on the newly synthesized low band gap π-conjugated polymer, PNDT-DTPyT is presented in Chapter 6. Transient grating experiments probing the energy and electron transfer mechanisms of both pure polymer thin films and polymer-PCBM bulk heterojunction thin films are discussed in detail. Results are found to correlate with overall photoconversion efficiencies for devices prepared in an identical manner. Chapter 7 presents a study on intramolecular electron transfer mechanisms in the prototypical transition metal polypyridyl complex, $Os^{II}(bpy)_3$. Transient absorption anisotropy is developed as a new experimental technique in which to ascertain the adiabaticity of electron transfer mechanisms; a property that is notoriously difficult to determine experimentally.

Finally, Chapter 8 presents specialized transient grating experiments probing the electron injection mechanism of the dye sensitized TiO_2 nanocluster system, $[(Ru(bpy)_2(4,4'-(PO_3H_2)_2bpy)]^{2+}/TiO_2$. Results provide surprising evidence of a large sub-ensemble of the system exhibiting strong dye-TiO_2 coupling (i.e, charge transfer character) even with the nominally weakly coupled phosphonate linkers. These conclusions are verified with identical experiments on a strongly coupled system, catechol-TiO2. The specialized technique used in this study is suggested as a simple and direct method to probe the "average" charge transfer character of a given system.

Algorithms for numerically correcting high order ultrafast pulse dispersions and for processing TG interferometric signals are given in Appendices 1 and 2, respectively. Supporting information for the studies discussed in Chapters 4-8 is included in Appendices 3-7.

1.6. REFERENCES

(1)   Pratt, L. R. Chem. Rev. 2002, 102, 2625-2626.

(2)   Soper, A. K.; Rossky, P. J. *Chem. Phys.* 2000, *258*, 107-108.

(3)   Dirac, P. A. M. *Proc. Roy. Soc. A.* 1927, *114*, 243-265.

(4)   Fermi, E. *Nuclear Physics*; University of Chicago Press: Chicago, 1950.

(5)   Marcus, R. A. *J. Chem. Phys.* 1965, *24*, 966-978.

(6)   Förster, T. *Ann. Phys.* 1948, *437*, 55-75.

(7)   Lin, S. H. *J. Chem. Phys.* 1996, *44*, 3759-3767.

(8)   Bixon, M.; Jortner, J. *J. Chem. Phys.* 1968, *48*, 715-726.

(9)   Henry, B. R.; Kasha, M. *Ann. Rev. Phys. Chem.* 1968, *19*, 161-192.

(10)   Mukamel, S. *Principles of Nonlinear Optical Spectroscopy*; Oxford University Press: New York, 1995.

(11)   Parson, W. W. *Modern Optical Spectroscopy: With Examples from Biophysics and Biochemistry*; Springer-Verlag Berlin Heidelberg: New York, 2007.

(12)   Wirth, M. J. *Anal. Chem.* 1990, *62*, 270-275 A.

(13)   Zewail, A. H. *Angew. Chemie* 2000, *39*, 2586-2631.

(14)   Bucksbaum, P. H. *Science* 2007, *317*, 766-769.

(15)   Bernstein, P. L. *The Power of Gold: The History on an Obsession*; John Wiley & Sons, Inc.: New York, 2000.

(16)   Rajesh, S.; Funston, A. M.; Mulvaney, P.; Murray, R. W. *Langmuir* 2009, *25*, 13840-13851.

(17)   Daniel, M.-C.; Astruc, D. *Chem. Rev.* 2004, *104*, 293-346.

(18)   Antonello, A.; Holm, A. H.; Instuli, E.; Maran, F. *J. Am. Chem. Soc.* 2007, *129*, 9836-9837.

(19)   Pasquato, L.; Pengo, P.; Scrimin, P. *J. Mater. Chem.* 2004, *14*, 3481-3487.

(20)   Wohltjen, H.; Snow, A. W. *Anal. Chem.* 1998, *70*, 2856-2859.

(21)   Nam, J.-M.; Thaxton, C. S.; Mirkin, C. A. *Science* 2003, *301*, 1884-1886.

(22)   Anker, J. N.; Hall, W. P.; Lyandres, O.; Shah, N. C.; Zhao, J. *Nat. Mater.* Van Duyne, R. P., *7*, 442-453.

(23)   Schultz, S.; Smith, D. R.; Mock, J. J.; Schultz, D. A. *Proc. Natl. Acad. Sci.* 2000, *97*, 996-1001.

(24)   Yguerabide, J.; Yguerabide, E. E. *Anal. Biochem.* 1998, *262*, 137-156.

(25)   Myroshnychenko, V.; Rodrígues-Fernández, J.; Pastoriza-Santos, I.; Funston, A. M.; Novo, C.; Mulvaney, P.; Liz-Marzán, L. M.; García de Abajo, F. J. *Chem. Soc. Rev.* 2008, *37*, 1792-1805.

(26)   Kelly, K. L.; Coronado, E.; Zhao, L. L.; Schatz, G. C. *J. Phys. Chem. B* 2003, *107*, 668-677.

(27)   Alivisatos, A. P. *Science* 1996, *271*, 933-937.

(28)   Ellert, C.; Schmidt, M.; Schmitt, C.; Reiners, T.; Haberland, H. *Phys. Rev. Lett.* 1995, *75*, 1731-1734.

(29)   Wang, C. R. C.; Pollack, S.; Dahlseid, T. A.; Koretsky, G. M.; Kappes, M. M. *Chem. Phys.* 1992, *96*, 7931-7937.

(30)   Murray, R. W. *Chem. Rev.* 2008, *108*, 2688-2720.

(31)   Zhu, M.; Aikens, C. M.; Hollander, F. J.; Schatz, G. C.; Jin, R. *J. Am. Chem. Soc.* 2008, *130*, 5883-5885.

(32)   Laaksonen, T.; Ruiz, V.; Liljeroth, P.; Quinn, B. M. *Chem. Soc. Rev.* 2008, *37*, 1836-1846.

(33)   Häkkinen, H. *Chem. Soc. Rev.* 2008, *37*, 1847-1859.

(34)   Varnavski, O.; Ramakrishna, G.; Kim, J.; Lee, D.; Goodson, T. *J. Am. Chem. Soc.* 2009, *132*, 16-17.

(35)   Jadzinsky, P. D.; Calero, G.; Ackerson, C. J.; Bushnell, D. A.; Kornberg, R. D. *Science* 2007, *318*, 430-433.

(36)   Walter, M.; Akola, J.; Lopez-Acevedo, O.; Jadzinsky, P. D.; Calero, G.; Ackerson, C. J.; Whetten, R. L.; Grönbeck, H.; Häkkinen, H. *Proc. Natl. Acad. Sci.* 2008, *105*, 9157-9162.

(37)   Aikens, C. M. *J. Phys. Chem. C* 2008, *112*, 19797-19800.

(38)   Link, S.; El-Sayed, M. A.; Schaaf, T. G.; Whetten, R. L. *Chem. Phys. Lett.* 2002, *356*, 240-246.

(39)   Jin, R. *Nanoscale* 2010, *2*, 343-362.

(40)   Heaven, M. W.; Dass, A.; White, P. S.; Holt, K. M.; Murray, R. W. *J. Am. Chem. Soc.* 2008, *130*, 3754-3755.

(41)   Whetten, R. L.; Price, R. C. *Science* 2007, *318*, 407-408.

(42)   Zhu, M.; Eckenhoff, W. T.; Pintauer, T.; Jin, R. *J. Phys. Chem. C* 2008, *112*, 14221-14224.

(43)   Knight, W. D.; Clemenger, K.; de Heer, W. A.; Saunders, W. A.; Chou, M. Y.; Cohen, M. L. *Phys. Rev. Lett.* 1984, *52*, 2141-2143.

(44)   Khanna, S. N.; Jena, P. *Phys. Rev. Lett.* 1992, *69*, 1664-1667.

(45)   de Heer, W. A. *Rev. Mod. Phys.* 1993, *65*, 611-675.

(46)   Reveles, J. U.; Khanna, S. N.; Roach, P. J.; Castleman, A. W. *Science* 2006, *307*, 231-235.

(47)   Kiran, B.; Jena, P.; X., L.; Grubisic, A.; Stokes, S. T.; Ganteför, G. F.; Bowen, K. H.; Burgert, R.; Schnöckel, H. *Phys. Rev. Lett.* 2007, *98*, 256801-256801-256804.

(48)   Miller, S. A.; Fields-Zinna, C. A.; Murray, R. W.; Moran, A. M. *J. Phys. Chem. Lett.* 2010, *1*, 1383-1387.

(49)   Miller, S. A.; Womick, J. M.; Parker, J. F.; Murray, R. W.; Moran, A. M. *J. Phys. Chem. C.* 2009, *113*, 9440-9444.

(50)   Clarke, T. M.; Durrant, J. R. *Chem. Rev.* 2010, *110*, 6736-6767.

(51)   Dennler, G.; Scharber, M. C.; Brabec, C. J. *Adv. Mater.* 2009, *21*, 1323-1338.

(52)   Heeger, A. J. *Synth. Met.* 2002, *125*, 23-42.

(53)   Salaneck, W. R.; Friend, R. H.; Brédas, J. L. *Phys. Rep.* 1999, *319*, 231-251.

(54)   Uy, R. L.; Price, S. C.; You, W. *Macromol. Rapid Commun.* 2012, *33*, DOI: 10.1002/marc.201200129.

(55)   Brédas, J.-L.; Cornil, J.; Heeger, A. J. *Adv. Mat.* 1996, *8*, 447-452.

(56)   Antoniadis, H.; Hsieh, B. R.; Abkowitz, M. A.; Jenekhe, S. A.; Stolka, M. *Synth. Met.* 1994, *62*, 265-271.

(57)   Reiβ, W.; Karg, S.; Dyakonov, V.; Meier, M.; Schwoerer, M. *Lumin.* 1994, *60-61*, 906-911.

(58)   Tang, C. W. *Appl. Phys. Lett.* 1985, *48*, 183-185.

(59)   Yu, G.; Gao, J.; Hummelen, J. C.; Wudl, F.; Heeger, A. J. *Science* 1995, *270*, 1789-1791.

(60)   Sariciftci, N. S.; Smilowitz, L.; Heeger, A. J.; Wudl, F. *Science* 1992, *258*, 1474-1476.

(61)   Kraabel, B.; Lee, C. H.; McBranch, D.; Moses, D.; Sariciftci, N. S.; Heeger, A. J. *Chem. Phys. Lett.* 1993, *213*, 389-394.

(62)   Sariciftci, N. S.; Braun, D.; Zhang, C.; Srdanov, V. I.; Heeger, A. J.; Stucky, G.; Wudl, F. *Appl. Phys. Lett.* 1993, *62*.

(63)   Nelson, J. Curr. Opin. Solid State Mat. Sci. 2002, 6, 87-95.

(64)   Halls, J. J. M.; Pichler, K.; Friend, R. H.; Moratti, S. C.; Holmes, A. B. *Appl. Phys. Lett.* 1996, *68*, 3120-3122.

(65)   Yang, C. L.; Tang, Z. K.; Ge, W. K.; Wang, J. N.; Zhang, Z. L.; Jian, X. Y. *Appl. Phys. Lett.* 2003, *83*, 1737.

(66)   Terao, Y.; Sasabe, H.; Adachi, C. *Appl. Phys. Lett.* 2007, *90*, 1035151-1035153.

(67)   Markov, D. E.; Amsterdam, E.; Blom, P. W. M.; Sieval, A. B.; Hummelen, J. C. *J. Phys. Chem. A* 2005, *109*, 5266-5274.

(68)   Markov, D. E.; Tanase, C.; Blom, P. W. M.; Wildeman, J. *Phys. Rev. B* 2005, *72*, 045217-045211-045216.

(69)   Scully, S. R.; McGehee, M. D. *J. Appl. Phys.* 2006, *100*, 034907-034901-034905.

(70)   Stübinger, T.; Brütting, W. *J. Appl. Phys.* 2001, *90*, 3632-3641.

(71)   Piliego, C.; Holcombe, T. W.; Douglas, J. D.; Woo, C. H.; Beaujuge, P. M.; Frechet, J. M. J. *Journal of the American Chemical Society* 2010, *132*, 7595-7597.

(72)   Liang, Y.; Xu, Z.; Xia, J.; Tsai, S.-T.; Wu, Y.; Li, G.; Ray, C.; Yu, L. *Advanced Materials* 2010, *22*, E135-E138.

(73)   Liang, Y.; Yu, L. *Accounts of Chemical Research* 2010, DOI:10.1021/ar1000296.

(74)   Chen, H.-Y.; Hou, J.; Zhang, S.; Liang, Y.; Yang, G.; Yang, Y.; Yu, L.; Wu, Y.; Li, G. *Nat Photon* 2009, *3*, 649-653.

(75)   Park, S. H.; Roy, A.; Beaupre, S.; Cho, S.; Coates, N.; Moon, J. S.; Moses, D.; Leclerc, M.; Lee, K.; Heeger, A. J. *Nature* Photonics 2009, *3*, 297-302.

(76) Miller, S. A.; Stuart, A. C.; Womick, J. M.; Zhou, H.; You, W.; Moran, A. M. *J. Phys. Chem. C.* 2011, *115*, 2371-2380.

(77) Service, R. F. *Science* 2011, *332*, 293.

(78) Green, M. A.; Emery, K.; Hishikawa, Y.; Warta, W.; Dunlop, E. D. *Prog. Photo. Res. Appl.* 2011, *20*, 12-20.

(79) Zhou, H.; Yang, L.; Stuart, A. C.; Price, S. C.; Liu, S.; You, W. *Angew. Chemie* 2011, *50*, 2995-2998.

(80) Price, S. C.; Stuart, A. C.; Yang, L.; Zhou, H.; You, W. *J. Am. Chem. Soc.* 2011, *133*, 4625-4631.

(81) Grätzel, M. *Nature* 2001, *414*, 338-344.

(82) Brattain, W. H.; Garrett, C. G. B. *Bell. Syst. Tech. J.* 1955, *34*, 129-176.

(83) Gerishcher, H. *J. Electrochem. Soc.* 1966, *113*, 1174-1182.

(84) Fujishima, A.; Honda, K. *Nature* 1972, *238*, 37-38.

(85) Serpone, N. *J. Phys. Chem. B* 2006, *110*, 24287-24293.

(86) Hagfeldt, A.; Boschloo, G.; Sun, L.; Kloo, L.; Pettersson, H. *Chem. Rev.* 2010, *110*, 6595-6663.

(87) Peter, L. M. *J. Phys. Chem. Lett.*, *2*, 1861-1867.

(88) O'Regan, B.; Grätzel, M. *Nature* 1991, *353*, 737-740.

(89) Gerishcher, H.; Tributsch, H. *Ber. Bunsen-Ges. Phys. Chem.* 1968, *72*, 437-455.

(90) Gerishcher, H.; Michel-Beyerle, M. E.; Rebentrost, F.; Tributsch, H. *Electrochim. Acta* 1968, *13*, 1509-1515.

(91) Ghosh, H. N.; Asbury, J. B.; Lian, T. *J. Phys. Chem. B* 1998, *102*, 6482-6486.

(92) Asbury, J. B.; Hao, E.; Wang, Y.; Ghosh, H. N.; Lian, T. *J. Phys. Chem. B* 2001, *105*, 4545-4557.

(93) Concepcion, J. J.; Jurss, J. W.; Brennaman, M. K.; Hoertz, P. G.; Patrocinio, A. O. T.; Iha, N. Y. M.; Templeton, J. L.; Meyer, T. J. *Acc. Chem Res.*, *42*, 1954-1965.

(94) Hanson, K.; Brennaman, M. K.; Luo, H.; Glasson, C. R. K.; Concepcion, J. J.; Song, W.; Meyer, T. J. *Appl. Mater. Interfaces* 2012, *4*, 1462-1469.

(95)   Ardo, S.; Meyer, G. J. *Chem. Soc. Rev.* 2009, *38*, 115-164.

(96)   Duncan, W.; Prezhdo, O. V. *Annu. Rev. Phys. Chem.* 2007, *58*, 143-184.

(97)   Miller, S. A.; West, B. A.; Curtis, A. C.; Papanikolas, J. M.; Moran, A. M. *J. Chem. Phys.* 2011, *135*, 081101-081101-081104.

(98)   Gerishcher, H. *Surf. Sci.* 1969, *18*, 97-122.

(99)   Gerishcher, H. *Photoche. Photobiol.* 1972, *16*, 243-260.

CHAPTER 2 . SPECTROSCOPY AND DYNAMICS IN CONDENSED PHASES

2.1. FERMI'S GOLDEN RULE

2.1.1. Standard Form

The following is a brief derivation of the well known rate law known as Fermi's Golden Rule.[1-3] Assuming an equilibrium system with population initially residing in state $|a\rangle$ one can calculate the transition between the initial state $|a\rangle$ and final state $|b\rangle$ following a weak time dependent perturbation. In the context of this dissertation, we assume an oscillatory perturbation with angular frequency $\omega = 2\pi\nu$ (i.e., an electromagnetic field), however, a similar derivation can be performed assuming any weak perturbation. The first order coefficient for the basis function "b" following the perturbation, $\hat{V}_{ba}(t')$, at $t=0$ is defined as

$$c_b^{(1)} = -\frac{i}{\hbar}\int_0^t \hat{V}_{ba}(t')e^{(i\omega_{ba}t')}dt'$$

(2.1)

where ω_{ba} is proportional to the energy gap between states $|a\rangle$ and $|b\rangle$. The time dependent oscillatory perturbation is defined as

$$\hat{V}_{ba}(t') = 2V_{ba}\cos(\omega t) = V_{ba}(e^{i\omega t'} + e^{-i\omega t'})$$

(2.2)

for $t \geq 0$. If this expression is inserted into Equation 2.1 we calculate the first order

coefficient as

$$c_b^{(1)}(t) = -\frac{i}{\hbar}V_{ba}\int_0^t (e^{i\omega t'} + e^{-i\omega t'})e^{(i\omega_{ba}t')}dt' = \frac{-iV_{ba}}{\hbar}\left[\frac{e^{i(\omega_{ba}+\omega)t}-1}{i(\omega_{ba}+\omega)} + \frac{e^{i(\omega_{ba}-\omega)t}-1}{i(\omega_{ba}-\omega)}\right] \qquad (2.3)$$

Assuming that states $|a\rangle$ and $|b\rangle$ are separate electronic energy levels and that the perturbative radiation is in the visible (or near visible) region of the electromagnetic spectrum, the frequencies ω_{ba} and ω will both be on the order of $10^{15}\,\text{s}^{-1}$. Therefore, when the perturbative radiation is on or near resonance to the energy gap, ω_{ba} (i.e., $\omega \cong \omega_{ba}$), the right term in Equation 2.3 will dominate entirely and the left term can be neglected.

The probability of finding the system in state $|b\rangle$ at time "t" if initially in state $|a\rangle$ at $t=0$, is given as the square of the first order coefficient

$$P_b(t) = \left|c_b^{(1)}(t)\right|^2 = \left|\frac{-iV_{ba}}{\hbar}\left[\frac{e^{i(\omega_{ba}-\omega)t}-1}{i(\omega_{ba}-\omega)}\right]\right|^2 = \frac{4|V_{ba}|^2}{\hbar^2(\omega_{ba}-\omega)^2}\sin^2\left[(\omega_{ba}-\omega)t/2\right] \qquad (2.4)$$

where Euler's formula was used in the simplification. A plot of $P_b(t)$ versus $\omega_{ba}-\omega$ at various values of "t" shown in Figure 2.1 demonstrates the intuitive results from Equation 2.4 in that the probability of finding the system in state $|b\rangle$ increases with time as long as the perturbative radiation is on or near on resonance with the energy gap between states $|a\rangle$ and $|b\rangle$.
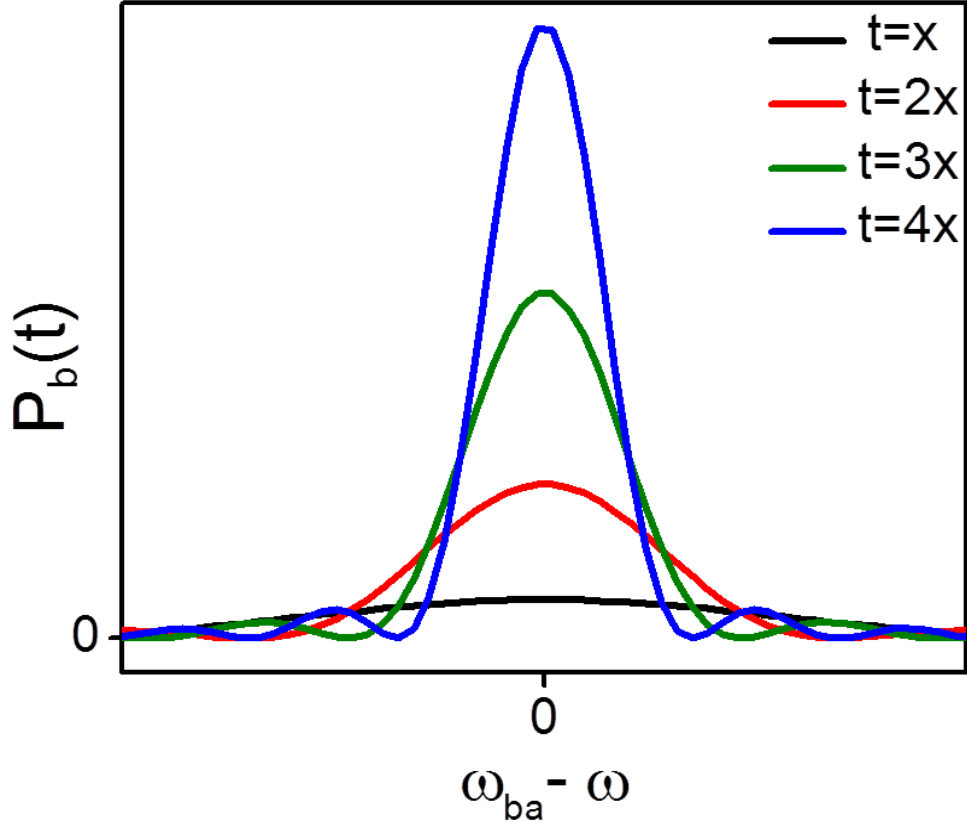
Figure 2.1: The probability of finding the system in state $|b\rangle$ at time "t" if initially residing in state $|a\rangle$ at $t = 0$ as calculated by Equation 2.4. As "t" increases, the probability of being found in state $|b\rangle$ increases as long as the perturbative radiation is on resonance with ω_{ba}.

Another way of looking at this result is to envision perturbing the system with a laser pulse that is long in duration and (necessarily) narrow in bandwidth.[4] In this situation, it is only possible to perturb the system when the laser frequency is very close to the resonant frequency because the narrow bandwidth will otherwise not overlap with the system resonance.

At very long times, the system will tend towards a "steady state" which can be represented by taking the limit of Equation 2.4 as time approaches infinity

$$\lim_{t\to\infty} P_b(t\to\infty) = \lim_{t\to\infty} \frac{4|V_{ba}|^2 \sin^2\left[(\omega_{ba}-\omega)t/2\right]}{\hbar^2(\omega_{ba}-\omega)^2} = \frac{2\pi t|V_{ba}|^2}{\hbar^2}\delta(\omega_{ba}-\omega)$$

$$\text{(2.5)}$$

$$\text{using} \quad \delta(x) = \lim_{t\to\infty} \frac{\sin^2(tx)}{\pi x^2 t}$$

In this limit, a very long lasting perturbation (i.e., monochromatic electromagnetic radiation) will only result in the system being in state $|b\rangle$ if the frequency exactly matches the energy gap between states $|a\rangle$ and $|b\rangle$. To obtain the steady state rate between states $|a\rangle$ and $|b\rangle$, one takes the time derivative of the steady state population in state $|b\rangle$.

$$k_{ba}(\omega) = \frac{\partial}{\partial t} P_b(t\to\infty) = \frac{2\pi|V_{ba}|^2}{\hbar^2}\delta(\omega_{ba}-\omega) \qquad \text{(2.6)}$$

In a realistic system where there is more than one initial or final state, one must consider transitions between all states. The net rate between starting states and final states is therefore a summation between all thermally populated starting states and final states.

$$k_{Total}(\omega) = \sum_a \sum_b P_a k_{ba} \qquad \text{(2.7a)}$$

$$P_a = \frac{e^{-\omega_a/k_B T}}{\sum_a e^{-\omega_a/k_B T}} \qquad \text{(2.7b)}$$

Substituting k_{ba} from Equation 2.6 results in the following expression for the total rate

$$k_{Total}(\omega) = \frac{2\pi}{\hbar^2} \sum_a \sum_b P_a |V_{ba}|^2 \delta(\omega_{ba}-\omega) \qquad \text{(2.8)}$$

which is Fermi's Golden Rule. Although Equation 2.8 has been derived here in the context of an electromagnetic perturbation, Fermi's Golden Rule is equally valid for any type of

32

external perturbation. Thus, the delta function can be given as a general energy gap between two states, which yields a more general form of Fermi's Golden Rule

$$k_{Total} = \frac{2\pi}{\hbar^2} \sum_a \sum_b P_a |V_{ba}|^2 \, \delta(E_b - E_a)$$

(2.9)

2.1.2 Reduced Description

Equation 2.9, although not written in the more recognizable manner using a density of states rather than discrete states, is a form of Fermi's Golden Rule. For condensed phase systems, however, it is an impractical expression due to the fact that in order to calculate the total rate, one must sum over the entire ensemble of states $|a\rangle$ and $|b\rangle$. There is, however, another way to consider the system discussed above, which allows Fermi's Golden Rule to be formulated in a more practical expression.[3, 5-7]

Equation 2.9 was obtained from a picture where the entire ensemble is considered all at once. The same system can be equivalently modeled by considering a two state system that undergoes interactions with a bath. These system-bath interactions cause fluctuations in the energy levels of states $|a\rangle$ and $|b\rangle$, therefore also causing fluctuations in the energy gap between the two states, $E_b - E_a$. According to the Ergodic hypothesis of statistical mechanics, for a microscopically fluctuating system that is macroscopically stationary in time, a time average of a single fluctuating parameter over very long times is equivalent to averaging the same parameter over the entire system ensemble.[5, 8]

$$\left\langle x(t) y^*(0) \right\rangle = \lim_{\tau \to \infty} \frac{1}{\tau} \int_0^\tau x(t + t') y^*(t') dt'$$

(2.10)

Using this reasoning, it is shown here that Equation 2.9 can written equivalently as an integral over time of a quantum time correlation function associated with the perturbative part of the Hamiltonian associated with the transition.[3, 5-7] First, Equation 2.9 must be converted to the time domain using the definition of the delta function

$$\delta(\omega) \equiv \frac{1}{2\pi} \int_{-\infty}^{\infty} dt\, e^{i\omega t} \qquad (2.11)$$

which yields

$$k_{ba} = \frac{1}{\hbar^2} \sum_a \sum_b P_a \left| V_{ba} \right|^2 \int_{-\infty}^{\infty} dt \exp\left[\frac{it}{\hbar} (E_b - E_a) \right] \qquad (2.12)$$

If one writes the matrix elements of V_{ba} explicitly, Equation 2.12 can be expanded to give the following

$$k_{ba} = \frac{1}{\hbar^2} \sum_a \sum_b P_a \int_{-\infty}^{\infty} dt \exp\left[\frac{it}{\hbar} (E_b - E_a) \right] \langle a|V|b\rangle \langle b|V|a\rangle \qquad (2.13)$$

Furthermore, if one recognizes the fact that $\exp(iH_0 t)|a\rangle = \exp(iE_a t)$, Equation 2.13 can be further expanded to yield

$$k_{ba} = \frac{1}{\hbar^2} \sum_a \sum_b P_a \int_{-\infty}^{\infty} \langle a|V|b\rangle \langle b|e^{iH_0 t} V e^{-iH_0 t}|a\rangle \qquad (2.14)$$

Finally because $\sum_b |b\rangle \langle b| = 1$, Equation 2.14 can be simplified to the final form

$$k_{ba} = \frac{1}{\hbar^2} \mathrm{Re} \int_{-\infty}^{\infty} dt \langle a|\hat{V}_I(0)\hat{V}_I(t)|a\rangle \qquad (2.15a)$$

$$k_{ba} = \frac{1}{\hbar^2} \text{Re} \int_{-\infty}^{\infty} dt \left\langle \hat{V}_I(t) \hat{V}_I(0) \right\rangle \tag{2.15b}$$

where $\hat{V}_I(t) = e^{iH_0 t} V e^{-iH_0 t}$. Although this derivation stressed specific eigenstates, Equation 2.15b is a general expression describing the transition rate of any system given that one has knowledge of the time dependent perturbation, $\hat{V}_I(t)$. For condensed phases where the system is coupled to the bath, this form of Fermi's Golden Rule is more practical to utilize than Equation 2.9. As will be exemplified in Chapters 2.2.1-2.2.3, simply by changing $\hat{V}_I(t)$, one can model rates of change under widely ranging conditions.

2.2. APPLICATIONS TO FERMI'S GOLDEN RULE

2.2.1. Absorption Lineshape

Perhaps the most intuitive way to envision broad absorption spectra in condensed phases is to picture transitions between a large ensemble of initial and final states where interactions with the surrounding environment (i.e., the bath) results in a distribution in energy gaps between these states. Because the transition rate versus frequency is related to the absorption lineshape, the absorption spectrum can be given by Equation 2.8 with $|V_{ba}|$ being the dipole moment, μ. However, given the extremely large number of bath states in a condensed phase system, summing over the entire system-bath ensemble as in Equation 2.8 is not a practical method for determining the absorption lineshape.

On the other the hand, with the reasoning used in Equation 2.15b, one averages over just the bath states instead of averaging over the entire system-bath ensemble. Furthermore,

consisting of a large number of randomly oriented variables, it is relatively straightforward to model the bath states, thus making this method a much more practical method for determining the absorption lineshape. In this method, one models a condensed phase absorption spectrum as a transition between a single ground state, $|a\rangle$, and a single excited state, $|b\rangle$, that undergo random fluctuations in energy due to random interactions with the bath (e.g., collisions with solvent molecules). The absorption lineshape is simply the Fourier transform of the correlation function of the dipole operator for the transition, (i.e., $\langle a|\hat{\mu}(t)\hat{\mu}(0)|a\rangle$).[3, 5-7]

$$L(\omega) \propto \int_{-\infty}^{\infty} dt \langle a|\hat{\mu}(t)\hat{\mu}(0)|a\rangle e^{-i\omega t} \tag{2.16}$$

Because of coupling to the bath, μ_{ba} is randomly fluctuating in time. This can be pictured as the dipole oscillation frequency fluctuating randomly in time about some average value as shown in in Figure 2.2.
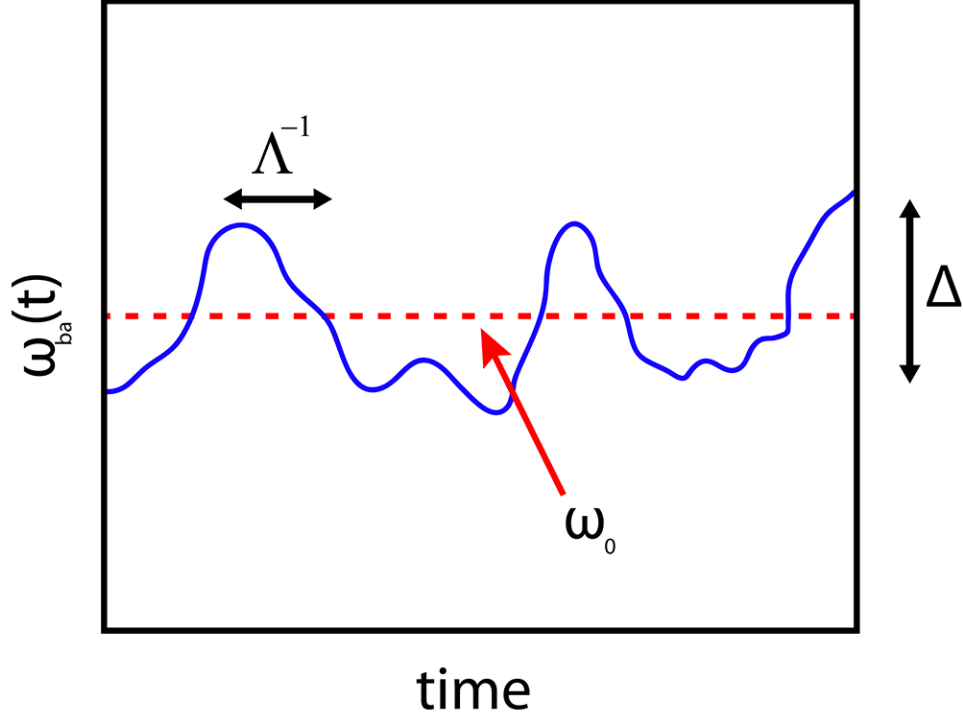
Figure 2.2: Coupling with the bath causes random fluctuations of the transition frequency, ω_{ba} between the single ground state $|a\rangle$ and single excited state $|b\rangle$. The transition frequency fluctuates about a mean frequency, ω_0 with a fluctuation amplitude, Δ. Finally, the timescale of bath fluctuations is governed by the correlation time, Λ^{-1}.

Performing a cumulant expansion on $\langle\hat{u}(t)\hat{u}(0)\rangle$ allows us to rewrite the correlation function

$$\langle a|\hat{u}(t)\hat{u}(0)|a\rangle = |\mu(0)|^2 \, e^{-\omega_0 t} \exp\left[-i\int_0^t d\tau_1 \langle\delta\omega(\tau_1)\rangle - \frac{1}{2}\int_0^t d\tau_1\int_0^t d\tau_2 \langle\delta\omega(\tau_2-\tau_1)\delta\omega(0)\rangle + ...\right] \quad (2.17)$$

where $\delta\omega(\tau_1)$ is the instantaneous fluctuation away from the mean resonance frequency,

ω_0.[3, 5-7] Thus, the time correlation function of the dipole operator has been reduced to a time

correlation function of the resonance frequency. Note also that Equation 2.17 is no longer

averaging over the absolute time, t, but is now averaging over some interval, $\tau_2 - \tau_1$. In a

macroscopic equilibrium system, if the fluctuations $\delta\omega(\tau_1)$ are normally distributed about the

mean frequency, ω_0, the first term of the cumulant expansion does not contribute.   In addition, if one assumes a bath with Gaussian statistics, the Central Limit Theorem finds that all higher order terms in the cumulant expansion also vanish.[5-7]   Thus, one can rewrite Equation 2.17 as the following

$$\langle a|\hat{u}(t)\hat{u}(0)|a\rangle = |\hat{u}(0)|^2 \exp(-\omega_0 t)\exp\left[\int_0^t d\tau_1 \int_0^t d\tau_2 \langle \delta\omega(\tau_2 - \tau_1)\delta\omega(0)\rangle\right]$$

$$= \exp[-i\omega_0 t - g(t)]$$

(2.18a)

$$g(t) = \int_0^t d\tau_1 \int_0^t d\tau_2 \langle \delta\omega(\tau_2 - \tau_1)\delta\omega(0)\rangle$$

(2.18b)

Where we have introduced the line broadening function, $g(t)$. For convenience, Equation 2.18b can be rewritten as the following

$$g(t) = \int_0^t d\tau_1 \int_0^t d\tau_2 \langle \delta\omega(\tau_2 - \tau_1)\delta\omega(0)\rangle = \int_0^t d\tau_1 \int_0^{\tau_1} d\tau_2 \langle \delta\omega(\tau_2 - \tau_1)\delta\omega(0)\rangle = \int_0^t dT(t-T)C(t)$$

(2.19a)

$$C(T) = \langle \delta\omega(\tau_2 - \tau_1)\delta\omega(0)\rangle$$

(2.19b)

where $T = \tau_1 - \tau_2$. The next step is to assume a form for the correlation function, $C(T)$, which is determined by the bath dynamics. The simplest function to assume is an exponential decay of the form

$$C(T) = \Delta^2 \exp(-\Lambda T)$$

(2.20)

where Δ is the fluctuation amplitude and Λ^{-1} is the correlation time or "memory" of a given fluctuation. (See Figure 2.2) The line broadening function $g(t)$ given by Equation 2.19 can therefore be rewritten as

$$g(t) = \Delta^2 \int_0^t dT(t-T)e^{-\Lambda T} = \frac{\Delta^2}{2\Lambda^2}\left[e^{-\Lambda t} + \Lambda t - 1\right] \tag{2.21}$$

and the absorption lineshape given in Equation 2.16 can now be written as

$$L(\omega) \propto \int_{-\infty}^{\infty} dt \left\langle a \middle| \hat{\mu}(t)\hat{\mu}(0) \middle| a \right\rangle e^{-i\omega t} = \int_{-\infty}^{\infty} dt \exp\left[-i\omega t\right]\exp[-i\omega_0 t - g(t)] \tag{2.22a}$$

$$L(\omega) \propto \int_{-\infty}^{\infty} dt \exp\left(-i\omega t\right)\exp\left[-i\omega_0 t - \frac{\Delta^2}{2\Lambda^2}\left[e^{-\Lambda t} + \Lambda t - 1\right]\right] \tag{2.22b}$$

There are two limits to the absorption lineshape that are the result of the line broadening function $g(t)$ and the relative magnitudes of Δ and Λ. In the homogeneous line broadening limit, the magnitude of the fluctuation amplitude is considerably larger than the inverse correlation time (i.e., $\Lambda/\Delta \gg 1$). In general terms, this means that the timescale of the bath motion is fast relative to the process of the molecular system undergoing absorption. In particular, the bath is much faster than the timescale of the molecule-photon interaction.[5] This means that the two states, $|a\rangle$ and $|b\rangle$ experience all possible configurations of the local bath environment on the timescale of the absorption process. For this reason, the homogenous line broadening limit is also referred to as the "fast modulation" limit. Under these conditions, Equation 2.22b can be simplified to the following expression:

$$L(\omega) \propto \int_{-\infty}^{\infty} dt \exp\left(-i\omega t\right)\exp\left[-i\omega_0 t - \frac{\Delta^2}{2\Lambda} t\right] \tag{2.23}$$

If the Fourier transform is carried out in this limit, the resulting absorption lineshape is Lorentzian, which is a spectral signature of being in the homogenous line broadening limit (Figure 2.3(A), black).

The other line broadening limit is the inhomogeneous limit or "slow modulation" limit. In this case, the time scale of the bath motions are slow compared to the timescale of the molecule-photon interaction. Therefore, states $|a\rangle$ and $|b\rangle$ experience only a single bath configuration which results in a narrow linewidth. In an ensemble measurement, different molecules will be under different static bath environments and therefore different transition frequencies. The resulting spectral broadening from the entire ensemble is referred to as inhomogeneous broadening. In this limit, $\Lambda/\Delta \ll 1$, therefore Equation 2.22b can be simplified to

$$L(\omega) \propto \int_{-\infty}^{\infty} dt \exp\left(-i\omega t\right) \exp\left[-i\omega_0 t - \frac{1}{2}\Delta^2 t^2\right] \qquad (2.24)$$

Carrying out the Fourier transform in Equation 2.24 results in Gaussian absorption lineshapes, which is a spectral signature of the being in the inhomogeneous line broadening limit. (Figure 2.3(A), red).
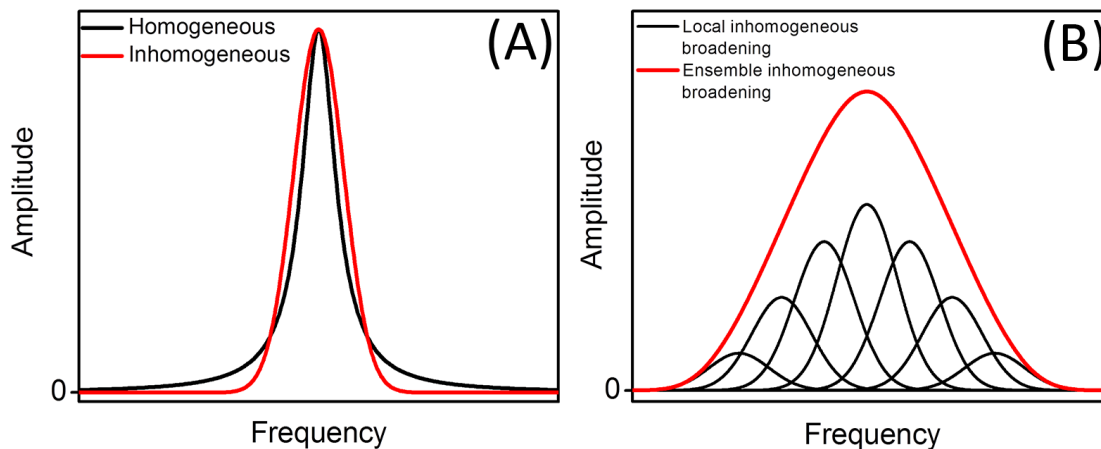
Figure 2.3: (A) Absorption lineshapes in the two broadening limits. Being in the homogeneous or "fast-modulation" limit results in Lorentzian lineshapes (black). Being in the inhomogeneous of "slow-modulation" limit results in Gaussian lineshapes (red). (B) The sum of the local inhomogeneous broadening from sub-ensembles that sample only one bath configuration (black) results in a broad absorption spectrum for the entire ensemble (red).

2.2.2. Förster Resonance Energy Transfer

Consider a system consisting of two isolated molecules, where one molecule, the donor, is initially in its excited electronic state and the other molecule, the acceptor, is initially its ground electronic state. Consider also that the Coulombic coupling between the two molecules is weak compared to the system-bath coupling strength.

$$H^{el-ph} \gg H^{Coul} \tag{2.25}$$

In this situation, transfer of the excitation energy localized on the donor molecule to become localized on the acceptor molecule is best described by the Förster model of resonance energy transfer (FRET)[3, 9]

$$D^* + A \rightarrow D + A^* \tag{2.26}$$

41

where, X^* represents being in the excited state of molecule X. Note that FRET is often referred to as fluorescence resonance energy transfer, however this is something of a misnomer as the energy transfer process is nonradiative. The rate of energy transfer between the donor and acceptor molecules in the Förster regime is well known and is generally given by an expression of the form

$$k_{DA} \propto |J_{DA}|^2 \int F_D(\omega) A_A(\omega) d\omega \qquad (2.27)$$

where, J_{DA}, represents the dipole-dipole coupling interaction between the donor and acceptor molecules, and the integral represents the overlap integral between the fluorescence spectrum of the donor molecule, $F_D(\omega)$, and the absorbance spectrum of the acceptor molecule, $A_A(\omega)$. At this point, one may recognize that Equation 2.27 is merely Equation 2.9 written in a different form, where, V_{ba}, is now given by the dipole-dipole coupling, J_{DA}. That is, it is merely another formulation of Fermi's Golden Rule written in a form suitable for the Förster regime. Remembering that Fermi's Golden Rule can also be written equivalently as a time integral of the perturbative part of the Hamiltonian (Equation 2.15b), below it is shown that Equation 2.27 can be derived in the same manner.[3]

The dipole-dipole coupling for the Förster transition is given by the following expression[9]

$$J_{DA} = \kappa \bullet \eta \left(\frac{|\mu_{eg,D}||\mu_{eg,A}|}{r_{DA}^3} \right) \qquad (2.28)$$

where r_{DA} is the intermolecular distance between the donor and acceptor molecules, η, is a constant used for unit conversion (5.04 cm^{-1} nm^3 D^{-2}), and $|\mu_{eg,D}|$ and $|\mu_{eg,A}|$ are the

magnitudes of the transition dipoles between the ground and excited states of the donor and acceptor molecules, respectively. The orientational factor, κ, governs the importance of the relative orientation of the two transition dipoles on the magnitude and sign of J_{DA} and will be discussed in detail below.

We can now insert the expression for the dipole-dipole coupling interaction, J_{DA}, into Equation 2.15b, which results in the following expression for the Förster rate

$$k_{DA} = \frac{1}{\hbar^2} \text{Re} \int_{-\infty}^{\infty} dt \left\langle e_D g_A \left| J_{DA}(t) J_{DA}(0) \right| e_D g_A \right\rangle \tag{2.29a}$$

$$k_{DA} = \frac{\eta^2}{\hbar^2} \text{Re} \int_{-\infty}^{\infty} dt \frac{\left\langle \kappa^2 \right\rangle}{r_{DA}^6} \left\langle e_D g_A \left| \mu_{eg,D}(t) \mu_{eg,A}(t) \mu_{eg,D}(0) \mu_{eg,A}(0) \right| e_D g_A \right\rangle \tag{2.29b}$$

It is worth noting that because the Hamiltonian is a Hermitian operator, one can write the basis set for the two molecule-two level system as a direct product of original basis states (e.g., $\left| e_D \right\rangle \left| g_A \right\rangle = \left| e_D g_A \right\rangle$) which allows Equation 2.29b two be written as shown.[1] Because the dipole operators act only on $\left| g_A \right\rangle$ or $\left| e_D \right\rangle$ and the donor and acceptor nuclear coordinates are orthogonal, Equation 2.29b can be rewritten as a product of correlation functions of the donor and acceptor molecules

$$k_{DA} = \frac{\eta^2}{\hbar^2} \text{Re} \int_{-\infty}^{\infty} dt \frac{\left\langle \kappa^2 \right\rangle}{r_{DA}^6} \left\langle e_D \left| \mu_{eg,D}(t) \mu_{eg,D}(0) \right| e_D \right\rangle \left\langle g_A \left| \mu_{eg,A}(t) \mu_{eg,A}(0) \right| g_A \right\rangle \tag{2.30}$$

Examination of Equation 2.30 should show strong similarities to the previous section. That is, the third correlation function in Equation 2.30, $\left\langle g_A \left| \mu_{eg,A}(t) \mu_{eg,A}(0) \right| g_A \right\rangle$, is equivalent to that used in the expression for the absorption lineshape derived above in Equation 2.16 for the acceptor molecule. Although not shown above, by the same reasoning the second

43

correlation function in Equation 2.30, $\langle e_D | \mu_{eg,D}(t)\mu_{eg,D}(0) | e_D \rangle$, represents the fluorescence

lineshape of the donor molecule. According to Parsival's theorem, we can now rewrite

Equation 2.30 as the following

$$k_{DA} = \frac{\eta^2 \langle \kappa^2 \rangle}{\hbar^2 r_{DA}^6} \left| \mu_{eg,D} \right|^2 \left| \mu_{eg,A} \right|^2 \int_{-\infty}^{\infty} F_D(\omega)A_A(\omega)d\omega \qquad (2.31)$$

where again, $F_D(\omega)$ represents the normalized fluorescence spectrum of the donor molecule

and $A_A(\omega)$ represents the normalized absorbance spectrum of the acceptor molecule.[10]

Thus, the equivalency of Equations 2.27 and 2.15 has been shown.

The factors on the outside of the integral of Equation 2.31 govern the donor-acceptor

dipole-dipole coupling. As mentioned above, the orientational average, $\langle \kappa \rangle$ is important to

both the sign and magnitude of the coupling and is given by the following expression

$$\kappa = \hat{\mu}_{eg,D} \bullet \hat{\mu}_{eg,A} - 3(\hat{\mu}_{eg,D} \bullet \hat{n}_{DA})(\hat{\mu}_{eg,A} \bullet \hat{n}_{DA}) \qquad (2.32)$$

where $\hat{n}_{DA}$ is the unit vector connecting between the donor and acceptor molecules.[8]

Equation 2.32 is only needed when the dipoles of each molecule are static with a well

defined orientation (e.g., embedded in a lattice structure). If, however, the transition dipoles

are initially randomly oriented and static on the timescale of the Förster energy transfer

process, then $\langle \kappa \rangle^2 = 2/3$.[8] On the other hand, if the dipoles are initially randomly oriented

and rotate on a timescale much faster than the rate of the Förster energy transfer process, then

$\langle \kappa \rangle^2 = 0.475$.[8]

2.1.3. Marcus Theory of Electron Transfer

Originally developed by Rudolph Marcus in the 1950's and ultimately leading to the 1992 chemistry Nobel prize, Marcus theory of electron transfer has been extraordinarily successful at describing the rates of electron transfer between weakly coupled species in condensed phase systems.[11]   Consider an electron transfer process occurring in a system consisting of two species; a donor, D and acceptor, A.

$$D + A \rightarrow D^+ + A^-$$
(2.33)

While these species can be as complex as one would like to imagine, Marcus theory describes the electron transfer process shown in Equation 2.33, as mediated by a single collective nuclear coordinate, q containing all nuclear degrees of freedom. This collective nuclear coordinate can include both intramolecular vibrational motion coupled to the electron transition (i.e., the "inner-sphere" contribution) and the nuclear motions of the surrounding solvent environment (i.e., the "outer-sphere" contribution).[11, 12] Marcus theory describes the electronic structure of the donor and acceptor states as Born-Oppenheimer quadratic free energy surfaces in "q-space" where electron transfer between the surfaces can occur at nuclear configurations where the states are degenerate. An example of this is shown in Figure 2.4 exhibiting a thermally activated electron transfer process where only the "outer-sphere" contribution to q is considered. Initially, electronic population resides on the donor potential energy surface at the minimum of the parabola. Thermal fluctuations in the solvent cause changes in the nuclear geometry. If $k_B T$ is greater than the energy activation barrier, $\Delta E^\dagger$, then it is possible for solvent fluctuations to modify the nuclear geometry enough so that the donor and acceptor potential energy surfaces cross. Once this occurs, an electron is

transferred onto the acceptor potential energy surface where the nuclear geometry subsequently relaxes to the equilibrium position at the bottom of the acceptor parabola.
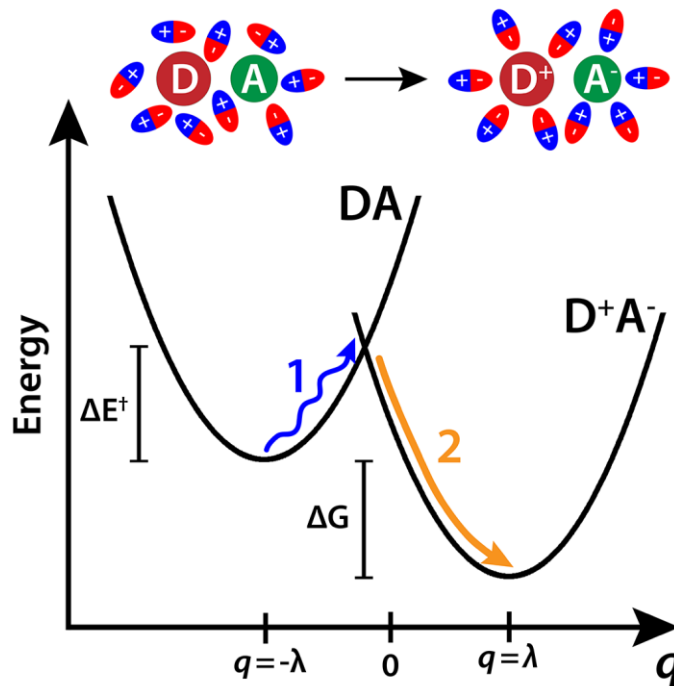
Figure 2.4: Donor (D) and acceptor (A) potential energy Born-Oppenheimer free energy surfaces as described by Marcus theory. Note that it is assumed that the two potential energy surfaces have the same curvature. Therefore, the nuclear configuration, q, is linear in energy.[6] In the example shown, a thermally activated electron transfer process is shown where only the solvent contribution (outer-sphere) is considered. First, solvent fluctuations alter the nuclear geometry randomly until the nuclear configuration, q is "correct" for the donor and acceptor surfaces to cross. Once this occurs, the electron transfers from the donor to the acceptor surface, which subsequently relaxes to the most stable nuclear configuration of the oxidized donor and reduced acceptor state.

The rate of electron transfer as described by Marcus theory is given by the following equation[11]

$$k_{ET} = \frac{2\pi |J|^2}{\hbar\sqrt{4\pi\lambda k_B T}} \exp\left(\frac{-(\Delta G + \lambda)^2}{4\lambda k_B T}\right)$$

(2.34)

where ΔG is the free energy change occurring upon electron transfer, J is the donor-acceptor coupling matrix element, and λ is the reorganization energy of the surrounding nuclei following electron transfer. As the donor and acceptor energy surfaces are Born-Oppenheimer surfaces, they can each be expressed as product states of the electronic and nuclear configurations (e.g., $|D\rangle = |d,n\rangle$ for the donor). Using the Condon approximation, the coupling between the donor and acceptor surfaces is defined as

$$V = J\left[|d\rangle\langle a| + |a\rangle\langle d|\right]$$
(2.35)

where "d" and "a" represent the donor and electronic configurations, respectively.

Marcus originally developed Equation 2.34 using a perturbation theory approach by calculating Franck-Condon factors for the overlap of the donor and acceptor potential energy surfaces. However, as will be shown here, Equation 2.34 can also be derived using the reduced description of Fermi's Golden rule discussed above[5-7]

First, we start with the general expression for the reduced description of Fermi's Golden Rule given above in Equation 2.15b

$$k_{ET} = \frac{1}{\hbar^2}\mathrm{Re}\int_{-\infty}^{\infty} dt \left\langle \hat{V}_I(t)\hat{V}_I(0) \right\rangle$$
(2.36)

As in Chapter 2.2.1, $\hat{V}_I(t) = e^{iH_0 t/\hbar}V e^{-iH_0 t/\hbar}$ which yields

$$k_{ET} = \frac{|J|^2}{\hbar^2}\int_{-\infty}^{\infty} dt\, e^{-i(E_A - E_D)t/\hbar}\left\langle e^{iH_D t/\hbar} e^{-iH_A t/\hbar}\right\rangle$$
(2.37)

Equation 2.37 can be written equivalently in the form of an Energy Gap Hamiltonian (i.e., $H_{DA} = H_A - H_D$) which is given by the following expressions

$$k_{ET} = \frac{|J|^2}{\hbar^2} \int\limits_{-\infty}^{\infty} dt\, e^{-i(E_A - E_D)t/\hbar} F(t) \qquad (2.38a)$$

$$F(t) = \left\langle \exp_+\left(-\frac{i}{\hbar} \int\limits_0^t dt' H_{DA}(t') \right) \right\rangle \qquad (2.38b)$$

$$H_{DA}(t) = e^{iH_D t/\hbar} H_{DA} e^{-iH_D t/\hbar} \qquad (2.38c)$$

In a process equivalent to that shown above for the derivation of the absorption lineshape (Equations 2.17-2.18), a cumulant expansion of Equation 2.38b yields the electron transfer rate in terms of a lineshape function, $g(t)$ and correlation function, $C_{DA}(t)$.

$$F(t) = \exp\left(\frac{-i}{\hbar} \lambda t - g(t) \right) \qquad (2.39a)$$

$$g(t) = \int\limits_0^t d\tau_2 \int\limits_0^{\tau_2} d\tau_1 C_{DA}\left(\tau_2 - \tau_1 \right) \qquad (2.39b)$$

$$C_{DA}(t) = \frac{1}{\hbar^2} \left\langle \delta H_{DA}(t) \delta H_{DA}(0) \right\rangle \qquad (2.39c)$$

$$\lambda = \left\langle H_{DA} \right\rangle \qquad (2.39d)$$

The lineshape function, $g(t)$ can be written as a sum of the nuclear coordinates that are coupled to the electron transfer.[7, 13]

$$g(t) = \sum_\alpha (d_\alpha^A - d_\alpha^D)^2 \left[\coth(\hbar\omega_\alpha / 2k_B T)(1 - \cos(\omega_\alpha t) + i(\sin(\omega_\alpha t) - \omega_\alpha t) \right] \qquad (2.40)$$

where ω_α is frequency of a specific vibrational motion in the system. For the inner-sphere contribution, this is a very intuitive equation as it allows one to show contributions from

48

specific vibrational frequencies, α. However, it is generally more convenient to express the lineshape function as a spectral density where coupling to a harmonic bath can describe both solvent (outer-sphere) and vibrational (inner-sphere) contributions to the electron transfer using the arbitrary form[6, 7]

$$g(t) = \int_0^\infty d\omega \rho(\omega) \left[\coth(\hbar\omega_\alpha / 2k_B T)(1 - \cos(\omega_\alpha t) + i(\sin(\omega_\alpha t) - \omega_\alpha t) \right] \qquad (2.41)$$

In either case, it is useful to consider the classical high temperature limit where only low frequencies are considered (i.e., $\hbar\omega \ll k_B T$). Neglecting the imaginary component of $g(t)$, and making the assumption that $\coth(\hbar\omega/2kT) \cong \dfrac{k_B T}{\hbar\omega}$, the electron transfer rate given by Equation 2.38a can now be written as

$$k_{ET} = \frac{|J|^2}{\hbar^2} \int_{-\infty}^\infty dt e^{-i(E_A - E_D + \lambda)t} \exp\left[\frac{-2Dk_B T}{\hbar\omega_0}(1 - \cos(\omega_0 t)) \right] \qquad (2.42)$$

where $D = (d_\alpha^A - d_\alpha^D)^2$. Again because we are assuming the high temperature limit, we can assume the "low frequency" limit of ω_0. Consequently,

$$\cos(\omega_0 t) \cong 1 - \frac{(\omega_0 t)^2}{2} \qquad (2.43)$$

and Equation 2.42 becomes

$$k_{ET} = \frac{|J|^2}{\hbar^2} \sqrt{\frac{\pi}{4\lambda k_B T}} \exp\left[\frac{-(E_A - E_D + \lambda)^2}{4\lambda k_B T} \right] \qquad (2.44)$$

where the reorganization energy λ is equal to $D\hbar\omega_0$. Note that for a thermally averaged rate, the standard change in free energy of the electron transfer process is given as $\Delta G^0 = E_A - E_D$ therefore we have reproduced Marcus' rate equation.

2.3 OPTICAL RESPONSE THEORY

2.3.1. Feynman Diagrams

According to time dependent perturbation theory the response function governing the response of a material to external field(s) in an Nth order spectroscopic process is the sum of 2^N classes of terms.[2] For higher order spectroscopies, such as the 3rd order transient grating technique utilized in this dissertation, keeping track of all possible terms can be a demanding task. Fortunately, there exist simple diagrammatic "bookkeeping" methods for computing all possible terms. In the 1980's Shaul Mukamel developed one method, now commonly called Mukamel diagrams, in which all terms in the response function can be derived by tracing all paths through the density matrix.[6] Providing similar information to Mukamel diagrams, double sided Feynman diagrams complement the former by providing specific information about how the wavevectors of the external field(s) interact with the system.[14, 15] Because several studies included in this dissertation utilize double sided Feynman diagrams, here we describe the rules governing their use. Specific examples of 1st and 3rd order processes will be discussed in the next two sections demonstrating the usefulness of these diagrams. It is worth noting that there are multiple conventions for drawing double sided Feynman diagrams.[14, 16, 17] Here we utilize the convention developed by Boyd, *et. al.*[16]

Figure 2.5 shows an example double sided Feynman diagram for a 1$^{\text{st}}$ order spectroscopic process for a simple two level system consisting of states $|a\rangle$ and $|b\rangle$. The time dependent density operator, $\hat{\rho}(t) = |\psi(t)\rangle\langle\psi(t)|$ is represented by the two vertical lines where the line on the left represents the ket, and the line on the right represents the bra. In this convention, time runs vertically from bottom to top. Each field matter interaction is represented by a wavy arrow. The radiated signal field is represented by the dashed wavy arrow. The number of field matter interactions shown in the diagram (not including the signal field) represents the order of the process. Field matter interactions represented by wavy arrows pointed towards the center of the diagram change the state index of the bra or ket such that the energy of the state increases. Field matter interactions represented by wavy arrows pointed away from the center of the diagram change the state index of the bra or ket such that the energy of the state decreases. If the arrow is pointed to the right, it represents a positive frequency and positive wavevector (i.e., $k > 0$) and vice versa. The signal frequency is given by the sum of the frequencies of all incoming fields

$$\omega_S = \sum_{n=1}^{N} \omega_n \qquad (2.45)$$

where "N" represents the order of the process. The system must always begin and end in a population; meaning that the bra and ket indices in the density operator must match before the first field matter interaction and after the signal field is radiated. Finally, the last step in the diagram is always the radiation of the signal field, which must be represented by the arrow pointing to the left while interacting with the ket.

51
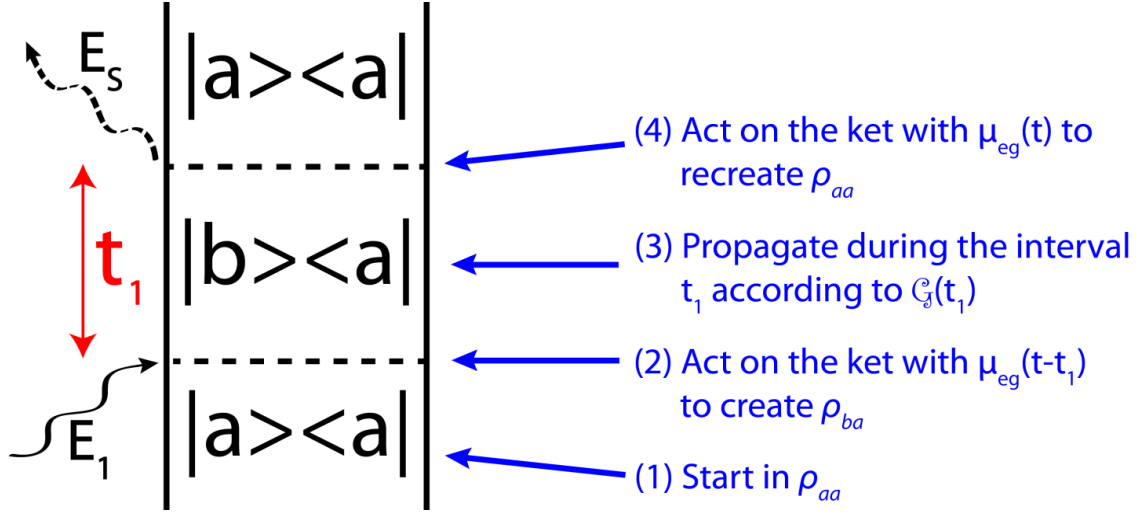
Figure 2.5: Double sided Feynman diagrammatic approach to time dependent perturbation theory. Vertical lines represent the density operator, $\hat{\rho}(t) = |\psi(t)\rangle\langle\psi(t)|$ where time runs vertically from bottom to top. This particular Feynman diagram represents a 1st order spectroscopic process between the two states, $|a\rangle$ and $|b\rangle$.

Following the above rules allows one to write all possible Feynman diagrams for a given order process. The rules for determining the response function term corresponding to each Feynman diagram are as follows. First, for every field matter interaction (including the signal field), one must include a transition dipole matrix element associated with the change in state index the interaction causes. For example, in Figure 2.5 the transition dipole matrix element associated with all field matter interactions would be given by $|\mu_{ba}|$ as each interaction causes the state index to go from either $a \rightarrow b$ or $b \rightarrow a$. For each interval between field matter interactions where the system is in a coherence between two states, a propagation function must be included to describe the time evolution of the system during this period. This propagation function is given by the Green function

$$\mathcal{G}(t_n) = \frac{i}{\hbar}\theta(t_n)\exp(-i\omega_{fi}t_n - \Gamma_{fi}t_n)$$ (2.46)

where $\theta(t_n)$ is the Heaviside step function, "t_n" refers to the nth propagation interval, Γ_{fi} is a phenomenological damping constant, and the indices "f" and "i" refer to the specific coherence of the system during the propagation interval. If the system is in a population in an interval between field matter interactions, the system is static and the propagation function is simply, $\frac{i}{\hbar}\theta(t_n)$. The term in the response function corresponding to a given Feynman diagram is simply the product of all transition dipole matrix elements and propagation functions. As an example, the term in the response function for the Feynman diagram shown in Figure 2.5 is given as the following

$$R(t_1) = \frac{i}{\hbar}\left|\mu_{ba}\right|^2 \theta(t_1)\exp(-i\omega_{ba}t_1 - \Gamma_{ba}t_1) \tag{2.47}$$

2.3.2. Linear Absorption

In spectroscopy, the material polarization induced by interaction with an external radiation field(s) is what radiates the observable signal field. Consequently, this is the main quantity of interest for spectroscopists. In this section, we will first rigorously derive the 1st order polarization of an absorption event in a two level system (g = ground state, e = excited state) excited by an external radiation field using time dependent perturbation theory (TDPT).[3] Secondly, we will show that the same result can be easily obtained using the corresponding double sided Feynman diagram while following the rules outlined in the previous section.

Using the same reasoning outlined above in Chapter 2.2.1, the first order polarization is given as the expectation value of the dipole operator, $\hat{\mu}$.

$$P^{(1)}(t) = \left\langle \psi^{(1)}(t) \left| \hat{\mu} \right| \psi^{(0)}(t) \right\rangle + \left\langle \psi^{(0)}(t) \left| \hat{\mu} \right| \psi^{(1)}(t) \right\rangle \tag{2.48}$$

Here we will consider the same process as the time evolution of the density operator, $\rho^{(1)}(t)$, following perturbation(s) from an external electromagnetic field. In this regime, the first order polarization is given as

$$P^{(1)}(t) = \mathrm{Tr}\left[\hat{\mu}\rho^{(1)}(t) \right] \tag{2.49a}$$

$$\rho^{(1)}(t) = \left(\frac{i}{\hbar}\right) \int_0^{\infty} dt_1 E_1(t - t_1) \mathcal{G}(t_1) V^{\circ} \rho^{(0)}(-\infty) \tag{2.49b}$$

where $\mathcal{G}(t_1)$ is the Green function that governs the propagation of the density matrix in the interval between the perturbative radiation field, E_1, and the radiation of the signal field. V° is a superoperator where its operation on some "dummy" operator, A, is defined by, $V^{\circ}A = \hat{\mu}A - A\hat{\mu}$. To understand Equation 2.49b it is useful to consider the integrand from right to left. If we assume that the system is initially in equilibrium and the gap between the ground and excited state is much larger than $k_B T$, the density operator before the interaction with the external field is given as

$$\rho^{(0)}(-\infty) = P(g)|g\rangle\langle g| + P(e)|e\rangle\langle e| = |g\rangle\langle g| \tag{2.50a}$$

$$\rho^{(0)}(-\infty) = \begin{pmatrix} P(g) & 0 \\ 0 & P(e) \end{pmatrix} = \begin{pmatrix} 1 & 0 \\ 0 & 0 \end{pmatrix} \tag{2.50b}$$

where $P(g)$ and $P(e)$ represent the initial populations of states g and e, respectively. That is, all of the population initially resides in the ground state. Assuming that the perturbative radiation is resonant with the energy gap between the ground and excited state, the transition dipole operator for this two level system is given as

54

$$\hat{\mu} = \left[\mu_{ge} |g\rangle\langle e| + \mu_{eg} |e\rangle\langle g| \right] \tag{2.51}$$

where $\mu_{eg} = \langle e|\mu|g\rangle$. Consequently, when the external field interacts with the system at time $t - t_1$, the superoperator V° operating on the initial density matrix in Equation 2.50a, $\rho^{(0)}(-\infty)$ is given by

$$
\begin{aligned}
V^\circ\rho^{(0)}(-\infty) &= \hat{\mu}\rho^{(0)}(-\infty) - \rho^{(0)}(-\infty)\hat{\mu} \\
&= \left[\mu_{ge} |g\rangle\langle e|g\rangle\langle g| + \mu_{eg} |e\rangle\langle g|g\rangle\langle g| \right] - \left[|g\rangle\langle g|g\rangle\langle e|\mu_{ge} + |g\rangle\langle g|e\rangle\langle g|\mu_{eg} \right] \\
&= \mu_{eg} |e\rangle\langle g| - \mu_{ge} |g\rangle\langle e|
\end{aligned} \tag{2.52}
$$

Following the interaction with the external field, the system evolves in this state for a time interval, t_1. The time evolution of the density operator during this interval is described by the Green function whose operation is defined as the following

$$
\begin{aligned}
\mathcal{G}(t_1)|e\rangle\langle g| &= \theta(t_1)e^{-iH^{(0)}t_1/\hbar} |e\rangle\langle g| e^{iH^{(0)}t_1/\hbar} \\
&= \theta(t_1)e^{-i\omega_{eg}t_1 - \Gamma_{eg}t_1} |e\rangle\langle g|
\end{aligned} \tag{2.53}
$$

where $\theta(t_1)$ is the Heaviside step function, ω_{eg} is the energy gap between the ground and excited states, and Γ_{eg} is a phenomenological damping constant added to avoid ill defined points. The Heaviside step function, which is equal to zero before $t - t_1$ and equal to one after $t - t_1$ is necessary to represent causality. That is, the system will not be evolving before the presence of the external field at $t - t_1$. If Equation 2.53 is applied to Equation 2.52 we can therefore rewrite the right side of the integrand in Equation 2.49b as the following

$$\mathcal{G}(t_1)V^\circ\rho^{(0)}(-\infty) = \theta(t_1)\mu_{eg} |e\rangle\langle g| e^{-i\omega_{eg}t_1 - \Gamma_{eg}t_1} - \theta(t_1)\mu_{ge} |g\rangle\langle e| e^{-i\omega_{ge}t_1 - \Gamma_{eg}t_1} \tag{2.54}$$

Following the time evolution during the interval, t_1, the signal field is radiated. This is represented mathematically by projecting from the left with the dipole operator, $\hat{\mu}$

$$
\begin{aligned}
&\hat{\mu}\mathcal{G}(t_1)V^\circ\rho^{(0)}(-\infty) \\
&= \big[|e\rangle\langle g| + |g\rangle\langle e|\big]\big[\theta(t_1)\mu_{eg}|e\rangle\langle g|e^{-i\omega_{eg}t_1 - \Gamma_{eg}t_1} - \theta(t_1)\mu_{ge}|g\rangle\langle e|e^{-i\omega_{ge}t_1 - \Gamma_{eg}t_1}\big] \\
&= \theta(t_1)|\mu_{eg}|^2\big[|g\rangle\langle g|e^{-i\omega_{eg}t_1 - \Gamma_{eg}t_1} - |e\rangle\langle e|e^{-i\omega_{ge}t_1 - \Gamma_{eg}t_1}\big]
\end{aligned}
\tag{2.55}
$$

According to Equation 2.49a we must now take the trace of Equation 2.55 (i.e., summing over the diagonal elements of the density matrix)

$$
\begin{aligned}
&\mathrm{Tr}\big[\hat{\mu}\mathcal{G}(t_1)V^\circ\rho^{(0)}(-\infty)\big] \\
&= \langle g|\hat{\mu}\mathcal{G}(t_1)V^\circ\rho^{(0)}(-\infty)|g\rangle + \langle e|\hat{\mu}\mathcal{G}(t_1)V^\circ\rho^{(0)}(-\infty)|e\rangle \\
&= \theta(t_1)|\mu_{eg}|^2\big[\langle g|g\rangle\langle g|g\rangle + \langle e|g\rangle\langle g|e\rangle e^{-i\omega_{eg}t_1 - \Gamma_{eg}t_1}\big] - \big[\langle g|e\rangle\langle e|g\rangle + \langle e|e\rangle\langle e|e\rangle e^{-i\omega_{ge}t_1 - \Gamma_{eg}t_1}\big] \\
&= \theta(t_1)|\mu_{eg}|^2\big[e^{-i\omega_{eg}t_1 - \Gamma_{eg}t_1} - e^{-i\omega_{ge}t_1 - \Gamma_{eg}t_1}\big]
\end{aligned}
\tag{2.56}
$$

The first order polarization of the absorption event can therefore now be written as

$$
P^{(1)}(t) = \int_0^\infty dt_1 \frac{i}{\hbar}\theta(t_1)|\mu_{eg}|^2\big[e^{-i\omega_{eg}t_1 - \Gamma_{eg}t_1} - e^{-i\omega_{ge}t_1 - \Gamma_{eg}t_1}\big]E_1(t - t_1)
\tag{2.57a}
$$

$$
P^{(1)}(t) = \int_0^\infty dt_1 S^{(1)}(t_1)E_1(t - t_1)
\tag{2.57b}
$$

where we have introduced the 1st order response function, $S^{(1)}(t_1)$, which is defined as the following

$$
S^{(1)}(t_1) = \frac{i}{\hbar}\theta(t_1)|\mu_{eg}|^2\big[e^{-i\omega_{eg}t_1 - \Gamma_{eg}t_1} - e^{-i\omega_{ge}t_1 - \Gamma_{eg}t_1}\big]
\tag{2.58}
$$

As was aforementioned, the response function at N^{th} order is always the sum of 2^N classes of terms. For the first order response function, there should therefore be only two

terms one needs to identify. Inspection of Equation 2.58 shows that the 1st order response function can be written as the following summation

$$S^{(1)}(t_1) = \frac{i}{\hbar} \theta(t_1) \left[R_1(t_1) - R_2(t_1) \right]$$

(2.59a)

$$R_1(t_1) = \left| \mu_{eg} \right|^2 e^{-i\omega_{eg} t_1 - \Gamma_{eg} t_1}$$
$$R_2(t_1) = \left[R_1(t_1) \right]^*$$

(2.59b)

where the two terms $R_1(t_1)$ and $R_2(t_1)$ are simply complex conjugates of one another. This is in fact the case for spectroscopy of any order. That is, although there is always a total of 2^N terms in the Nth order response function, one needs to determine $2^N/2$ terms as half of the terms are simply the complex conjugates of the others.

It should now be clear that even for the simplest possible case discussed above consisting of a two level system in a 1st order absorption experiment, performing a rigorous derivation of all terms in the response function using TDPT is an arduous task. Below it is shown that Equation 2.58 can be reproduced easily using the double sided Feynman diagrams and rules discussed in the previous section.

Consider the double sided Feynman diagram shown in Figure 2.6(A) and the corresponding energy ladder diagram shown in Figure 2.6(B) (Note that for simplicity, bra and kets will no longer be shown in all subsequent Feynman diagrams). According to the rules described in Chapter 2.31 this is the only possible Feynman diagram for a first order absorption process (i.e., $2^1/2 = 1$). In this Feynman diagram there are two field matter interactions (i.e., interaction with E_1 and E_S) to consider, and both result in a change of state index of either $g \rightarrow e$ or $e \rightarrow g$. Therefore we must add a term of $\left| \mu_{ge} \right| \left| \mu_{eg} \right| = \left| \mu_{eg} \right|^2$ to the

57

response function term. There is only one time interval, t_1, between field matter interactions in this diagram and the system is in a coherence between the ground and excited state during this interval. The Green function governing the propagation of the system during t_1 is therefore given by

$$\mathcal{G}(t_1) = \frac{i}{\hbar}\theta(t_1)\exp(-i\omega_{eg}t_1 - \Gamma_{eg}t_1) \tag{2.60}$$

The term in the response function corresponding to Figure 2.6(A) is simply the product of these two expressions and is given as

$$R_1(t_1) = \frac{i}{\hbar}\left|\mu_{eg}\right|^2 \theta(t_1)\exp(-i\omega_{eg}t_1 - \Gamma_{eg}t_1) \tag{2.61}$$

The other term in the response function is simply the complex conjugate of Equation 2.61 and is given as

$$R_2(t_1) = \frac{i}{\hbar}\left|\mu_{eg}\right|^2 \theta(t_1)\exp(-i\omega_{ge}t_1 - \Gamma_{eg}t_1) \tag{2.62}$$

Thus, Equation 2.58 has been reproduced without a rigorous derivation.
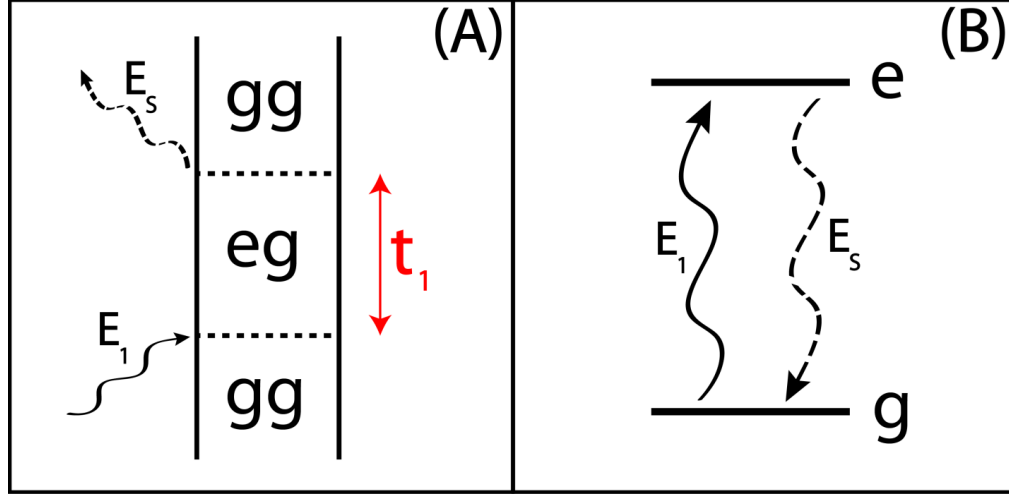
Figure 2.6: (A) Double sided Feynman diagram corresponding to a 1st order absorption process. (B) The corresponding energy ladder diagram for the same process showing the excitation of the system from ground state, $|g\rangle$ to excited state, $|e\rangle$ through the field matter interaction with field, E_1. Following the propagation interval, t_1 the system radiates the signal field, E_S thus relaxing the system back to the ground state, $|g\rangle$.

In any order spectroscopy it is often convenient to consider the response of a system in the frequency domain rather than the time domain. This is particularly true in linear absorption where the sole experimental observable is the absorption spectrum. A frequency domain picture of the system response is obtained by performing a Fourier transform on Equation 2.57

$$\alpha(\omega) = \frac{i|\mu_{eg}|^2}{\hbar} \int_{-\infty}^{\infty} dt_1 \theta(t_1) \left[e^{-i\omega_{eg}t_1 - \Gamma_{eg}t_1} - e^{-i\omega_{ge}t_1 - \Gamma_{eg}t_1} \right] e^{i\omega t_1}$$

$$= \frac{|\mu_{eg}|^2}{\hbar} \left[-\frac{1}{\omega - \omega_{eg} + i\Gamma_{eg}} + \frac{1}{\omega + \omega_{eg} + i\Gamma_{eg}} \right]$$

(2.63)

Equation 2.63 describes the frequency domain response of a single molecule in the system and is referred to as the polarizability. Note that the two terms included in the polarizability

are simply complex conjugates of one another. To obtain the macroscopic response of the system one simply multiplies Equation 2.63 by the density of molecules, N to obtain

$$\chi^{(1)}(\omega) = \frac{N|\mu_{eg}|^2}{\hbar}\left[-\frac{1}{\omega-\omega_{eg}+i\Gamma_{eg}}+\frac{1}{\omega+\omega_{eg}+i\Gamma_{eg}}\right] \tag{2.64}$$

where $\chi^{(1)}(\omega)$ is referred to as the linear susceptibility. The susceptibility is an important quantity in that it controls the induced frequency domain polarization and thus the frequency of the radiated signal field. That is,

$$P^{(1)}(\omega) = E_S(\omega)\chi^{(1)}(\omega) \tag{2.65}$$

where, $E_S(\omega)$, represents the spectrum of the external field. Because the radiated signal field deconstructively interferes with the input field subsequently causing a frequency dependent reduction in transmission, one can say that the susceptibility directly controls the system's absorbance cross spectrum. Specifically it is the imaginary portion of the susceptibility that controls the absorption spectrum[6]

$$L(\omega) \propto \text{Im}\left[\chi^{(1)}(\omega)\right] \tag{2.66}$$

2.3.3. Four-Wave Mixing Signal Components

The majority of the experiments discussed in Chapters 4-8 utilize the 3rd order spectroscopic technique known as transient grating spectroscopy. Unlike the first order absorption discussed in the previous section, transient grating spectroscopy contains more than one "class" of signal. Here will be discussed the three basic classes of signals whose time domain response functions will be derived using the double sided Feynman diagram technique discussed in Chapter 2.3.1.

A detailed description of transient grating spectroscopy is discussed below in Chapter 3.6. Briefly, three beams are focused in a boxcar geometry and spatially overlapped onto a sample. Two of the beams consist of identical pulses (i.e., the "pump" pulses) while the third beam (the "probe") can be the same as the "pump" or can be at a different frequency/bandwidth. The two "pump" beams arrive at the sample simultaneously and excite an electronic transition in the sample. The "probe" beam is on a variable delay with respect to the "pump" beams and monitors relaxation of the system as a function of time following excitation. The 3rd order polarization induced by these perturbations is given by the following equation[6, 18]

$$P^{(3)}(t) = \int_0^\infty \int_0^\infty \int_0^\infty S^{(3)}(t_1, t_2, t_3) E_{Pump}(t - t_1 - t_2 - t_3) E_{Pump}(t - t_2 - t_3) E_{Probe}(t - t_3) dt_1 dt_2 dt_3 \qquad (2.67)$$

where $S^{(3)}$ is the 3rd order response function, E_{Pump} is the pump field, E_{Probe} is the probe field, and t_n represents the time interval between field matter interactions. What is measured experimentally is the signal field radiated by the induced 3rd order polarization. This field is radiated in the momentum conserving phase matching direction, $k_s = -k_1 + k_2 + k_3$ where k_1 and k_2 represent the wave vectors of the two pump beams and k_3 is the wave vector of the probe beam. This is important not only because the signal is radiated in a background free direction but also because the phase matching condition reduces the total number of response functions terms that must be considered. That is, although there are $2^3=8$ total possible Feynman diagrams for a three level 3rd order response, not all have signal fields that are radiated in the "correct" phase matching direction. For a three level system consisting of a ground state $|g\rangle$, excited state $|e\rangle$, and higher lying excited state $|f\rangle$ Figure 2.7 shows the

61

six possible Feynman diagrams for a transient grating spectroscopic process. Note that it is assumed that the energy gap between levels is considerably greater than k_BT; therefore, all population initially resides in the ground state.
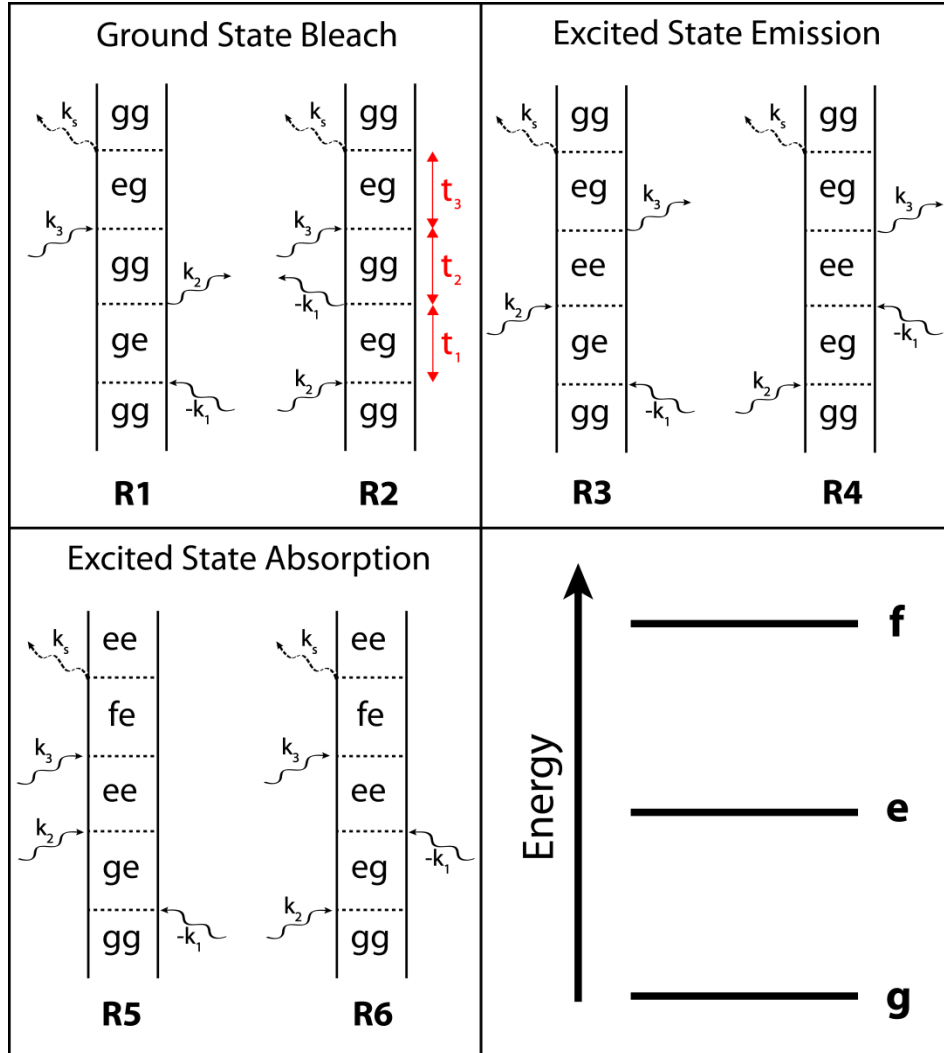
Figure 2.7: The six possible double sided Feynman diagrams for a transient grating spectroscopic process on a three level system. Note that it is assumed that population initially resides entirely in the ground state, (i.e., $|E_e - E_g| \gg k_B T$).

These six allowed diagrams can be further subdivided into three classes of signals based on the change in state index caused by the "probe" pulse field matter interaction. For a more qualitative discussion of the classes of 3rd order spectroscopic signals, see Chapter 3.5 below on transient absorption spectroscopy. As the state index of the ket changes from "g" to "e" upon interaction with the "probe" pulse, the two Feynman diagrams R_1 and R_2, are referred to as ground state bleach (GSB). Thus, in probing GSB, one is measuring the dynamics of the ground state wave packet. Following the rules outlined in Chapter 2.3.1, one can derive the response functions associated with GSB. For example, for the term R_1, the transition dipole matrix elements are $|\mu_{eg}|$, $|\mu_{ge}|$, $|\mu_{eg}|$, and $|\mu_{ge}|$ for interactions with k_1, k_2, k_3, and k_s, respectively. Thus, the net transition dipole matrix factor for R_1 is $|\mu_{eg}|^4$. There are three time intervals (i.e., t_1, t_2, and t_3) between field matter interactions to consider in R_1. Only during t_1 and t_3 is the system in a coherence between two states, however. Therefore, Green functions must be included for only the intervals t_1 and t_3. Consequently, the term in the response function corresponding to R_1, is given by

$$
\begin{aligned}
R_1(t_1,t_2,t_3) &= \frac{-i}{\hbar^3}|\mu_{eg}|^4 \, \theta(t_1)\theta(t_2)\theta(t_3)\exp(-i\omega_{ge}t_1 - \Gamma_{ge}t_1)\exp(-i\omega_{eg}t_3 - \Gamma_{eg}t_3) \\
&= \frac{-i}{\hbar^3}|\mu_{eg}|^4 \, \theta(t_1)\theta(t_2)\theta(t_3)\exp\left[-i(\omega_{ge}t_1 + \omega_{eg}t_3) - \Gamma_{ge}t_1 - \Gamma_{eg}t_3\right]
\end{aligned}
\tag{2.68}
$$

The term R_2 is simply the complex conjugate of R_1, therefore its contribution to the response function is given as

$$
R_2(t_1,t_2,t_3) = \frac{-i}{\hbar^3}|\mu_{eg}|^4 \, \theta(t_1)\theta(t_2)\theta(t_3)\exp\left[(-i\omega_{eg}(t_1+t_3) - \Gamma_{eg}(t_1+t_3)\right]
\tag{2.69}
$$

The terms R_3 and R_4 represent a different class of signal referred to as excited state emission (ESE). Unlike GSB which probes the dynamics of the ground state wave packet, ESE probes the excited state wave packet dynamics when the probe field matter interaction induces emission from the excited state wave packet. Using the same reasoning as above, the ESE terms in the response function are as follows.

$$R_3(t_1,t_2,t_3) = \frac{-i}{\hbar^3} |\mu_{eg}|^4 \, \theta(t_1)\theta(t_2)\theta(t_3) \exp\left[-i(\omega_{ge}t_1 + \omega_{eg}t_3) - \Gamma_{ge}t_1 - \Gamma_{eg}t_3\right] \qquad (2.70a)$$

$$R_4(t_1,t_2,t_3) = \frac{-i}{\hbar^3} |\mu_{eg}|^4 \, \theta(t_1)\theta(t_2)\theta(t_3) \exp\left[(-i\omega_{eg}(t_1 + t_3) - \Gamma_{eg}(t_1 + t_3)\right] \qquad (2.70b)$$

The third and final class of 3rd order signal in transient grating is represented by Feynman diagrams R_5 and R_6. Because the state index changes from the excited state "e" to higher excited state "f" during the interaction with the "probe" pulse, this class of signal is referred to as excited state absorption (ESA). Like excited state emission, ESA probes the dynamics of the excited state wave packet, however instead of inducing emission ESA excites the wave packet to a higher lying energy level. The terms in the response function for ESA are as follows

$$R_5(t_1,t_2,t_3) = \frac{-i}{\hbar^3} |\mu_{eg}|^2 |\mu_{fe}|^2 \, \theta(t_1)\theta(t_2)\theta(t_3) \exp\left[-i(\omega_{ge}t_1 + \omega_{fe}t_3) - \Gamma_{ge}t_1 - \Gamma_{fe}t_3\right] \qquad (2.71a)$$

$$R_6(t_1,t_2,t_3) = \frac{-i}{\hbar^3} |\mu_{eg}|^2 |\mu_{fe}|^2 \, \theta(t_1)\theta(t_2)\theta(t_3) \exp\left[-i(\omega_{eg}t_1 + \omega_{fe}t_3) - \Gamma_{eg}t_1 - \Gamma_{fe}t_1\right] \qquad (2.71b)$$

It was discussed above that there are only six terms that contribute to the 3rd order response function for a three level system. In most realistic systems, however, there are more than three states to consider. Therefore, in order to determine the response function and resulting transient grating signal field, one must consider all possible Feynman diagrams

64

showing transitions between all states including non radiative transitions between states during the interval, t_2. However, even with these further complications the classes of the signals are still limited to only ground state bleach, excited state emission, and excited state absorption.

2.4. REFERENCES

(1)   Atkins, P.; Friedman, R. *Molecular Quantum Mechanics*; Oxford University Press: New York, 2005.

(2)   Boyd, R. W. *Nonlinear Optics*, 3rd. ed.; Elsevier: Burlington, MA, 2008.

(3)   Moran, A. M. Chemistry 487: Introduction to Molecular Spectroscopy: Class Notes, 2012.

(4)   Trebino, R. Frequency-Resolved Optical Gating: The Measurement of Ultrashort Laser Pulses; Kluwer Academic: Boston, MA, 2000.

(5)   Nitzan, A. Chemical Dynamics in Condensed Phases: Relaxation, Transfer, and Reactions in Condensed Molecular Systems; Oxford University Press: New York, 2006.

(6)   Mukamel, S. *Principles of Nonlinear Optical Spectroscopy*; Oxford University Press: New York, 1995.

(7)   Tokmakoff, A. *Time-Dependent Quantum Mechanics and Spectroscopy*, <http://www.mit.edu/~tokmakof/TDQMS/index.htm> , 2012.

(8)   Parson, W. W. Modern Optical Spectroscopy: With Examples from Biophysics and Biochemistry; Springer-Verlag Berlin Heidelberg: New York, 2007.

(9)   Förster, T. *Ann. Phys.* 1948, *437*, 55-75.

(10)   Kaplan, W. *Advanced Calculus, 4th ed.*; Addison-Wesley: Reading, MA, 1992.

(11)   Marcus, R. A. *J. Chem. Phys.* 1965, *24*, 966-978.

(12)   Barbara, P. F.; Meyer, T. J.; Ratner, M. A. *J. Phys. Chem.* 1996, *100*, 13148-13168.

(13)   Jortner, J. *J. Chem. Phys.* 1976, *64*, 4860-4867.

(14)   Yee, T. K.; Gustafson, T. K. *Phys. Rev. A.* 1978, *18*, 1597-1617.

(15)   Druet, S. A. J.; Taran, J.-P. E. *Prog. Quant. Electr.* 1981, *7*, 1-72.

(16)   Boyd, R. W.; Mukamel, S. *Phys. Rev. A.* 1984, *29*, 1973-1983.

(17)   Prior, Y. *IEEE J. Quantum Electron.* 1984, *QE-20*, 37-42.

(18)   Brixner, T.; Mančal, T.; Stiopkin, I. V.; Fleming, G. R. *J. Chem. Phys.* 2004, *121*, 4221-4236.

CHAPTER 3 . BACKGROUND ON NONLINEAR SPECTROSCOPY TECHNIQUES

3.1. INTRODUCTION

Since the introduction of ultrafast lasers, there have been continual advances in technology resulting in ever shorter, more reliable, and more powerful pulses[1-5] As an example, the application of the chirped pulse amplification technique has greatly increased the attainable energies from solid state lasers by stretching pulses in time before amplification.[6-9] Another example is the development of the Kerr lens mode-locking Titanium Sapphire oscillator by Sibbet, et. al. in 1991, which has greatly decreased the difficulty in working with ultrafast laser systems and has allowed ultrafast lasers to become much more practical experimental devices.[1] Today, Ti:Sapphire ultrafast lasers have become "turn-key" and it is now possible to generate sub-15 fs visible pulses and obtain pulse energies up to the mJ level.[3, 4, 10-12]

In all experiments described herein, a commercial system (Quantronix Q-Lite seeded Integra C Ti:Sapphire amplifier) was used to generate the laser fundamental of 130 fs, 800 nm pulses with energies of 2.0 mJ at a 1 kHz repetition rate. As is described in the following sections, the laser fundamental was subsequently used to drive both homebuilt noncollinear optical parametric amplifiers (NOPA) as well as a hollow core fiber setup in order to generate visible ultrashort pulses for use in experiments. As discussed next in Chapter 3.2, dispersion accumulation in these broadband pulses is characterized using the frequency

optical gating technique and offset with a combination of a prism compression and numerical correction techniques.   Fundamentals of the conventional "pump-probe" technique, transient absorption spectroscopy, are discussed in Chapter 3.5.   Finally, the specialized "pump-probe" technique known as transient grating spectroscopy is introduced in Chapter 3.6. This technique yields information that is equivalent to transient absorption, yet has several benefits which will be discussed.

3.2. DISPERSION MANAGEMENT

3.2.1. Accumulation of Dispersion in Ultrafast Pulses

Ignoring the spatial portion of the of the electric field, the propagation of an ultrashort laser pulse in time can be described by the following expression

$$E(t) = \xi(t)e^{-i\omega_0 t + \theta(t)}$$

(3.1)

where ξ_t is a Gaussian envelope function establishing the duration of the field, ω_0 is the carrier frequency or center frequency of the pulse, and $\theta(t)$ is the temporal phase of the pulse. An intuitive way of thinking about $\theta(t)$ is that it determines the time relationships between when different frequencies contained in the pulse's bandwidth arrive. In Figure 3.1, one can observe a graphic representation of Equation 3.1 where in this case, $\theta(t)$ is constant over the entire duration of the pulse.   That is, all frequencies contained in the pulse bandwidth arrive at the same time and the pulse is said to be "compressed". In practice, by the time an ultrashort pulse propagates through an experimental setup and arrives at the sample position, the temporal phase will not be constant over the duration of the pulse. This

69

is because the pulse will have interacted with any dispersive media (air, glass, etc.) it has propagated through; ultimately affecting the phase of the pulse. Moreover, as is shown below, the changes in the phase are accumulative; meaning that the longer the propagation distance, the more the phase is affected.
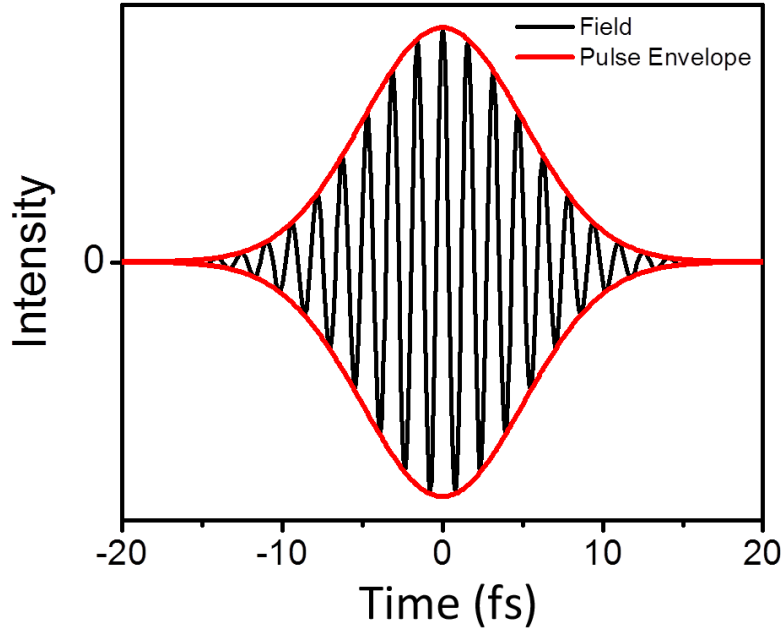
Figure 3.1: The Gaussian pulse envelope of a ~10 fs laser pulse (red) and the oscillating real electric field (black). Because this pulse is compressed all frequencies contained in the pulse bandwidth arrive simultaneously.

It is mathematically easier to deal with these phase accumulations by working in the frequency domain.[13] Applying a Fourier transform to Equation 3.1 results in the following expression for the same pulse in the frequency domain

$$E(\omega) = \int_{-\infty}^{\infty} E(t)e^{(-i\omega t)}dt = \int_{-\infty}^{\infty} \xi(t)e^{-i\omega_0 t + \theta(t)}e^{(-i\omega t)}dt$$
$$= S(\omega)e^{-i\theta_{Pulse}(\omega)}$$

(3.2)

70

where $S(\omega)$ and $\theta_{Pulse}(\omega)$ are the spectral amplitude and phase, respectively. Note that because it is irrelevant to the following discussion, the carrier wave frequency, ω_0, has been omitted from the argument. It is also worth noting that the negative frequency components that result from the Fourier transform have been ignored. In the frequency domain, the output field of an ultrashort pulse after it has propagated through a dispersive material is related to the input material through the simple relationship

$$
\begin{aligned}
E_{output}(\omega) &= E_{input}(\omega)r(\omega)e^{-i\theta_{Material}(\omega)} \\
&= S(\omega)e^{-i\theta_{Pulse}(\omega)}r(\omega)e^{-i\theta_{Material}(\omega)} \\
&= S(\omega)r(\omega)e^{-i(\theta_{Pulse}(\omega)+\theta_{Material}(\omega))}
\end{aligned}
\tag{3.3}
$$

where $r(\omega)$ is the frequency dependent attenuation of the material. This factor can modify the spectrum of the pulse, however as we are interested in the phase of the pulse, we can ignore this here. Working in the frequency domain has significantly simplified the problem in that the material's effect on the phase is now simply a sum of the phase accumulated by propagation through the material, $\theta_{Material}(\omega)$, with the original phase of the pulse, $\theta_{Pulse}(\omega)$. The total material phase accumulated by propagation of an ultrashort pulse, is given by the relation

$$
\theta_{Material}(\omega) = \sum_i n_i(\omega)\frac{\omega L_i}{c}
\tag{3.4}
$$

where L_i, is the length of propagation through and $n_i(\omega)$ is the frequency dependent index of refraction (i.e., dispersion), respectively, of the material, i.[14, 15] Thus, it is clear that amount of phase accumulated by propagating through a dispersive material is linearly related to the distance the pulse has propagated through the material.

71

It is common practice to expand the total phase of the pulse in a Taylor series about

the pulse carrier frequency, ω_0

$$\Phi(\omega) = \theta_{Pulse}(\omega) + \theta_{Material}(\omega)$$

$$= \theta_0 + (\omega - \omega_0)\theta_1 + \frac{(\omega - \omega_0)^2}{2}\theta_2 + \frac{(\omega - \omega_0)^3}{6}\theta_3 + ... \qquad (3.6)$$

Keeping in mind that the group delay of the pulse as a function of frequency is defined as[14]

$$t_{group}(\omega) \equiv \frac{\partial \Phi(\omega)}{\partial \omega} \qquad (3.7)$$

we can now describe exactly how the phase accumulated through propagation of dispersive

materials affects the frequency versus time information of an ultrashort pulse.

For "normal" ultrashort pulses that contain many optical cycles within the pulse

envelope, the accumulated zeroth-order dispersion or "absolute phase", θ_0, is irrelevant as a

small shift of phase relative to the pulse envelope has very little noticeable effect on the

pulse. It is only when one is dealing with extremely short pulses that contain only a few

optical cycles within the pulse envelope that θ_0 becomes important.   Similarly, the

accumulated first order dispersion or "group delay," θ_1 is unimportant as it represents a

frequency independent shift in the time of the pulse. That is, it delays all frequencies of the

pulse in time by the same value.

It is not until you reach the third term in the expansion where the results become

important. The accumulated second order dispersion, θ_2, can be observed as a shift in time

that is linearly dependent on the frequencies in the pulse. This is commonly termed group

velocity dispersion (GVD), and the result is that pulses become linearly "chirped" in time as can be seen schematically in Figure 3.2. Generally speaking, this is undesirable as the total pulse length has now increased, thus reducing the time resolution of the experiment. In practice it is advantageous to limit the amount of dispersive material the pulse has to propagate through, by using the smallest number of transmissive optics as possible. One can also design experimental setups to utilize low dispersive materials for any essential transmissive optics. It is possible to calculate the amount of GVD introduced by a particular material using the following expression relating the wavelength dependent index of refraction to the GVD of the material[15]

$$GVD = \frac{\lambda^3}{2\pi c^2} \left(\frac{d^2 n}{d\lambda^2} \right) \tag{3.8}$$

For commonly used materials, however, GVD has already been tabulated as a function of propagation distance.[15]
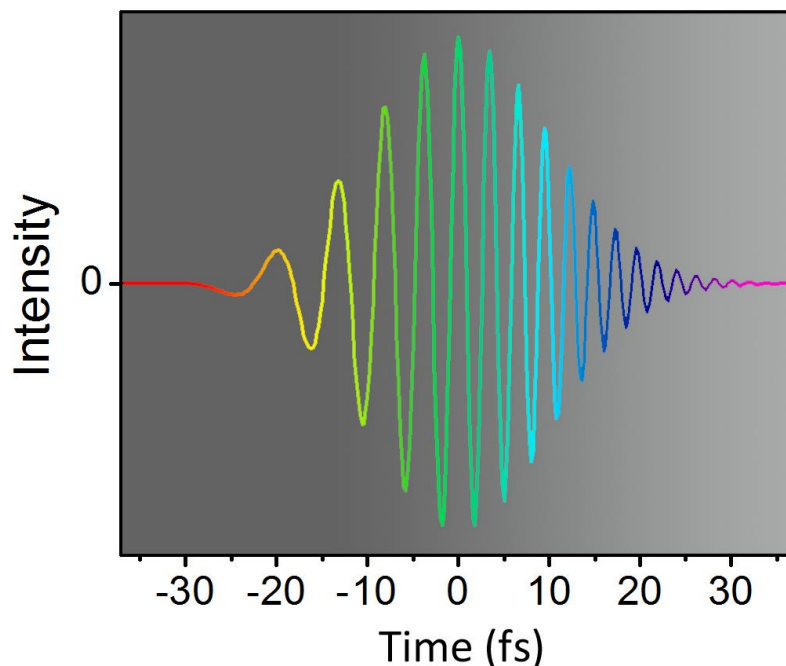
Figure 3.2: Schematic of the oscillating real electric field of a linearly "chirped" pulse. As time increases, the instantaneous frequency of the pulse increases linearly with time. Note that this has also had the effect of increasing the total pulse length in time.

For relatively narrowband visible pulses, (FWHM < ~1000 cm^{-1}) one can generally truncate the Taylor expansion of the phase at the second order dispersion term. For more broadband pulses, however, higher order terms become important as the magnitude of $\omega - \omega_0$ can now become large. For example, in several of the experiments discussed in Chapters 4-8, the third order dispersion (TOD) term corresponding to the magnitude of θ_3, can be seen to have a large effect on many of the broadband "probe" pulses utilized. TOD, results in pulses having a quadratic dependence on the pulse frequencies or a "parabolic chirp." An excellent example of this is shown below in Figure 3.3 in Chapter 3.2.2.

Like group velocity dispersion, TOD results in the total pulse length increasing in time. Fortunately, as will be discussed below in Chapter 3.2.3, there exists a simple method

for correcting GVD in ultrashort pulses using a prism pair compressor. Unfortunately, however, it is considerably more difficult to completely negate the effects of TOD using simple techniques. Again, it is advantageous to use the smallest number of transmissive optics and to use consideration when selecting the materials used in order to reduce the TOD accumulated.

3.2.2. Frequency Resolved Optical Gating (FROG)

In the previous section we've seen that due to the phase accumulation acquired while propagating through dispersive materials, the instantaneous frequency of ultrashort laser pulses can change rapidly. This pulse dispersion can have a significant impact on experiments (e.g., time resolution), so it is very important for spectroscopists to be able to characterize it. Unfortunately, no detectors exist that are fast enough to directly resolve ultrashort pulses in time. In fact, with ultrashort laser pulses being the shortest events known to mankind, the only thing that is fast enough to resolve an ultrashort pulse is another ultrashort pulse. Fortunately, experimental techniques that utilize this concept, such as frequency resolved optical gating (FROG)[14], are easy to perform and provide all the information needed to characterize a pulse's phase information.

Analogous to the more well known intensity autocorrelation (or cross-correlation) techniques, which measure a pulse's intensity as a function of time, the FROG technique measures a pulse's spectrum as a function of time (i.e., its spectrogram). However, unlike the former where no phase information is obtained, the FROG technique is capable of fully characterizing a pulse's dispersion. An example FROG spectrogram recorded with a transient grating beam geometry of a broadband ultrashort laser pulse can be seen in Figure

3.3 Not only does this spectrogram give us the intensity of the pulse as a function of time, but it also tells us when each frequency in the pulse is arriving in time. This particular pulse exhibits strong quadratic frequency dependence and is thus a good example of a pulse containing TOD.
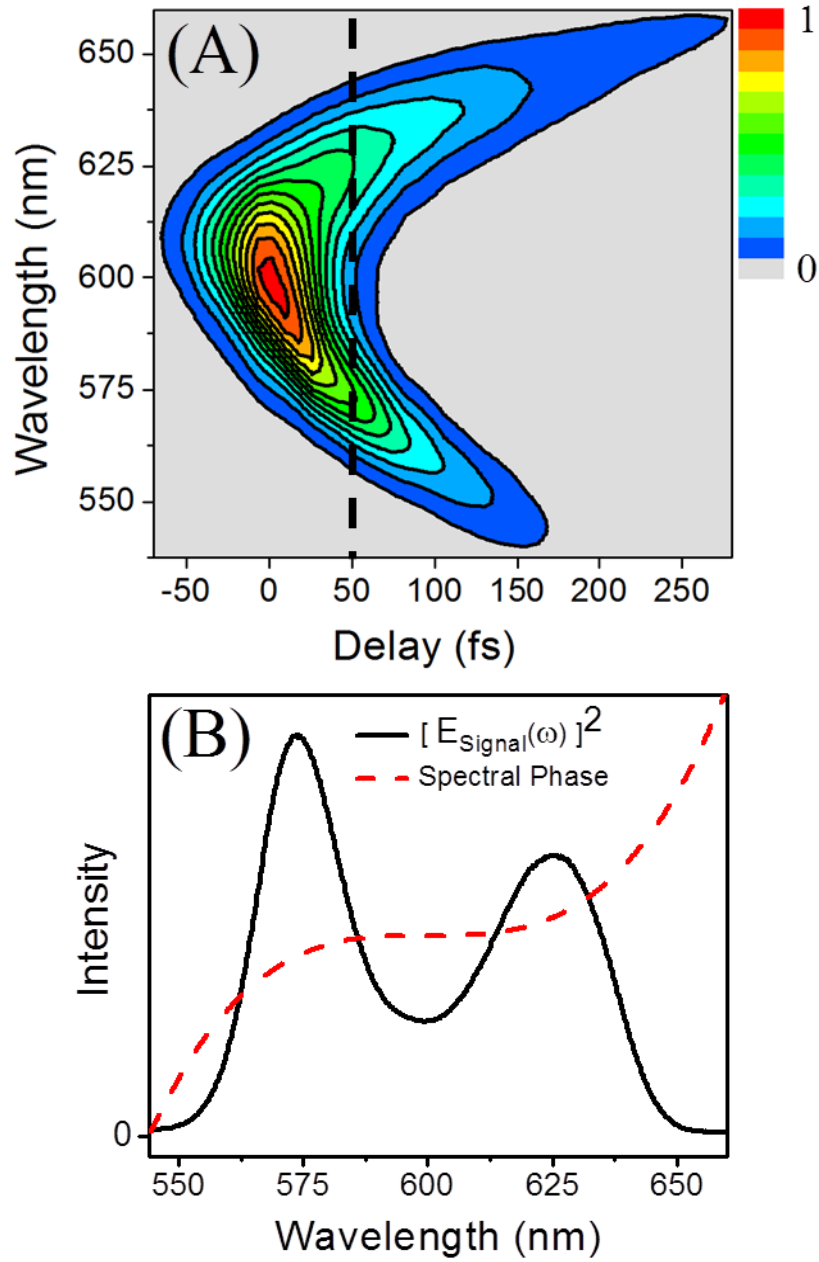
Figure 3.3: (A) Example pulse spectrogram measured with the FROG technique utilizing a transient grating beam geometry. Strong quadratic frequency dependence indicates a large amount of third order dispersion in the pulse. (B) Measured signal pulse intensity spectrum at *T*=50fs with cubic phase overlaid. Note that the phase shown here is shown for illustrative purposes only.

Experimentally, a FROG measurement is performed by spatially overlapping two or more ultrashort pulses in an "instantaneously" responding medium and delaying one pulse (the gate pulse(s)) with respect to the others. Depending on the beam geometry used, some nonlinear optical process occurs at each pulse delay resulting in the emission of a signal field, which is spectrally resolved. When the signals from all pulse delays are combined, the result is the FROG spectrogram. This process is shown schematically in Figure 3.4 for a simple two pulse FROG. Because the medium responds "instantly," the spectrogram is not medium dependent and yields information only about the pulse being characterized. It is important to note that the gate pulse only contributes to the intensity of the signal pulse and not to the phase (i.e, frequency).[14] Consequently, it is possible to perform a FROG measurement using either identical pulses for the gate and measured pulses or entirely different pulses.

$$E_{Signal} = E(t)E_{Gate}(t-T)$$

$E(t)$

$E_{Gate}(t-T)$

T 0

Time
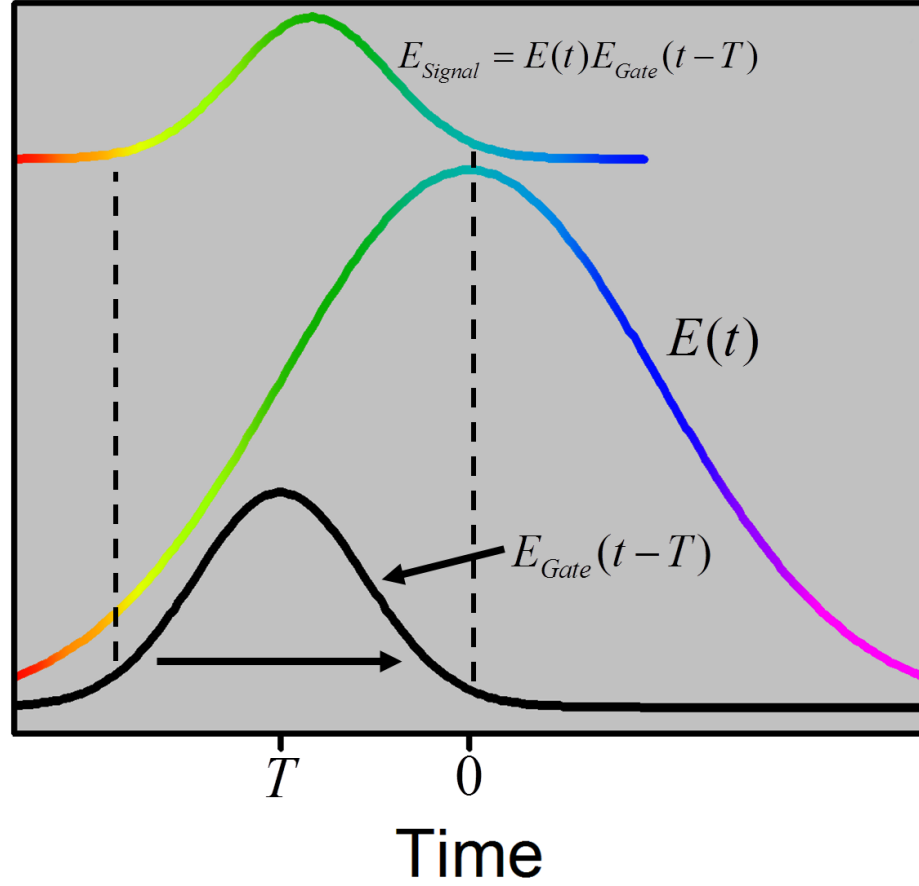
Figure 3.4: Schematic of the pulse progression in a simple FROG experiment utilizing two unique ultrashort pulses. The shorter pulse (black) gates out a portion of the longer linearly "chirped" Gaussian pulse (multicolored) resulting in a measurable signal pulse at each delay, *T*. Note that the gate pulse only contributes intensity to the signal and does not contribute phase information. Also note that although a two color FROG experiment is shown here, this technique works equally well if the gate pulse and the pulse to be measured are identical (i.e., spectrally resolved autocorrelation).

All FROG pulse characterizations performed throughout the experiments discussed in this dissertation were performed using a transient grating beam geometry (See Chapter 3.6 for details). In brief, three pulses are spatially overlapped in an "instantaneously" responding medium such as fused silica glass or chloroform. The two identical gate pulses arrive at the medium simultaneously and at a fixed time. The pulse to be characterized arrives at a

variable delay, T. The resulting background free signal field as a function of time is given by the following expression[14]

$$E_{Signal}(t,T) \propto E_{Gate}(t)E_{Gate}^*(t)E_{Pulse}(t-T) \qquad (3.9)$$

where $E_{Gate}(t)$ is the electric field of the two identical gate pulses (* denotes complex conjugate), and $E_{Pulse}(t)$ is the electric field of the pulse being characterized. Spectrally resolving the signal with a spectrometer yields the squared magnitude of the Fourier transform of the time dependent signal field[14]

$$I_{FROG}(\omega,T) = \left| E_{Gate}(t)E_{Gate}^*(t)E_{Pulse}(t-T)e^{-i\omega t}dt \right|^2 \qquad (3.10)$$

which is the experimental FROG spectrogram of the pulse.

3.2.3. Prism Compression

As was discussed above in Chapter 3.2.1 group velocity dispersion (GVD) accumulated while propagating through dispersive materials causes ultrashort pulses to be linearly "chirped" in time. Propagation through nearly all materials contributes positive GVD leading to pulses with low frequency components arriving before high frequency components (i.e., positive "chirp"). Fortunately, there exist several pulse "compressing" techniques that utilize gratings or prisms in which positive "chirp" can be compensated for by propagating pulses through an optical path that adds a controlled amount of negative dispersion.[13, 14, 16, 17] One of the simplest of these pulse compressors involves propagating the beam through a series of prisms.[16]

A schematic of the prism compressor used in compressing pulses for in the experiments discussed in Chapters 4-8 is shown in Figure 3.5. First, a positively "chirped" femtosecond pulse, as indicated by the slant in the input FROG spectrogram, is aligned onto prism #1, which disperses the beam into its component frequencies. Note that mirror #2 (M2) is vertically offset from the beam and does not interact with it at this time. In order to minimize the reflection loss at the prism surface for p-polarized radiation, the beam enters and exits the prism at the Brewster angle. This also allows for accurate and consistent alignment of the setup as the Brewster angle coincides with the minimum deviation of the beam path. The now dispersed beam travels to prism #2, which collimates the dispersed frequencies. Like prism #1, the beam enters and exits prism #2 at the Brewster angle. Mirror #1 (M1) reflects the dispersed beam back along the reverse path with a slight vertical offset. Traversing backwards through the prisms negates the actions of the forward path such that the beam exiting the compressor is spatially identical to the original beam. Because of the vertical offset applied by M1, the beam is now level with M2, and the beam is reflected away from the original pathway.

It is clear from examination of Figure 3.5 that due to the separation of the beam colors by prism #1, the optical path length of the different frequencies contained in the beam are not equal. It may appear from initial inspection that the lower frequency components actually have a shorter net path length as the distance traveled between prism #1 and prism #2 is shorter for lower frequencies. This would ultimately have the effect of increased positive dispersion on the pulses as it would further delay the high frequency components relative to the low frequency components. Although this reasoning is correct, one must consider the fact that the beam also has to propagate through prism #2, where the optical path

length is considerably greater for higher frequency components. The propagation length inside of prism #2 is also strongly dependent on the separation between prisms, where a longer inter-prism separation results in a larger ratio between the path lengths of lower and higher frequencies inside of prism #2. Consequently, there is a competition between the positive GVD accumulated from propagating between prism #1 and #2 and the negative GVD accumulated from propagating within prism #2. This can be summarized mathematically by the expression[15, 16]

$$GVD_{Prism} \approx \frac{\lambda^3}{2\pi c^2}\left[-8\mathrm{d}\left(\frac{dn}{d\lambda}\right)^2 + 4\left(\frac{d^2n}{d\lambda^2}\right)2D\right] \qquad (3.11)$$

where λ is the wavelength of light, c is the speed of light, d is the tip to tip prism separation, D is the beam diameter, and n is the index of refraction of the prism material. In this expression, the first term is always negative and is proportional to the distance, d, between the two prisms. Thus, increasing the inter-prism distance increases the negative GVD accumulated by the prism compressor. The second term is always positive and is dependent on the on the path lengths through the prisms. This is easily controlled experimentally as one can simply move the prisms forwards and backwards in the beam (X_1 and X_2 in Figure 3.5). The net result is a highly adjustable pulse compressor in which there are three parameters (d, X_1, and X_2) with which an operator can fine tune the magnitude and sign of the GVD introduced by the compressor. Thus, "chirped" pulses can be compressed to make all frequencies arrive simultaneously as is shown schematically in Figure 3.5 where the input pulse is positively "chirped," and the output pulse is compressed.
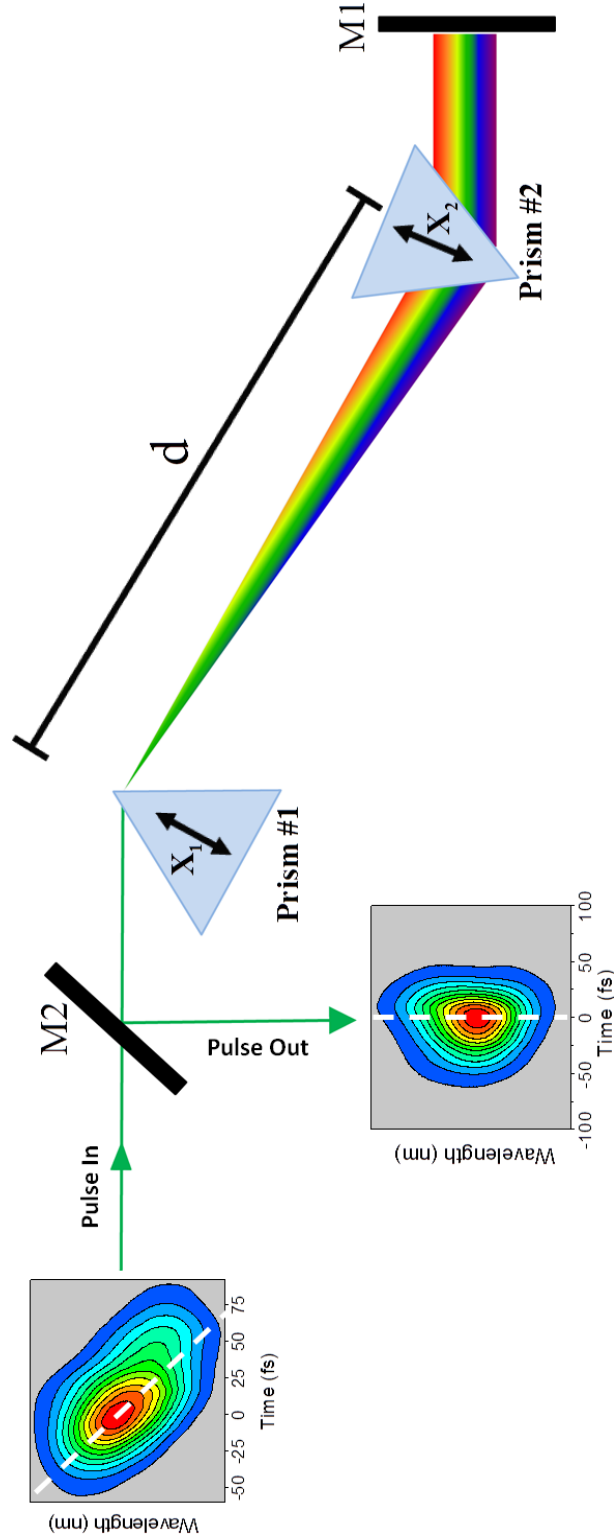
Figure 3.5: Schematic for a simple prism pair pulse compressor used for compressing ultrashort pulses utilized in Chapters 4-8. Key: M = Mirror, d = tip to tip prism separation, X = Prism position controlling the internal propagation path length of beams.

3.2.4. Numerical Correction of Third Order Dispersion

For large bandwidth ultrashort pulses (FWHM > ~1000 cm^{-1}) accumulated third order dispersion begins to become a serious issue. Unfortunately, unlike GVD which can be completely negated with the simple prism compressor described in the previous section, the quadratic time-frequency dependence inherent to TOD cannot be cancelled simultaneously at all frequencies. Because it is often beneficial to observe the spectral dependence of a signal at early pulse delay times, a signal processing routine has been developed in which the effects of TOD are numerically corrected for the "probe" pulse. It is worth noting that use of this algorithm is only necessary when one is observing signals at delay times that are on the same order as the effects of the TOD (i.e., < ~1 ps). At long pulse delays (T >>1 ps), the slight inaccuracy in the frequency dependent zero pulse delay (i.e., "time zero") introduced by TOD is insignificant to the overall pulse delay.

The data processing algorithm developed for this technique is included in the appendices. Herein is qualitatively described the method used. First, the pulse's phase is characterized by performing a FROG measurement in an "instantaneously" responding medium. At each measured frequency, the pulse delay at which the maximum signal occurs is determined. This value is defined as the frequency dependent time zero and is represented in Figure 3.6(A) as the dotted line. Time zero is plotted versus frequency and fit to a polynomial. Although a parabolic polynomial should be sufficient for fitting the effects of TOD, (i.e., truncating Equation 3.6 at the fourth term in the expansion), in practice, it is often necessary to use cubic or higher order polynomials. This suggests that although the TOD dominates the frequency-time information in the pulse, there is also an effect from higher order dispersion(s) as well.

The polynomial fit is subsequently input into the algorithm, which interprets the information as how far off in time each frequency in the pulse is from the time at which the first frequencies in the pulse arrive (i.e., absolute time zero). Because the data was collected using discrete steps in time, the algorithm determines how many time indices each frequency is off from the absolute time zero index, and then shifts each row in the data matrix by the necessary number of indices. The result is a new data matrix in which all frequencies arrive at the absolute time zero. An example of this algorithm being used in practice can be seen in Figure 3.6 where the effects of TOD observed in a FWHM= 2500 cm^{-1} broadband pulse centered at ~640 nm in fused silica are negated. The top panel represents the FROG spectrum as measured, while the bottom panel gives the numerically processed data. It is important to note that although the algorithm makes it appear that all frequencies contained in the pulse arrive at the same time, it is only a numerical correction and one is not actually "compressing" the pulse with this technique. That is, the frequency dependent time resolution has not been altered by the algorithm. This can clearly be seen in Figure 3.6(B) by the existence of the "lobes" in the spectrogram far from the carrier frequency, ω_0, where the time resolution is worse the farther one is from the center of the pulse.

In order to utilize this algorithm in an experiment on a more interesting sample, the "instantaneously" responding medium is replaced by the sample to be measured without changing any experimental parameters (beam alignment, prism settings, etc.). Following data collection, the same polynomial fit obtained in the calibration steps above is used to process the new data. It is important to note that one cannot simply perform the algorithm directly on samples as materials that are on resonant with the excitation frequency do not necessarily respond instantaneously and can also exhibit sample dependent spectral shifts on

short time scales. Determination of these spectral shifts is in fact why the algorithm is necessary in the first place.
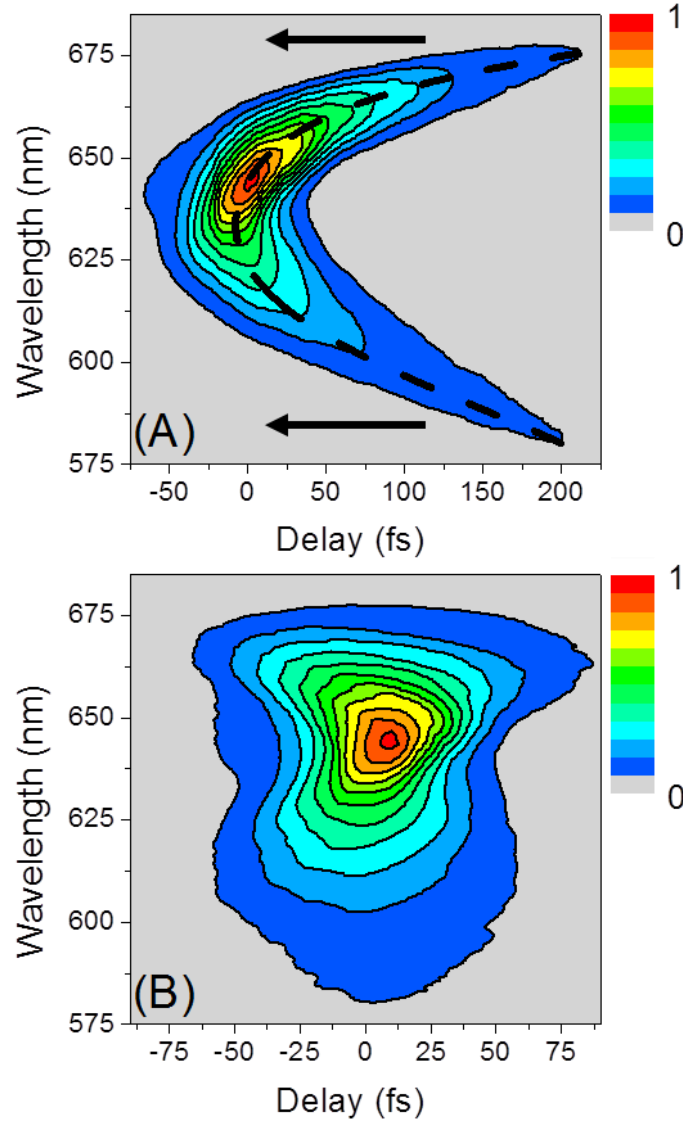
Figure 3.6: Numerical algorithm that adjusts for the effects of TOD in ultrashort pulses. (A) FROG spectrogram of a FWHM= 2500 cm^{-1} broadband pulse centered at ~640 nm measured in fused silica as collected. Dotted line represents the frequency dependent "time zero" of the pulse. Arrows represent the fact that the algorithm forces all frequencies to have a common time zero. (B) Numerically corrected spectrogram of the same pulse. Note that the existence of the "lobes" far from the carrier frequency indicates the fact that the algorithm does not correct for the frequency dependent instrument response.

3.3. NONCOLLINEAR OPTICAL PARAMETRIC AMPLIFICATION

3.3.1. Introduction

Although Ti:Sapphire lasers have proven to be very reliable sources of intense femtosecond pulses, by themselves they are limited experimentally by their narrow tuning range about the fundamental region (800 nm). Fortunately, this limited tunability can be improved considerably if Ti:Sapphire lasers are used in conjunction with other optical setups such as optical parametric amplifiers (OPA).[18-23] OPAs function by utilizing optical parametric generation (OPG), which can be succinctly summarized as follows.

In a suitable nonlinear crystal, such as β-barium borate (BBO), a high frequency high intensity beam (pump) and a lower frequency low intensity beam (seed) are overlapped both spatially and in time. A nonlinear interaction (difference frequency generation) occurs and the pump beam supplies a fraction of its energy to the seed beam; amplifying its intensity by many orders of magnitude (up to 10^7).[18] The creation of this amplified beam, now referred to as the signal beam, is concurrent with the generation of a third beam (idler), at the difference frequency between the pump and signal frequency.

$$\omega_p - \omega_s = \omega_i \qquad (3.12)$$

Where ω_p, ω_s, and ω_i are the pump, signal, and idler frequencies, respectively.[18] The OPG process can be thought of as a "feedback" mechanism where, in the presence of an intense pump beam, a seed photon at the signal wavelength stimulates the generation of both a signal and idler photon. Likewise, because of the symmetry of Equation 3.12, amplification of this newly created idler photon causes the generation of a new signal photon, which can then interact again to create another signal and idler photon. The process repeats itself many

times over with each successive cycle increasing the number of signal and idler photons available to perpetuate the process. This "feedback" between the signal and idler results in both having gains that are exponentially dependent on the propagation length through the crystal.[18]

In order for the amplification process to be efficient, phase matching (i.e., momentum conservation) of the wave vectors must also occur which is given by the well known expression

$$\Delta k = k_p - k_s + k_i = 0 \qquad (3.13)$$

where k_p, k_s, and k_i are the pump, signal, and idler wave vectors, respectively.[18] Because BBO crystals are birefringent, one achieves phase matching simply by orienting the crystal properly. In practice, this means that one can tune the frequency of the signal and idler beams simply by rotating the BBO crystal about a single axis. In principle, the signal frequency can range from $\dfrac{\omega_p}{2}$ to ω_p, however the range is often limited by the spectrum of the seed pulse and the absorption spectrum of the nonlinear crystal being used.[18]

3.3.2. Group Velocity Mismatch

Unfortunately, achieving the above phase matching condition given in Equation 3.13 does not simultaneously assure that the group velocities of the pump, signal, and idler pulses in the BBO crystal are equal. That is, due to the difference in carrier frequencies, the pump pulse propagates slower than the signal pulse in the BBO crystal which in turn propagates slower than the idler pulse. This is shown schematically in Figure 3.7(A) for the signal and

idler beams. As the propagation distance in the BBO crystal increases, the idler wavefront will lead the signal wavefront by an ever increasing amount. Because signal and idler photons are continuously regenerated from one another, new signal photons are being added onto the leading edge of the signal pulse and idler photons are being added to the trailing edge of the idler pulse. This has the net result of
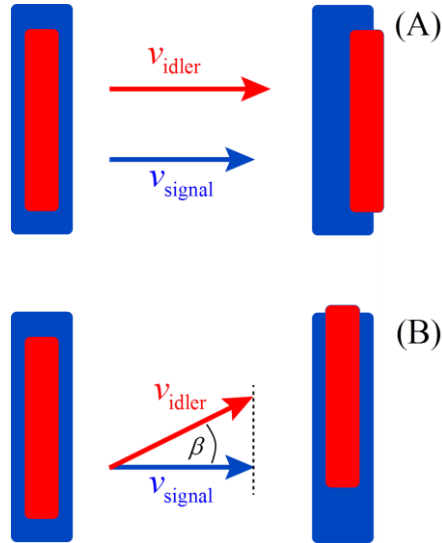
Figure 3.7: Schematic of the group velocity mismatch between the generated signal (blue) and idler (red) pulses within a nonlinear crystal during OPG. (A) Collinear beam geometry results in the lower frequency idler pulse propagating faster than the higher frequency signal pulse. Parametric generation of new signal and idler photons from the leading and trailing edges of the signal and idler pulse, respectively, results in a lengthening of both pulses in time. (B) Noncollinear beam geometries of the signal and idler at a suitable crossing angle, β, allows for group velocity matching in the propagation direction of the signal pulse. As a result, considerably shorter signal and idler pulses can be created than in a collinear beam geometry.

increasing both pulses in time, and correspondingly decreasing their bandwidth.[18, 19] Group velocity mismatch can be resolved by using very thin BBO crystals, where the propagation distance is so short that the idler and signal pulses are effectively always overlapped. However, as the amplification of the signal and idler beams is exponentially dependent on the propagation distance through the crystal, this has the effect of significantly reducing

output intensities.[18]   It is worth noting that group velocity mismatch is not a problem for the pump pulse as its excess intensity allows it to be stretched considerably in time before entering the BBO crystal, therefore ensuring a constant time overlap with the signal and idler pulses.

Fortunately, there is a simple solution to the problem of group velocity mismatch. Gale and coworkers demonstrated in the 1990s that by simply changing the angle between the propagating signal and idler beam in the crystal one can match the group velocities by altering the projection of the idler group velocity vector onto the signal group velocity vector.[24-27]   This is exhibited schematically in Figure 3.7(B)   In practice, one alters the angle between the signal and idler by changing the angle between the seed and pump beams as they overlap in the BBO crystal.   This type of OPA is referred to as a noncollinear optical parametric amplifier (NOPA), which has demonstrated the ability to generate significantly shorter pulses with much broader bandwidths than collinear OPAs.[19, 28-32]

3.3.3. Experimental Setup

Herein is described one of several NOPAs constructed to generate tunable femtosecond visible pulses for use in the experiments discussed below in Chapters 4-8.   A schematic of the NOPA design is shown in Figure 3.8.   An 800 nm fundamental beam generated from the Ti:Sapphire laser discussed above consisting of 1mJ, 130 fs pulses is split into two beams by a 98% reflective beam splitter. (BS1-800-98-1025-45S) The weaker beam (~20 μJ) is further attenuated by a variable neutral density filter (Thorlabs, NDC-50C-2M) to yield ~5 μJ pulses. This beam is focused onto a 2 mm thick sapphire crystal (Meller Optics,

MSW050/080), which results in the creation of supercontinuum white light pulses with spectra ranging from ~480-750 nm (gray).[33, 34] This broadband "seed" pulse is focused by spherical mirror #1 (Thorlabs, P01 silver coating) onto BBO #2. (Castech®, Type I, 1 mm thick, $\theta=32°$)

The majority of the 800 nm fundamental that is reflected by the original 98% beam splitter is sent onto translation stage #1 in order to be able to match the path lengths between the pump and seed beams. This beam is down-collimated to a beam diameter of ~7.5 mm and is propagated through BBO #1 (Castech®, Type I, 1.5 mm thick, $\theta=32°$). Second harmonic generation in BBO #1 creates 400 nm pump pulses containing ~100 uJ of energy. After removing the excess 800 nm fundamental with a dielectric filter (CVI Melles Griot, TLM1-800nm), the pump beam is propagated through 20 cm of fused silica glass block in order to stretch it in time to match the highly "chirped" continuum seed pulses. Note that before propagating through the fused silica, the beam is up-collimated with a telescope to a beam diameter of ~1 cm to avoid photodamage in the glass. Following the fused silica, the pump beam is down collimated by a factor of three and focused by a telescope to a position slightly behind BBO #2. Note that down collimation was performed in order to match the spot sizes of the pump and seed beams as closely as possible. Note also that the pump was not focused directly onto BBO #2 to avoid photodamage to the crystal.

Interaction of the pump beam with the seed beam through an OPG amplification process in BBO #2 results in the creation of a signal beam (green). Note that creation of the corresponding idler beam is not shown here. In order to provide further amplification, the signal beam is collimated and refocused back onto BBO #2 in the opposite direction by spherical mirror #2. Similarly, the remaining pump beam is recycled and is also refocused

back onto BBO #2, where a second stage of OPG amplification occurs. Time overlap for this second amplification process is achieved by adjusting translation stage #2. Output signal pulse energies with this setup typically range from 10-20 μJ.
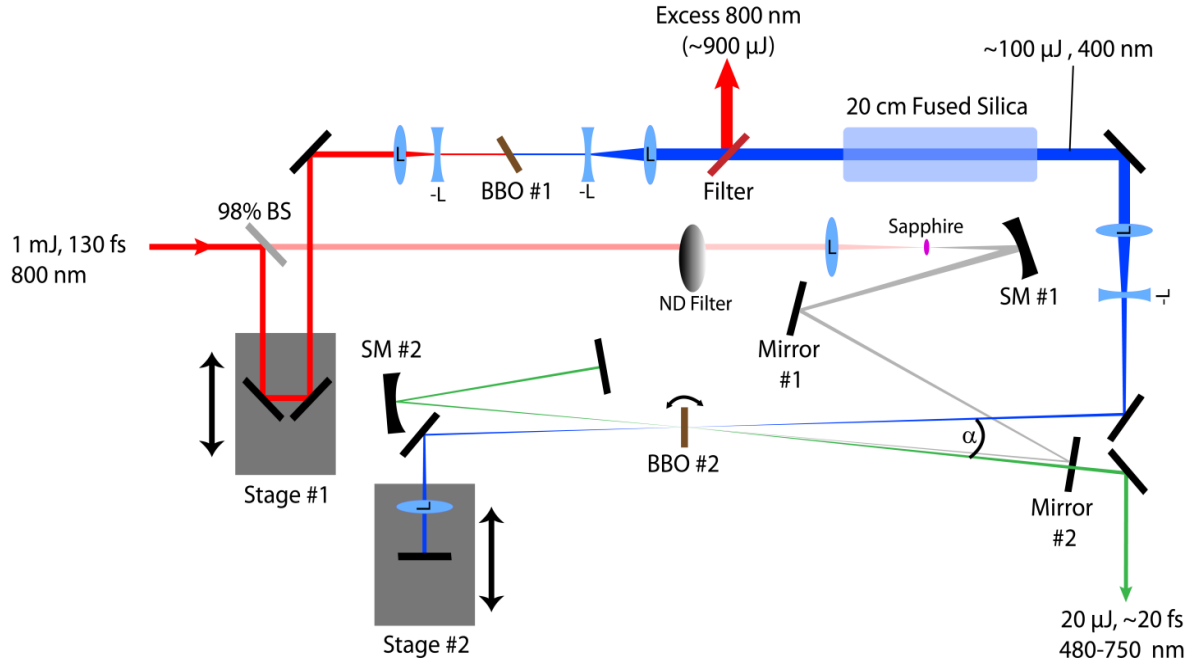
Figure 3.8: Schematic of a noncollinear optical parametric amplifier (NOPA) designed for the creation of femtosecond visible pulses (480-750 nm) at various pulse duration/bandwidths. Key: BS= beam splitter, L= positive focal length lens, -L=negative focal length lens, BBO = Type I β-barium borate crystal, SM=silver coated spherical mirror, ND filter = variable neutral density filter.

There are two main adjustable parameters with this setup. Rotation of BBO #2 alters the phase matching condition of the pump and seed beams and tunes the frequency of the signal beam. The signal frequencies that are obtainable are limited by the spectra of the continuum and span from ~480-750 nm. Example spectra spanning most of the tunable range are given in Figure 3.9(A). The other main adjustable parameter is the angle, α, between the pump and seed beams. As discussed above, this alters the group velocity mismatch of the signal and idler beams, thus affecting the pulse length/bandwidth. The

angle, α, is altered by adjusting the alignment of mirrors #1 and #2 and making a corresponding adjustment to stage #1 to match the change in seed path length. Figure 3.9(B) exhibits example spectra generated at various values of α demonstrating the bandwidth tunability of this setup.
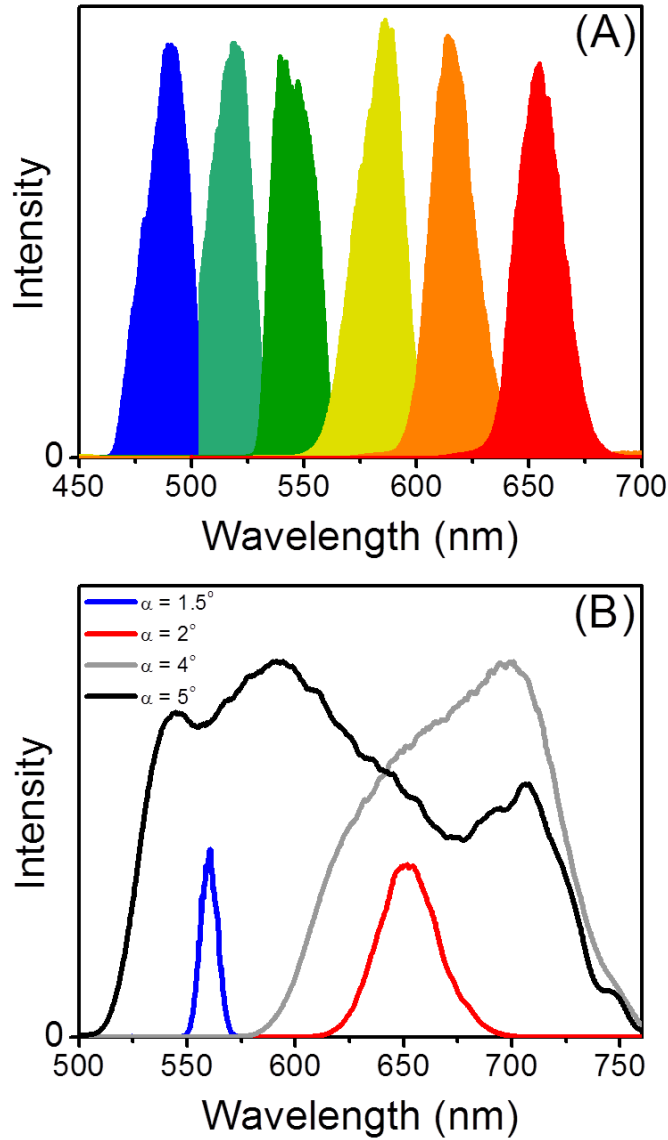
Figure 3.9: (A) Example spectra of ~20 fs visible pulses generated with a homebuilt NOPA at various phase matching conditions. (B) NOPA spectra generated at various angles, α, between the pump and seed beams which exhibits the bandwidth tunability of the NOPA setup. Spectral bandwidth shown here ranges from FWHM= 300 cm^{-1} at the narrowest possible angle with this setup (blue) to FWHM=5,300 cm^{-1} (black).

3.4. PULSE BROADENING WITH HOLLOW CORE FIBER

Although the noncollinear optical parametric amplifier discussed in the previous section has greatly increased the tunability of femtosecond pulses generated from our Ti:Sapphire laser system, it is limited by the spectrum of the continuum seed pulses to wavelengths greater than ~480 nm. Many systems of interest contain electronic transitions whose resonant frequencies are at higher energies than this.[35-38] It has therefore been necessary to develop other techniques to create femtosecond pulses at still lower wavelengths. The simplest technique to produce sub-480 nm pulses is second harmonic generation of the 800nm Ti:Sapphire fundamental in a suitable nonlinear crystal (e.g., BBO). Unfortunately, the generated 400 nm pulses cannot be shorter in duration than the fundamental and are in fact usually longer due to group velocity mismatch between 400 nm and 800 nm pulses (See Figure 3.7).

Spectral broadening due to self phase modulation while propagating through noble gas filled narrow optical fibers has proven to be an effective technique in shortening intense ultrafast pulses.[39-41] Below is briefly described a hollow core fiber fabricated by West, *et. al.* for both spectral broadening of 400 nm second harmonic pulses and generation of 267 nm pulses (third harmonic of 800 nm).[42] The setup is similar to that of Bradforth and co-workers and performs similarly.[43] Approximately 130 fs (FWHM = 160 cm^{-1}) second harmonic pulses (400 nm, 40 µJ) are focused into a 30 cm long hollow fused silica fiber with cavity diameter of 75 µm. The fiber is filled with a controlled pressure of argon gas (1-2 atm). Upon output of the fiber, pulse spectra are broadened significantly, where the extent of spectral broadening is controlled by the gas pressure. Figure 3.10(B) compares the spectrum of an input 400 nm pulse to the spectrally broadened pulse. In this example, the output

bandwidth is approximately 900 cm^{-1} corresponding to a Fourier transform-limited pulse duration of ~24 fs. Unfortunately, structure in the pulse spectra prohibits the pulse from reaching the transform limit. In practice, spectrally broadened 400 nm pulses typically are around 35 fs in duration. Still, this corresponds to a 3.7x increase in time resolution.
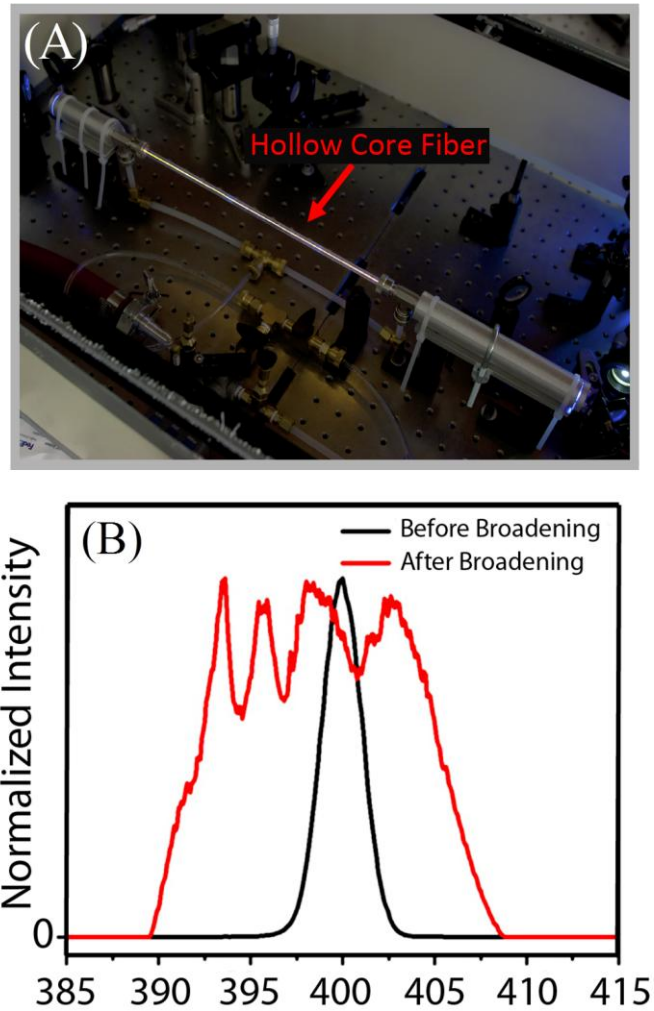
Figure 3.10: (A) Hollow core fiber setup for spectrally broadening 400 nm second harmonic pulses from a Ti:Sapphire laser. (B) Spectra of pulses before (black) and after (red) propagation through the hollow core fiber. Broadening corresponds to decrease in pulse length of about 3.7x.

3.5. TRANSIENT ABSORPTION SPECTROSCOPY

Energy and charge transfer processes occurring in materials often take place on an ultrafast timescale (i.e., fs-ps). Conventional measurement techniques are far too slow to directly resolve these events, thus necessitating techniques with faster time resolution. Perhaps the most common technique utilized for resolving such short processes is transient absorption (TA) spectroscopy, which relies on the extremely short duration of ultrashort laser pulses for its unparalleled time resolution. Below, the discussion is limited to visible TA spectroscopy; however it is worth noting that the technique is utilized in other spectral regions.[44, 45]

Although not straightforward in practice, conceptually, TA spectroscopy is easy to understand. It is simply an analog to the widely used steady state linear absorption spectroscopy with the only difference being that instead of probing a system at equilibrium, one measures the absorption spectra of a non-equilibrium system as a function of time. TA spectroscopy is a 3rd order "pump-probe" spectroscopy. First, a "pump" beam is used to excite a sample out of its equilibrium state. In visible TA, the "pump" frequency is resonant with an electronic transition in the sample leading to a fraction of the molecular ensemble being promoted to an electronic excited state(s). Depending on the experimental conditions, (pump intensity, extinction coefficient, etc.) the fraction of the ensemble that is excited can range from <1% to tens of percents.[46] Following excitation, a second pulse (the "probe" pulse) is propagated through the excited sample volume at a variable delay, T, with respect to the two "pump" pulses. As this is not always appreciated, it is worth noting that being a 3rd order spectroscopic process, the "pump" beam actually supplies two field matter interactions in TA spectroscopy (See Chapter 2.3.3). The "probe" pulse is used to monitor the system as

it relaxes following excitation. At each delay, T, the transmitted "probe" pulse is dispersed into its component frequencies and its spectrum is measured with a suitable detector system. Since one is interested in how the excited system differs from the equilibrium system, the transmitted "probe" spectrum is measured both with the "pump" beam blocked and unblocked. The difference absorption spectrum, $\Delta A(\omega)$, is then calculated for each value of the pulse delay

$$\Delta A(\omega, T) = A_{Excited}(\omega, T) - A_{Equilibrium}(\omega) \tag{3.14}$$

where $A_{Excited}(\omega, T)$ is the absorption spectrum of the system with the "pump" unblocked, and $A_{Equilibrium}(\omega)$ is the absorption spectrum of the system with the "pump" blocked.

TA is a powerful technique in that examining how $\Delta A(\omega, T)$ changes as a function of pulse delay one is directly monitoring dynamical processes occurring in the system. Furthermore, TA spectra are simple to interpret as they can contain contributions from only a few classes of signals. As was discussed above in Chapter 2.3.3, for a two level system, only ground state bleach (GSB) and excited state emission (ESE) signals can be observed in TA spectra. GSB corresponds to a decreased ground state population in the excited system due to the fact that the "pump" beam has promoted a fraction of the ensemble to an excited state. Consequently, absorption from population in the ground state of the excited system is less than the absorption from population in the ground state of the unexcited system. This results in a net negative sign in $\Delta A(\omega, T)$. Because this type of signal is dependent on the ground state absorption spectrum, GSB is only observed in TA spectra at frequencies containing resonances in the equilibrium linear absorption spectrum.

ESE corresponds to the emission of light from the excited state population that is stimulated by the perturbation of the "probe" pulse. Because, the radiated field is collinear with the "probe pulse," more light reaches the detector and this registers as a decrease in $A_{Excited}(\omega,T)$. Thus, ESE is also observed as a net negative sign in $\Delta A(\omega,T)$. ESE can be distinguished from GSB due to the fact that at long pulse delays the signal will be observed to be occurring in the same spectral region as the steady state fluorescence spectrum of the system. That is, it is Stoke shifted with respect to the GSB signal. It is interesting to note that at short pulse delays (i.e, before nuclear relaxation has occurred) ESE will be observed in the same spectral region as the GSB and nuclear relaxation can actually be directly observed as a spectral red shift of the ESE signal.[47, 48]

For systems containing more than two states, a third type of signal can be observed. If the "probe" pulse is resonant with the energy gap between the excited state populated by the "pump" pulse, and higher energy excited state(s), population will be transferred to these higher lying states. Thus, "probe" intensity is absorbed, which results in a net increase in $A_{Excited}(\omega,T)$. Consequently, excited state absorption (ESA) is a positive contribution to ΔA.

As an example the TA spectrum of the dye, $[(Ru(bpy)_2(4,4'\text{-}(PO_3H_2)_2bpy)]Cl_2$ adsorbed onto TiO_2 nanoparticles recorded at T=5 ps following 400 nm "pump" excitation can be seen in Figure 3.11. Comparison of the TA spectrum to the equilibrium ground state absorption spectrum in this example clearly exhibits the strong contribution of GSB at shorter wavelengths. Around 600 nm and higher, the TA signal becomes positive indicating that an ESA transition(s) in the sample has become dominant in this spectral region. Although the dye fluoresces near 650 nm, ESE is not observed in this signal as the dye

excited state population is very quickly "quenched" following a sub 150 fs electron transfer from the dye to the TiO$_2$ (See Chapter 8).
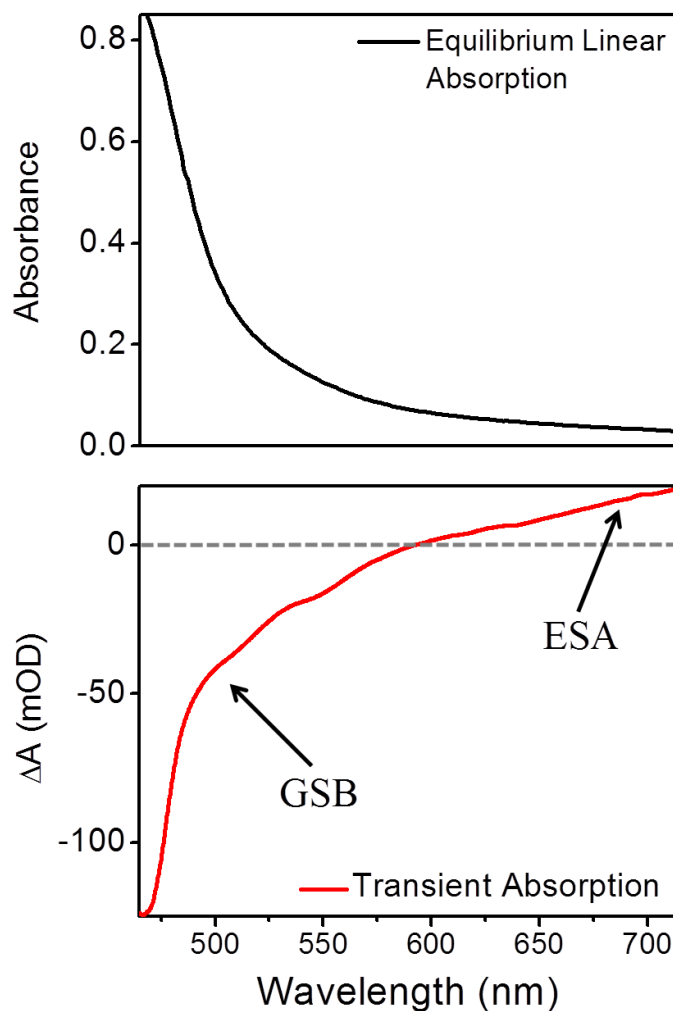
Figure 3.11: Top panel exhibits the equilibrium linear absorption spectrum of the dye, [(Ru(bpy)$_2$(4,4'-(PO$_3$H$_2$)$_2$bpy)]Cl$_2$ adsorbed onto TiO$_2$ nanoparticles. Bottom panel exhibits the TA spectrum of the same system recorded at T=5 ps following 400 nm "pump" excitation. Comparison of the TA spectrum to the equilibrium ground state absorption spectrum in this example clearly exhibits the strong contribution of GSB at shorter wavelengths. At longer wavelengths the ESA signal corresponding to a neutral ligand-metal charge transfer transition dominates.[49] ESE is not observed in this sample due to sub-150 fs quenching of excited state population through electron transfer from the dye to the TiO$_2$.

3.6. TRANSIENT GRATING SPECTROSCOPY

3.6.1. Introduction

Like TA spectroscopy, transient grating (TG) spectroscopy is a 3rd order "pump-probe" spectroscopic technique. Both the fundamental physics and the measured signals with both techniques are analogous. For example, although TG spectroscopy is capable of obtaining the dispersive signal component (i.e., changes in refractive index)[50-53], if only the absorptive signal component is considered, TG spectroscopy signals are exactly equivalent to TA spectroscopy signals.[54, 55] For this reason, even though all time resolved experiments discussed in this dissertation are collected using a TG experimental setup, the terms "transient grating" and "transient absorption" are used interchangeably in Chapters 4-8.

As discussed in Chapter 2.3.3 TG and TA spectroscopic signals are radiated by an induced 3rd order polarization following interactions with three external fields. The induced polarization is mathematically described by the following expression[55, 56]

$$P^{(3)}(t) = \int_0^\infty \int_0^\infty \int_0^\infty S^{(3)}(t_1,t_2,t_3) E_{Pump}(t-t_1-t_2-t_3) E_{Pump}(t-t_2-t_3) E_{Probe}(t-t_3) dt_1 dt_2 dt_3 \qquad (3.15)$$

where again $S^{(3)}(t_1,t_2,t_3)$ represents the response function of the system, $E_{Pump}(t-t_1-t_2-t_3)$ and $E_{Pump}(t-t_2-t_3)$ represent the first and second interacting "pump" fields, respectively, and $E_{Probe}(t-t_3)$ represents the "probe" field. A schematic of the pulse sequence for both spectroscopies is shown in Figure 3.12, which is useful for understanding the optical processes occurring. First, two identical "pump" pulses arrive at the sample simultaneously (i.e., $\tau = 0$) and excite an electronic transition in the sample. Note that although the peak of both "pump" pulses arrive simultaneously, there can be an interval between the two field

matter interactions, t_1, due to the nonzero pulse duration. Following these first two interactions, the excited system relaxes during an experimentally controlled delay, T. Following this delay, the "probe" pulse interacts with the sample which stimulates the radiation of the signal field at time, t.
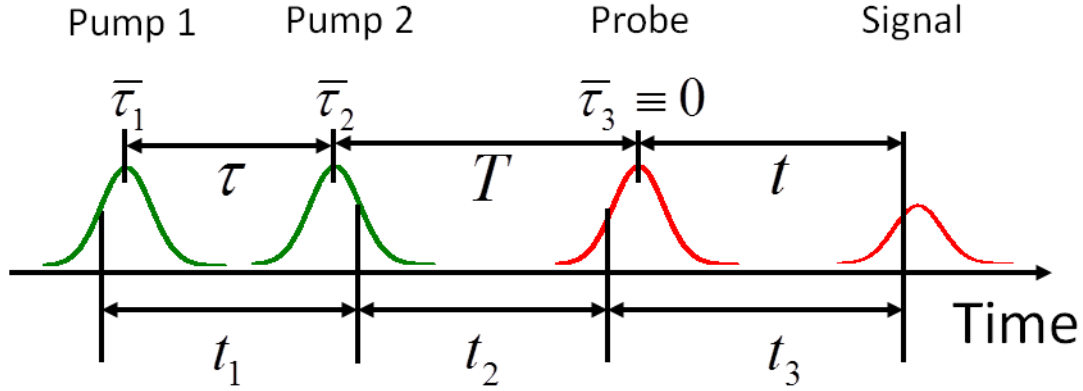
Figure 3.12: Pulse sequence describing a 3rd order spectroscopic experiment such as transient grating or transient absorption. Pulse centers are defined as $\bar{\tau}_i$ where the delay between the pulses is given by $\tau = \bar{\tau}_2 - \bar{\tau}_2$ and $T = \bar{\tau}_3 - \bar{\tau}_2$. Field matter interactions occur at times $t - t_1 - t_2 - t_3$ and $t - t_2 - t_3$ for the first and second "pump" interactions, respectively, $t - t_3$ for the "probe" interaction, and t for the radiation of the signal field.

Experimentally, TG spectroscopy differs from TA spectroscopy only by the beam geometry utilized. Specifically, TG spectroscopy utilizes two noncollinear "pump" beams to supply the two excitation interactions, while in TA spectroscopy both interactions come from a single "pump" beam. For both spectroscopies, the signal beam is radiated in the phase matching direction, $k_s = -k_1 + k_2 + k_3$ where k_1 and k_2 represent the wave vectors of the two "pump" beams and k_3 is the wave vector of the "probe" beam. As is shown schematically in Figure 3.13, this phase matching condition results in the signal being radiated in a background free direction for TG spectroscopy.
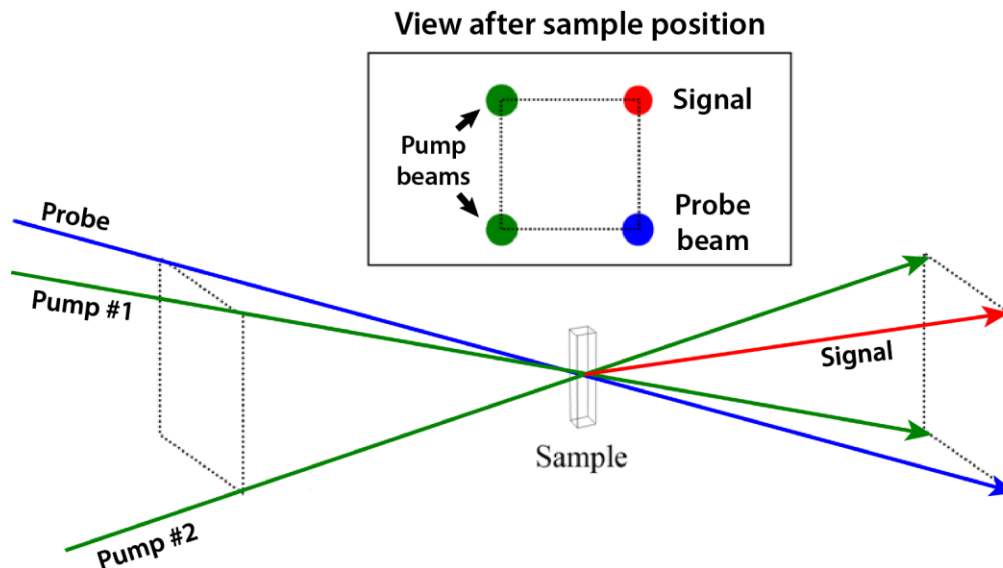
Figure 3.13: Beam geometry used in a TG spectroscopy experiment. Green and blue lines represent the "pump" beams and "probe" beams, respectively. The signal beam (red) is radiated in the phase matching direction, $k_s = -k_1 + k_2 + k_3$, which corresponds to a background free direction.

This is an enormous advantage for TG spectroscopy over TA spectroscopy where, according to the same phase matching condition, the signal beam is radiated collinearly with the transmitted "probe" beam. Signals for both techniques are typically ~1000 times less intense than the "probe" beam; thus making it technically difficult to separate the signal intensity from the overwhelming "probe" intensity in TA spectroscopy. TA spectroscopists compensate for this by using high intensity "pump" beams in order to increase the signal strength. Unfortunately, this both complicates signal interpretation by creating undesirable high photoexcitation densities and can also cause sample photodegredation. For TG spectroscopy, the background free signal means that the signal does not have to be separated from the "probe" intensity. Consequently, much lower "pump" intensities can be utilized and detection of extremely weak signals is possible as the only requirement is that the signal intensity is greater than the noise level of the detector.

The fact that all three beams are spatially separate in TG spectroscopy also allows experimentalists to individually control aspects of each field matter interactions. For example, by controlling the delay of each "pump" pulse individually, one can perform more complex experiments such as photon echo.[57-65] More relevant to this dissertation, however, is the individual control of the pulse polarizations that the TG geometry affords. This allows one to utilize a variety of tensor elements to obtain specialized information about the system. The TG experiments discussed in Chapter 8 that utilize "cross-polarized" tensor elements are an excellent example of the power of this specialized capability as sample information is obtained that cannot be observed using conventional TA spectroscopy.

3.6.2. Interferometric Signal Detection

Although the background free signal radiated in visible TG spectroscopy can be measured directly by a detector (i.e., homodyne detection), this is generally not the optimal technique of recording the signal. First, because the response of the electronics in detector systems is far too slow to directly resolve the oscillating electric field of the signal, one is limited to measuring the quadratic response of the field (i.e., the intensity). Generally, one is more interested in the linear response of the signal electric field, so this is not ideal. More importantly, however, is the fact that by measuring the square of the signal field, one loses all phase information that was contained in the signal. It is therefore impossible to separate the dispersive and absorptive signal components and also to determine the net sign of the signal (e.g., GSB or ESA).

Optical heterodyne signal detection (OHD) is an established method for solving both of these problems. OHD is an interferometric technique in which a steady state reference beam, generally referred to as the local oscillator (LO), is mixed coherently with the signal beam before arriving at the detector. The resulting interferogram is recorded where the total intensity on the detector is given by[56, 66]

$$I = |E_{LO}|^2 + |E_S(t)|^2 + 2|E_{LO}E_S(t)|\cos(\phi_{LO} - \phi_S) \qquad (3.16)$$

where E_{LO} is the local oscillator field, $E_S(t)$ is the time dependent signal field, and ϕ_{LO} and ϕ_S are the phases of the local oscillator and signal fields, respectively. The constant term $|E_{LO}|^2$ can easily be eliminated either at the time of data collection through such techniques as lock-in detection or can be subtracted subsequent to data collection through numerically processing. In the experiments discussed herein, the local oscillator intensity term is numerically removed through a Fourier transform/apodization routine, which is included in the appendices. In the limit of the local oscillator intensity being much greater than the signal intensity (i.e., $|E_{LO}|^2 \gg |E_S(t)|^2$) the term $|E_S(t)|^2$ can be neglected; therefore reducing the measured signal intensity to the following

$$I = 2|E_{LO}E_S(t)|\cos(\phi_{LO} - \phi_S) \qquad (3.17)$$

Thus, it is clear that with OHD detection the detector response is linear with respect to the signal field and the phase information required to characterize the components of the signal field is still present. Furthermore, the measured signal is amplified by a factor of $2|E_{LO}/E_S(t)|$ over the homodyne detected signal.[66] This signal enhancement further increases the capability of TG spectroscopy for measuring extremely weak signals. An

example of the increase in signal quality afforded by heterodyne signal detection can be seen in Figure 3.14 where TG measurements on cyclohexane recorded using both heterodyne and homodyne signal detection techniques are shown.
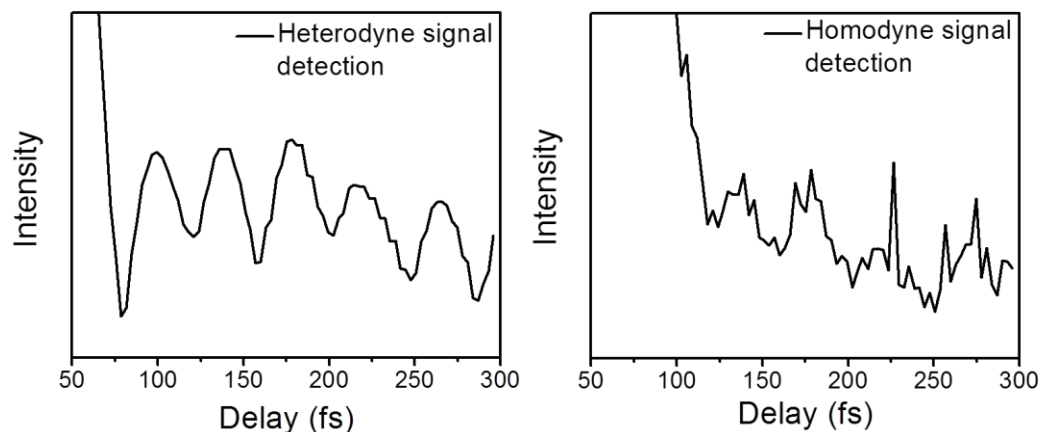
Figure 3.14: Example of the increase in signal to noise ratio afforded by the use of heterodyne signal detection over homodyne signal detection. The left panel shows the absolute value of the heterodyne TG signal field of cyclohexane excited and probed with ~15 nJ pulses centered at 266 nm. Data collection time was approximately 5 minutes. The right panel represents the exact same experiment except that the signal was not measured interferometrically. Note that the oscillations shown represent low frequency nuclear motion in cyclohexane. These oscillations are clearly much more distinct in the heterodyne signal than the homodyne signal.

3.6.3. Diffractive Optic Based Phase Stabilization

Although OHD is certainly not a new signal detection technique, it has historically been difficult to implement with visible TG spectroscopy due to the technical requirement of phase stability in this spectral region. Specifically, in order to obtain reliable data, the relative phase between the signal and local oscillator, $\Delta\phi \equiv \phi_{LO} - \phi_S$ must remain constant throughout the course of the experiment. For TG experiments, this relative phase must be

expanded to contain the phases of all input pulses which can be described by the following expression[66]

$$\Delta\phi = \frac{\pi}{2} + \phi_\chi + (\phi_{Pump\ 1} - \phi_{Pump\ 2}) - (\phi_{LO} - \phi_{pr}) \qquad (3.18)$$

where $\phi_{Pump,n}$ and ϕ_{pr} refer to the "pump" and "probe" phases, respectively. The term ϕ_χ is the phase shift due to the complex nonlinear susceptibility and the $\frac{\pi}{2}$ term is added to correspond to the phase shift between the induced 3rd order polarization and the radiated field. As the phase of each beam is a function of the path length traversed, minor variations in the path length caused by vibrations, air currents, and or small changes in temperature can cause large fluctuations in the relative phase for visible pulses. Perhaps the most obvious solution to this problem is to engineer the TG setup to have excellent mechanical stability and to control parameters such as the temperature, humidity, and air currents with a great deal of precision. Although OHD has been demonstrated to be effective in this manner,[67] it is rather cumbersome and requires a great deal of care to perform experiments. Another common solution to this problem has been to continuously monitor the relative phase difference, $\Delta\phi$, throughout the course of the experiment and to input this information back into the interferometer through a feedback loop. This allows one in real time to directly counteract the phase fluctuations by adjusting the position of one or more of the optics with a piezoelectric transducer.[68,69] This active phase stabilization technique is unfortunately quite expensive and also introduces unwanted complexity to the experiment.

The heterodyne TG spectrometer utilized in this dissertation is based on a much simpler and practical setup developed in the late 1990's that utilizes diffractive optics and

common optics for all beams.[56, 66, 70-77] The primary difference between this device design and previous designs is the manner in which the "pump", "probe", and local oscillator beams are generated and propagated through the setup. In previous designs, individual beams are propagated through the setup using independent optics all of which undergo uncorrelated vibrations. Furthermore, the beams are often not spatially located near one another and thus do not "sample" the same fluctuations in temperature/air currents. In the design utilized herein, all four beams are generated by propagating a single "pump" and "probe" beam through a diffractive optic. This separates the beams into the ± 1 diffraction orders; thus creating the two identical "pump" beams and the identical "probe" and local oscillator beams. The angle between these generated beams is very small (~5°) thus, they are all located spatially in the same general region and "sample" the same fluctuations in temperature/air currents. More importantly, because the beams are close to one another, they can all be propagated through the setup using common optics. Thus all beams "sample" the same vibrations and the corresponding phase fluctuations of the individual beams are self canceling.[56] The result is a passively phase stabilized system that requires no exceptional mechanical stability or moving parts. Specifics of the experimental setup are shown below in Chapter 3.6.5.

3.6.4. Tensor Elements

So far, the spatial directionality of the optical response for a given system has been ignored for clarity. In reality, however, the response of a system can depend very strongly on the vector properties (i.e., the polarization) of the applied field(s). Mathematically, the optical susceptibility for any spectroscopic order, $\chi^{(n)}(\omega)$, is a tensor of rank $n+1$. That is, the rank equals the number of fields that are involved in the process. The number of tensor

107

elements in the $\chi^{(n)}(\omega)$ tensor is given by $3^{(n+1)}$. Thus for the linear susceptibility, the number of tensor elements is equal to $3^{(2)} = 9$. That is, there are nine possible permutations of the field polarizations that must be considered.

Being a 3rd order process, TG spectroscopy is considerably more complicated as there are a total of $3^4 = 81$ possible tensor elements to consider. The frequency domain induced polarization in any 3rd order spectroscopy is given by

$$P_l^{(3)}(\omega_s) = \chi_{ijkl}^{(3)} E_i(\omega_1) E_j(\omega_2) E_k(\omega_3)$$
(3.19)

where $E_i(\omega_1)$ and $E_j(\omega_2)$ represent the spectra of the two "pump" fields, and $E_k(\omega_3)$ represents the spectrum of "probe" field. The term, $\chi_{ijkl}^{(3)}$, represents the susceptibility corresponding to a specific tensor element, $ijkl$. It would seem to be a monumental task to perform experiments with all possible polarization permutations of the four fields. Fortunately, in a bulk isotropic system, only twenty one of the possible eighty one tensor elements are non zero due to symmetry.[78] Furthermore, because in an isotropic system, there is no sense in emphasizing any particular Cartesian direction over the other two, seventeen of these tensor elements are simply equal permutations of others. Thus, practically speaking, if one wants to explore all possible polarization aspects of a given system with TG spectroscopy, there are really only four tensor elements that the system must be probed with. Specifically, these tensor elements are: ZZZZ, XXZZ, ZXXZ, and ZXZX.[78] In this format, going from left to right the letters represent the polarizations of the first and second "pump" fields, the "probe" field, and the radiated signal field. Here, as in all cases in this dissertation, the letter Z represents a polarization that is vertical with respect to the lab frame, and the letter X represents a polarization that is perpendicular to the lab frame. Again, note

that this spatial direction is only chosen for convenience and does not have any special importance in an isotropic system.

As the ZZZZ and XXZZ tensor elements have both "pump" interactions containing the same polarization, they can be measured with both TG spectroscopy and with conventional TA spectroscopy. This is not the case with the ZXXZ and ZXZX tensor elements, however. For these "cross polarized" tensor elements, the two "pump" fields are orthogonally polarized to one another. In order to perform measurements with these tensor elements, one must have the ability to control the polarizations of each individual interaction. As TG spectroscopy utilizes two spatially separate "pump" beams, this is easily accomplished. For TA spectroscopy, where both "pump" interactions are supplied by a single beam, this control is impossible. Although often overlooked, this is another important advantage for TG spectroscopy as very important information can sometimes be observed only when using a certain tensor element. This is exemplified in Figure 3.15 where the results of a TG spectroscopy experiment are shown for a $[(Ru(bpy)_2(4,4'-(PO_3H_2)_2bpy)]$ sensitized-TiO_2 system using both a "conventional" ZZZZ tensor element, and the "cross polarized" tensor element ZXZX. In the ZXZX signal, oscillations in the signal corresponding to an impulsively induced vibration in the TiO_2 are clearly seen. Observation of these coherences proves that for at least a measureable fraction of the total ensemble, strong dye-TiO_2 coupling exists (See Chapter 8). As these coherences are not evident in either the ZZZZ or the XXZZ (not shown) tensor element data, this surprising result could not have been discovered using conventional TA spectroscopy.
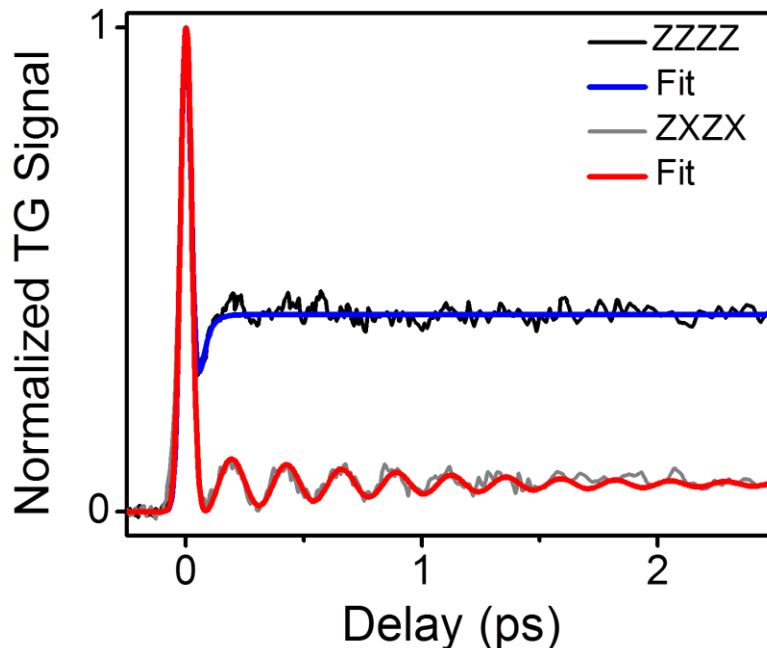
Figure 3.15: Absolute value of the TG signal field measured at 530 nm following 400 nm excitation of $[(Ru(bpy)_2(4,4'-(PO_3H_2)_2bpy)]$ sensitized TiO_2 nanoparticles. Experiments performed with the specialized tensor element ZXZX (gray) exhibit oscillations corresponding to a molecular vibration in TiO_2, which provides surprising evidence for strong dye-TiO_2 coupling. As these coherences are not observed in the more conventional ZZZZ tensor element (black), these results would not be observable with TA spectroscopy. See Chapter 8 for a more detailed discussion of these experiments.

3.6.5. Experimental Setup

Here is described the TG setup constructed for use the in experiments discussed in Chapters 4-8, which is shown schematically in Figure 3.16. A single "pump" beam (blue) and a single "probe" beam (red) are focused by a spherical mirror (not shown) onto a custom designed 80 g/mm transmission grating (Holoeye) at a horizontal angle of approximately 5°. Prior to entering the setup, the "probe" beam is delayed with respect the "pump" beam with a motorized translation stage (Newport GTS150). Note also that prior to being focused onto the transmission grating, both beams propagate parallel to one another; thus the beams are

spatially overlapped in the transmission grating. The grating produces an angle of 4.65° at 590 nm between the ±1 diffraction orders which are vertically offset from one another. Vertical offset is represented in Figure 3.16 by solid and dashed lines of the same color. Efficiency into the ±1 diffraction orders is approximately 25%. All other diffraction orders and the residual non-diffracted beams are blocked with a spatial filter (not shown). All four beams are collimated by spherical mirror #1 which is tilted slightly horizontally from the propagation direction to direct the beams towards spherical mirror #2. During this period the LO beam is attenuated by a factor of approximately 1000 by propagating through a 2 mm thick fused silica variable neutral density filter (Thorlabs, NDC-50C-2M). In order to make the "probe" beam arrive at the sample position ~800 fs after the LO, the "probe" is propagated through a 2 mm thick fused silica window (Edmund) and two 175μm thick quartz microscope coverslips (Fisher) in addition to a wave plate (Thorlabs). During this period, both "pump" beams are also propagated through identical wave plates. Thus, they arrive at the sample simultaneously and their polarizations can be individually controlled. Spherical mirror #2 focuses the beams onto the sample position, where the signal is radiated in the $k_s = -k_{pump1} + k_{pump2} + k_{probe}$ phase matching direction. Due to the boxcar geometry of the beams (see inset), the signal and LO beams propagate collinearly after the sample position. After the sample, a spatial filter blocks all other beams while simultaneously blocking any scattered light. The signal/LO beams are collimated by a lens and propagated through a Calcite polarizer in order to block all unwanted signal polarizations. Note that this is the only way to make sure that the final index in the tensor element being measured is the desired Z or X. The interference pattern generated by the signal and LO beams is dispersed in a 0.3 m spectrograph and detected with a back-illuminated CCD (Princeton Instruments

111

PIXIS 100B). With this setup, all four beams are directed by common optics and beams are never more than 4 cm apart from one another. Thus, all beams "sample" the same environmental fluctuations, and exhibit exceptional passive phase stability. The standard deviation in phase fluctuations over a three hour period is 0.2 radians.
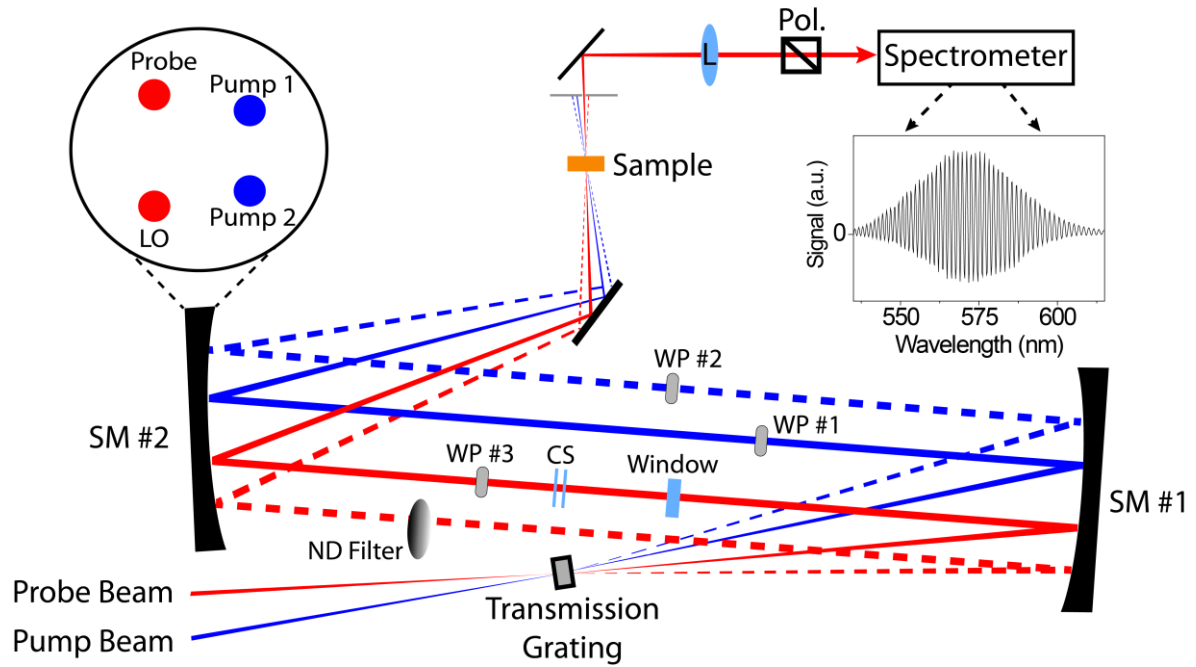
Figure 3.16: Homebuilt diffractive optic based TG setup used in experiments described in Chapters 4-8. Key: SM = spherical mirror, CS = quartz microscope coverslip, WP = wave plate, ND filter = variable neutral density filter, L = lens, LO = local oscillator, and Pol. = polarizer.

3.7. REFERENCES

(1)   Spence, D. E.; Kean, P. N.; Sibbett, W. *Opt. Lett.* 1991, *16*, 42-44.

(2)   Kapteyn, H. C.; Murnane, M. M. 1994, *5*, 20-28.

(3)   Backus, S.; Durfee, C. G. I.; Murnane, M. M.; Kapteyn, H. C. *Rev. Sci. Instrum.* 1998, *69*, 1207-1223.

(4)   Steinmeyer, G.; Sutter, D. H.; Gallmann, L.; Matuschek, N.; Keller, U. *Science* 1999, *286*, 1507-1512.

(5)   Valdmanis, J. A.; Fork, R. L. *IEEE J. Quantum Electron.* 1986, *22*, 112-118.

(6)   Strickland, D.; Mourou, G. *Opt. Commun.* 1985, *56*, 219-221.

(7)   Maine, P.; Strickland, D.; Bado, P.; Pessot, M.; Mourou, G. *IEEE J. Quantum Electron.* 1988, *24*, 398-403.

(8)   Pessot, M.; Squier, J.; Bado, P.; Mourou, G.; Harter, D. J. *IEEE J. Quantum Electron.* 1989, *25*, 61-66.

(9)   Pessot, M.; Maine, P.; Mourou, G. *Opt. Commun.* 1987, *62*, 419-421.

(10)   Asaki, M. T.; Huang, C. P.; Garvey, D.; Zhou, J.; Kapteyn, H. C.; Murnane, M. M. *Opt. Lett.* 1993, *18*, 977-979.

(11)   Zhou, J.; Taft, G.; Huang, C. P.; Murnane, M. M.; Kapteyn, H. C.; Christov, I. *Opt. Lett.* 1994, *19*, 1149-1151.

(12)   Stingl, A.; Lenzner, M.; Spielmann, C.; Krausz, F. *Opt. Lett.* 1995, *20*, 602-604.

(13)   Diels, J.; Rudolf, W. *Ultrashort Laser Pulse Phenomena*, Second ed.; Academic Press: Massachusetts, 2006.

(14)   Trebino, R. Frequency-Resolved Optical Gating: The Measurement of Ultrashort Laser Pulses; Kluwer Academic: Boston, MA, 2000.

(15)   Newport Corporation, 2006; Vol. 2012.

(16)   Fork, R. L.; Martinez, O. E.; Gordon, J. P. *Opt. Lett.* 1984, *9*, 150-152.

(17)   Treacy, E. B. *IEEE J. Quantum Electron.* 1969, *QE-5*, 454-458.

(18)   Cerullo, G.; Silvestri, S. D. *Rev. Sci. Instrum.* 2003, *74*, 1-18.

(19)   Riedle, E.; Beutter, M.; Lochbrunner, S.; Piel, J.; Schenkl, S.; Spörlein, S.; Zinth, W. *Appl. Phys. B.* 2000, *71*, 457-465.

(20)   Piskarskas, A. P.; Stabinis, A. P.; Pyragaite, V. *IEEE J. Quantum Electron.* 2010, *46*, 1031-1038.

(21)   Greenfield, S. R.; Wasielewski, M. R. *Opt. Lett.* 1995, *20*, 1394-1396.

(22)   Greenfield, S. R.; Wasielewski, M. R. *Appl. Opt.* 1995, *34*, 2688-2691.

(23)   Yakovlev, V. V.; Kohler, B.; Wilson, K. R. *Opt. Lett.* 1994, *23*, 2000-2002.

(24)   Driscoll, T. J.; Gale, G. M.; Hache, F. *Opt. Commun.* 1994, *110*, 638-644.

(25)   Gale, G. M.; Cavallari, M.; Driscoll, T. J.; Hache, F. *Opt. Lett.* 1995, *20*, 1562-1564.

(26)   Gale, G. M.; Cavallari, M.; Hache, F. *15* 1997, 702-714.

(27)   Gale, G. M.; Hache, F.; Cavallari, M. *IEEE J. Sel. Top. Quantum Electron.* 1998, *4*, 224-229.

(28)   Willhelm, T.; Piel, J.; Riedle, E. *Opt. Lett.* 1997, *22*, 1494-1496.

(29)   Cerullo, G.; Nisoli, M.; Silvestri, S. D. *Appl. Phys. Lett.* 1997, *71*, 3616-3618.

(30)   Shirakawa, A.; Kobayashi, T. *Appl. Phys. Lett.* 1998, *72*, 147-149.

(31)   Cerullo, G.; Nisoli, M.; Stagira, S.; Silvestri, S. D. *Opt. Lett.* 1998, *23*, 1283-1285.

(32)   Baltuška, A.; Fuji, T.; Kobayashi, T. *Opt. Lett.* 2002, *27*, 306-308.

(33)   Fork, R. L.; Shank, C. V.; Hirlimann, C.; Yen, R.; Tomlinson, W. J. *Opt. Lett.* 1983, *8*, 1-3.

(34)   Alfano, R. R. The Supercontinuum Laser Source: Fundamentals with Updated References, Second ed.; Springer: New York, 2006.

(35)   Miller, S. A.; West, B. A.; Curtis, A. C.; Papanikolas, J. M.; Moran, A. M. *J. Chem. Phys.* 2011, *135*, 081101-081101-081104.

(36)   Miller, S. A.; Stuart, A. C.; Womick, J. M.; Zhou, H.; You, W.; Moran, A. M. *J. Phys. Chem. C.* 2011, *115*, 2371-2380.

(37)   Miller, S. A.; Fields-Zinna, C. A.; Murray, R. W.; Moran, A. M. *J. Phys. Chem. Lett.* 2010, *1*, 1383-1387.

(38)   Miller, S. A.; Womick, J. M.; Parker, J. F.; Murray, R. W.; Moran, A. M. *J. Phys. Chem. C.* 2009, *113*, 9440-9444.

(39)   Nisoli, M.; Silvestri, S. D.; Svelto, O. *Appl. Phys. Lett.* 1996, *68*, 2793-2795.

(40)   Nisoli, M.; Stagira, S.; Svelto, O.; Sartania, S.; Cheng, Z.; Lenzner, M.; Spielmann, C.; Krausz, F. *Appl. Phys. B.* 1997, *65*, 189-196.

(41)   Kolevatova, O. A.; Naumov, A. N.; Zheltikov, A. M. *Opt. Commun.* 2003, *217*, 169-177.

(42)   West, B. A.; Womick, J. M.; Moran, A. M. *J. Chem. Phys.* 2011, *135*, 114505-114501-114509.

(43)   Jailaubekov, A. E.; Bradforth, S. E. *Appl. Phys. Lett.* 2005, *87*, 021107-021101-021103.

(44)   Herbst, J.; Heyne, K.; Diller, R. *Science* 2002, *297*, 822-825.

(45)   Schenkl, S.; van Mourik, F.; van der Zwan, G.; Haacke, S.; Chergui, M. *Science* 2005, *309*, 917-920.

(46)   Berera, R.; van Grondelle, R.; Kennis, J. T. *Photosynth. Res.* 2009, *101*, 105-118.

(47)   Kovalenko, S. A.; Ruthmann, J.; Ernsting, N. P. *Chem. Phys. Lett.* 1997, *271*, 40-50.

(48)   Vos, M. H.; Jones, M. R.; Hunter, C. N.; Breton, J.; Lambry, J.-C.; Martin, J.-L. *Biochemistry* 1994, *33*, 6750-6757.

(49)   Wallin, S.; Davidsson, J.; Modin, J.; Hammarström, L. *J. Phys. Chem. A* 2005, *109*, 4697-4704.

(50)   Nelson, K. A.; Caselegno, R.; Miller, R. J. D.; Fayer, M. D. *J. Chem. Phys.* 1982, *77*, 1144-1152.

(51)   Terazima, M.; Hara, T.; Hirota, N. *Chem. Phys. Lett.* 1995, *246*, 577-582.

(52)   Hara, T.; Nirota, N.; Terazima, M. *J. Phys. Chem.* 1996, *100*, 10194-10200.

(53)   Vöhringer, P.; Scherer, N. F. *J. Phys. Chem.* 1995, *99*, 2684-2695.

(54)   Jonas, D. M. *Ann. Rev. Phys. Chem.* 2003, *54*, 425-463.

(55)   Mukamel, S. *Principles of Nonlinear Optical Spectroscopy*; Oxford University Press: New York, 1995.

(56)   Brixner, T.; Mančal, T.; Stiopkin, I. V.; Fleming, G. R. *J. Chem. Phys.* 2004, *121*, 4221-4236.

(57)   Womick, J. M.; Miller, S. A.; Moran, A. M. *J. Phys. Chem. B* 2009, *113*, 6630-6639.

(58)   Womick, J. M.; Miller, S. A.; Moran, A. M. *J. Phys. Chem. A* 2009, *113*, 6587-6598.

(59)   Womick, J. M.; Moran, A. M. *J. Phys. Chem. B* 2009, *113*, 15747-15759.

(60)   Womick, J. M.; Moran, A. M. *J. Phys. Chem. B* 2009, *113*, 15771-15782.

(61)   West, B. A.; Womick, J. W.; McNeil, L. E.; Tan, K. J.; Moran, A. M. *J. Phys. Chem. C* 2010, *114*, 10580-10591.

(62)   West, B. A.; Womick, J. M.; McNeil, L. E.; Tan, K. J.; Moran, A. M. *J. Phys. Chem. B* 2011, *115*, 5157-5167.

(63)   Womick, J. M.; Liu, H.; Moran, A. M. *J. Phys. Chem. A* 2011, *115*, 2471-2482.

(64)   West, B. A.; Womick, J. M.; Moran, A. M. *J. Phys. Chem. A* 2011, *115*, 8630-8637.

(65)   West, B. A.; Womick, J. M.; Moran, A. M. *J. Chem. Phys.* 2011, *135*, 114505-114501-114509.

(66)   Goodno, G. D.; Dadusc, G.; Miller, R. J. *J. Opt. Soc. Am. B* 1998, *15*, 1791-1794.

(67)   Strauss, J.; Hundhausen, M.; Ley, L. *Appl. Phys. Lett.* 1996, *69*, 875-877.

(68)   Matsuo, S.; Tahara, T. *Chem. Phys. Lett.* 1997, *264*, 636-642.

(69)   Pohl, D. W. *IBM J. Res. Dev.* 1979, *23*, 604-614.

(70)   Maznev, A. A.; Nelson, K. A. *Opt. Lett.* 1998, *23*, 1319-1321.

(71)   Maznev, A. A.; Nelson, K. A.; Rogers, J. A. *Opt. Lett.* 1998, *23*, 1319-1321.

(72)   Cowan, M. L.; Ogilvie, J. P.; Miller, R. J. D. *Chem. Phys. Lett.* 2004, *386*, 184-189.

(73)   Moran, A. M.; Maddox, J. B.; Hong, J. W.; Kim, J.; Nome, R. A.; Bazan, G. C.; Scherer, N. F. *J. Chem. Phys.* 2006, *124*, 194904:194901-194915.

(74)   Khurmi, C.; Berg, M. A. *J. Phys. Chem. A* 2008, *112*, 3364-3375.

(75)   Underwood, D. F.; Blank, D. A. *J. Phys. Chem. A* 2003, *107*, 956-961.

(76)   Gundogdu, K.; Stone, K. W.; Turner, D. B.; Nelson, K. A. *Chem. Phys.* 2007, *341*, 89-94.

(77)   Kim, J.; Wong, C. Y.; Nair, P. S.; Fritz, K. P.; Kumar, S.; Scholes, G. D. *J. Phys. Chem. B* 2006, *110*, 25371-25382.

(78)   Boyd, R. W. *Nonlinear Optics*, 3rd. ed.; Elsevier: Burlington, MA, 2008.

CHAPTER 4 . FEMTOSECOND RELAXATION DYNAMICS OF $Au_{25}L_{18}^{-}$

MONOLAYER PROTECTED CLUSTERS

4.1. INTRODUCTION

Research interest in gold nanoparticles is motivated both by their basic science and by applications in biomedicine,[1,2] catalysis[3,4] and chemical sensing.[5-7] The ability to control electronic and optical properties by preparing particles with different sizes and shapes constitutes the basis for these wide-ranging applications.[8] For example, the sensitivity of surface plasmon resonances to morphology is well-established for nanoparticles in the 3-100 nm size range.[9,10] An understanding of electronic structure rooted in quasi-continuous band structure is appropriate for this size regime, whereas quantization effects become dominant in particles with sizes less than 1.5 nm (i.e., clusters).[11-13] Quantum mechanical effects govern optical spectra[14] and electrochemical charging behavior of sub-1.5 nm dia. clusters,[13,15] which leads naturally to a description involving molecule-like electronic orbitals sensitive to the particular bond connectivity of the system. Deeper understanding of the relationship between electronic structure and sub-1.5 nm particle morphology requires the study of systems with (exactly) known geometries. Crystal structures recently obtained for thiol-protected gold clusters have opened this avenue of investigation.[16-19]

In this investigation, femtosecond transient absorption experiments are used to study excited state relaxation of the gold cluster anion, $Au_{25}(SCH_2CH_2Ph)_{18}^{-}$, whose x-ray crystal structure was recently determined in both the anionic[17] and neutral[19] forms. The structure

consists of an icosahedral Au_{13} core to which six –SR-Au-SR-Au-SR- semi-rings are bonded (R = CH_2CH_2Ph). The experiments excite the two lowest energy bands of electronic states localized on the Au_{13} core (450 and 680 nm) then monitor electronic and nuclear relaxation of the system as it reaches quasi-equilibrium in the lowest energy fluorescing state(s) localized on the exterior semi-rings moieties (1000 nm) . Earlier optical and ligand exchange studies support the interpretation that fluorescence occurs from excited states localized on the semi-rings.[20,21] Within the approximate T_h point group, the HOMO, LUMO and LUMO+1 levels are respectively 3-fold, 2-fold, and 3-fold degenerate.[19,22,23] Theoretical treatments of the system assign the 450 nm and 680 nm bands to 9-fold degenerate HOMO→LUMO+1 and 6-fold degenerate HOMO→LUMO excitations, respectively.[19,23] Experimental distinction of the "superatom" and molecular models for the electronic structure of the cluster is the primary emphasis of this work.[24] To this end, the present experiments examine the sensitivity of the optical response to the applied field frequencies and polarizations with an instrument possessing exceptional time resolution (i.e., 20-40 fs).

The stabilities of sub-nanometer Au clusters are explained by the superatom model for cluster stability, which has proven quite effective for understanding the properties of clusters whose crystal structures have been measured so far.[24] The superatom model essentially fills angular momentum shells of a jellium sphere, where closed shells correspond to maximum stability.[25] For the present 25 atom Au cluster, electron donation occurs at each of the twelve sites where semi-rings bond to the Au_{13} core due to the high polarity of the Au-S bonds, resulting in a formal +5 charge of the core. Thus, 8 electrons remain localized to the core and the $1S^2 1P^6$ shells of the jellium sphere are fully occupied.[22] Recent investigations[24] of a related monolayer-protected 102 atom Au cluster find that the

conduction electrons do not concentrate at the core/semi-ring interface, but are delocalized within the core. Below it is shown that femtosecond laser spectroscopies complement these earlier studies with their sensitivity to electronic structure.

4.2. EXPERIMENTAL METHODS

The $Au_{25}(SCH_2CH_2Ph)_{18}^-$ cluster is prepared according to published procedures.[17] Femtosecond spectroscopy experiments utilize a diffractive-optic based four-wave mixing interferometer[26,27] for signal detection with spectral interferometry.[28,29] Here we report only the absorptive components of the measured "transient grating" signal fields;[30] this representation is equivalent to conventional "pump-probe" spectroscopy.[31,32] Further information on the interferometer is given in Chapter 3.6. Measurements are performed at 1 kHz repetition rate with 50-100 nJ, 20-30 fs laser pulses focused to 100 micron full width half maximum spot sizes at the sample position. In the discussion below, the pump and probe pulse polarizations are parallel unless otherwise specified. The sample concentration is adjusted to give an absorbance of approximately 0.3 in a 1 mm path length at the wavelength for which the pump laser spectrum is centered. Dichloromethane is the solvent used for the measurements presented here. However, we find similar dynamics in both toluene and acetonitrile.

4.3. RESULTS AND DISCUSSION

Figure 4.1(a) overlays a portion of the ground state (i.e., linear) absorption spectrum of the cluster with the absorption spectrum of the electronically excited cluster. The excited state spectrum is measured after the system has reached quasi-equilibrium (i.e., nuclei in equilibrium with excited state charge distribution) in its lowest energy excited state 10 ps

after excitation with a 20 fs, 530 nm laser pulse. The signal exhibits broadband absorption between excited electronic states over the full 575-800 nm wavelength range, where signals with positive and negative signs represent net absorptive and bleach contributions, respectively. The bleach of the ground state, which possesses a spectral profile similar to that of the ground state absorption spectrum in Figure 4.1(a), destructively interferes with the absorptive signal component and causes a minimum in the signal amplitude at 680 nm. Figure 4.1(b) shows that the signal minimum shifts from 690 nm to 670 nm within the first 10 ps after excitation, where most of the dynamics occur in < 1 ps.
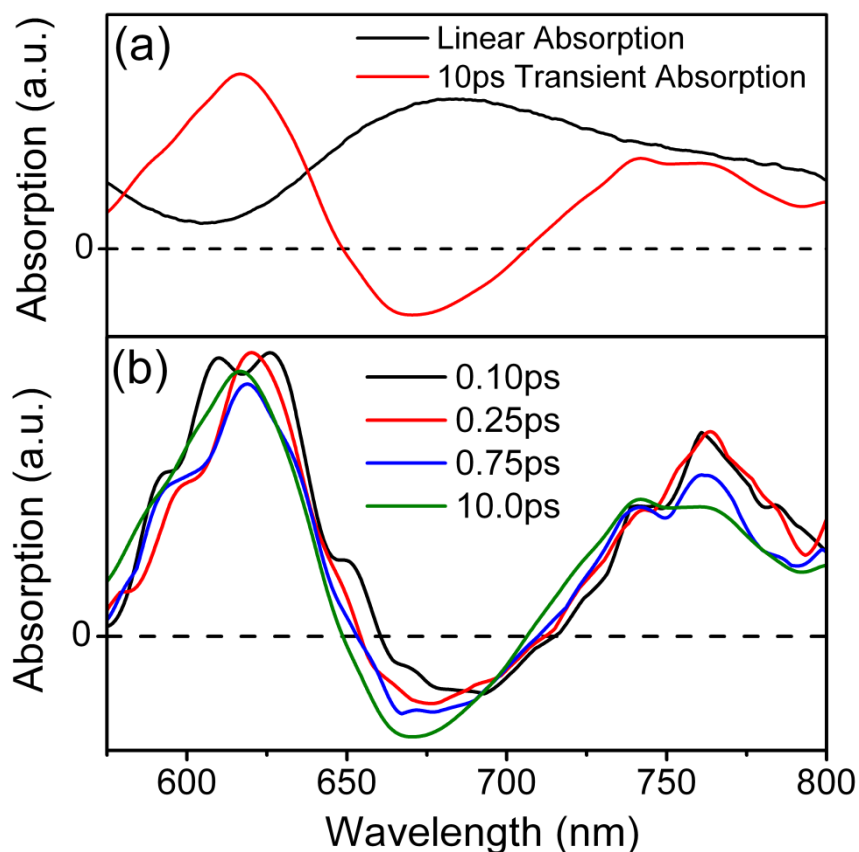
Figure 4.1: (a) Linear absorption spectrum (black) of the gold cluster. Transient absorption spectrum 10 ps after excitation with a 530 nm laser pulse (red). The shape of the transmission spectrum ceases to evolve after the first few picoseconds. (b) Transient absorption spectrum at various delay times following excitation with a 530 nm laser pulse.

The measurement in Figure 4.1(b) give further support to the interpretation that fluorescence occurs from states local to the semi-rings, rather than from states which are relaxed continuations (i.e., Stokes shifted) of the HOMO-LUMO excitations (i.e., absorption at 680 nm). It is well-established that transient absorption measurements see the nuclear relaxation associated with a Stokes shift as an increase in the stimulated emission wavelength with increasing T.[31] For $Au_{25}(SCH_2CH_2Ph)_{18}^-$, this red-shift would be seen as initiation of the signal minimum at 690 nm at $T=0$ followed by a continuous red-shift to 1000 nm (i.e., peak of steady state fluorescence) with increasing T.[21] We see no evidence of these dynamics for $T <100$ ps, which far exceeds the sub-picosecond nuclear relaxation time scale expected for a solution with dichloromethane solvent.[33] Therefore, these data support a picture in which the 4500 cm^{-1} energy dissipation needed for the system to fluorescence at 1000 nm occurs by way of (discontinuous) heat loss associated with an internal conversion process.

The results resemble those obtained for similar experiments investigating > 1.5 nm diameter gold nanoparticles, where the transient transmission spectrum is a superposition of a broad absorptive interband component (i.e., d-band and surface plasmon) with the bleach of the plasmon resonance.[34-37] The ground state plasmon bleach of Au colloids shifts to shorter wavelengths in the first picosecond due to equilibration of the electrons in the conduction band; lower frequency interband transitions are suppressed when electrons relax to the bottom of the conduction band. Similarly, the blue shift of the signal minimum (i.e., the bleach) observed in Figure 4.1(b) suggests that light absorption at 530 nm vacates the highest energy orbitals that are occupied in the ground electronic state (i.e., HOMO is 3-fold

degenerate). This transient excited state electron configuration allows photoexcitation of electrons from deeper lying occupied molecular orbitals into the vacated orbitals at the top of the valence band. In fact, the calculations of Zhu et al. suggest that the manifold of d-band states becomes fairly dense in the 575-800 nm wavelength range associated with excitation into the HOMO orbital.[14]

Figure 4.2(a) presents temporal profiles of transient absorption signals, $S(t)$, measured at four different detection wavelengths. Table 4.1 summarizes the time constants obtained from exponential fits of the data in Figure 4.2(a) using the phenomenological equation

$$S(T) = A_0 + A_1 \exp(-T/\tau_1) + A_2 \exp(-T/\tau_2) \qquad (4.1)$$

Sub-100 fs delay times are not accounted for in the fit because of the uncertainty in separating solute and solvent contributions to the signal when the pump and probe pulses are overlapped in the sample.[38] The signal measured at 680 nm (i.e., in the vicinity of the bleach) contrasts with the three other detection wavelengths in that sub-picosecond relaxation dynamics are not detected. This difference is explained by the small amount of solvent reorganization expected to occur around the ground state "hole" following photoexcitation.[31]
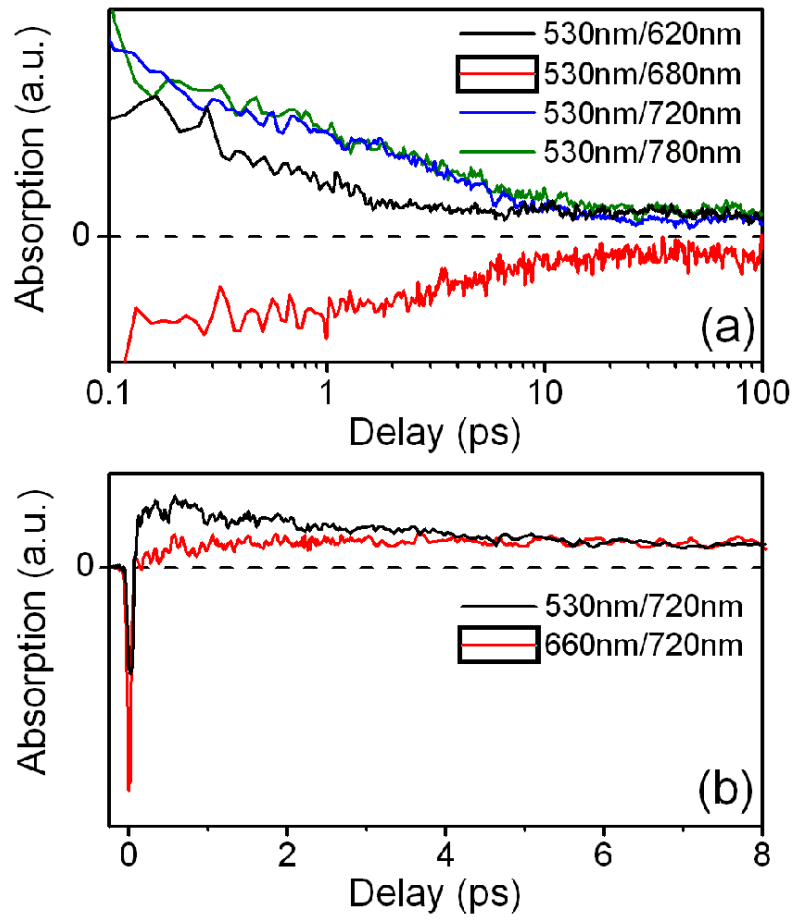
Figure 4.2: (a) Transient absorption signals at selected probe wavelengths following excitation with a 530 nm laser pulse. The pump and probe wavelengths are indicated in the Figure legend as $\lambda_{pump} / \lambda_{probe}$. (b) Transient absorption signals measured with a probe wavelength of 720 nm after excitation at 530 nm (black) and 660 nm (red).

Table 4.1. Fits of Transient absorption signals at various detection wavelengths with pumping at 530 nm

Parameter[a]	620nm	680nm	720nm	780nm
A_0	0.045	-0.036	0.034	0.05
A_1	0.19	--------------	0.32	0.12
τ_1	0.27	--------------	0.12	0.71
A_2	0.12	-0.14	0.22	0.16
τ_2	1.3	4.7	4.1	5.3

[a]Equation 4.1.

Figure 4.3 interprets internal conversion between the excited states corresponding to the 450 and 680 nm transitions in the ground state absorption spectrum as giving rise to the sub-picosecond time constant. Indeed, spatial overlap of the wavefunctions for these two nominally Au_{13} core-localized states should facilitate the fast non-radiative transition. Another requirement for fast internal conversion is energy conservation at a thermally accessible nuclear configuration. Spectral overlap in the two ground state absorption bands near 600 nm reflects a nuclear configuration where the two excited states are degenerate. Quantized vibrations with large Franck-Condon factors may further enhance the internal conversion rate, and it is also possible that the radial breathing mode of the core (discussed below) plays an important role in the non-radiative transition. Jahn-Teller active modes participate in the transition within the approximate T_h symmetry of the system.
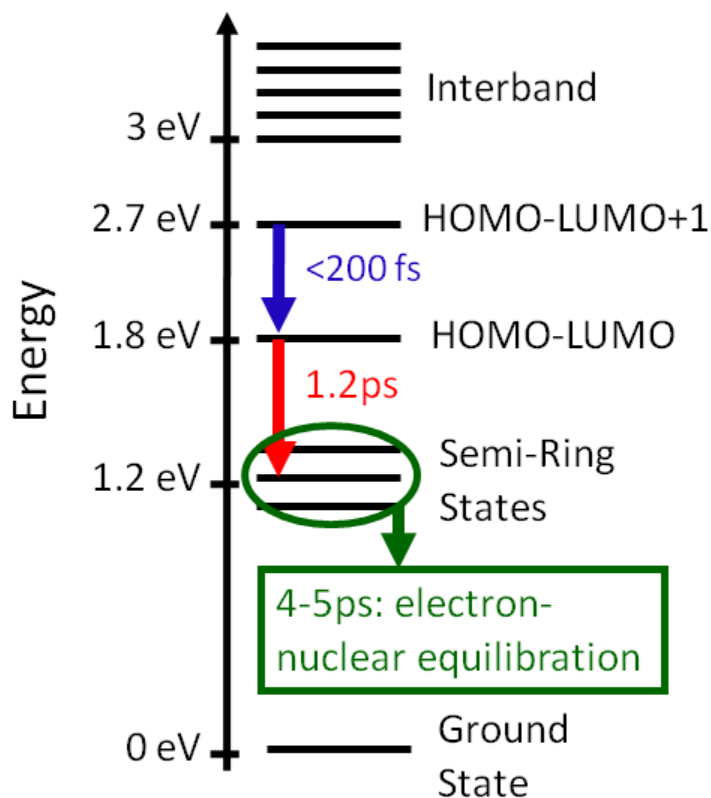
Figure 4.3: Electronic relaxation scheme obtained by analysis of femtosecond transient absorption experiments. Internal conversion processes occur on time scales of 200 fs and 1.2 ps. The HOMO-LUMO and HOMO-LUMO+1 states are 6-fold and 9-fold degenerate, respectively. Equilibration of the nuclear structure with the excited state charge distribution requires 4-5 ps.

The fact that the time constant greater than 1 ps lengthens as the probe wavelengths increases suggests that (at least) two distinct relaxation processes occur on this longer time scale. Figure 4.3 assigns the 1.2 ps time constant measured with a 620 nm probe pulse to internal conversion from optically pumped states local to the Au_{13} core into the states of the semi-rings. The cluster does not fluoresce at 620 nm.[21] Therefore, the 1.2 ps time constant measured at 620 nm may correspond only to the bleach of the ground state and absorption

between excited states. By contrast, time constants greater than 4 ps are measured at 725-800 nm detection wavelengths where stimulated emission from the semi-ring states to the ground state contributes to the signal (i.e., the signal wavelength overlaps with the steady state fluorescence spectrum).[21] Signals detected in this wavelength range are particularly sensitive to electronic and nuclear relaxation dynamics associated with the semi-ring manifold of states (e.g., internal conversion, vibrational cooling).[31,39] Our data suggest at least one decay component with a time constant much longer than 100 ps. This observation is consistent with an earlier investigation for this same system in which the lowest energy excited state lifetime was found to exceed 1 ns.[40]

Experiments comparing decay profiles at different pump pulse frequencies are useful for distinguishing electronic and nuclear equilibration processes because the pump photon energy in excess of the "band gap" must be dissipated as heat within the solute and surrounding solvent. Time constants associated with this heat dissipation are readily detected with transient absorption experiments.[31] Figure 4.2(b) overlays transient absorption signals measured at a probe wavelength of 720 nm following excitation at 530 nm and 660 nm. The picosecond relaxation time constant is clearly absent for excitation with a 660 nm pump pulse. Therefore, this pair of measurements supports assignment of the 4-5 picosecond relaxation time constants measured with 530 nm excitation (see Table 4.1) to equilibration between the excited state charge distribution and the nuclear geometry. That is, photoexcitation at 530 nm imparts an additional 3700 cm^{-1} of energy (i.e., versus excitation at 660 nm) that must be dissipated as heat as the system equilibrates; the difference in the decay profiles of Figure 4.2(b) reflects the relaxation bottleneck. A recent study of equilibrium self-exchange in the $[Au_{25}(SC2Ph)_{18}]^{0/1-}$ electron transfer couple also senses strong coupling

between the Au_{25} electronic charge distribution and intramolecular nuclear coordinates.[41] The measurement in Figure 4.2(b) represents a good estimate for the time scale of intramolecular relaxation found to be important in the electron transfer couple.

The superatom view of the Au_{13} core as a jellium sphere contrasts with a molecular perspective of the cluster in which electronic orbital formation is governed by bond connectivity. The ability to experimentally distinguish between these two pictures is important for physical insight. One viable approach examines polarization anisotropy in the transient absorption response. Transient anisotropy measurements sense the orientationally averaged transition dipole orientations of an ensemble, which must vanish in the limit of a spherically symmetric system.[42] Figure 4.4 presents transient anisotropies, $r(T)$, calculated with

$$r(T) = \frac{S_{\parallel}(T) - S_{\perp}(T)}{S_{\parallel}(T) + 2S_{\perp}(T)}$$

(4.2)

where $S_{\parallel}(T)$ and $S_{\perp}(T)$ respectively represent signals acquired with parallel and perpendicular pump and probe polarizations (see Appendix A3.2). The measured anisotropies decay to zero within 100 fs for both measurements using 530 nm pump pulses, whereas a negative anisotropy persists for up to 1 ps delay with excitation at 660 nm. These measurements suggest that the sub-200 fs internal conversion process occurring between electronic states of the core (see Figure 4.3) causes fast decays in the optical anisotropy. Apparently, with 530 nm excitation the degeneracies of the Au_{13} core energy levels[14,22] give rise to internal conversion channels terminating in multiple electronic states with varying transition dipole orientations. Thus, the superposition of signals radiated by these sub-

ensembles quickly randomizes the orientation of the macroscopic polarization vector. By contrast, with excitation at 660 nm the system retains memory of the photoexcited transition dipole orientation until the population relaxes into the manifold of semi-ring states at $T > 1$ ps.
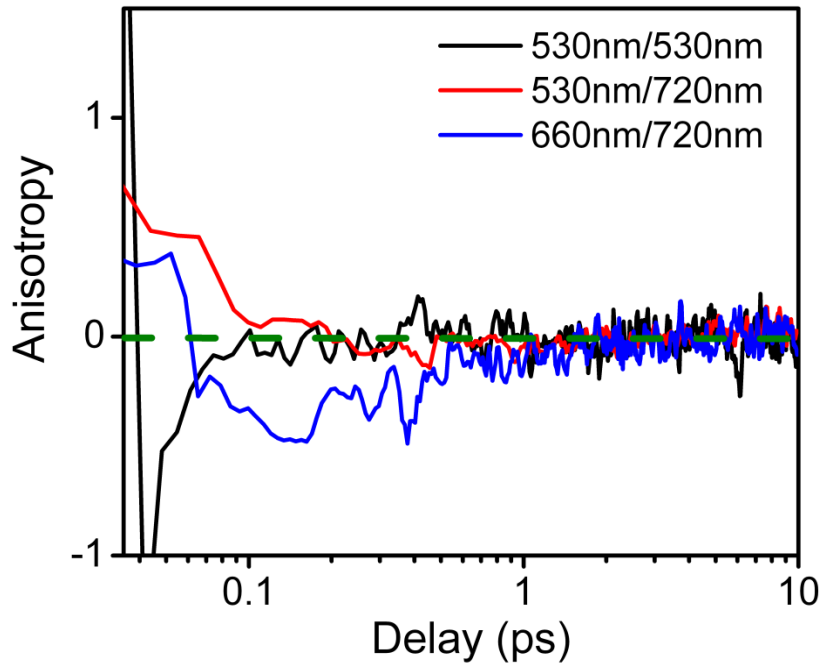
Figure 4.4: Anisotropy [Eq. (2)] in the transient absorption response for three different pulse configurations. The pump and probe wavelengths are indicated in the Figure legend as $\lambda_{pump} / \lambda_{probe}$.

Insight into the mechanical properties of >1nm gold nanoparticles has been obtained by the investigation of acoustic radial breathing modes using femtosecond spectroscopies.[43] We observe an impulsively excited Au-Au bond stretching vibration for experiments in which the probe pulse in tuned to the 660-700 nm spectral range primarily sensitive to the ground state bleach; this vibration reflects nuclear motion on the ground state potential

energy surface. Figure 4.5 shows how the nuclear coherences of the cluster and solvent superpose in the measured signal. The cluster vibration is centered at 80 cm^{-1}, and is phase-shifted by about 90 degrees compared to vibrations of the dichloromethane solvent. The radial breathing vibration of a colloidal Au nanoparticle is well-described as an acoustic spheroidal mode of an elastic sphere with a frequency given by[43,44]

$$\omega_{vib} = \frac{c_l \eta}{2\pi R c} \tag{4.3}$$

where c_l is the longitudinal speed of sound, R is the particle radius and η is a particular eigenvalue for the spheroidal vibrations ($\eta = 2.93$) . Using this formula, a vibrational frequency of 103 cm^{-1} is obtained with the measured 0.98 nm Au$_{13}$ core diameter.[17] The discrepancy in the measured and calculated mode frequencies may be associated with the mass of the semi-rings, which are not accounted for by the model. The experimental examination of a wider variety of clusters and the use of *ab initio* quantum chemistry calculations will be needed for deeper insight into this issue. Au-S bond stretching vibrations at 290 cm^{-1} have been detected in spontaneous resonant Raman experiments with excitation at 785 nm.[41] The insensitivity of the pump-probe technique to this resonance may be due to competing signal components (i.e. excited state population relaxation) not present in spontaneous Raman experiments. It is also possible that the Franck-Condon factor governing the Raman signal amplitude is larger at 785 nm than at 660 nm. The measurement of a Raman excitation profile in this wavelength range would settle this issue.[45,46]
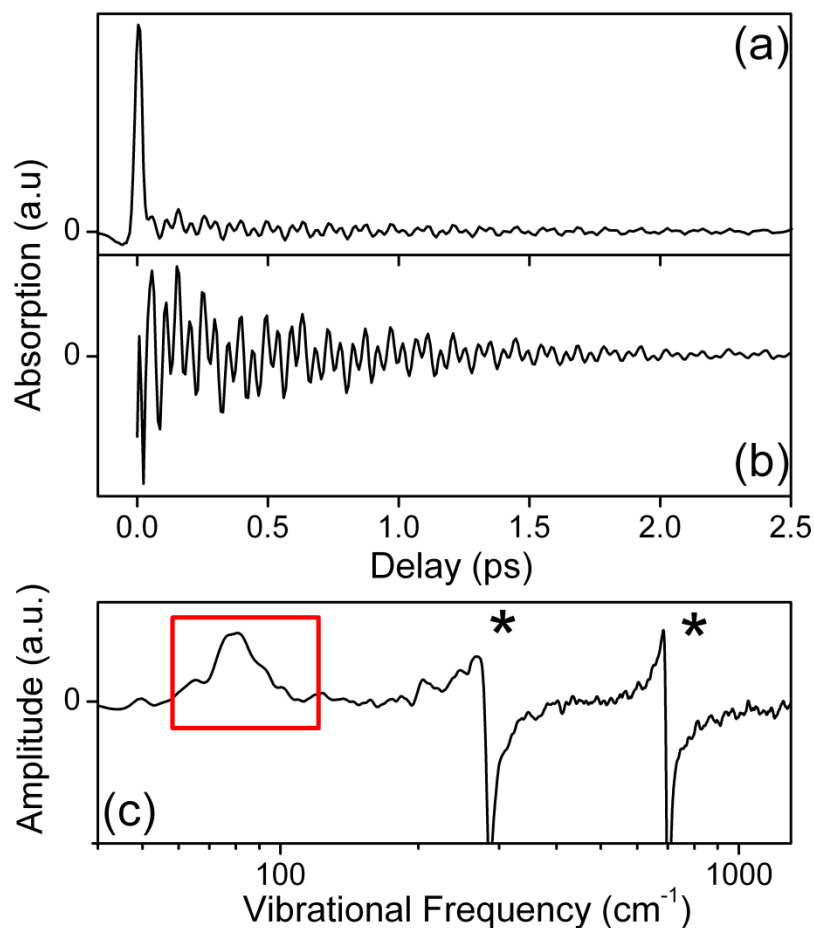
Figure 4.5: (a) Transient absorption signal for excitation and probing with a 17 fs, 640 nm laser pulse. (b) Nuclear component of signal obtained by subtraction of exponential decay. (c) Imaginary part of the Fourier transform for nuclear signal component. Solvent (dichloromethane) resonances are marked with asterisks. The 80 cm^{-1} vibration of the cluster is enclosed in a box.

4.4. SUMMARY AND CONCLUSIONS

In summary, the present study points to the success of the superatom model for describing the electronic structure of $Au_{25}(SCH_2CH_2Ph)_{18}^-$. The fastest components in the relaxation scheme presented of Figure 4.3 reflect significant wavefunction overlap for states nominally localized to the Au_{13} core, whereas the slower core to semi-ring internal conversion process is consistent with wavefunctions partially localized to these two regions

of the cluster. The superatom model supports this real-space view of wavefunction localization. The cluster exhibits a short-lived optical anisotropy which distinguishes its transient electronic structure from that of a system with spherical symmetry. However, the rapid sub-picosecond decay in the anisotropy supports the superatom model's approximation of the core as a quasi-spherical system (i.e., jellium sphere). The observation of an 80 cm^{-1} radial breathing mode local to the Au$_{13}$ core suggests similarties between the mechanical properties of monolayer protected Au clusters and Au colloids. Future investigations will compare dynamics for a wider variety of Au cluster with different sizes. Examination of the optical response over a broader wavelength range (e.g. ultraviolet and near infrared) will further enhance physical insight.

4.5. REFERENCES

(1)   Schultz, S.; Smith, D. R.; Mock, J. J.; Schultz, D. A. *Proc. Natl. Acad. Sci.* 2000, *97*, 996-1001.

(2)   Yguerabide, J.; Yguerabide, E. E. *Anal. Biochem.* 1998, *262*, 137-156.

(3)   Antonello, S.; Holm, A. H.; Instuli, E.; Maran, F. *J. Am. Chem. Soc.* 2007, *129*, 9836-9837.

(4)   Pasquato, L.; Pengo, P.; Scrimin, P. *J. Mater. Chem.* 2004, *14*, 3481-3487.

(5)   Wohltjen, H.; Snow, A. W. *Anal. Chem.* 1998, *70*, 2856-2859.

(6)   Nam, J.-M.; Thaxton, C. S.; Mirkin, C. A. *Science* 2003, *301*, 1884-1886.

(7)   Anker, J. N.; Hall, W. P.; Lyandres, O.; Shah, N. C.; Van Duyne, R. P. *Nature Materials* 2008, *7*, 442-453.

(8)   Pileni, M. P. *J. Phys. Chem. C* 2007, *111*, 9019-9038.

(9)   Myroshnychenko, V.; Rodríguez-Fernández, J.; Pastoriza-Santos, I.; Funston, A. M.; Novo, C.; Mulvaney, P.; Liz-Marzán, L. M.; de Abajo, F. J. G. *Chem. Soc. Rev.* 2008, *37*, 1792-1805.

(10)   Kelly, K. L.; Coronado, E.; Zhao, L. L.; Schatz, G. C. *J. Phys. Chem. B* 2003, *107*, 668-677.

(11)   Ellert, C.; Schmidt, M.; Schmitt, C.; Reiners, T.; Haberland, H. *Phys. Rev. Lett.* 1995, *75*, 1731-1734.

(12)   Wang, C. R. C.; Pollack, S.; Dahlseid, T. A.; Koretsky, G. M.; Kappes, M. M. *J. Chem. Phys.* 1992, *96*, 7931-7937.

(13)   Murray, R. *Chem. Rev.* 2008, *108*, 2688-2720.

(14)   Zhu, M.; Aikens, C. M.; Hollander, F. J.; Schatz, G. C.; Jin, R. *J. Am. Chem. Soc.* 2008, *130*, 5883-5885.

(15)   Laaksonen, T.; Ruiz, V.; Liljeroth, P.; Quinn, B. M. *Chem. Soc. Rev.* 2008, *37*, 1836-1846.

(16)   Whetten, R. L.; Price, R. C. *Science* 2007, *318*, 407-408.

(17)   Heaven, M. W.; Dass, A.; White, P. S.; Holt, K. M.; Murray, R. W. *J. Am. Chem. Soc.* 2008, *130*, 3754-3755.

(18)   Jadzinsky, P. D.; Calero, G.; Ackerson, C. J.; Bushnell, D. A.; Kornberg, R. D. *Science* 2007, *318*, 430-433.

(19)   Zhu, M.; Eckenhoff, W. T.; Pintauer, T.; Jin, R. *J. Phys. Chem. C* 2008, *112*, 14221-14224.

(20)   Lee, D.; Donkers, R. L.; Wang, G.; Harper, A. S.; Murray, R. W. *J. Am. Chem. Soc.* 2004, *126*, 6193-6199.

(21)   Wang, G.; Huang, T.; Murray, R. W.; Menard, L.; Nuzzo, R. G. *J. Am. Chem. Soc.* 2005, *127*, 812-813.

(22)   Akola, J.; Walter, M.; Whetten, R. L.; Häkkinen, H.; Grönbeck, H. *J. Am. Chem. Soc.* 2008, *130*, 3756-3757.

(23)   Aikens, C. M. *J. Phys. Chem. C* 2008, *112*, 19797-19800.

(24)   Walter, M.; Akola, J.; Lopez-Acevedo, O.; Jadzinsky, P. D.; Calero, G.; Ackerson, C. J.; Whetten, R. L.; Grönbeck, H.; Häkkinen, H. *Proc. Natl. Acad. Sci.* 2008, *105*, 9157-9162.

(25)   Knight, W. D.; Clemenger, K.; de Heer, W. A.; Saunders, W. A.; Chou, M. Y.; Cohen, M. L. *Phys. Rev. Lett.* 1984, *52*, 2141-2143.

(26)   Goodno, G. D.; Dadusc, G.; Miller, R. J. D. *J. Opt. Soc. Am. B* 1998, *15*, 1791-1794.

(27)   Maznev, A. A.; Nelson, K. A.; Rogers, J. A. *Opt. Lett.* 1998, *23*, 1319-1321.

(28)   Lepetit, L.; Chériaux, G.; Joffre, M. *J. Opt. Soc. Am. B* 1995, *12*, 2467-2474.

(29)   Gallagher, S. M.; Albrecht, A. W.; Hybl, J. D.; Landin, B. L.; Rajaram, B.; Jonas, D. M. *J. Opt. Soc. Am. B* 1998, *15*, 2338-2345.

(30)   Moran, A. M.; Park, S.; Scherer, N. F. *J. Phys. Chem. B* 2006, *110*, 19771-19783.

(31)   Mukamel, S. *Principles of Nonlinear Optical Spectroscopy*; Oxford University Press: New York, 1995.

(32)   Jonas, D. M. *Annu. Rev. Phys. Chem.* 2003, *54*, 425-463.

(33)   Horng, M. L.; Gardecki, J. A.; Papazyan, A.; Maroncelli, M. *J. Phys. Chem.* 1995, *99*, 17311-17337.

(34)   Sun, C.-K.; Vallée, F.; Acioli, L. H. *Phys. Rev. B* 1994, *50*, 15337-15348.

(35)   Hodak, J. H.; Martini, I.; Hartland, G. V. *J. Phys. Chem. B* 1998, *102*, 6958-6967.

(36)   Ahmadi, T. S.; Logunov, S. L.; El-Sayed, M. A. *J. Phys. Chem.* 1996, *100*, 8053-8056.

(37)   Park, S.; Pelton, M.; Liu, M.; Guyot-Sionnest, P.; Scherer, N. F. *J. Phys. Chem. C* 2007, *111*, 116-123.

(38)   Moran, A. M.; Nome, R. A.; Scherer, N. F. *J. Chem. Phys.* 2006, *125*, 031101:031101-031104.

(39)   Fleming, G. R. *Chemical Applications of Ultrafast Spectroscopy*; University Press: New York, 1986.

(40)   Link, S.; El-Sayed, M. A.; Schaaf, T. G.; Whetten, R. L. *Chem. Phys. Lett.* 2002, *356*, 240-246.

(41)   Parker, J. F.; Choi, J.-P.; Wang, W.; Murray, R. W. *J. Phys. Chem. C* 2008, *112*, 13976-13981.

(42)   Andrews, D. L.; Thirunamachandran, T. *J. Chem. Phys.* 1977, *67*, 5026-5033.

(43)   Hodak, J. H.; Henglein, A.; Hartland, G. V. *J. Chem. Phys.* 1999, *111*, 8613-8621.

(44)   Tamura, A.; Higeta, K.; Ichinokawa, T. *J. Phys. C: Solid State Phys.* 1982, *15*, 4975-4991.

(45)   Kelley, A. M. *J. Phys. Chem. A* 1999, *103*, 6891-6903.

(46)   McHale, J. *Molecular Spectroscopy*; Prentice Hall: Upper Saddle Creek River, NJ,1999.

CHAPTER 5 . NONLINEAR OPTICAL SIGNATURES OF CORE AND LIGAND ELECTRONIC STATES IN $Au_{24}PdL_{18}$

5.1. INTRODUCTION AND BACKGROUND

One area of vital fundamental research involving gold nanoparticles aims to understand the effects of particle morphology on electronic and optical properties. Principal in this field of study is Mie's classical solution of Maxwell's equations, which is valid for spherical systems of arbitrary size.[1-3] More recently, the preparation of nanoparticles with a wide variety of shapes (e.g., triangles, rods) has motivated the development of sophisticated numerical models.[4,5] In parallel with these efforts, research has also begun to explore the emergence of quantum effects occurring at particle diameters of 1-2 nm (i.e., metal-to-molecule transition).[6-16] Crystal structure determinations of Au monolayer protected clusters (MPC) possessing 25 and 102 atoms have been essential for understanding relationships between the cluster geometry and electronic structure.[11,13,16-19] Together with *ab initio* computational methods, an elegant superatom model has been particularly useful for understanding the origin of MPC stability.[9,12,20,21] The superatom model essentially confines valence electrons of the MPC core within a quasi-spherical potential, thereby yielding angular momentum shells that occupy according to an Aufau principle. Despite these advances, the real-space nature of electronic states in MPCs is not yet fully understood. In particular, experiments and theory are still working towards a robust description of electronic states localized to the cores and ligands in MPCs.

Here, two optical signatures of electronic state localization in MPCs are examined. The first signature assigns broad photoluminescence spectra near 1 μm to electronic states localized on the ligands. This signature derives from comprehensive electrochemical measurements for a 25-atom Au MPC, which show that photoluminescence occurs below the HOMO-LUMO gap.[22] It should be noted that Reference 22 mistakenly assigned Au_{25} as Au_{38}. The generality of ligand-localized states in other MPCs was established with ligand exchange studies and the measurement of size-independent emission frequencies for MPCs ranging in size from 11 to 201 Au atoms.[23] Ligand-localized electronic states readily explain these measurements, but their existence has not yet been confirmed by *ab initio* electronic structure calculations.[9,13,14] To settle this issue, theory must ultimately account for these observations and explain the properties of solute-solvent interactions in condensed phases (e.g., Stokes shifts, optical line shapes).[24] It is hoped that the present set of experiments will be helpful in achieving this goal. The second signature was proposed in our earlier investigation of femtosecond relaxation dynamics in $Au_{25}(SCH_2CH_2Ph)_{18}^-$ (hereafter referred to as Au_{25}).[25] The interpretation of these measurements was facilitated by the known crystal structure of Au_{25}; Au_{25} possesses a quasi- icosahedral Au_{13} core surrounded by six -SR-Au-SR-Au-SR- "semiring" ligand moieties ($R=CH_2CH_2Ph$). Our transient absorption experiments excited electronic states local to the Au_{13} core then monitored a 1.2 ps internal conversion transition between core and semiring states. Weak overlap between the core and semiring electronic wavefunctions in Au_{25} is manifest in this relatively slow internal conversion time scale, which is more than 6 times slower than equilibration of electrons within the Au_{13} core.

In this investigation, we examine the electronic structure of $Au_{24}Pd(SCH_2CH_2Ph)_{18}$ (hereafter referred to as $Au_{24}Pd$) using a variety of optical measurements. All experimental evidence suggests that $Au_{24}Pd$ possesses a structure similar to that of Au_{25}.[26,27] However, the location of the Pd atom, among three possible locations (center of core, core surface, semi-ring), is not yet known. Density functional theory calculations find that substitution of the Pd atom at the center of the core yields the most stable structure but does not produce the best fit to optical and electrochemical experiments.[28] Nonetheless, precise knowledge of the bond connectivity of $Au_{24}Pd$ is not the point of the present investigation. Rather we use $Au_{24}Pd$ to test the generality of the two aforementioned optical signatures representing core and ligand-localized electronic states. To this end, it is useful to begin with consideration of fundamental aspects of electronic structure, which are particularly well-defined for the parent molecule Au_{25}. The HOMO, LUMO and LUMO+1 levels of Au_{25} are respectively 3-fold, 2-fold, and 3-fold degenerate.[13,14,29] Electronic excitations involving these orbitals absorb radiation across the full visible spectrum. Theoretical calculations suggest that $Au_{24}Pd$ exhibits electronic structure similar to Au_{25} when the Pd atom is located at the center of the core, whereas the orbital degeneracies are broken when the Pd atom resides on the surface of the core and/or one of the ligands.[28] This basis of molecular orbitals serves as a useful starting point for discussing the spectroscopy of core excitations in $Au_{24}Pd$.

5.2 RESULTS AND DISCUSSION

The comparison of linear absorption spectra for $Au_{24}Pd$ and Au_{25} shown in Figure 5.1 suggests that the presence of the Pd atom is not a small perturbation. Well-resolved peaks in the absorption spectrum (e.g., 450nm, 680nm) of Au_{25} fade into a quasi-exponentially

decaying line shape in $Au_{24}Pd$. The blue shift of absorbance spectra measured at 200K (Figure 5.1) indicates that the line widths of both MPCs, in part, reflect thermal population within the manifold of core electronic states. That is, the temperature dependence suggests that energy gaps between the three nearly degenerate HOMO orbitals are less than k_BT at room temperature (~0.026 eV). This interpretation is consistent with density functional theory calculations that estimate a <0.04 eV range in orbital energies imposed by symmetry breaking.[14] Based on spectral coverage similar to Au_{25} and recent theoretical calculations,[28] we conclude that the oscillator strength of $Au_{24}Pd$ is dominated by excitations local to the metal core. We remark that the spectrum measured for $Au_{24}Pd$ does not closely resemble theoretical predictions.[28] This discrepancy may be attributed to the fact that the experiments are conducted in solution, whereas the calculations correspond to the isolated system. The near-perfect agreement in photoluminescence maxima for $Au_{24}Pd$ and Au_{25} shows that $Au_{24}Pd$ conforms to the trend of size-independent emission frequencies previously established for Au monolayer-protected clusters. Thus, $Au_{24}Pd$ satisfies the first signature of ligand-localized electronic states.
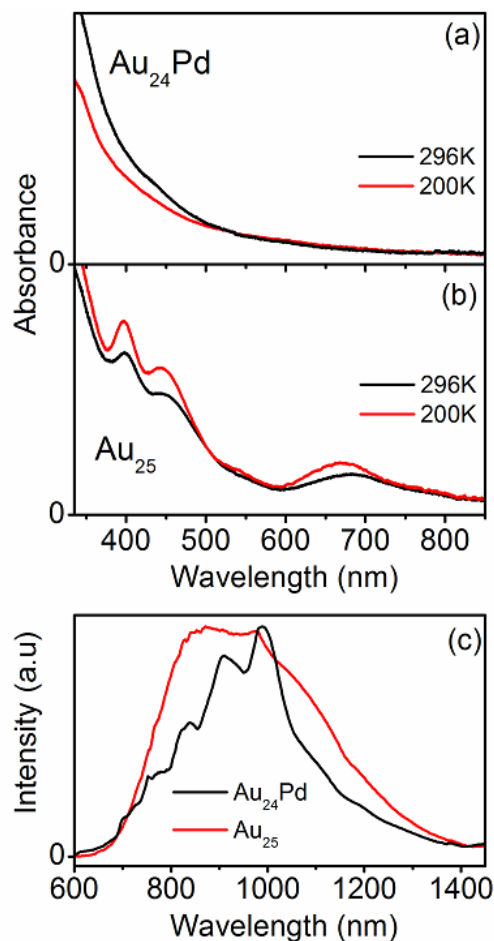
Figure 5.1: (a) Linear absorption spectrum of $Au_{24}Pd$ at 296 K (black) and 200 K (red). (b) Linear absorption spectrum of Au_{25} at 296 K (black) and 200 K (red). (c) Photoluminescence spectra of $Au_{24}Pd$ (black) and Au_{25} (red) at 296K. $Au_{24}Pd$ and Au_{25} are respectively excited at 400 nm and 530 nm. Periodic structure in the photoluminescence spectrum of $Au_{24}Pd$ in the 700-1000 nm range is an artifact of the measurement.

Before discussing the time-resolved measurements, we first address a couple of issues important to the interpretation of the steady state spectra in Figure 5.1. First, it should be mentioned that the charge of the Au_{25} cluster is -1, as in our earlier investigation.[25] The Au_{25} anion satisfies the 8-electron count needed to obtain a closed shell S^2P^6 superatom electron configuration.[12] By contrast, $Au_{24}Pd$ must possess a charge of -2 to similarly achieve the stable S^2P^6 configuration because the Pd atom in $Au_{24}Pd$ is zero-valent (i.e., d^{10}

configuration).[28] We therefore suggest that the charge of the $Au_{24}Pd$ in solution is -2. It was recently found that Au_{25}(-1) can be oxidized in air to form the neutral Au_{25}(0).[19] For this reason, both compounds used in this work were stored under nitrogen to prevent oxidation.

It is also important to rule out photoluminescence of small quantities of Au_{25} in the $Au_{24}Pd$ sample. Mass spectrometry and electrochemistry experiments have already demonstrated that highly purified samples of $Au_{24}Pd$ are obtained with prolonged solvent fractionation.[26] In addition, the linear absorption spectrum of the $Au_{24}Pd$ solution in Figure 5.1(a) exhibits no resonance at 680 nm, thereby ensuring that a large concentration of Au_{25} is not present. Also, because the photoluminescence spectra of Au_{25} and $Au_{24}Pd$ possess different line widths, it is clear that Au_{25} makes only negligible contributions (if any) to the emission spectrum of in Figure 5.1(c). Reference 23 shows that monolayer-protected clusters do not generally possess equivalent line widths despite emitting at nearly the same wavelength.

Technical aspects of the transient grating (TG) experiments are described in Chapter 3.6. Briefly, the measurements excite the clusters with 20 fs, 530 nm laser pulses then monitor electronic relaxation in the 525-780 nm wavelength range using a continuum probe pulse. Pulses possess energies of 75 nJ and are focused to 100 μm FWHM spot sizes at the sample position. Pump and probe polarizations are set orthogonal to suppress the amplitude of the coherent spike in the region of pulse overlap near zero delay. Anisotropy is not detected in the TG signal of $Au_{24}Pd$. The time resolution is shorter than 90 fs at all detection wavelengths reported here. The clusters were dissolved in dichloromethane to give an absorbance of 0.53 at 530 nm in a 1.0 mm path length. The sample cuvette was continuously oscillated during data acquisition to suppress photodegradation. Spectral interferometry is

used for signal detection.[30,31] However, the absolute value of the measured TG signal field is used to obtain relaxation time constants because of noise in the signal phase associated with motion of the sample.
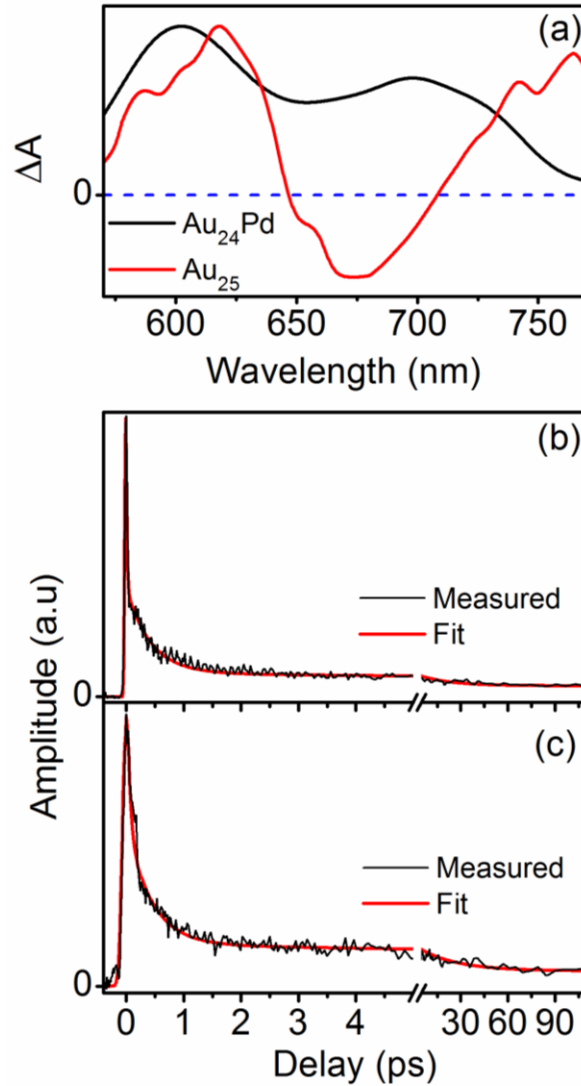
Figure 5.2: (a) Real part of transient grating signal spectrum (i.e., equivalent to conventional transient absorption, ΔA) for $Au_{24}Pd$ (black) and Au_{25} (red) at 5 ps delay with excitation at 530nm. Signals with negative and positive signs respectively signify the bleach of the ground state and absorption between excited states. (b) Absolute value of the transient grating signal field measured at (b) 630 nm and (c) 700 nm. Fits are obtained with Equation 5.1.

The transient absorption spectrum of $Au_{24}Pd$ shown in Figure 5.2 reveals broadband absorption between excited states in the 570-770 nm range, whereas that of Au_{25} possesses a net "bleach" near 675 nm. We find that both cluster possess weak net signal intensity at wavelengths less than 550 nm due to interference between excited state absorption (ESA) signal components and the bleach of the ground state. The ESA nonlinearity of Au_{25} has been assigned to interband excitations based on the density functional theory calculations of Zhu et al.[13] These calculations further explain the broad ESA line width of Au_{25} by a large density of d electronic states in the relevant energy range. Strong ESA nonlinearities involving interband excitations are generally observed in the visible wavelength range for Au nanoparticles with diameters >1.5 nm.[32-34] In this respect, the optical nonlinearities of MPCs closely resemble those of larger Au colloids.

Relaxation time constants are obtained by fitting the TG signal profiles using the phenomenological equation

$$S(t;w) = \sum_{m=1}^{3} \int_{-\infty}^{t} dt' G(t';w) A_m \exp(-t'/\tau_m) dt' \qquad (5.1)$$

Equation 5.1 uses a Gaussian instrument response function, $G(t';w)$, to deconvolute the finite instrument response width, w, from the three exponential decay components m. Figures 5.2(b) and 5.2(c) show two example TG signal profiles at 630 nm and 700 nm, respectively. Here, and at all detection wavelengths, we find an extremely short (< 50 fs) decay component whose exact value is not well-determined because it is comparable to the time resolution of the apparatus. As in Au_{25}, we assign this short decay component to electronic relaxation within the metal core. In addition, time constants of approximately 500 fs were found at all signal detection wavelengths between 620 and 750 nm (Figure 5.3). This

component is assigned to internal conversion between core and ligand-localized electronic states based on its similarity to the 1.2 ps decay time measured for Au_{25}.[25] Finally, a much slower decay process (18-36 ps) is evident at all detection wavelengths. Figure 5.3(b) shows that this decay constant possesses a detection wavelength dependence, which approximates the shape of a Gaussian function. We interpret the wavelength dependence as the line shape of an ESA nonlinearity localized to the semiring moieties. Finally, the τ_3 decay process is assigned to nuclear relaxation occurring in response to the localization of the excitation on the ligands.
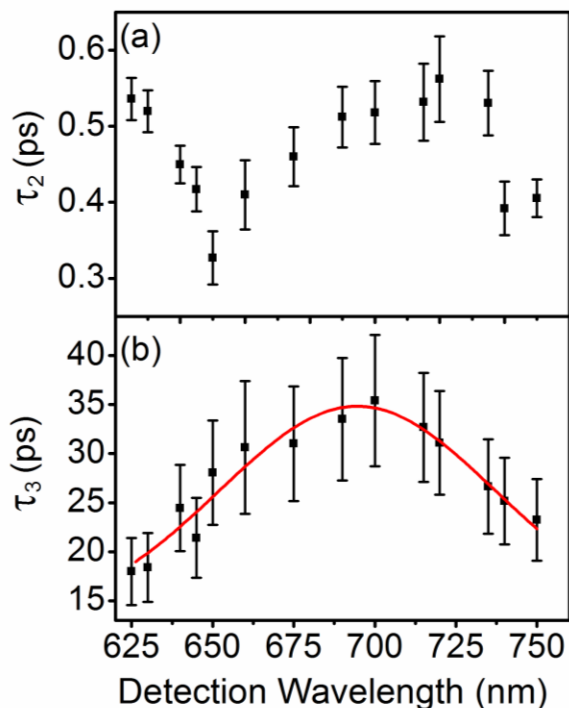
Figure 5.3: Time constants (a) τ_2 and (b) τ_3 obtained with a fit of absolute value of transient grating signal field (see Equation 5.1). The time constants, τ_3, in (b) are fit to a Gaussian function (red line) with 695 nm peak and standard deviation of 43 nm. Error bars associated with each time constant are given in each panel. Example fits are shown in Figures 5.2(b) and 5.2(c). All fitting parameters are tabulated in Appendix A4.2.
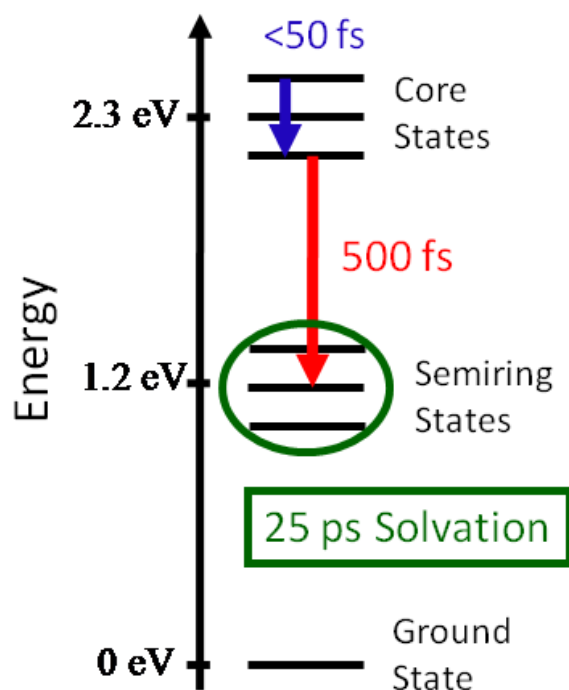
Figure 5.4: Electronic relaxation scheme obtained by analysis of transient grating experiments. Equilibration of electrons within the metal core occurs in <50 fs, whereas the 500 fs time constant is assigned to internal conversion between core and ligand-localized electronic states. Nuclear relaxation of the semiring moieties (i.e., ligands) occurs in 25 ps.

Information obtained from the TG experiments is summarized with the relaxation scheme presented in Figure 5.4. Following photoexcitation of the metal core, the electronic population first equilibrates within the core in <50 fs then undergoes internal conversion into the semiring manifold of excited states in approximately 500 fs. The relaxation scheme is consistent with that shown in Chapter 4 for Au_{25} in which a 1.2 ps internal conversion process between the core and ligand-localized states was observed. It is not immediately clear why the relaxation dynamics are 2.4 times faster in $Au_{24}Pd$. To date, theoretical models have been used to treated linear optical properties and electrochemistry, but have not yet examined the dynamics of excited electronic states. Superior wavefunction overlap between

the core and ligand-localized states could explain faster relaxation in $Au_{24}Pd$. However, further experimental and theoretical studies will be needed to reach firm conclusions. Still, it is useful to consider the origins of the dynamics in the context of recent experimental and theoretical work.

Density functional theory (DFT) calculations have investigated three isomers of $Au_{24}Pd$ with the Pd atom located in the center of the core (C), on the core surface (S), and in the ligand (L).[28] The calculations predict that the C isomer of $Au_{24}Pd$ has linear optical properties similar to Au_{25}, which is inconsistent with Figures 5.1(a) and 5.1(b). In addition, ligand exchange measurements point to the L isomer.[26] Clearly, the dynamics in the TG signals also encode signatures of the isomer electronic structure. DFT calculations predict a significant geometric distortion of the L isomer in which the Pd atom in the semiring relaxes towards the Au_{13} core. By contrast, large geometric changes were not predicted in the C and S isomers. We hypothesize that this distortion promotes faster internal conversion in $Au_{24}Pd$. The possibility that both S and L isomers are present in the sample should also be considered. Our data would then suggest that both isomers of $Au_{24}Pd$ possess nearly identical relaxation times. In any case, the findings do not preclude correlation of the dynamics with the structure because all isomers present relax according to the scheme in Figure 5.4. The important conclusion drawn here is that the separation in time scales associated with photoexcited core electron equilibration and core-to-semiring internal conversion first determined in Au_{25} persists in $Au_{24}Pd$. This separation in time scales is a dynamic signature of localized electronic states.

5.3. SUMMARY AND CONCLUSION

In summary, the present study establishes the presence of core and ligand-localized electronic states in $Au_{24}Pd$. First, it was shown that $Au_{24}Pd$ conforms to the trend of size-independent emission frequencies observed for Au MPCs ranging in size from 11 to 201 Au atoms.[23] Also, as in Au_{25}, femtosecond TG experiments find that equilibration of photoexcited core electrons in $Au_{24}Pd$ is roughly 10 times faster than core-to-semiring internal conversion. This separation in time scales is consistent with relatively small wavefunction overlap for core and ligand-localized electronic wavefunctions. While the basis of core and ligand-localized states is useful for discussion of the present experiments, it is likely that a more complex model will be needed to fully understand finer details of dynamics and make predictions for other MPCs. In fact, *ab initio* calculations clearly show that it is a poor approximation to regard optical absorption spectra as the simple sum of core and semiring contributions.[14] It is hoped that the present set of experiments will be useful for future theoretical investigations of electronic structure and condensed phase relaxation dynamics in MPCs.

5.4 REFERENCES

(1)   Mie, G. *Ann. Phys.* 1908, *25*, 377-455.

(2)   Kerker, M. The Scattering of Light and Other Electromagnetic Radiation; Academic: New York, 1969.

(3)   Bohren, C. F.; Huffman, D. R. Absorption and Scattering of Light by Small Particles: New York, 1983.

(4)   Kelly, K. L.; Coronado, E.; Zhao, L. L.; Schatz, G. C. *107* 2003, 668-677.

(5)   Gray, S. K.; Kupka, T. *Phys. Rev. B* 2003, *68*, 045415.

(6)   Daniel, M.-C.; Astruc, D. *Chem. Rev.* 2004, *104*, 293-346.

(7)   Laaksonen, T.; Ruiz, V.; Liljeroth, P.; Quinn, B. M. *Chem. Soc. Rev.* 2008, *37*, 1836-1846.

(8)   Murray, R. W. *Chem. Rev.* 2008, *108*, 2688-2720.

(9)   Häkkinen, H. *Chem. Soc. Rev.* 2008, *37*, 1847-1859.

(10)   Varnavski, O.; Ramakrishna, G.; Kim, J.; Lee, D.; Goodson, T. *J. Am. Chem. Soc.* 2009, *132*, 16-17.

(11)   Jadzinsky, P. D.; Calero, G.; Ackerson, C. J.; Bushnell, D. A.; Kornberg, R. D. *Science* 2007, *318*, 430-433.

(12)   Akola, J.; Walter, M.; Whetten, R. L.; Häkkinen, H.; Grönbeck, H. *J. Am. Chem. Soc.* 2008, *130*, 3756-3757.

(13)   Zhu, M.; Aikens, C. M.; Hollander, F. J.; Schatz, G. C.; Jin, R. *J. Am. Chem. Soc.* 2008, *130*, 5883-5885.

(14)   Aikens, C. M. *J. Phys. Chem. C* 2008, *112*, 19797-19800.

(15)   Link, S.; El-Sayed, M. A.; Schaaf, T. G.; Whetten, R. L. *Chem. Phys. Lett.* 2002, *356*, 240-246.

(16)   Jin, R. *Nanoscale* 2010, *2*, 343-362.

(17)   Heaven, M. W.; Dass, A.; White, P. S.; Holt, K. M.; Murray, R. W. *J. Am. Chem. Soc.* 2008, *130*, 3754-3755.

(18)   Whetten, R. L.; Price, R. C. *Science* 2007, *318*, 407-408.

(19)   Zhu, M.; Eckenhoff, W. T.; Pintauer, T.; Jin, R. *J. Phys. Chem. C* 2008, *112*, 14221-14224.

(20)   Khanna, S. N.; Jena, P. *Phys. Rev. Lett.* 1992, *69*, 1664-1667.

(21)   de Heer, W. A. *Rev. Mod. Phys.* 1993, *65*, 611-675.

(22)   Lee, D.; Donkers, R. L.; Wang, G.; Harper, A. S.; Murray, R. W. *J. Am. Chem. Soc.* 2004, *126*, 6193-6199.

(23)   Wang, G.; Huang, T.; Murray, R. W.; Menard, L.; Nuzzo, R. G. *J. Am. Chem. Soc.* 2005, *127*, 812-813.

(24)   Mukamel, S. *Principles of Nonlinear Optical Spectroscopy*; Oxford University Press: New York, 1995.

(25)   Miller, S. A.; Womick, J. M.; Parker, J. F.; Murray, R. W.; Moran, A. M. *J. Phys. Chem. C* 2009, *113*, 9440-9444.

(26)   Fields-Zinna, C. A.; Crowe, M. C.; Dass, A.; Weaver, J. E. F.; Murray, R. W. *Langmuir* 2009, *25*, 7704-7710.

(27)   Jiang, D.; Da, S. *Inorg. Chem.* 2009, *48*, 2720-2722.

(28)   Kacprzak, K. A.; Lehtovaara, L.; Akola, J.; Lopez-Acevedo, O.; Häkkinen, H. *Phys. Chem. Chem. Phys.* 2009, *11*, 7123-7129.

(29)   Akola, J.; Walter, M.; Whetten, R. L.; Häkkinen, H.; Grönbeck, H. *J. Am. Chem. Soc.* 2008, *130*, 3756-3757.

(30)   Lepetit, L.; Chériaux, G.; Joffre, M. *J. Opt. Soc. Am. B* 1995, *12*, 2467-2474.

(31)   Gallagher, S. M.; Albrecht, A. W.; Hybl, J. D.; Landin, B. L.; Rajaram, B.; Jonas, D. M. *J. Opt. Soc. Am. B* 1998, *15*, 2338-2345.

(32)   Hodak, J. H.; Henglein, A.; Hartland, G. V. *J. Chem. Phys.* 1999, *111*, 8613-8621.

(33)   Hodak, J. H.; Martini, I.; Hartland, G. V. *J. Phys. Chem. B* 1998, *102*, 6958-6967.

(34)   Ahmadi, T. S.; Logunov, S. L.; El-Sayed, M. A. *J. Phys. Chem.* 1996, *100*, 8053-8056.

CHAPTER 6 . EXCITED STATE PHOTOPHYSICS IN A LOW BAND GAP

POLYMER WITH HIGH PHOTOVOLTAIC EFFICIENCY

6.1. INTRODUCTION

One approach to improving the efficiencies of polymer/fullerene bulk heterojunction (BHJ) solar cells involves the development of new polymers with small band gaps tuned to capture as much of the solar spectrum as possible.[1,2] To this end, numerous polymers with small band gaps have been synthesized and tested in typical BHJ device configurations; however, only a few of them have demonstrated promising power conversion efficiencies (>6%).[3-9] In addition to probing equilibrium physical properties in these materials (e.g., band gap and orbital energies), fundamental photophysical studies are needed to establish relationships between molecular structure and the dynamics governing device performance (e.g., energy and charge transport).[10,11] Collectively, such studies will lead to a deeper understanding of structure/property correlations in high performance materials. Moreover, the design rationale distilled in fundamental studies has practical implications for the future development of new materials.[12-14] Only a few such studies have been conducted on newly discovered high performance low band gap materials,[15-17] with exceptions to well studied polythiophenes (e.g., P3HT) [18-20] and poly(phenylenevinylene)s (e.g., MDMO-PPV).[21,22]

We recently reported a new low band gap polymer, PNDT-DTPyT, that supports an overall power conversion efficiency as high as 6% in optimized BHJ devices.[9] In this study, we present a broad investigation of this new material (cf., Figure 6.1), spanning aspects of its

fundamental photophysics to the measurement of BHJ device efficiencies. PNDT-DTPyT is synthesized based on the "weak donor-strong acceptor" strategy,[23-25] which derives from the commonly employed "donor-acceptor" (D-A) approach to achieving smaller band gaps in conjugated polymers.[26,27] The PNDT-DTPyT investigated in this study, consists of NDT (naphtho[2,1-*b*:3,4-*b'*]dithiophene) as the "weak donor", and DTPyT (4,7-di(4-alkyl-2-
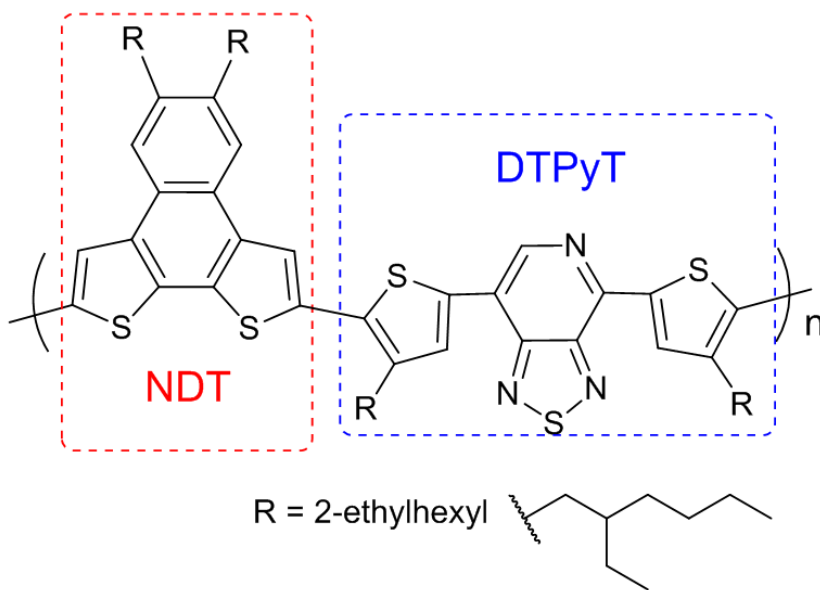
Figure 6.1: Structure of the repeat unit in PNDT-DTPyT. Electron donor (NDT) and acceptor (DTPyT) functional groups govern the HOMO-LUMO energy gap. The lowest energy electronic transition possesses charge transfer character.

thienyl)-thiadiazolo[3,4-*c*]pyridine) as the "strong acceptor", with all side chains being 2-ethylhexyl.[28] In the D-A copolymers, overlapping orbitals localized on the donor and acceptor moieties gives rise to low frequency optical charge transfer transitions beneficial for solar light harvesting.[23,29] PNDT-DTPyT possesses a nearly ideal band gap (~1.55 eV) in addition to a LUMO energy (– 3.39 eV) suitable for use in BHJ devices incorporating PCBM as the electron accepting species. In addition, the quasi-planar structure of PNDT-DTPyT

promotes stacking of polymer chains, thereby facilitating chain-chain interactions and improving the overall mobility of photoexcitations in the polymer.

Here the influences of electronic structure and morphology on energy transport in PNDT-DTPyT are examined using a variety of spectroscopic measurements. Experiments conducted with the pure polymer film focus primarily on the closely related issues of heterogeneity in the sizes of electronic excitations (i.e., excitons) and vibronic coupling. Steady state absorption and fluorescence line shapes of PNDT-DTPyT are examined at temperatures ranging from 100K to 300K. Together, electronic structure calculations and an empirical model yield a quantitative distribution in exciton sizes, which suggests that strong coupling with the environment localizes the excited states to fairly small segments of the polymer. Femtosecond transient grating (TG) measurements are then used to establish connections between energy transport kinetics and the exciton sizes. Signatures of distinct energy transfer mechanisms are observed and attributed to local morphologies. In addition, fluorescence quenching experiments and TG spectroscopy probe charge injection efficiencies in films composed of both PNDT-DTPyT and PCBM. Signatures of charge separation are shown to correlate well between these two techniques. The attainment of photovoltaic power conversion efficiencies for the same films complements the spectroscopic measurements. Connections are discussed between the measured device efficiencies and the microscopic information provided by the optical spectroscopies.

Previous theoretical and experimental studies on conjugated polymers provide a framework for interpreting the present spectroscopic signatures of energy transport in pure PNDT-DTPyT polymer films.[30-51] The Förster mechanism is known to provide a realistic description for systems, such as PNDT-DTPyT, in which the energy donor and acceptor

152

couple through the transition moments corresponding to the lowest energy optical transitions. The nature of the energy transfer process is the main factor governing energy transfer dynamics; whether it is intrachain or interchain.[35,36] Intrachain energy transfer describes events in which photoexcitations hop across "kinks" in the polymer backbone separating regions of double-bond conjugation, whereas interchain energy transfer involves the migration of photoexcitations between neighboring polymer chains. Interchain transitions, which typically take place in a few picoseconds, are 1-2 orders of magnitude faster than intrachain dynamics.[35,36] Theoretical calculations show that this large disparity in kinetics originates primarily in the magnitudes of electrostatic couplings between the energy donor and acceptor moieties.[37] In addition, the role of the environment should not be understated. Large environmental reorganization energies promote trapping of photoexcitations onto short segments of conjugated polymers. Therefore, in energy transfer processes the wave functions at the donor sites are generally quite localized, and therefore possess small transition dipoles that couple weakly to those at the acceptor sites. Of course, the reorganization energy also controls energy transport through the spectral overlap parameter in the Förster rate formula, so its impact on the overall kinetics depends on the details of the system at hand.

6.2 EXPERIMENTAL METHODS

The synthesis of PNDT-DTPyT is described in Reference 9. A slightly different polymer was used in this study: all side chains anchored on the PNDT-DTPyT were 2-ethylhexyl (C6,2) to minimize effects of the side chains.[28] PNDT-DTPyT and PNDT-DTPyT:PCBM thin films (~100 nm thick) are prepared by spin coating the sample solutions

in 1,2 dichlorobenzene solvent onto 1.5 mm thick fused silica glass substrates. The absorbance of all films is approximately 0.13 at 600 nm. Linear absorbance spectra are measured with an HR2000 Ocean Optics spectrometer and deuterium-tungsten lamp. Steady state fluorescence experiments use a He:Ne laser to excite the samples with 0.1 mW at 633 nm. The samples are moved continuously using a linear actuator during fluorescence measurements to suppress photo-bleaching. Emission is detected with a thermoelectrically cooled and back-illuminated CCD. A liquid nitrogen cooled cryostat (Optistat-DN, Oxford Instruments) is used for low temperature measurements.

The TG spectrometer employed in this work has been described in detail elsewhere[52,53] including Chapter 3.6. In brief, all one-color experiments excite the sample films with 20 fs laser pulses centered at 16670 cm^{-1}. Two-color experiments excite the films with 20 fs "pump" pulses centered at 20400 cm^{-1}, then monitor relaxation with a continuum "probe" pulse spanning the 15150-18520 cm^{-1} range. As discussed in Reference 54, the width of the instrument response over the full probe spectrum is reduced to less than 90 fs by minimizing dispersion of the probe pulse at 16670 cm^{-1} using a prism compressor. Spectral interferometry is utilized for signal detection.[55,56] Only the absorptive component of the TG signal field is presented here, which yields information similar to that obtained in a conventional transient absorption measurement.[57] Unless otherwise noted, all experiments are conducted in a configuration in which the three applied laser pulses and the signal possess parallel electric field polarizations. All laser pulses possess approximately 1 nJ of energy and are focused to 120 μm fwhm spot sizes at the sample position. With the resulting pump laser fluence of 5.3×10^{13} photons/cm^2, we estimate that 1 in every 100 repeat units is photoexcited (cf., Appendix A5.2). Even at this low power density, photobleaching of the

film is observed after approximately 30 minutes exposure to the laser. Data acquisition times are therefore kept to less than 10 minutes.

BHJ photovoltaic devices are fabricated with a typical configuration of ITO/PEDOT:PSS (40nm)/polymer:PC61BM/Ca(40nm)/Al(70nm). Glass substrates coated with patterned indium-doped tin oxide (ITO) are purchased from Thin Film Devices, Inc. The 150 nm sputtered ITO pattern has a resistivity of 15Ω. Prior to use, the substrates are ultra-sonicated for 20 minutes in acetone followed by deionized water and then 2-propanol. The substrates are dried under a stream of nitrogen and treated with UV-Ozone for over 30 minutes. A filtered dispersion of PEDOT:PSS in water (Baytron PH500) is then spun cast onto clean ITO substrates and baked at 140 °C for 15 minutes. A blend of polymer and PCBM is dissolved in chlorinated solvent and heated at 110 °C for 8 hours. All of the solutions are then spun cast onto a PEDOT:PSS layer and dried at room temperature in a glovebox under nitrogen atmosphere for 12 hours. Next, a 40 nm film of calcium and a 70 nm aluminum film are thermally deposited at a pressure of $\sim 1 \times 10^{-6}$ mbar. We fabricate 8 devices per substrate, with an active area of 0.12 cm^2 per device. Device characterization is carried out under AM 1.5G irradiation with the intensity of 100 mW/cm^2 (Oriel 91160, 300 W) using a certified standard silicon cell calibrated by NREL. Current density versus potential (*J*-V) curves are recorded with a Keithley 2400 digital source meter. All fabrication steps following the addition of the PEDOT:PSS layer to the ITO substrate and subsequent device characterizations are performed in gloveboxes under nitrogen atmosphere.

6.3 RESULTS AND DISCUSSION

6.3.1. Signatures of Optical Heterogeneity in Optical Line Shapes

It is well-established that the geometry of a polymer backbone governs the effective conjugation lengths over which electronic states delocalize.[34,36,37,47,58] In amorphous polymer films, the distribution in planar segment sizes is directly reflected in the line shapes of optical spectra, where shorter segments possess larger excitation frequencies (i.e., smaller confinement volumes). Electronic energy transfer (EET) is also sensitive to the polymer morphology because of its effect on the resonance frequencies at donor and acceptor sites. In the Förster regime, the environment at the EET donor site is fully relaxed; excitations become trapped on fairly short segments. By contrast, the distribution in EET acceptor segment lengths reflects the full geometric heterogeneity found in the ground state at equilibrium. The temperature dependence of the steady state spectra of PNDT-DTPyT shown in Figure 6.2 can be interpreted in terms of the sizes of the excitations contributing to the signals. The absorbance spectra of the lowest energy transition exhibit a reduction in amplitude at frequencies >14000 cm^{-1} with decreasing temperature, whereas the onset of absorption at frequencies <14000 cm^{-1} is essentially independent of temperature. This behavior suggests that a reduction in temperature promotes exciton delocalization (lower energy electronic resonances). The nature of nuclear motions suppressed at lower temperatures is unclear. However, one sensible hypothesis is that the torsional angles between repeat units may be smaller (on average) at lower temperatures, thereby enhancing effective conjugation lengths. By contrast, the fluorescence spectra not only exhibit a red-shift of more than 400cm^{-1} upon cooling from 300K to 100K but also become narrower. The

red-shift in the fluorescence spectra associated with decreasing temperature is, in part, caused by the migration of photoexcitations onto longer segments.
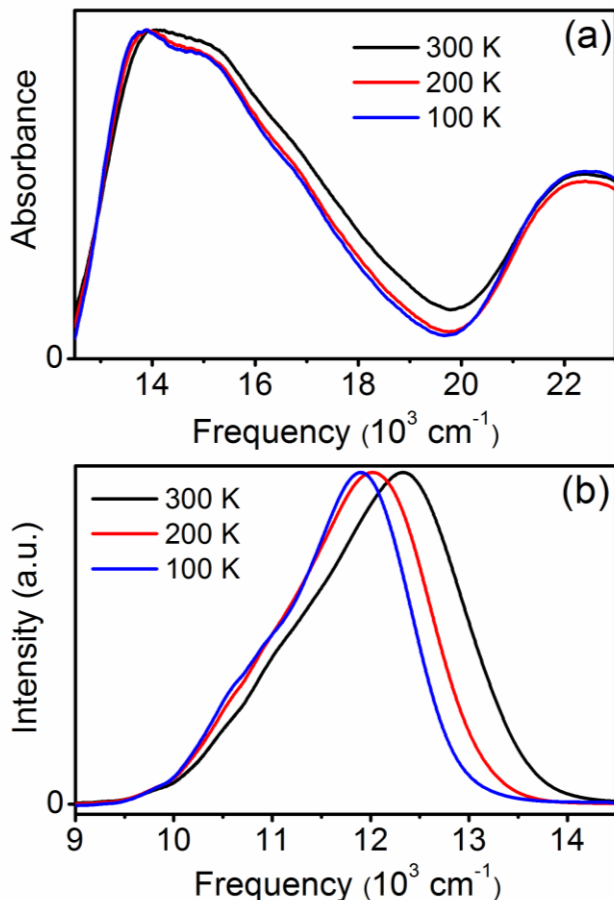
Figure 6.2: (a) Linear absorbance and (b) fluorescence spectra of pure PNDT-DTPyT films measured at 100K (blue), 200K (red), and 300K (black). In the absorbance spectra, lower temperatures promote an overall red-shift associated with exciton delocalization. The fluorescence line shapes are influenced by both the migration of photoexcitations onto longer segment lengths and the suppression of thermal fluctuations.

In principle, full information on heterogeneity in the sizes of electronic excitations can be extracted by analysis of the optical line shapes. However, such an analysis generally requires many parameters, some of which are not presently available for PNDT-DTPyT (e.g., the Franck-Condon progressions of the intramolecular modes). Therefore, in this work, useful semi-quantitative information is obtained with a physically motivated

phenomenological model. We write the absorbance line shape, $\sigma(\omega)$, of the PNDT-DTPyT film as

$$\sigma(\omega) = \int_{0}^{\infty} ds \, G(s) f(s) \varepsilon(\omega, s) \qquad (6.1)$$

where the line shape of a segment with length s is given by

$$\varepsilon(\omega, s) = \sum_{i=1}^{2} A_i \exp\left[\frac{-\left(\omega - \omega_i(s) - (i-1)\eta - \xi\right)^2}{2\Delta_i^2} \right] \qquad (6.2)$$

and the distribution in segment lengths is taken to obey a log-normal distribution

$$G(s) = \left(\frac{1}{s\delta\sqrt{2\pi}} \right) \exp\left[-\frac{(\ln s - \mu)^2}{2\delta^2} \right] \qquad (6.3)$$

Here $\varepsilon(\omega, s)$ sums over two components, i, representing the purely electronic (0-0) transition and a higher frequency effective vibronic transition needed to capture the skew in the spectrum caused by the Franck-Condon progression.

Parameterization of Equations 6.1-6.3 is achieved through a combination of empirical fitting and electronic structure calculations. As shown in Figure 6.3, the line width, Δ_i, and amplitude, A_i, of component i is found by fitting the fluorescence spectrum at 300K. These parameters are obtained by fitting the fluorescence spectrum because it is most closely related to the meaning of the parameter Δ_i, which represents the line width of a particular segment length (i.e., not the sum of many segment sizes as would be found in the absorbance spectrum). To make this point clear, we note two fundamental assumptions made in parameterization of Equations 6.1-6.3 using quantities associated with the fluorescence

158

spectrum: (i) both the ground and excited state free energy surfaces are parabolic and possess

the same curvature; (ii) all segment sizes have the same Δ_i. These assumptions are not only

physically reasonable but also necessary to keep the number of adjustable parameters in the

model manageable (i.e., a unique fit to measured signals is ultimately desired). ZINDO

electronic structure calculations are used to obtain the oscillator strength, $f(s)$, and

transition frequency, $\omega_i(s)$, associated with segment size s. The fitting parameter, ξ, in

Equation 6.2 accounts for the offset in the calculated $\omega_i(s)$ with respect to the measured

spectrum. Figure 6.3 displays ZINDO results obtained for oligomers ranging from 1-10

repeat units, where the structures of the oligomers are periodic in a NDT-DTPyT repeat unit

whose geometry is optimized at the B3LYP/3-21G level. Appendix A5.1 presents the

molecular structures and summarizes further details involved in these calculations. Finally,

the parameters of $G(s)$, which capture the heterogeneity in molecular conformations, are left

adjustable for fitting the measured absorbance spectrum.
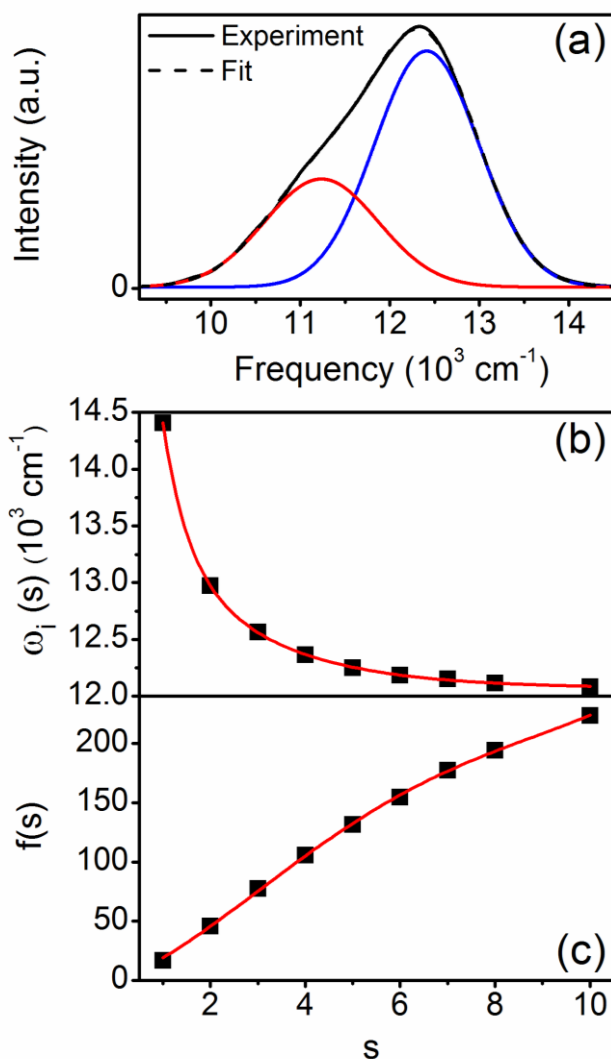
Figure 6.3: (a) Fit of fluorescence spectrum measured at 300K using Equation 6.2. The blue and red components respectively capture the 0-0 transition and the (effective) vibronic progression of intramolecular modes. Fitting parameters are given in Table 6.1. (b) Frequencies and (c) oscillator strengths corresponding to the lowest energy electronic transitions of PNDT-DTPyT oligomers computed using the ZINDO method. The black squares are obtained directly from the calculations and the red lines are obtained from fits employing a polynomial expansion.

Table 6.1. Parameters used to fit linear absorption spectrum.

Parameter	Value
[a] A_1	1.0
[a] A_2	0.46
[a] Δ_1	582 cm^{-1}
[a] Δ_2	633 cm^{-1}
[a] η	1175 cm^{-1}
[a] ξ	950 cm^{-1}
[b] μ	0.03
[b] δ	0.76

[a]Parameter of Equation 6.2.

[b]Parameter of Equation 6.3.

The fit of the linear absorbance spectrum for the lowest energy electronic transition obtained using Equations 6.1-6.3 is displayed in Figure 6.4. Our model, which employs only three adjustable parameters, leads to a unique fit of the measurement. The aspect of the line shape most challenging to capture is the skew. Figure 6.3 shows that shorter segments possess smaller oscillator strengths. However, the dependence of $f(s)$ on the segment length is not sufficient to explain the skew in the spectrum. We find that a reasonable fit is achieved by invoking a log-normal distribution, $G(s)$. The $G(s)$ found here possesses a mean and standard deviation of 1.4 and 1.2, respectively. Using $\lambda = \Delta_1^2 / 2k_B T$, a nuclear reorganization energy of 800cm^{-1} is calculated using the line width of the 0-0 transition shown in Figure 6.3. While this nuclear reorganization is only a rough estimate, the robust physical insight it supports is that the photoexcitations in PNDT-DTPyT interact strongly with their environments. We remark that the 1400cm^{-1} difference between peaks in the absorbance and fluorescence spectra is consistent with a reorganization energy near 800cm^{-1} (i.e., Stokes shift is twice the reorganization energy for a Gaussian bath).[59] Using the same

procedure, reorganization energies obtained at 200K and 100K are respectively 650 cm^{-1} and 530 cm^{-1} (cf., Figure A5.12 in Appendix 5).
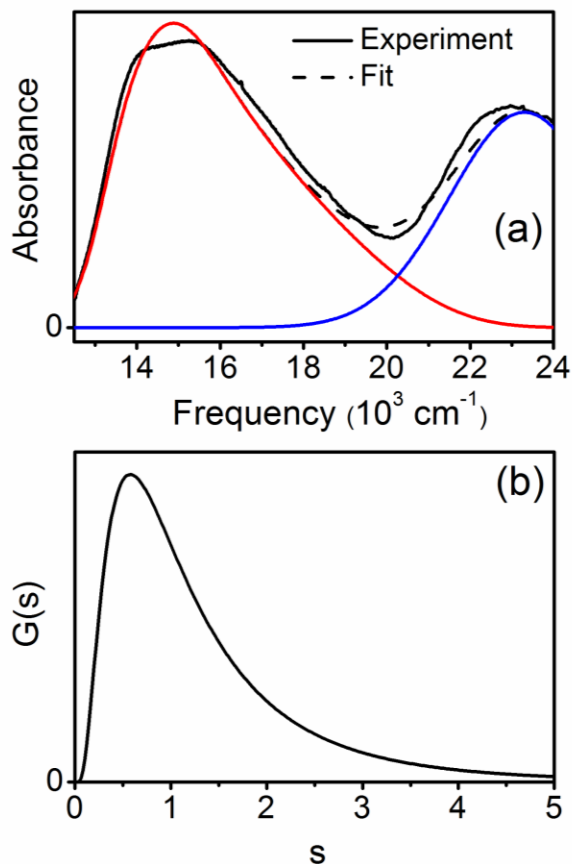
Figure 6.4: (a) Fit of linear absorption spectrum at 300K achieved using Equation 6.1. Parameters are adjusted to fit the lowest energy electronic transition shown in red. We postulate a Gaussian line shape (blue) centered at 23300 cm^{-1} to capture the region of overlapping amplitude near 20170cm^{-1}. (b) Log-normal distribution, $G(s)$, used to obtain the line shape of the lowest energy transition shown in panel (a). The mean and standard deviation of $G(s)$ are respectively 1.4 and 1.2.

In summary, the analysis of absorbance and fluorescence spectra presented in this Section suggests that the charge transfer excitations of PNDT-DTPyT localize onto short segments of the polymer due to strong coupling with the environment. Textbook signatures of geometric heterogeneity in PNDT-DTPyT are observed in the temperature-dependent

spectra shown in Figure 6.2. The red-shift of the fluorescence spectra found with decreasing temperature reflects an increase in the average excitation size. In addition, the fit of the absorption spectrum at 300K provides information on the equilibrium distribution of conformations in the ground electronic state. This distribution significantly favors segment sizes less than ~3 repeat units (cf., Figure 6.4). As to physical insight into the apparently strong system-bath coupling in PNDT-DTPyT, we hypothesize that because the charge transfer excitation necessarily involves a major change in electron density, the environment must respond by significantly rearranging the surrounding nuclei.

6.3.1. Electronic Relaxation in Pure Polymer Films

This Section examines electronic relaxation in pure PNDT-DTPyT films with TG spectroscopy. Quantitative information is obtained by fitting signals with the phenomenological equation

$$S(T) = \sum_m \int_{-\infty}^{T} G(t;w)A_m \exp\left[-(T-t)/\tau_m\right] dt \tag{6.4}$$

where $G(t;w)$ is a Gaussian function used to deconvolute the instrument response width, w, from the relaxation processes. In general, electronic and nuclear relaxation are not readily distinguished with a single experiment. Signal interpretation is facilitated by measurement of the anisotropy

$$r(T) = \frac{S_{\parallel}(T) - S_{\perp}(T)}{S_{\parallel}(T) + 2S_{\perp}(T)} \tag{6.5}$$

where $S_\parallel$ and $S_\perp$ respectively denote configurations in which the excitation and detection pulses possess parallel and perpendicular electric field polarizations. In PNDT-DTPyT and other conjugated polymers, the decay of $r(T)$ primarily reflects the depolarization of the signal caused by the incoherent hopping of excitations.[39,60,61]

Figure 6.5 presents the absorptive part of a TG signal acquired with 16670cm^{-1} excitation and detection pulses. Optimal fits are achieved with an expansion in four exponential functions whose time constants range from the 120 fs to 130 ps (cf., Table 6.2). The 7.2 ps process found in the individual tensor element, $S_\parallel$, closely matches the time scale of interchain hopping observed in other polymers.[36,37,39] We therefore assign this component to similar energy transport dynamics in PNDT-DTPyT. However, the interpretation of the two shorter time constants at 120fs and 0.98ps is less clear because nuclear relaxation likely occurs on a similar time scale. For this reason, it is quite interesting that the two short decay components also contribute to the anisotropy. Because the 120fs component is too fast to represent incoherent energy transfer, we assign it to self-trapping of the electronic excitation (i.e., contraction of the exciton size) caused by nuclear relaxation.[39,60-64] In addition, we suggest that the 0.98ps process represents a mechanism of energy transfer distinct from that corresponding to the ~7.2ps time constant. For example, the origin of the two time constants may be geometric in nature. Interactions between neighboring PNDT-DTPyT chains are thought to promote stacking of the planar moieties. Thus, the two processes may both represent interchain energy transfer but differ in whether they involve stacked or non-stacked neighbors. This idea will be pursued further in future work as a strong conclusion cannot yet be drawn. Finally, large error bars are associated with the 14.3ps time constant in the

anisotropy because the amplitudes of both tensor elements are small in this delay range, and

the noise in $r(T)$ is relatively large. Therefore, we do not assign this component.
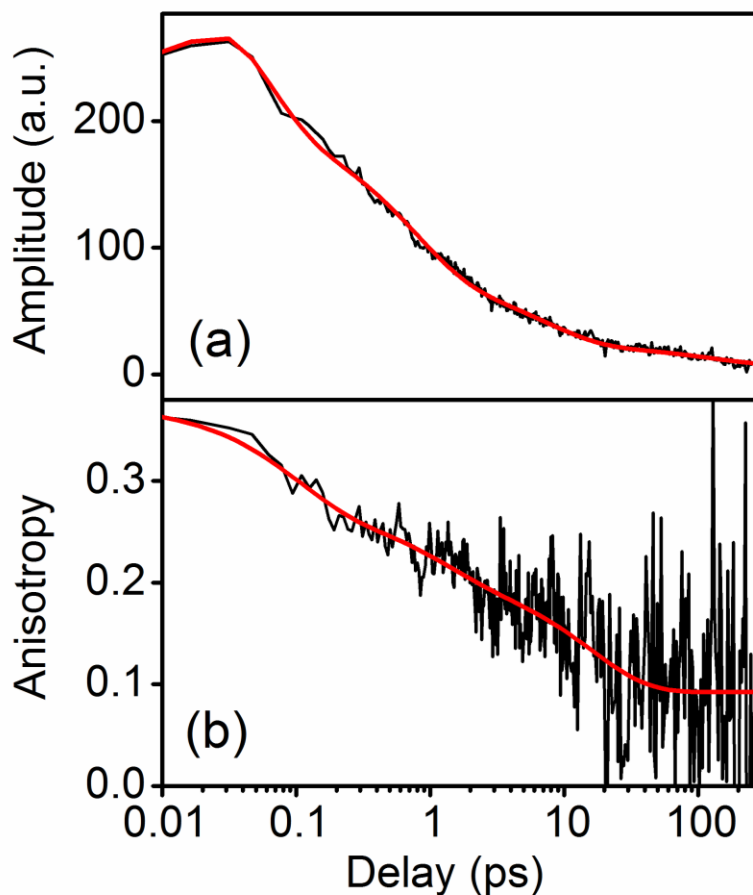
Figure 6.5: (a) Absorptive part of measured TG signal (black) and fit (red) for an experiment employing 20fs, 16670 cm^{-1} excitation and detection pulses. All fields possess parallel polarizations. (b) Measured anisotropy (black) and fit (red) for an experiment utilizing the same lasers pulses as panel (a). Noise in the anisotropy at long delay times is caused by the reduction in signal amplitude for the individual tensor elements. All fitting parameters are given in Table 6.2.

Table 6.2. Transient absorption fitting parameters for pure PNDT-DTPyT films.

[a]Parameter	[b] $S_\parallel(T)$	[c] $r(T)$
A_1	0.41 ± 0.01	0.11 ± 0.02
τ_1/ps	0.12 ± 0.01	0.08 ± 0.03
A_2	0.35 ± 0.01	0.07 ± 0.02
τ_2/ps	0.98 ± 0.07	1.1 ± 0.2
A_3	0.15 ± 0.01	0.11 ± 0.02
τ_3/ps	7.2 ± 0.7	14.3 ± 6.0
A_4	0.08 ± 0.01	0.10 ± 0.01
τ_4/ps	130 ± 36	∞

[a] Parameters of Equation 6.4.

[b] $S_\parallel$ denotes a tensor element in which excitation and detection are conducted with parallel electric field polarizations.

[c] Calculated with Equation 6.5.

Energy transfer dynamics are also investigated using an experiment in which excitation is achieved at 20400 cm^{-1} and the dynamics are probed in the 15150-18520 cm^{-1} range. A 20400 cm^{-1} pulse is used for excitation to eliminate scattered light from the detection window. All evidence suggests that energy transfer still initiates in the lowest energy excited state, which indicates that internal conversion between excited states on a particular segment is much faster than energy transfer between spatially separated segments. Signals acquired in this configuration are displayed in Figure 6.6. The signals are fit using a sum of exponential functions for which the parameters are given in Table 6.3. As should be expected, similar decay components are found in both the one-color and two-color experiments, where ~1ps and ~10ps time constants associated with incoherent hopping are again detected. It is interesting that a systematic increase in these two time constants is found with increasing detection frequency. This observation can be explained by invoking the Förster rate formula

$$k_{da} = \frac{2\pi}{\hbar} |V_{da}|^2 J_{da}$$ (6.6)

where J_{da} is spectral overlap between the donor and acceptor and V_{da} is the coupling between donor and acceptor transition moments. The calculated oscillator strengths presented in Figure 6.3, which are proportional to the squares of the transition dipoles, increase as the electronic resonance frequencies decrease. Interactions between these same transition dipoles governs the magnitude of V_{da}. Thus, the electrostatic coupling should generally be larger when longer segments are involved. Therefore, it stands to reason that, given moderate spectral overlap, an increase in the energy transfer rate should be observed with decreasing detection frequency (i.e., with increasing segment length). We suggest that a rate enhancement originating in the magnitude of V_{da} is the most likely explanation for the measured dispersion in time constants shown in Figure 6.6.
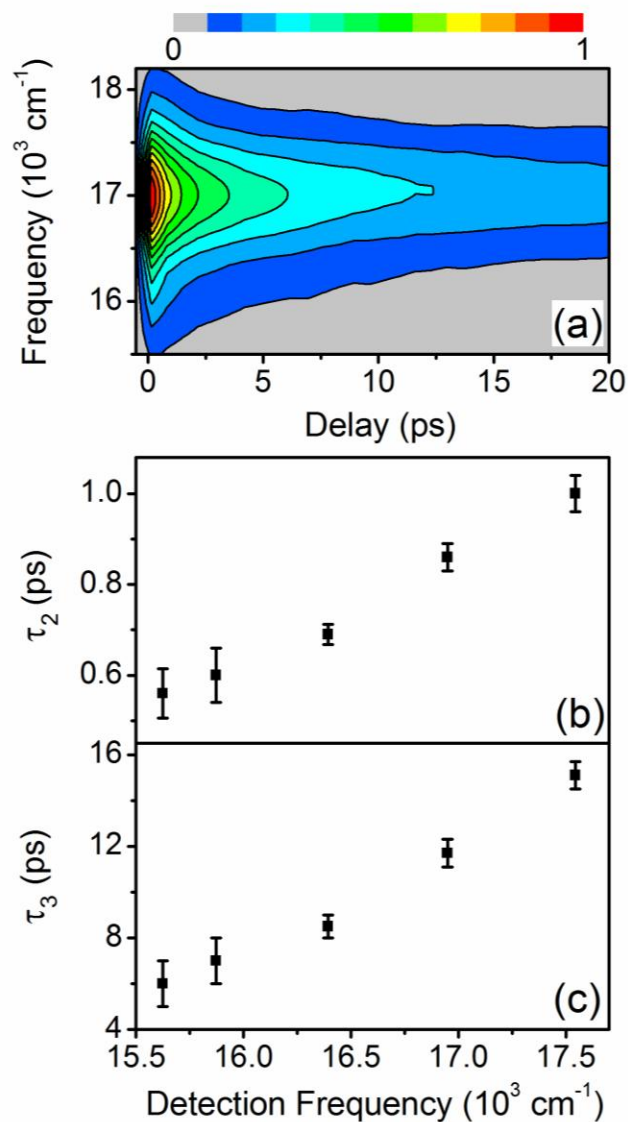
Figure 6.6: (a) Absorptive part of TG signal measured with excitation at 20400 cm^{-1}. Signals are normalized to 1 and plotted on a linear scale. The (b) τ_2 and (c) τ_3 time constants are obtained by fitting slices of the TG signal in panel (a) at particular detection frequencies. Fitting parameters are given in Table 6.3. Fits are displayed in Figure A5.13 of Appendix 5.

Table 6.3. Fitting parameters for transient absorption of pure PNDT-DTPyT films with broadband signal detection

[a]Parameter	17540 cm^{-1}	16950 cm^{-1}	16400 cm^{-1}	15870 cm^{-1}	15630 cm^{-1}
A_1	0.62 ± 0.02	0.73 ± 0.02	0.82 ± 0.04	0.60 ± 0.14	0.86 ± 0.05
[b]τ_1/ps	0.07 ± 0.03	0.04 ± 0.02	0.02 ± 0.02	0.03 ± 0.02	0.01 ± 0.01
A_2	0.25 ± 0.01	0.17 ± 0.01	0.11 ± 0.01	0.25 ± 0.03	0.08 ± 0.005
τ_2/ps	1.00 ± 0.04	0.86 ± 0.03	0.69 ± 0.02	0.6 ± 0.06	0.56 ± 0.05
A_3	0.13 ± 0.01	0.07 ± 0.004	0.05 ± 0.004	0.11 ± 0.01	0.04 ± 0.002
τ_3/ps	15.1 ± 0.6	11.7 ± 0.6	8.5 ± 0.5	7.0 ± 1.0	6.0 ± 1.0
A_4	NA	0.02 ± 0.002	0.02 ± 0.001	0.03 ± 0.004	0.02 ± 0.001
τ_4/ps	NA	100 ± 10	240 ± 45	51 ± 7	56 ± 8

[a] Parameters of Equation 6.4.

[b] The τ_1 time constants are shorter than the 90fs time resolution of this experiment with the exception of detection at 16400 cm^{-1}. This component is not well-determined and only signifies the presence of a sub-90fs process.

Individual tensor elements are sensitive to all non-radiative processes that influence the signal amplitude (e.g., quenching by impurities and photoproducts). Therefore, the assignment of dynamics observed in the $S_\parallel$ tensor element to energy transfer must be made with caution. For this reason, we have shown the relaxation time scales observed in both the anisotropy and individual tensor elements to be consistent (cf., Table 6.2). Moreover, the 1ps and 10ps time constants found for PNDT-DTPyT are consistent with energy transfer time scales established for other polymer systems. [37,39,60-64] For example, a 5 ps time constant associated with energy transfer was found in films composed of a polyindenofluorene polymer.[37] Studies of poly(3-hexylthiopene) in solution even find energy transfer time scales identical to those reported here (i.e., 1 and 10 ps).[39] In fact, the ultrafast exciton localization mechanisms proposed for poly(3-hexylthiopene)[46] and polyphenylene vinylene[65] are similar in nature to that which we propose to explain the 120fs time constant found in the anisotropy

of PNDT-DTPyT; we hypothesize that exciton localization is driven by nuclear relaxation on this time scale.

Finally, we comment on a technical issue important to the interpretation of the TG signals in this Section. Studies of conjugated polymers have observed signatures of interactions between electronic excitations.[66-69] In the present experiments, low power densities are intentionally used to suppress such effects. With the pump laser fluence of 5.3 $\times 10^{13}$ photons/cm^2, we estimate that only 1 in 100 monomer units is photoexcited at zero pulse delay. Moreover, an average distance between photoexcitations of 18 nm is obtained by treating the polymer as an amorphous melt (cf., Appendix A5.2). Excitons in conjugated polymers generally diffuse ~10 nm within their lifetime.[10,70-77] Therefore, we conclude that in the present experiments the electronic excitations do not interact on the delay range considered <10ps. The sensitivity afforded by combining TG spectroscopy with spectral interferometry makes possible the suppression of such undesired effects.

6.3.3. PNDT-DTPyT/PCBM BHJ Mixtures

In comparison to energy transport in pure polymers, an understanding of the fundamental processes surrounding charge separation is less well-defined in BHJ materials possessing electron acceptors such as fullerenes. Complexities abound in such mixtures due to phase segregation and heterogeneity in film morphologies.[34,78-80] One general challenge facing spectroscopic studies of complex materials is the assignment of signal components. Here TG experiments are conducted on thin films containing both PNDT-DTPyT and PCBM. Central to signal interpretation in these experiments is knowledge of the species that

170

is photoexcited in the "pump" step. Figure 6.7 presents TG signals acquired under identical conditions for films composed of pure PCBM and a 1:1 (weight ratio) mixture of PNDT-DTPyT and PCBM. This comparison suggests that all optical nonlinearities in which the laser pulses interact with only PCBM can be neglected. Thus, the dependence of the TG signals on the PCBM concentration found below should be understood as a result of interactions between PNDT-DTPyT and PCBM.
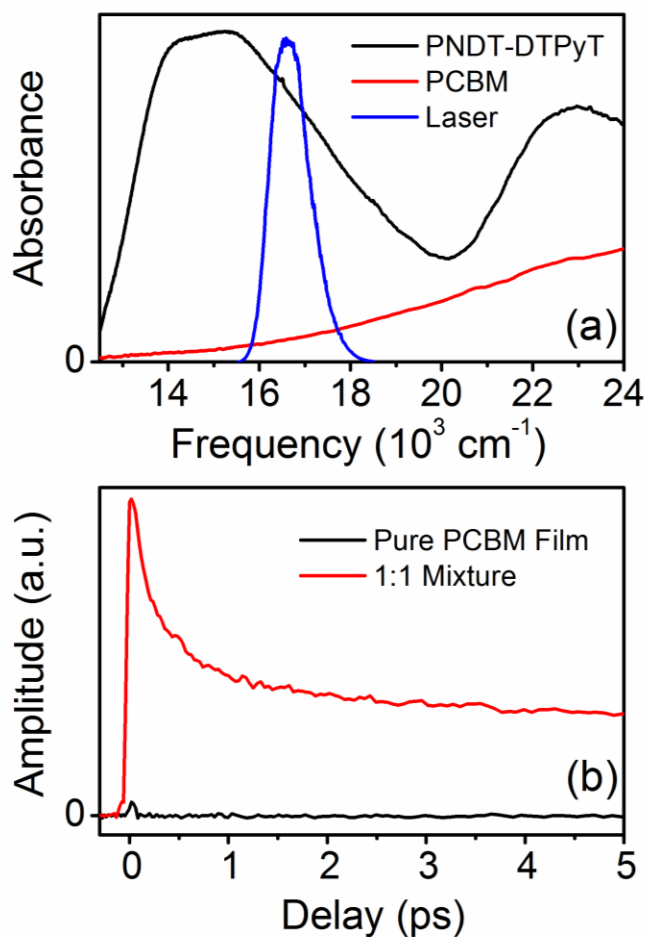
Figure 6.7: Experimental evidence that signal components in which PCBM is both excited and probed can be neglected for PNDT-DTPyT/PCBM mixtures. (a) Absorbance spectra of PNDT-DTPyT (black) and PCBM (red) are overlaid with the spectrum of the laser (blue). (b) Absorptive part of TG signal for pure PCBM film (black) and a film composed of a 1:1 mixture of PNDT-DTPyT and PCBM (red). These TG experiments employ 20fs, 16670 cm^{-1} excitation and detection pulses.

As shown in Figure 6.8, the presence of PCBM correlates with an increase in the TG signal amplitude at long delay times. In agreement with previous transient absorption studies of related materials,[66,81-83] we interpret this increase in amplitude as a signature of electron transfer from PNDT-DTPyT to PCBM. Subsequent to electron transfer, it follows that the species responsible for radiating the TG signals are the positive polaron in the polymer domain (PNDT-DTPyT$^+$) and the negative polaron in the PCBM domain (PCBM$^-$). PNDT-DTPyT$^+$ absorbs significantly at 16670cm^{-1} and therefore must contribute to the TG response. In addition, PCBM$^-$ possesses a resonance near 10000cm^{-1}, but absorbs quite weakly near 16670cm^{-1} so its contribution is probably relatively minor.[84,85] Closer examination of the dynamics at delay times <10ps shows that the deviation in TG signal amplitudes for films with different PCBM concentrations begins near 500fs, which suggests that a significant accumulation in separated charges has already occurred. This finding is consistent with several investigations of BHJ materials possessing fullerene acceptors, where it has been concluded that electron transfer occurs on the sub-picosecond time scale when photoexcitations in the polymer are initiated near the interface with the PCBM domain.[22,61,66,81,82,86-90] It is difficult to conclusively interpret the dynamics on longer time scales because charge separation becomes convoluted with the diffusion of electronic excitations in the polymer. Therefore, based on the present measurements we propose only two strong conclusions: (i) the increase in TG signal amplitude at long delay times is a signature of charge separation; (ii) a significant amount of separated charge is accumulated in less than 500fs.
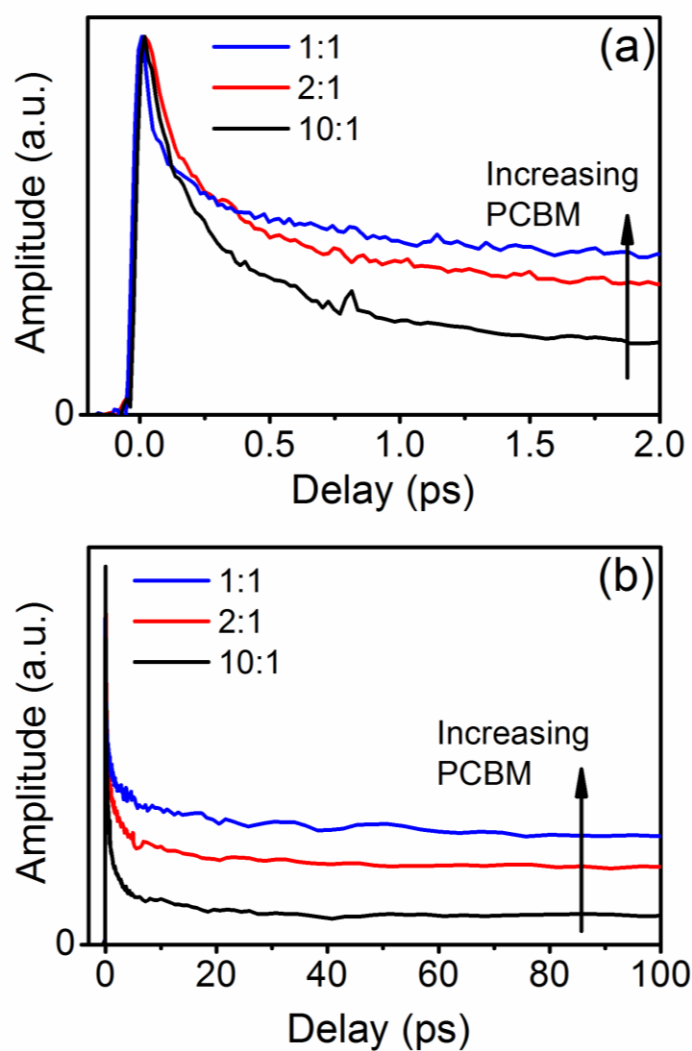
Figure 6.8: Absorptive parts of TG signals acquired for various weight ratios, PNDT-DTPyT:PCBM. All experiments employ 20fs, 16670 cm^{-1} excitation and detection pulses. The increase in signal amplitude at long delay times is a signature of electron transfer from PNDT-DTPyT to PCBM. Panels (a) and (b) display the same data on two different time scales. Fitting parameters are given in Table 6.4. Fits are displayed in Figure A5.14 of Appendix 5.

Table 6.4. Transient absorption fitting parameters for blends of PNDT-DTPyT and PCBM

[a]Parameter	10:1	2:1	1:1
A_1	0.49 ± 0.01	0.47 ± 0.02	0.56 ± 0.02
τ_1/ps	0.100 ± 0.02	0.13 ± 0.05	0.060 ± 0.02
A_2	0.30 ± 0.01	0.25 ± 0.02	0.203 ± 0.006
τ_2/ps	0.720 ± 0.04	0.56 ± 0.06	0.56 ± 0.03
A_3	0.18 ± 0.01	0.19 ± 0.02	0.099 ± 0.006
τ_3/ps	7.8 ± 0.8	4.0 ± 0.5	7 ± 1
A_4	$0.030 \pm 0.002*$	$0.092 \pm 0.005*$	0.14 ± 0.02
τ_4/ps	∞	∞	200 ± 60

[a] Parameters of Equation 6.4.

Fluorescence quenching measurements are conducted on the composite films to confirm the interpretation of TG signals. Experiments on similar BHJ materials identify fluorescence quenching as a signature of non-radiative relaxation caused by electron transfer to PCBM.[86,91,92] We quantify the effect of charge separation on fluorescence quantum yield, Q_C, as

$$Q_C = \frac{I_C}{I_0} \tag{6.7}$$

where I_C is the integrated fluorescence intensity for a film with concentration C. Of course, minor differences in optical densities of the films are taken into account when computing Q_C. The results are normalized to the signal intensity acquired for the pure polymer film, I_0. As expected, Figure 6.9 shows that the amount of fluorescence decreases with increasing PCBM concentration. The opposing trend found in the TG signal amplitude in Figure 6.8 suggests that these two measurements interrogate the same process from different perspectives. The decrease in the number of (emitting) photoexcitations in the PNDT-DTPyT domain occurs

concomitant with an increase in the concentration of the positive (PNDT-DTPyT$^+$) and negative (PCBM$^-$) polarons.
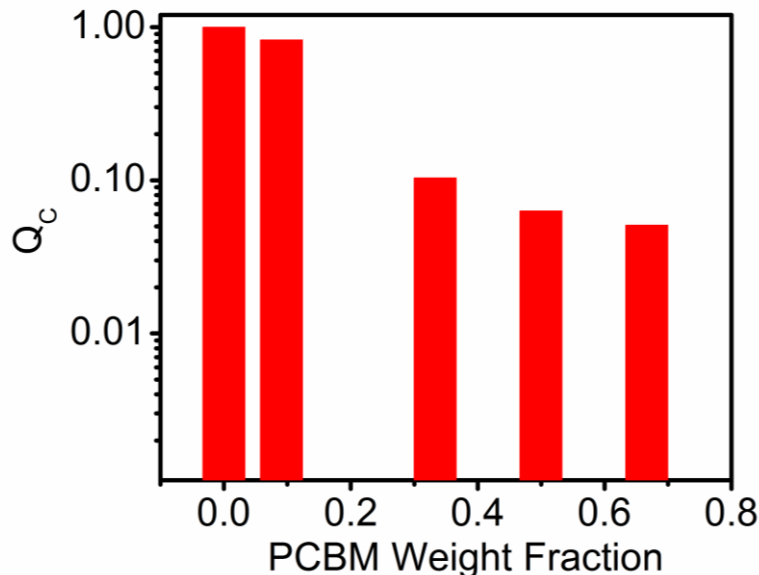
Figure 6.9: Signature of charge separation obtained from fluorescence quenching experiments. Charge separation causes a decrease in the fluorescence quantum yield, Q_C, defined by Equation 6.7.

Current-voltage curves measured for selected PNDT-DTPyT/PCBM films are shown in Figure 6.10 and summarized in Table 6.5. As the PCBM concentration increases from a weight fraction of 0.09 to 0.5, the overall power conversion efficiency of the film increases from 0.25% to 4.08%. This improvement in efficiency originates in a decrease in the average interfacial distance between PCBM domains. With a shorter distance to travel, a greater fraction of the photoexcitations in the polymer domain is able to diffuse to an interface with PCBM and undergo electron transfer, thereby increasing the charge carrier density and overall power conversion efficiency. The TG signals and fluorescence quenching experiments are also sensitive to this aspect of the film morphology. The measured device

efficiencies reveal a maximum at a weight fraction of 0.5. The suppression in device efficiency observed at larger PCBM concentrations may be caused by sparse hole percolation pathways in the polymer domain (i.e., poor hole mobility). Further insight into this behavior is a goal of ongoing work.
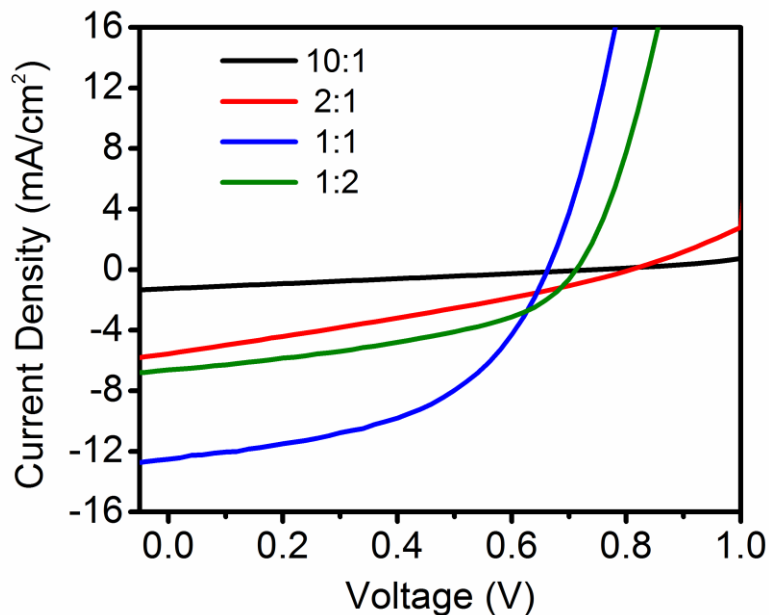
Figure 6.10: Current-Voltage curves measured for BHJ devices consisting of different PNDT-DTPyT:PCBM weight ratios. Data was obtained while illuminating the films with simulated natural sunlight (100 mW/cm^2).

Table 6.5. Photovoltaic performance of PNDT-DTPyT/PCBM bulk heterojunction devices at various PCBM concentrations.

Polymer/ PCBM	[a]V_{oc} (V)	[b]J_{sc} (mA/cm^2)	[c]FF	[d]η (%)
10:1	0.75	1.25	0.25	0.25
2:1	0.81	5.56	0.28	1.3
1:1	0.67	12.51	0.49	4.08
1:1.5	0.75	10.78	48.3	3.91
1:2	0.71	6.63	43.9	2.05

(a) Open circuit voltage

(b) Short circuit current.

(c) Fill factor

(d) Power conversion efficiency

6.4. CONCLUSION

In summary, several spectroscopic experiments have been used to investigate fundamental photophysics in films composed of a pure polymer, PNDT-DTPyT, and mixtures of PNDT-DTPyT with PCBM. PNDT-DTPyT is a newly synthesized polymer whose small band gap is tuned for optimal photovoltaic performance. The present study reaches five main conclusions. First, the analysis of steady state spectroscopic line shapes suggests that the electronic excitations are localized to fairly small segments of the polymer. Figure 6.4 shows that the distribution in segment sizes is estimated by a log-normal function with a mean of 1.4 segments and a standard deviation of 1.2. Second, the lowest energy electronic transition, which possesses charge transfer characteristics, induces significant nuclear relaxation in the surrounding environment. A reorganization energy of 800cm^{-1} is calculated using the fluorescence line width; this estimate is also consistent with the frequency difference between the peaks of the absorption and fluorescence spectra. Third, TG spectroscopy for the pure polymer detects two energy transfer processes occurring on time scales of approximately 1 ps and 10 ps (cf., Figures 6.5 and 6.6). We hypothesize that

distinct geometries underlie this difference in rates. For example, it may be that the two processes reflect energy transfer between stacked and non-stacked neighbors. Observation of a change in the relative amplitudes of the two decay processes in the TG profiles for films containing various degrees of crystallinity may prove useful for resolving this issue. Experiments on another conjugated polymer find that altering synthetic procedures (e.g. spin casting rate, solvent, etc.) can have a significant effect on the amount of crystallinity in polymer films.[93,94] Fourth, signatures of charge separation are observed with TG spectroscopy at delay times as early as 500fs. It should be noted that electron transfer on this time scale has been observed in related systems.[50,61,66,81,86,87,89,90,95] Fifth, Figures 6.8 and 6.9 show that both fluorescence quenching and TG spectroscopy observe an increase in charge separation efficiency with increasing PCBM concentration. This increase in charge separation is attributed to a reduction in the average distance between PCBM domains, which in turn suppresses the radiative deactivation of photoexcitations in the polymer domains. Power conversion efficiencies measured for these films are consistent with this interpretation.

Ideally, the microscopic information obtained in this study will inform the optimization of devices utilizing PNDT-DTPyT. Of course, it was clear *a priori* that the small band gap of PNDT-DTPyT is advantageous for solar light harvesting. As shown in Figure 6.1, the electronic structure is engineered using donor and acceptor moieties whose overlapping orbitals give rise to a low frequency charge transfer transition. One main conclusion of this work is that the increase in the dipole moment associated with this charge transfer transition drives significant reorganization in the surrounding environment (i.e., large reorganization energy). This substantial nuclear reorganization energy, in turn, limits the exciton size (cf., Figure 6.4) and may suppress energy transport. Future work will investigate

the prospect that exciton diffusion in PNDT-DTPyT (or related systems) can overcome undesired effects associated with strong vibronic coupling through the control of film morphology and/or alteration of functional groups in the polymer. Recent work by one of our groups suggests that side-chains can be leveraged to enhance photovoltaic performance.[28]

6.5. REFERENCES

(1)   Cheng, Y.-J.; Yang, S.-H.; Hsu, C.-S. *Chem. Rev.* 2009, *109*, 5868-5923.

(2)   Chen, J.; Cao, Y. *Acc. Chem. Res.* 2009, *42*, 1709-1718.

(3)   Piliego, C.; Holcombe, T. W.; Douglas, J. D.; Woo, C. H.; Beaujuge, P. M.; Fréchet, J. M. J. *J. Am. Chem. Soc.* 2010, *132*, 7595-7597.

(4)   Liang, Y.; Yu, L. *Acc. Chem. Res.* 2010, *43*, 1227.

(5)   Liang, Y.; Xu, Z.; Xia, J.; Tsai, S.-T.; Wu, Y.; Li, G.; Ray, C.; Yu, L. *Adv. Mat.* 2010, *22*, E135-E138.

(6)   Chen, H.-Y.; Hou, J.; Zhang, S.; Liang, Y.; Yang, G.; Yang, Y.; Yu, L.; Wu, Y.; Li, G. *Nature Photonics* 2009, *3*, 649-653.

(7)   Park, S. H.; Roy, A.; Beaupré, S.; Cho, S.; Coates, N.; Moon, J. S.; Moses, D.; Leclerc, M.; Lee, K.; Heeger, A. J. *Nature Photonics* 2009, *3*, 297-302.

(8)   Chen, Y.-C.; Yu, C.-Y.; Fan, Y.-L.; Hung, L.-I.; Chen, C.-P.; C., T. *Chem. Comm.* 2010, *46*, 6503-6505.

(9)   Zhou, H.; Yang, L.; Price, S. C.; Knight, K. J.; You, W. *Angew. Chem., Int. Ed.* 2010, *49*, 7992-7995.

(10)   Clarke, T. M.; Durrant, J. R. *Chem. Rev.* 2010, *110*, 6736.

(11)   Groves, C.; Reid, O. G.; Ginger, D. S. *Acc. Chem. Res.* 2010, *43*, 612-620.

(12)   Thompson, B. C.; Fréchet, J. M. J. *Angew. Chem. Int. Ed.* 2008, *47*, 58-77.

(13)   Koster, L. J. A.; Mihailetchi, V. D.; Blom, P. W. M. *Appl. Phys. Lett.* 2006, *88*, 093511.

(14)   Scharber, M. C.; Mühlbacher, D.; Koppe, M.; Denk, P.; Waldauf, C.; Heeger, A. J.; Brabec, C. J. *Adv. Mat.* 2006, *18*, 789-794.

(15)   Veldman, D.; Ipek, O.; Meskers, S. C. J.; Sweelssen, J.; Koetse, M. M.; Veenstra, S. C.; Kroon, J. M.; Bavel, S. S. v.; Loos, J.; Janssen, R. A. J. *J. Am. Chem. Soc.* 2008, *130*, 7721-7735.

(16)   Clarke, T. M.; Ballantyne, A.; Jamieson, F.; Brabec, C.; Nelson, J.; Durrant, J. R. *Chem. Comm.* 2008, 89-91.

(17)   Hwang, I. W.; Soci, C.; Moses, D.; Zhu, Z.; Waller, D.; Gaudiana, R.; Brabec, C.; Heeger, A. *Adv. Mat.* 2007, *19*, 2307-2312.

(18)   Ohkita, H.; Cook, S.; Astuti, Y.; Duffy, W.; Tierney, S.; Zhang, W.; Heeney, M.; McCulloch, I.; Nelson, J.; Bradley, D. D. C.; Durrant, J. R. *J. Am. Chem. Soc.* 2008, *130*, 3030-3042.

(19)   Dennler, G.; Scharber, M. C.; Brabec, C. J. *Adv. Mat.* 2009, *21*, 1323-1338.

(20)   Piris, J.; Dykstra, T. E.; Bakulin, A. A.; Loosdrecht, P. H. M. v.; Knulst, W.; Trinh, M. T.; Schins, J. M.; Siebbeles, L. D. A. *J. Phys. Chem. C* 2009, *113*, 14500-14506.

(21)   Blom, P. W. M.; Mihailetchi, V. D.; Koster, L. J. A.; Markov, D. E. *Adv. Mat.* 2007, *19*, 1551-1566.

(22)   Pensack, R. D.; Asbury, J. B. *J. Am. Chem. Soc.* 2009, *131*, 15986-15987.

(23)   Zhou, H.; Yang, L.; Stoneking, S.; You, W. *ACS Applied Materials & Interfaces* 2010, *2*, 1377-1383.

(24)   Price, S. C.; Stuart, A. C.; You, W. *Macromolecules* 2010, *43*, 4609-4612.

(25)   Zhou, H.; Yang, L.; Xiao, S.; Liu, S.; You, W. *Macromolecules* 2010, *43*, 811-820.

(26)   Havinga, E. E.; Tenhoeve, W.; Wynberg, H. *Synth. Met.* 1993, *55-57*, 299-306.

(27)   Ajayaghosh, A. *Chem. Soc. Rev.* 2003, *32*, 181-191.

(28)   Yang, L.; Zhou, H.; You, W. *J. Phys. Chem. C* 2010, *114*, 16793.

(29)   van Mullekom, H. A. M.; Vekemans, J. A. J. M.; Havinga, E. E.; Meijer, E. W. *Mater. Sci. Eng., R.* 2001, *32*, 1-40.

(30)   Förster, T. *Ann. Physik* 1948, *437*, 55-75.

(31)   Dogariu, A.; Gupta, R.; Heeger, A. J.; Wang, H. *Synth. Met.* 1999, *100*, 95-100.

(32)   van Amerongen, H.; Valkunas, L.; van Grondelle, R. *Photosynthetic Excitons*; World Scientific: Singapore, 2000.

(33)   Wohlgenannt, M.; Graupner, W.; Wenzel, F. P.; Tasch, S.; List, E. J. W.; Leising, G.; Graupner, M.; Hermetter, A.; Rohr, U.; Schlichting, P.; Geerts, Y.; Scherf, U.; Müllen, K. *Chem. Phys.* 1998, *227*, 99-109.

(34)   Schwartz, B. J. *Annu. Rev. Phys. Chem.* 2003, *54*, 141-172.

(35)   Schwartz, B. J.; Nguyen, T. Q.; Wu, J.; Tolbert, S. H. *Synth. Met.* 2001, *116*, 35-40.

181

(36)   Beljonne, D.; Pourtois, G.; Silva, C.; Hennebicq, E.; Herz, L. M.; Friend, R. H.; Scholes, G. D.; Setayesh, S.; Müllen, K.; Brédas, J. L. *Proc. Natl. Acad. Sci.* 2002, *99*, 10982-10987.

(37)   Hennebicq, E.; Pourtois, G.; Scholes, G. D.; Herz, L. M.; Russell, D. M.; Silva, C.; Setayesh, S.; Grimsdale, A. C.; Müllen, K.; Brédas, J.-L.; Beljonne, D. *J. Am. Chem. Soc.* 2005, *127*, 4744-4762.

(38)   Averbeke, B. V.; Beljonne, D. *J. Phys. Chem. A* 2009, *113*, 2677-2682.

(39)   Wells, N. P.; Boudouris, B. W.; Hillmyer, M. A.; Blank, D. A. *J. Phys. Chem. C* 2007, *111*, 15404-15414.

(40)   Collini, E.; Scholes, G. D. *Science* 2009, *323*, 369-373.

(41)   Scholes, G. D. *Annu. Rev. Phys. Chem.* 2003, *54*, 57-87.

(42)   Nguyen, T.-Q.; Wu, J.; Doan, V.; Schwartz, B. J.; Tolbert, S. H. *Science* 2000, *288*, 652-656.

(43)   Ahn, T.-S.; Wright, N.; Bardeen, C. J. *Chem. Phys. Lett.* 2007, *446*, 43-48.

(44)   Gaab, K. M.; Bardeen, C. J. *J. Phys. Chem. B* 2004, *108*, 4619-4626.

(45)   Lammi, R. K.; Barbara, P. F. *Photochem. Photobiol. Sci.* 2005, *4*, 95-99.

(46)   Wells, N. P.; Blank, D. A. *Phys. Rev. Lett.* 2008, *100*, 086403-086401-086404.

(47)   Vardeny, Z. V., Ed. Ultrafast Dynamics and Laser Action of Organic Semiconductors; CRC Press: Boca Raton, 2009.

(48)   Milota, F.; Sperling, J.; Szocs, V.; Tortschanoff, A.; Kauffmann, H. F. *J. Chem. Phys.* 2004, *120*, 9870-9885.

(49)   Sperling, J.; Benesch, C.; Kuna, L.; Kauffmann, H. F.; Milota, F. *Synth. Met.* 2004, *143*, 315-322.

(50)   Pensack, R. D.; Asbury, J. B. *J. Phys. Chem. Lett.* 2010, *1*, 2255-2263.

(51)   Gaab, K. M.; Bardeen, C. J. *J. Phys. Chem. A* 2004, *121*, 10801-10806.

(52)   Womick, J. M.; Miller, S. A.; Moran, A. M. *J. Phys. Chem. B* 2009, *113*, 6630-6639.

(53)   Womick, J. M.; Miller, S. A.; Moran, A. M. *J. Phys. Chem. A* 2009, *113*, 6587-6598.

(54)   Miller, S. A.; Moran, A. M. *J. Chem. Phys. A* 2010, *114*, 2117-2126.

(55)   Lepetit, L.; Chériaux, G.; Joffre, M. *J. Opt. Soc. Am. B* 1995, *12*, 2467-2474.

(56)   Gallagher, S. M.; Albrecht, A. W.; Hybl, J. D.; Landin, B. L.; Rajaram, B.; Jonas, D. M. *J. Opt. Soc. Am. B* 1998, *15*, 2338-2345.

(57)   Jonas, D. M. *Annu. Rev. Phys. Chem.* 2003, *54*, 425-463.

(58)   Skotheim, T. A., Reynolds, J. R., Ed. *Conjugated Polymers: Theory, Synthesis, Properties, and Characterization*; CRC Press: Taylor and Francis Group: Boca Raton, 2007.

(59)   Mukamel, S. *Principles of Nonlinear Optical Spectroscopy*; Oxford University Press: New York, 1995.

(60)   Grage, M. M.-L.; Zaushitsyn, Y.; Yartsev, A.; Chachisvilis, M.; Sundström, V.; Pullerits, T. *Phys. Rev. B.* 2003, *67*.

(61)   Xie, Y.; Li, Y.; Xiao, L.; Qiao, Q.; Dhakal, R.; Zhang, Z.; Gong, Q.; Galipeau, D.; Yan, X. *J. Phys. Chem. C* 2010, *114*, 14590.

(62)   Beenken, W. J. D.; Pullerits, T. *J. Phys. Chem. B* 2003, *108*, 6164-6169.

(63)   Tretiak, S.; Saxena, A.; Martin, R. L.; Bishop, A. R. *Phys. Rev. Lett.* 2002, *89*, 097402-097401-097404.

(64)   Ruseckas, A.; Wood, P.; Samuel, I. D. W.; Webster, G. R.; Mitchell, W. J.; Burn, P. L.; Sundström, V. *Phys. Rev. B* 2005, *72*, 115214-115211-115215.

(65)   Yang, X.; Dykstra, T. E.; Scholes, G. D. *Phys. Rev. B* 2005, *71*, 045203.

(66)   Kraabel, B.; Hummelen, J. C.; Vacar, D.; Moses, D.; Sariciftci, N. S.; Heeger, A. J.; Wudl, F. *J. Chem. Phys.* 1996, *104*, 4267-4273.

(67)   Bakulin, A. A.; Hummelen, J. C.; Pshenichnikov, M. S.; van Loosdrecht, P. H. M. *Adv. Funct. Mater.* 2010, *20*, 1653-1660.

(68)   Kraabel, B.; Klimov, V. I.; Kohlman, R.; Xu, S.; Wang, H.-L.; McBranch, D. W. *Phys. Rev. B.* 2000, *61*, 8501-8515.

(69)   Xu, Q.-H.; Moses, D.; Heeger, A. J. *Phys. Rev. B.* 2003, *68*, 174303-174301-174305.

(70)   Nelson, J. Curr. Opin. Solid State Mat. Sci. 2002, 6, 87-95.

(71)   Halls, J. J. M.; Pichler, K.; Friend, R. H.; Moratti, S. C.; Holmes, A. B. *Appl. Phys. Lett.* 1996, *68*, 3120-3122.

(72)   Yang, C. L.; Tang, Z. K.; Ge, W. K.; Wang, J. N.; Zhang, Z. L.; Jian, X. Y. *Appl. Phys. Lett.* 2003, *83*, 1737.

183

(73)   Terao, Y.; Sasabe, H.; Adachi, C. *Appl. Phys. Lett.* 2007, *90*, 103515.

(74)   Markov, D. E.; Amsterdam, E.; Blom, P. W. M.; Sieval, A. B.; Hummelen, J. C. *J. Phys. Chem. A* 2005, *109*, 5266-5274.

(75)   Markov, D. E.; Tanase, C.; Blom, P. W. M.; Wildeman, J. *Phys. Rev. B* 2005, *72*, 045217-045211-045216.

(76)   Scully, S. R.; McGehee, M. D. *J. Appl. Phys.* 2006, *100*, 034907-034901-034905.

(77)   Stübinger, T.; Brütting, W. *J. Appl. Phys.* 2001, *90*, 3632-3641.

(78)   Hoppe, H.; Sariciftci, N. S. *J. Mater. Chem.* 2006, *16*, 45-61.

(79)   Martinson, A. B. F.; Massari, A. M.; Lee, S. J.; Gurney, R. W.; Splan, K. E.; Hupp, J. T.; Nguyen, S. T. *J. Electrochem. Soc.* 2006, *153*, A527-A532.

(80)   Eigner, A. A.; Konold, P. E.; Massari, A. M. *J. Phys. Chem. B* 2009, *113*, 14549-14554.

(81)   Vacar, D.; Maniloff, E. S.; McBranch, D. W.; Heeger, A. J. *Phys. Rev. B.* 1997, *56*, 4573-4577.

(82)   Moses, D.; Dogariu, A.; Heeger, A. J. *Phys. Rev. B* 2000, *61*, 9373-9379.

(83)   Müller, J. G.; Lupton, J. M.; Feldmann, J.; Lemmer, U.; Scharber, M. C.; Sariciftci, N. S.; Brabec, C. J.; Scherf, U. *Phys. Rev. B* 2005, *72*, 195208-195201-195209.

(84)   Guldi, D. M.; Prato, M. *Acc. Chem. Res.* 2000, *33*, 695-703.

(85)   Yamamoto, S.; Guo, J.; Ohkita, H.; Ito, S. *Adv. Funct. Mater.* 2008, *18*, 2555-2562.

(86)   Sariciftci, N. S.; Smilowitz, L.; Heeger, A. J.; Wudl, F. *Science* 1992, *258*, 1474-1476.

(87)   Martini, I. B.; Ma, B.; Da Ros, T.; Helgeson, R.; Wudl, F.; Schwartz, B. J. *Chem. Phys. Lett.* 2000, *327*, 253-262.

(88)   Pensack, R. D.; Banyas, K. M.; Asbury, J. B. *J. Phys. Chem. C* 2010, *114*, 5344-5350.

(89)   Brabec, C. J.; Zerza, G.; Cerullo, G.; De Silvestri, S.; Luzzati, S.; Hummelen, J. C.; Sariciftci, S. *Chem. Phys. Lett.* 2001, *340*, 232-236.

(90)   Guo, J.; Ohkita, H.; Benten, H.; Shinzaburo, I. *J. Am. Chem. Soc.* 2010, *132*, 6154-6164.

(91)   Wienk, M. M.; Struijk, M. P.; Janssen, R. A. J. *Chem. Phys. Lett.* 2006, *422*, 488-491.

(92)   Ayzner, A. L.; Tassone, C. J.; Tolbert, S. H.; Schwartz, B. J. *J. Phys. Chem. C* 2009, *113*, 20050-20060.

(93)   Craig, I. M.; Tassone, C. J.; Tolbert, S. H.; Schwartz, B. J. *J. Chem. Phys.* 2010, *133*, 044901.

(94)   Clark, J.; Chang, J.-F.; Spano, F. C.; Friend, R. H.; Silva, C. *Appl. Phys. Lett.* 2009, *94*, 163306.

(95)   Moses, D.; Dogariu, A.; Heeger, A. J. *Chem. Phys. Lett.* 2000, *316*.

CHAPTER 7 . NONLINEAR OPTICAL DETECTION OF ELECTRON TRANSFER

ADIABATICITY IN METAL POLYPYRIDYL COMPLEXES

7.1. INTRODUCTION

Condensed phase electron transfer (ET) processes abound in biology and modern technologies.[1-5] The importance of charge separation to the production of solar fuels is principal among the motivations for understanding the physics of ET.[6,7] Numerous theoretical and experimental studies of ET dynamics have been performed over many years yet the understanding of dynamical solvent effects has remained elusive due to the complexity of solute-solvent interactions.[8-13] In the nonadiabatic limit, solvation dynamics are taken to occur on a time scale much faster than ET and play no role in rate determination, whereas reaction adiabaticity arises for systems in which ET and solvent motion occur on comparable time scales. The central challenge in studying ET adiabaticity is separating the contributions of solvation dynamics from aspects of the (static) free energy surfaces controlling ET kinetics in nonadiabatic rate formulas.[14-17] That is, solvents with different relaxation time scales also generally possess free energy surfaces with different energy gaps and/or curvatures. This issue is not only of fundamental interest. Research aiming to control photoinduced dynamics by embedding chemical constituents in rigid media may benefit from further understanding of ET adiabaticity.[18,19]

Kramers' theory of condensed phase chemical dynamics establishes a physical picture of how ET adiabaticity emerges in condensed phases.[20] Kramers' model interpolates

between regimes distinguished by the magnitude of friction imposed on reaction trajectories by solute-solvent interactions.[21,22] In the limit of small friction, the solvent imparts the kinetic energy needed for a reaction trajectory to overcome an activation energy barrier. The rate scales linearly with friction in this regime.[23,24] However, the solvent impedes reactions and the dynamics become diffusive with high friction. The intermediate point at which the role of friction changes from promoting a rate increase to a rate decrease is known as the Kramers turnover.[25-27] For ET reactions, the nonadiabatic rate constant, k_{na}, is corrected for the regime of high friction with an adiabaticity parameter, v_{ad}, using

$$k_{ad} = \frac{k_{na}}{1+v_{ad}} \tag{7.1}$$

where

$$v_{ad} = \frac{\tau_{total}}{\hbar} \sqrt{\frac{\pi V^4}{\lambda k_B T}} \tag{7.2}$$

The donor-acceptor coupling strength V, solvent reorganization energy λ, and solvation time scale τ_{total} contribute to v_{ad}. The parameters, λ and τ_{total}, are taken to be associated with the solvent here but in fact they can also represent low frequency (compared to $k_B T$) intramolecular motion coupled to the electron transfer transition. Chapter 7.2.1 makes clear that these two parameters must be defined with respect to a common nuclear coordinate. Experiments designed to parameterize Equation 7.2 are not necessarily easy to implement. For example, the time scale of solvation is most readily obtained by time resolved fluorescence Stokes shift measurements, which can be quite challenging for systems with small extinction coefficients and/or low emission quantum yields.[28] In this regard, the

development of readily applied experimental techniques sensitive to the nature of electronic structure and dynamics are of significant value.

In this investigation, femtosecond laser spectroscopies are used to investigate photoinduced relaxation dynamics and ET adiabaticity in the prototypical metal polypyridal complex, $Os^{II}(bpy)_3$. The absorption spectrum of $Os^{II}(bpy)_3$ (Figure 7.1) exhibits a broad line shape extending from 500-700 nm, which represents resonances with metal-to-ligand charge transfer (MLCT) excited states possessing mixed singlet and triplet spin multiplicity.[29-31] It is thought that one of the four MLCT transitions associated with each ligand dominates the optical response of $Os^{II}(bpy)_3$ because its oscillator strength is large compared to the other three transitions. Thus, for the purposes of the present investigation, we will assume that one MLCT transition is associated with each ligand. The interpretation of earlier spectroscopic studies supports this viewpoint.[32-34] The central issue we address here is the adiabaticity of interligand ET transitions occurring subsequent to photoexcitation. In particular, we aim to understand the wavefunction compositions of the MLCT states. Delocalized (adiabatic) MLCT states take hold when interligand couplings are large compared to system-bath interaction strengths, whereas diabatic states are the most appropriate basis when the MLCT wavefunctions contract to the individual ligands. The important general contribution of the present study is a model for clearly distinguishing the optical nonlinearities corresponding to adiabatic and nonadiabatic ET regimes.
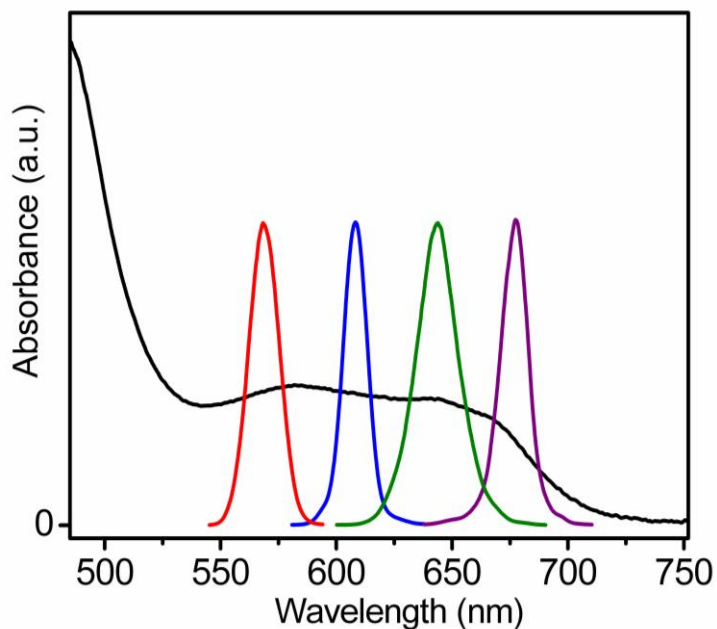
Figure 7.1: Absorbance spectrum of $Os^{II}(bpy)_3$ overlaid with spectra of laser pulses used in time-resolved experiments.

Below we identify terms in the nonlinear response function allowed and forbidden with adiabatic and diabatic bases. It is suggested that the key difference in nonlinearities for these two regimes of ET derives from the contributions of interligand couplings to the Hamiltonian. Here the zeroeth order non-perturbative component of the Hamiltonian, $H^{(0)}$, is defined in the basis of (diabatic) ligand sites. In this basis, the nonadiabtic rate formula describes how the (perturbative) interligand coupling, H', promotes non-radiative transitions between electronic states localized to the individual ligands. By contrast, ET adiabaticity implies that H' is too large to be taken as a perturbation. For systems in which ET is adiabatic, the zeroeth order states giving rise to the optical response must be defined with respect to the full system Hamiltonian, $H^{(0)} + H'$. The size of H' (compared to the system-bath interaction strength) not only decides the extent to which electronic states are

189

delocalized between ligands, but also controls which classes of terms in the response function are allowed to radiate signals. The following section discusses how the contribution of a particular group of coherent "cross-terms" increases with the reaction adiabaticity. Careful analysis of these terms leads to well-defined spectroscopic signatures sensitive to ET adiabaticity.

Many aspects of $Os^{II}(bpy)_3$ important to the present investigation were examined by Papanikolas and co-workers using pump-probe spectroscopies.[33,34] This prior work found that excitation of the low energy portion of the absorption spectrum (at 693 nm) populates MLCT excited states who undergo interligand electron transfer processes with a time constants of 7.8 ps. Both pump-probe experiments and molecular dynamics simulations were used to address the nature of the MLCT excited states. These data suggested that strong system-bath interactions in the ground state promote significant heterogeneity in the energies of the MLCT states, which in turn localizes the excited state wavefunctions to the individual ligands. Signatures of ET adiabaticity were detected with measurements comparing interligand electron transfer dynamics in solutions with acetonitrile and ethylene glycol solvents. Much is owed to this earlier work in setting up the framework for the present investigation, which obtains additional insight with a 22-fold increase in time-resolution and the use of different experimental techniques. Improved time-resolution provides better information on the excited state composition at the instant of photon absorption.

7.2. THEORY

7.2.1 Background on Electron Transfer Adiabaticity

The origin of electron transfer (ET) adiabaticity is made clear by considering the perturbative expansion of the rate with respect to the coupling between diabatic states[35]

$$K = V^2 C_2 + V^4 C_4 + \cdots \qquad (7.3)$$

The coefficients, C_2 and C_4, are two-time and four-time correlation functions of the coupling, V. A unified view of ET dynamics and optical nonlinearities gives insight into the nature of these terms.[13] C_2 is closely related to the linear absorption line shapes, whereas C_4 can be understood in terms of the correlation functions controlling four-wave mixing processes (e.g., fluorescence, Raman, pump-probe). Odd-ordered terms represent pathways terminating in the transition state and do not contribute to Equation 7.3. The expansion is truncated at the leading term in the nonadiabatic limit, which essentially means that all reaction trajectories reaching the transition state form products. The nonadiabatic limit is subject to a paradox in which solvent friction is fully neglected at the transition state, whereas kinetic energy dissipates instantaneously upon product formation.[22] By contrast, C_4 accounts for the finite time scale of nuclear motion coupled to the ET transition. The reaction adiabaticity of Equation 7.1 is obtained by resummation of the terms higher than second order in Equation 7.3.[13,35-37] Sparpaglione and Mukamel derived a formula for v_{ad} that is exact in the slow modulation limit of system-bath interactions; this resummation is therefore better-defined than the resummation found with the Landau-Zener expression.[35] The adiabaticity associated with ET between states a and b is written with respect to τ_{total},

which represents the sum of the time constants associated with relaxation in the free energy

wells, a and b (i.e., $\tau_{total} = \tau_a + \tau_b$).[13] The relaxation time for free energy well a is given by

$$\tau_a = \exp\left(\frac{-q_a^2}{2}\right)\int_0^\infty dt\left\{\frac{1}{\sqrt{1-M^2(t)}}\exp\left(\frac{q_a^2 M(t)}{1+M(t)}\right)-1\right\} \tag{7.4}$$

where $M(t)$ is a solvation correlation function and q_a^2 is defined as

$$q_a^2 = \frac{\left(\delta G^0 + \lambda\right)^2}{2\lambda k_B T} \tag{7.5}$$

The parameters of Equation 7.5 involved in interligand ET of $Os^{II}(bpy)_3$ have been obtained

by earlier investigations.[32-34] The free energy gap, δG^0, is zero by symmetry, whereas the

reorganization energy, λ, is approximately 3500 cm^{-1}. The solvation correlation function

$M(t)$ for $Os^{II}(bpy)_3$ in acetonitrile has not been measured. However, multiple experimental

investigations, including the study of the closely related compound $Ru^{II}(bpy)_3$,[38,39] find that

the time scale of polar solvation dynamics for coumarin in acetonitrile provides a reasonable

estimate.[40] We therefore assume this correlation function in the following calculation.

Figure 7.2 displays the dependence of τ_a and ν_{ad} on the reorganization energy, where we

find that $\nu_{ad} < 4.6$ in the range $\lambda = 1800\text{-}4700$ cm^{-1} considered in earlier work.[34] At the value

of the reorganization energy used in Figure 16 of Reference 34, $\lambda = 3500$ cm^{-1}, the

adiabaticity parameter and relaxation time are 2.3 and 290 fs, respectively. The main

conclusion to be drawn from this calculation is that while the effects of adiabaticity are

certainly measurable, it is of only minor importance to the interligand ET rate for $Os^{II}(bpy)_3$

in acetonitrile. Several recent investigations of ET adiabaticity have found ν_{ad} parameters

with similar magnitudes.[15-17]   The next two sections obtain expressions for the transient

absorption anisotropy that will discern whether or not $Os^{II}(bpy)_3$ has an optical nonlinearity

characteristic of a diabatic or adiabatic basis.
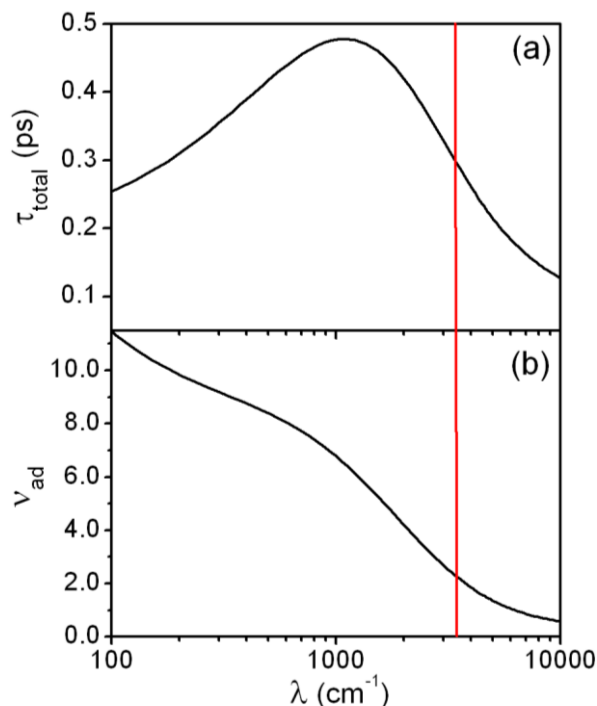
Figure 7.2 (a) Time scale of solvent relaxation calculation with Equation 7.4, τ_a. (b)
Electron transfer adiabaticity, ν_{ad}, obtained with Equation 7.2.

7.2.2 Transient Absorption Anisotropy in the Diabatic Basis

The nonlinear optical response of $Os^{II}(bpy)_3$ has previously been treated in a diabatic

basis to model pump-probe experiments in which excited state absorption was the dominant

signal generation mechanism.[32-34]   Here we generalize this model to incorporate the ground

state bleach (GSB) and excited state emission (ESE) signal components because their

contributions are not negligible in the present experiments.   In the diabatic basis, the

nonlinear optical response views $Os^{II}(bpy)_3$ as three weakly coupled three-level systems

(Figure 7.3). This model assumes that the couplings are weak compared to the system-bath interaction strength and can therefore be treated as a perturbation governing ET kinetics (i.e., nonadiabatic rate formula). Thus, the zeroeth order states participating in both radiative and non-radiative transitions are localized to the individual ligands.

Figure 7.3 shows how the transition dipoles of the MLCT transitions project onto the structure of $Os^{II}(bpy)_3$ in the diabatic basis. We emphasize that our experimental configuration excites and probes only in the spectral region corresponding to the triplet MLCT states. Our model therefore neglects the manifold of higher energy singlet MLCT states. The transition dipoles connecting the ground state to the MLCT excited states, μ_{ge}, are collinear with the axes joining the Os atoms to the bonds between aromatic rings of the bipyridine ligands. These are the dipoles with which the first two "pump" fields interact with in the experiment. The probe field can again interact with the "pumped' μ_{ge} dipole to generate a bleach response (i.e., either ground state bleach or excited state emission). Alternatively, the probe field interacts with the μ_{ef} transition dipole of the electronically excited ligand, which is oriented at 90 degrees with respected to the corresponding μ_{ge} dipole. We will hereafter refer to this excited state transition as absorption of the bipyridine radical.
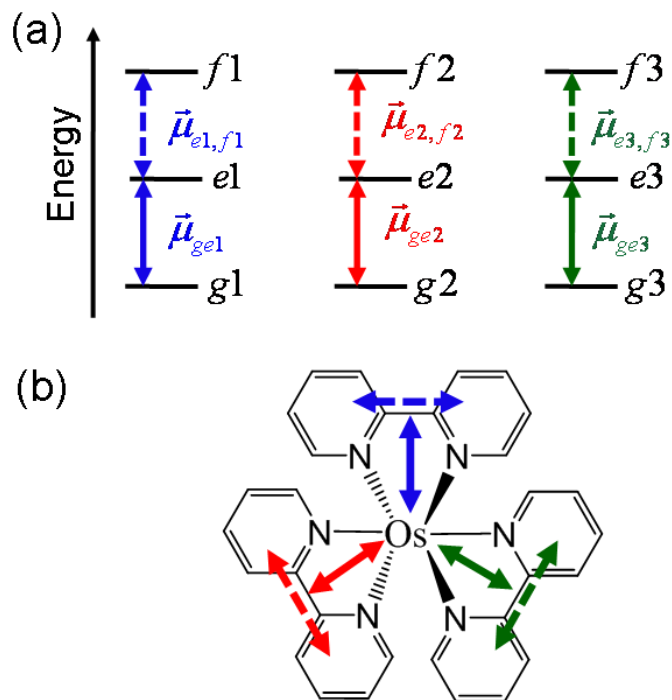
Figure 7.3: (a) The diabatic basis associates a three-level system with each ligand. Couplings, J_e and J_f, are perturbations that do not influence optical resonance frequencies or transition dipoles. (b) Transition dipoles overlaid on structure of $Os^{II}(bpy)_3$.

Feynman diagrams representing all terms in the response function are presented in Figure 7.4. The terms in the response function partition as follows: R_3 and R_4 represent the ground state bleach (GSB); R_1, R_2, $^{IC}R_1$ and $^{IC}R_2$ represent excited state emission (ESE); $R_1{}^*$, $R_2{}^*$, $^{IC}R_1{}^*$ and $^{IC}R_2{}^*$ represent excited state absorption (ESA).[41] The important aspect of the nonadiabatic response is that, with the exception of the "incoherent" terms (i.e., IC terms in the bottom row), $Os^{II}(bpy)_3$ behaves as three completely independent three-level systems. This neglect of interligand coupling in the zeroeth order Hamiltonian imposes restrictions on the nonlinearity: terms in the first two rows of Figure 7.4 with $a \neq b$ are forbidden; the index c in $R_1{}^*$, $R_2{}^*$, $^{IC}R_1{}^*$ and $^{IC}R_2{}^*$ represents only excited states localized
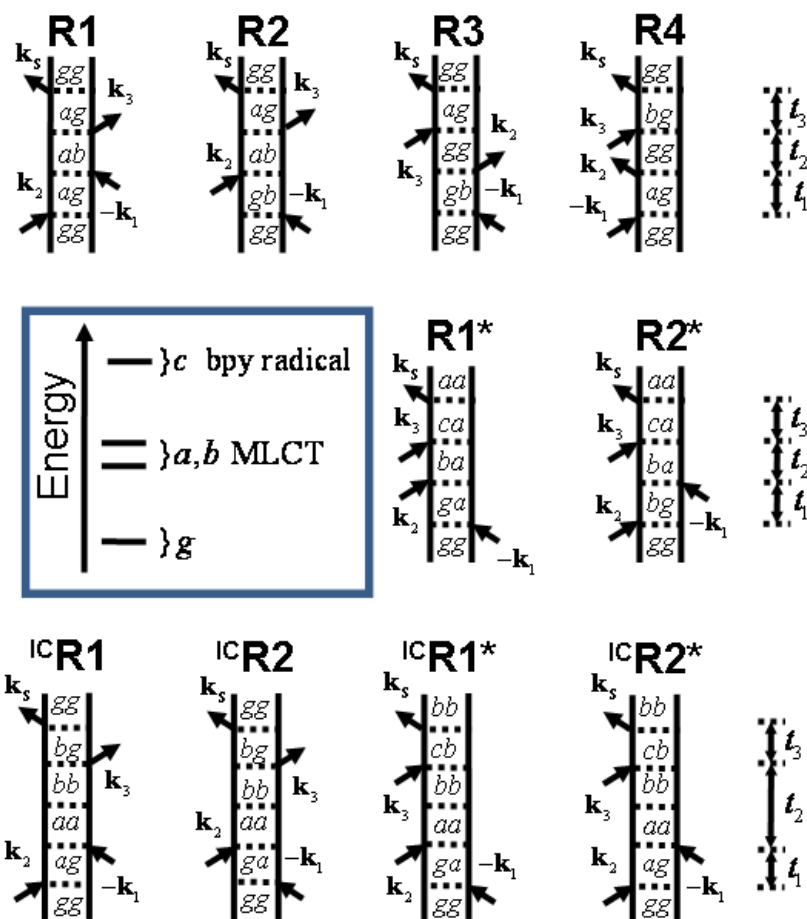
Figure 7.4: Feynman diagrams contributing to transient absorption signals. The dummy indices a and b sum over the three excited states in the MLCT manifold. The states c correspond to the (three) excited states involving electrons localized on the bipyridine ligands (i.e., bipyridine radicals). In the adiabatic limit, R_1, R_2, R_3, R_4, R_1* and R_2* are unrestricted in that terms in which $a \neq b$ contribute, whereas the nonlinearities are limited to terms where $a = b$ in the diabatic basis.

on the ligand whose MLCT state is populated during t_2. Sensitivity to interligand ET during the t_2 interval is fully captured by the terms in the bottom row of Figure 7.4. The present experiments are insensitive to the $^{IC}R_1$ and $^{IC}R_2$ terms because the signal frequency red-shifts out the detection window on a time scale much faster (<100 fs) than interligand ET.

Therefore, the interligand ET dynamics are probed primarily through the $^{IC}R_1^*$ and $^{IC}R_2^*$ terms.

Our analysis of the nonlinear response is performed by expressing signals as tensor elements weighted by transition dipole magnitudes without explicit treatment of the optical line shapes. This approach enables clear distinction of nonadiabatic and adiabatic nonlinearities with minimum complexity. The full (lengthy) derivation of these terms is given in Appendix 6. Expressions for the GSB and ESE signals involving parallel, ZZZZ, and perpendicular, ZZXX, pump and probe polarizations are given by

$$S_{ZZZZ}^{GSB} = \frac{6}{5}\mu_{eg}^4 \tag{7.6}$$

$$S_{ZZXX}^{GSB} = \frac{2}{5}\mu_{eg}^4 \tag{7.7}$$

$$S_{ZZZZ}^{ESE}(T) = \frac{6}{5}\mu_{eg}^4 M(T) \tag{7.8}$$

$$S_{ZZXX}^{ESE}(T) = \frac{2}{5}\mu_{eg}^4 M(T) \tag{7.9}$$

where the symmetry of the system is used to equate all MLCT transition dipoles to μ_{eg}. Equations 7.6 and 7.7 associate the GSB response with the R_3 and R_4, whereas R_1 and R_2 describe ESE with Equations 7.8 and 7.9. The solvation correlation function, $M(T)$, is included to capture the dynamic Stokes shift of the ESE terms. ESE initially radiates inside the detection window (defined by the probe laser spectrum) but shifts to lower frequency as the solvent reorganizes. Measurement of steady-state emission for $Os^{II}(bpy)_3$, show that the

ESE terms emit at frequencies low compared to the probe laser spectra used here.[42] Similarly, the R_1* and R_2* ESA terms yield

$$S_{ZZZZ}^{ESA}(T) = \mu_{eg}^2 \mu_{fe}^2 \left\{ \frac{2}{5} G_{et}(T) + \frac{3}{5}\left(1 - G_{et}(T)\right) \right\}$$

(7.10)

$$S_{ZZXX}^{ESA}(T) = \mu_{eg}^2 \mu_{fe}^2 \left\{ \frac{4}{5} G_{et}(T) + \frac{7}{10}\left(1 - G_{et}(T)\right) \right\} \qquad (7.11)$$

where $G_{et}(T)$ describes dynamics in the anisotropy ascribed to ET

$$G_{et}(T) = A\exp\left(-T/\tau_{et1}\right) + B\exp\left(-T/\tau_{et2}\right) \qquad (7.12)$$

Equation 7.12 separates ET dynamics into two mechanisms. We associate τ_{et2} with incoherent electron hopping between the fully relaxed ligands (i.e., consistent with excitation on the low energy side of the absorption band). The time constant, τ_{et1}, is defined in the following section.

Equations 7.10 and 7.11 assume D_3 symmetry before and after interaction with the pump fields. However, the experimental data show that these equations capture the $T = 0$ response but produce anisotropies deviating from experimental values at pulse delays greater than 1 picosecond. We therefore postulate that solvation of the photoexcited ligand reduces the D_3 symmetry of the ground state to C_2 symmetry in the MLCT excited state. Furthermore, we assume that the excited state transition dipoles of the two ligands still in their ground states at $T = 0$ rotate by 15° (with respect to the pumped transition dipole) as the solvent reorganizes (see Appendix 6). The ESA tensor elements are then written as

$$S_{ZZZZ}^{ESA}(T) = \mu_{eg}^2 \mu_{fe}^2 \left\{ \frac{2}{5} G_{et}(T) + \left(1 - G_{et}(T)\right) \left[\frac{3}{5} M(T) + \frac{4}{5} \left(1 - M(T)\right) \right] \right\} \quad (7.13)$$

$$S_{ZZXX}^{ESA}(T) = \mu_{eg}^2 \mu_{fe}^2 \left\{ \frac{4}{5} G_{et}(T) + \left(1 - G_{et}(T)\right) \left[\frac{7}{10} M(T) + \frac{3}{5} \left(1 - M(T)\right) \right] \right\} \quad (7.14)$$

In Equations 7.13 and 7.14, $G_{et}(T)$ accounts for the decay of the R_1^* and R_2^* terms that occurs concomitant with growth of the $^{IC}R_1^*$ and $^{IC}R_2^*$ terms due to ET in the t_2 interval between field matter interactions.

These individual signal components are combined to compute the transient absorption response with

$$S_{ZZZZ}(T) = S_{ZZZZ}^{GSB} + S_{ZZZZ}^{ESE}(T) - S_{ZZZZ}^{ESA}(T) \quad (7.15)$$

$$S_{ZZXX}(T) = S_{ZZXX}^{GSB} + S_{ZZXX}^{ESE}(T) - S_{ZZXX}^{ESA}(T)$$

$$(7.16)$$

The transient absorption anisotropy is obtained using

$$r(T) = \frac{S_{ZZZZ}(T) - S_{ZZZZ}(T)}{S_{ZZZZ}(T) + 2S_{ZZXX}(T)} \quad (7.17)$$

The anisotropy, $r(T)$, substitutes T for t_2 because the experimental pulse durations are short compared to τ_{et2}. Figure 7.5 presents transient absorption signals and anisotropies calculated with Equation 7.17. The ratio μ_{ef} / μ_{ge} is set equal to 7.5 to produce an anisotropy profile consistent with the experimental data shown below. The solvation correlation function, $M(T)$, is an exponential function with a 100 fs time constant. The calculation shows that the dynamics in the anisotropy mainly reflect the interligand ET time constant,

τ_{et2}, of 600 fs; the *A* and *B* coefficients of $G_{et}(T)$ are set equal to 0 and 1, respectively.

These calculations show that the asymptotic value of the anisotropy increases by 0.14 with

$D_3 \rightarrow C_2$ symmetry breaking. Thus, symmetry breaking should be readily detected in

experiments.
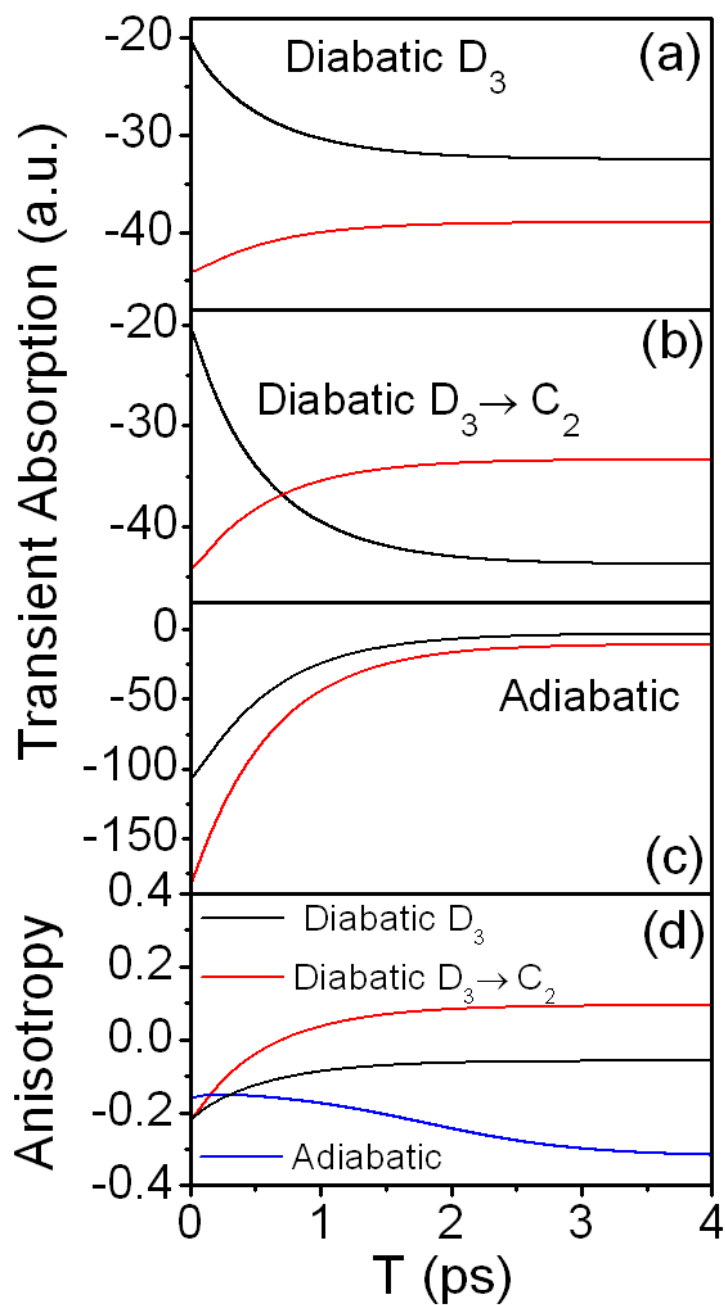
Figure 7.5: Transient absorption signals in diabatic basis for $S_{zzzz}(T)$ (black) and $S_{zzzz}(T)$ (red) tensor elements. Equations 7.10 and 7.11 are used to comput the ESA signal component. (b) Same as (a) except that Equations 7.13 and 7.14 are used to compute the ESA signal component. (c) Same as (a) for adiabatic basis. (d) Anisotropies computed using Equation 7.15 for panels (a) (black); (b) (red); and (c) (blue).

7.2.3 Transient Absorption Anisotropy in an Adiabatic Basis

Attainment of an expression for the transient absorption anisotropy valid in the adiabatic limit requires first defining the zeroeth order states controlling the optical response. The Hamiltonian written in the local basis defined in the previous section block diagonalizes as

$$H_{MLCT} = \begin{pmatrix} \hbar\omega_{eg} & J_e & J_e \\ J_e & \hbar\omega_{eg} & J_e \\ J_e & J_e & \hbar\omega_{eg} \end{pmatrix} \tag{7.18}$$

and

$$H_{BPY} = \begin{pmatrix} \hbar\omega_{fg} & J_f & J_f \\ J_f & \hbar\omega_{fg} & J_f \\ J_f & J_f & \hbar\omega_{fg} \end{pmatrix} \tag{7.19}$$

Here the H_{MLCT} and H_{BPY} blocks respectively represent MLCT states and excited states localized on the bipyridine radicals. The key difference between Equations 7.18-7.19 and the nonadiabatic treatment of the system is that the "intraband" couplings, J_e and J_f, are used to define the zeroeth-order states participating in radiative and non-radiative transitions. Thus, non-radiative electronic relaxation now proceeds through internal conversion rather than electronic coupling between localized donor and acceptor states. The eigenstates of this Hamiltonian are readily found as symmetry adapted linear combinations of the D_3 point group (see Appendix 6). We obtain three MLCT states, $\{\varepsilon\}$, and three bipyridine radical states, $\{\phi\}$. An energy level diagram of the system is presented in Figure 7.6.
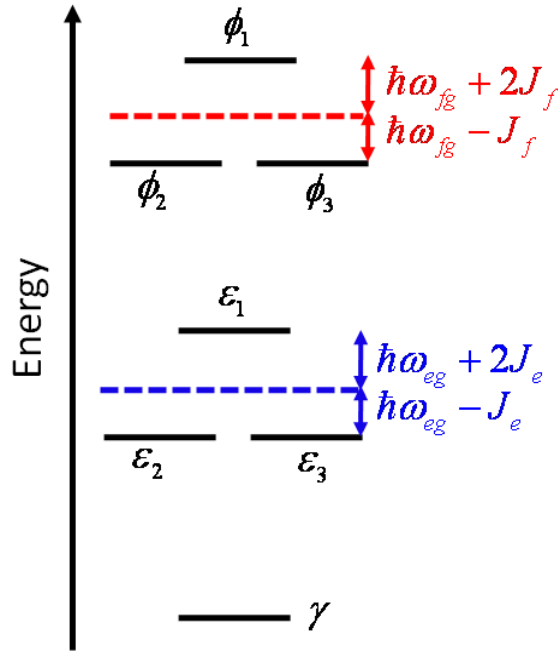
Figure 7.6: Electronic structure in adiabatic basis found with D_3 symmetry. Eigenvectors are given in Appendix 6. The levels, $\{\varepsilon\}$ and $\{\phi\}$, are respectively associated with the MLCT band and bipyridine radical electronic states.

Expressions for the transient absorption anisotropy are obtained differently in the nonadiabatic and adiabatic limits. In the adiabatic basis set, the diagrams in Figure 7.4 have unrestricted summations and do not constrain the ESA nonlinearities to particular ligands. Furthermore, we derive expressions for the various signals components consistent with Figure 7.6 by neglecting terms evolving as excited state electronic coherences in t_2. These terms may only contribute to ESE and ESA terms at times short compared to dephasing, which we estimate at less than 20 fs based on photon echo measurements of $Os^{II}(bpy)_3$ (not shown). The signal components used to compute the transient absorption anisotropy are

$$S_{ZZZZ}^{GSB} = \frac{2}{5}\mu_{\gamma\varepsilon 2}^4 + \frac{2}{5}\mu_{\gamma\varepsilon 3}^4 + \frac{4}{15}\mu_{\gamma\varepsilon 2}^2\mu_{\gamma\varepsilon 3}^2 \tag{7.19}$$

$$S_{ZZXX}^{GSB} = \frac{2}{15}\mu_{\gamma\varepsilon2}^4 + \frac{2}{15}\mu_{\gamma\varepsilon3}^4 + \frac{8}{15}\mu_{\gamma\varepsilon2}^2\mu_{\gamma\varepsilon3}^2 \tag{7.20}$$

$$S_{ZZZZ}^{ESE}(T) = M(T)\left[\frac{4}{5}\mu_{\gamma\varepsilon2}^4 + \frac{4}{5}\mu_{\gamma\varepsilon3}^4\right] \tag{7.21}$$

$$S_{ZZXX}^{ESE}(T) = M(T)\left[\frac{4}{15}\mu_{\gamma\varepsilon2}^4 + \frac{4}{15}\mu_{\gamma\varepsilon3}^4\right] \tag{7.22}$$

$$\begin{aligned}
S_{ZZZZ}^{ESA}(T) = {} & \mu_{\gamma\varepsilon2}^2 G_{et}(T)\left\{\frac{2}{15}\mu_{\varepsilon2,\phi1}^2 + \frac{2}{15}\left(1+2\cos^2(70.5°)\right)\mu_{\varepsilon2,\phi2}^2 + \frac{2}{15}\mu_{\varepsilon2,\phi3}^2\right\} \\
& + \mu_{\gamma\varepsilon3}^2 G_{et}(T)\left\{\frac{2}{15}\mu_{\varepsilon3,\phi1}^2 + \frac{2}{5}\mu_{\varepsilon3,\phi2}^2 + \frac{2}{15}\mu_{\varepsilon3,\phi3}^2\right\} \\
& + \mu_{\gamma\varepsilon2}^2\left[1-G_{et}(T)\right]\left\{\frac{2}{5}\mu_{\varepsilon3,\phi1}^2 + \frac{2}{15}\mu_{\varepsilon3,\phi2}^2 + \frac{2}{15}\left(1+2\cos^2(70.5°)\right)\mu_{\varepsilon3,\phi3}^2\right\} \\
& + \mu_{\gamma\varepsilon3}^2\left[1-G_{et}(T)\right]\left\{\frac{2}{5}\mu_{\varepsilon2,\phi1}^2 + \frac{2}{15}\mu_{\varepsilon2,\phi2}^2 + \frac{2}{5}\mu_{\varepsilon2,\phi3}^2\right\}
\end{aligned} \tag{7.23}$$

$$\begin{aligned}
S_{ZZXX}^{ESA}(T) = {} & \mu_{\gamma\varepsilon2}^2 G_{et}(T)\left\{\frac{4}{15}\mu_{\varepsilon2,\phi1}^2 + \frac{2}{15}\left(2-\cos^2(70.5°)\right)\mu_{\varepsilon2,\phi2}^2 + \frac{4}{15}\mu_{\varepsilon2,\phi3}^2\right\} \\
& + \mu_{\gamma\varepsilon3}^2 G_{et}(T)\left\{\frac{4}{15}\mu_{\varepsilon3,\phi1}^2 + \frac{2}{15}\mu_{\varepsilon3,\phi2}^2 + \frac{4}{15}\mu_{\varepsilon3,\phi3}^2\right\} \\
& + \mu_{\gamma\varepsilon2}^2\left[1-G_{et}(T)\right]\left\{\frac{2}{15}\mu_{\varepsilon3,\phi1}^2 + \frac{4}{15}\mu_{\varepsilon3,\phi2}^2 + \frac{2}{15}\left(2-\cos^2(70.5°)\right)\mu_{\varepsilon3,\phi3}^2\right\} \\
& + \mu_{\gamma\varepsilon3}^2\left[1-G_{et}(T)\right]\left\{\frac{2}{15}\mu_{\varepsilon2,\phi1}^2 + \frac{4}{15}\mu_{\varepsilon2,\phi2}^2 + \frac{2}{15}\mu_{\varepsilon2,\phi3}^2\right\}
\end{aligned} \tag{7.24}$$

It should noted that the GSB and ESA signal components possess cross-terms involving all excited states in the ε and ϕ manifolds (without restriction), whereas such signal components are not found in the formulas presented in Chapter 7.2.2.

Figure 7.6 emphasizes the type of nonlinearity forbidden in the diabatic basis and its impact on the transient absorption anisotropy. In the diabatic basis, the zeroeth order states are fully independent. The transition dipoles interacting with the "pump" pulses must be the

same as those interacting with the probe and radiating the signal field. Terms in which pairs of interactions occur with different excited states cannot contribute because, in essence, these excited states do not share the same ground state. By contrast, coherent "cross terms" in which $a \neq b$ contribute in the adiabatic basis when the interligand coupling is used to define the zeroeth order states with which the fields interact (Equations 7.18 and 7.19 and Figure 7.7). This class of nonlinearity influences the transient absorption anisotropy and defines clear spectroscopic signatures distinguishing between adiabatic and nonadiabatic regimes of ET.
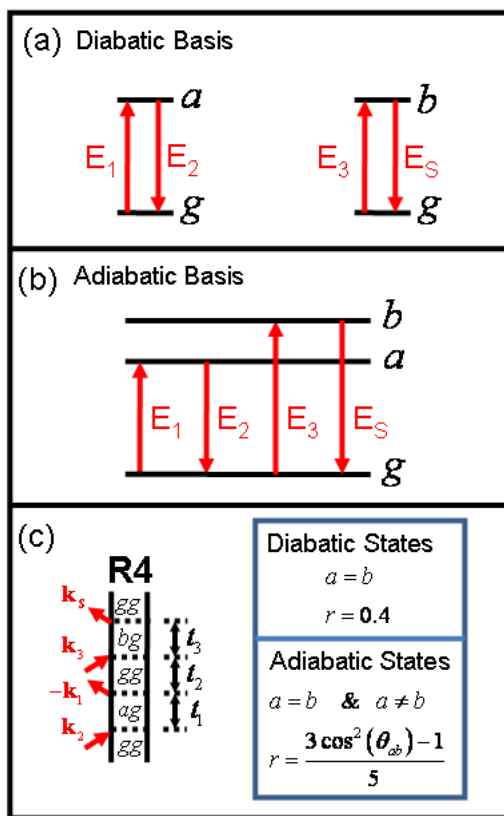
Figure 7.7: (a) Sequences with pairs of field-matter interactions occurring with diabatic MLCT transitions localized to different ligands, $a \neq b$, are forbidden. (b) Pairs of field-matter interactions with different MLCT transitions, $a \neq b$, are allowed in the (delocalized) adiabatic basis. (c) Field-matter interaction sequence for the R4 diagram. The transient absorption anisotropy of R4 depends on relative MLCT transition dipole orientations only in the adiabatic basis.

Figure 7.5 presents transient absorption signals and anisotropies for the adiabatic basis computed with the same input parameters used for the diabatic basis with one exception. In the adiabatic basis, the ESA component is weaker and the ratio μ_{ef} / μ_{ge} is set equal to 10 (rather than 7.5 in the diabatic basis) so that the calculated signals have the same sign as those measured experimentally. The anisotropy obtained with the adiabatic basis differs substantially from that found in the diabatic basis. In the adiabatic basis, the anisotropy has an initial value of -0.16 and decays with increasing pulse delay, T, whereas the anisotropy increases with T in the diabatic basis. This comparison of signals computed with different bases makes clear the sensitivity of transient absorption anisotropy to electronic structure.

7.2.4. Activated and Activationless Electron Transfer Mechanisms in Os^{II}(bpy)$_3$

The free energy surfaces for Os^{II}(bpy)$_3$ shown in Figure 7.8 define activated and activationless ET mechanisms. This picture is motivated by the studies of Papanikolas and co-workers who detected a fast depolarization mechanism in transient absorption anisotropy experiments, which became more evident as the pump pulses were tuned to higher frequency.[33,34] Activated dynamics occur when electronic excitation promotes population into the free energy well below the avoided crossing. Transitions must then surmount a barrier equal to 25% of the estimated 3500 cm^{-1} solvent reorganization energy. By contrast, a nuclear wavepacket is initiated above the avoided crossing when the excitation frequency is tuned to higher energy. Solvation drives the wavepacket through one of three ET channels with equally weighted probabilities. The process terminates with the electron localized on

206

one of the three bipyridine ligands. The key for understanding transient absorption anisotropy measurements is that the excitation depolarizes when the wavepacket moves through the avoided crossing.
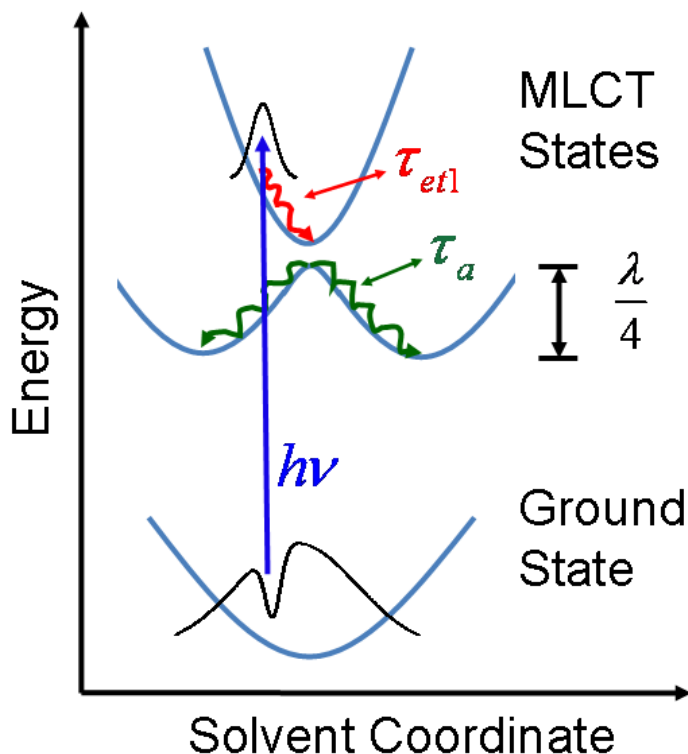
Figure 7.8: Schematic depicting the effect of the pump laser frequency on dynamics in the transient absorption anisotropy. A wavepacket initiates on the upper quasi-adiabatic surface, relaxes to the avoided crossing with time constant τ_{et1}, then depolarizes as electrons localize on the individual ligands.

The time scale of nuclear relaxation is a key parameter influencing the adiabaticity of an ET reaction (see Equation 7.1). Figure 7.8 associates the time scale, τ_a, with the rate at which a wavepacket relaxes in the free energy well of one of the quasi-diabatic states. Thus, it may be possible to measure this time constant with a series of transient absorption experiments in which the pump pulse frequency is tuned. Figure 7.8 is certainly a useful way to understand the dynamics, but should be understood as schematic. It is unlikely that

quantitative information can be derived from a model defining all three free energy surfaces with respect to the same solvent coordinate. That is, the nuclear coordinates that couple to optical excitation between the ground and MLCT excited states are not necessarily the same as those displaced by interligand ET. Moreover, the ground state solvent configuration is more symmetric than that of an excited MLCT state with an electron localized on one of the ligands.[33,34] The central point we wish to motivate is that activationless ET channels become more prominent with increasing excitation frequency. These solvation processes, in turn, cause decay of the transient absorption anisotropy with time constant τ_{et1}, which is the first component in Equation 7.12.

7.3. EXPERIMENTAL METHODS

$[Os^{II}(bpy)_3](PF_6)_2$ was obtained as a gift from J. M. Papanikolas. All experiments were performed with solutions prepared in acetonitrile. Attempts to apply transient absorption methods to $Os^{II}(bpy)_3$ in methanol and ethylene glycol were thwarted by insufficient solubility. We find that high solute concentration is needed to compensate for weak transient absorption signals obtained when pumping and probing between 500 and 700 nm. In part, the requirement for high solute concentration reflects the 250 μm effective path length for which pump and probe pulses overlap in our apparatus. In principle, smaller beam crossing angles (see below) could increase the path length. However, group velocity mismatch would then degrade time resolution in experiments employing laser pulses with different carrier frequencies. The absorbance of the solution was 0.3 at 600 nm in a 0.5 mm path length flow cell. Absorbance spectra were measured before and after experiments to confirm the absence of sample degradation.

The one-color transient grating (TG) experiments in this investigation use the same equipment and procedures described elsewhere.[43-45] Briefly, the TG experiments use a diffractive optic-based interferometer similar to those reported in several earlier publications.[46-51] The apparatus applies three pulses (E_1, E_2 and E_3) in a boxcars laser beam geometry and heterodyne detects the signal with a reference field (i.e., local oscillator) which is collinear with the signal after the sample. We refer to the $E_1 \& E_2$ pulses, which arrive at the sample simultaneously, as "pump" pulses because they play the same role as the single pump pulse used in a conventional transient absorption experiment. Similarly, E_3 is referred to as the probe pulse. Pulses with durations of 20 fs and energies of 100 nJ are focused to 120 um spot size at the sample. Signals are detected by spectral interferometry using a back-illuminated CCD array (Princeton Instruments PIXIS 100B) mounted on a 0.3 meter spectrograph. Integration times are 100-200 ms. Signals are processed using a Fourier transform algorithm.[52-54] Phase angles (i.e., absorptive versus dispersive) of the TG signals are defined by reference to the pure acetonitrile solution using established procedures.[55,56]

Anisotropies compare tensor elements for real (absorptive) TG signal components measured in immediate succession, where each tensor element represents an average of 15 scans of the optical delay line. This representation is identical to that of a conventional transient absorption experiment. Because the TG signals emitted by $Os^{II}(bpy)_3$ are particularly weak, a mechanical shutter is used to chop the $E_1 \& E_2$ beams for suppression of scattered probe light. This procedure averages the difference in 3-5 interferograms with the shutter open and closed at each delay point. Each individual scan of the optical delay line required 10-15 minutes. Long data acquisition times lead to an increase in the error in the anisotropy by about a factor of two compared to earlier applications using this same

apparatus.[43,45] The experiments were repeated several times and suggest that this procedure yields an error of approximately +/- 0.04 in the anisotropy.

The TG measurements presented in Figure 7.11 use an E_1 & E_2 pulse-pair and E_3 pulse derived from separate optical parametric amplifiers. The spectrum of the E_3 "probe" pulse spans the 500-750 nm range and we are unable to fully compensate for the dispersion over this broad bandwidth using a prism compressor. The overlap of particular spectral components in E_3 with the compressed E_1 & E_2 pulse-pair is taken into account numerically using a procedure commonly employed for conventional two-pulse transient absorption spectroscopy with a continuum probe.[57] TG signals obtained with the pure acetonitrile solvent are used as a reference to numerically correct the dependence of "time-zero" on the signal emission frequency. We obtain a full-width half maximum instrument response of <100 fs at signal emission frequencies of 13300-20000 cm^{-1} with use of a prism compressor configured to minimize dispersion at 16800 cm^{-1} (see Appendix 6). This procedure applies only to the data presented in Figure 7.11. All one-color experiments in this study apply laser pulses with time-bandwidth products less than 0.52.

7.4. EXPERIMENTAL RESULTS AND DISCUSSION

The transient absorption measurements shown in Figure 7.9 investigate the issues outlined in Chapter 7.2. First, it is important to note that the positive sign of the signals represents the dominance of ESA signal components involving absorption between excited states. Signals with negative signs (net bleach) are not detected at probe wavelengths between 530 nm and 730 nm. We estimate that the μ_{ef} transition dipole probed from 530-730 nm is 5-10 times larger than the μ_{ge} MLCT transition dipole based on our theoretical model. Earlier transient absorption experiments probed an intense ESA resonance localized to the bipyridine ligands at wavelengths near 370 nm.[32-34] The polarization dependence of the ESA transition detected at visible wavelengths is quite similar to the resonance detected in the UV. Signals measured with ZZZZ and ZZXX polarization conditions respectively possess sub-picosecond rising and decaying components particularly evident at the pump wavelengths of 680 nm and 645 nm. By contrast, the signal amplitudes of both tensor elements depend more weakly on the pulse delay at $T <1$ ps for pump wavelengths of 610 nm and 570 nm.
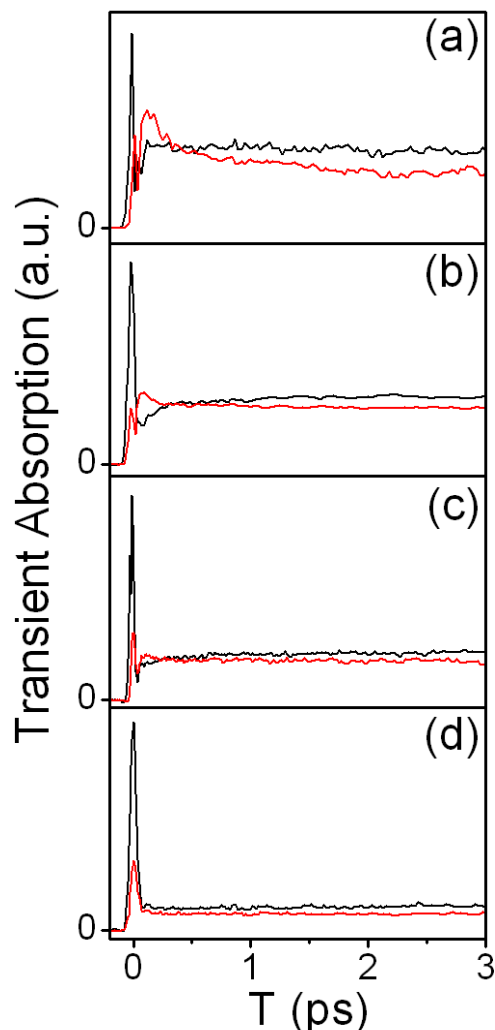
Figure 7.9: Transient absorption signals measured with ZZZZ (black) and ZZXX (red) tensor elements and pump/probe wavelengths: (a) 680nm/610nm; (b) 645nm/645nm; (c) 610nm/610nm; (d) 570nm/570nm. Transient absorption is defined as the real part of the experimentally measured transient grating signal field, where the positive sign represents absorption between excited states.

Anisotropies corresponding to the transient absorption signals in Figure 7.9 are shown in Figure 7.10. At pump wavelengths of 610 and 680 nm, the anisotropy is close to -0.2 at T =0 ps, then increases to approximately 0.1 at T =3 ps. This behavior is remarkably similar to the calculated signals shown in Figure 7.5 in which $D_3 \rightarrow C_2$ symmetry breaking is modeled in the diabatic basis, which gives strong support to the view of the electronic structure conveyed

by Figure 7.3. The fitting parameters given in Table 7.1 decompose the signal into activationles, τ_{et1}, and activated, τ_{et2}, time constants. The r_1 and r_2 parameters suggest that the two mechanisms contribute equally at 680 nm, whereas the activationless component is approximately 3.8 times larger at 645 nm. At shorter pump wavelengths, activationless ET dynamics are not well-resolved within the 25 fs time resolution of the experiments. The initial value of the anisotropy is close to -0.1 at 610 nm, whereas at 570 nm the anisotropy is equal to 0.07 at $T = 0$ ps. These observations point to dominance of the activationless ET mechanism at the shorter pump wavelengths.
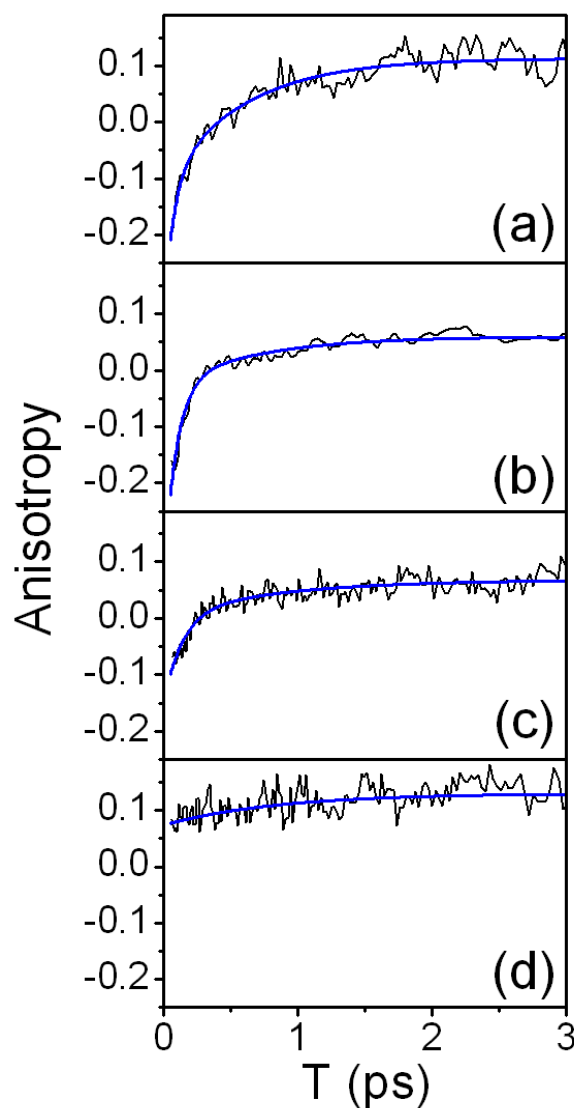
Figure 7.10: Transient absorption anisotropies calculated using the data in Figure 7.9 with the pump/probe wavelengths: (a) 680nm/610nm; (b) 645nm/645nm; (c) 610nm/610nm; (d) 570nm/570nm. Fitting parameters are given in Table 7.1.

The probe wavelength dependence of the anisotropy is examined in Figure 7.11, where excitation is achieved with a 20 fs pump pulse centered at 680 nm. At short T, the anisotropy increases as the probe wavelength becomes shorter, whereas the anisotropy is essentially independent of the probe wavelength at $T > 1$ ps. This wavelength dependence

Table 7.1. Fits to Anisotropies in Figure 7.10

[a]Parameter	680nm/610nm	645nm/645nm	610nm/610nm	570nm/570nm
r_0	0.11	0.06	0.07	0.13
r_1	-0.23	-0.34	-0.15	------------
r_2	-0.22	-0.09	-0.06	-0.06
τ_{et1} /fs	40	90	140	------------
τ_{et2} /fs	590	670	860	850

[a]Fit to Equation $r(T) = r_0 + r_1 \exp\left(-T/\tau_{et1}\right) + r_2 \exp\left(-T/\tau_{et2}\right)$

partly reflects interference with the signal bleach involving the (nominally) singlet MLCT transitions absorbing at wavelengths shorter than 500 nm (Figure 7.1). These transitions possess larger oscillator strengths than the triplet MLCT transitions and may contribute significantly even with little overlap between the laser spectrum and their line shapes. For this reason, our examination of the pump wavelength dependence in Figures 7.9 and 7.10 does not tune the excitation wavelength shorter than 570 nm.
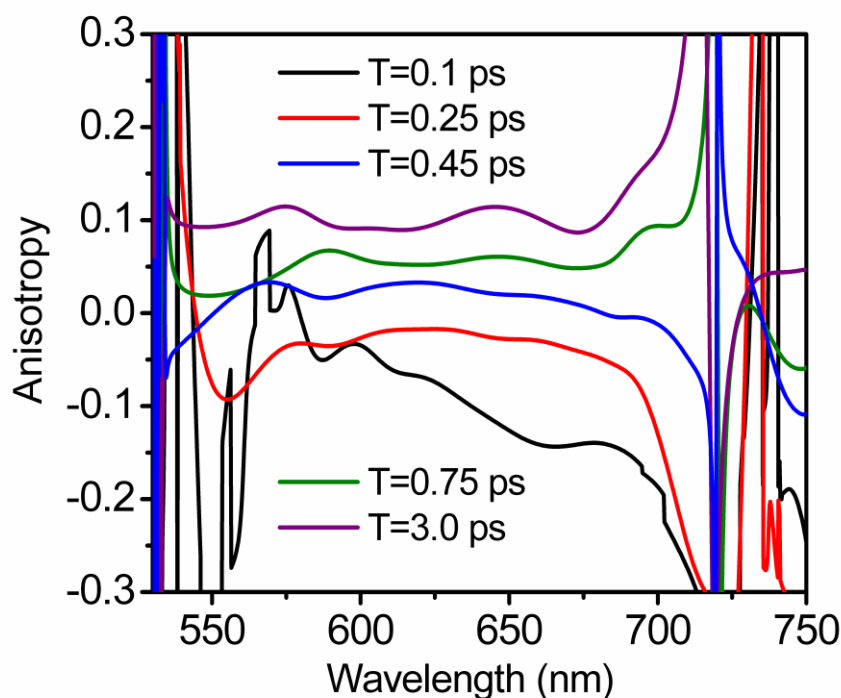
Figure 7.11: Transient absorption anisotropies obtained with excitation at 680 nm and a broadband probe pulse with a spectrum spanning the 500-750 nm range. Delay times, T, are given in the Figure legend.

The transient absorption anisotropy data gives important insight into the electronic structure of $Os^{II}(bpy)_3$. First, the data show that the excited states are diabatic even at the instant of photon absorption (i.e., at the Franck-Condon geometry). The measured signals are quite different than those computed with an adiabatic basis in Figure 7.5, but closely resemble those obtained with a diabatic basis. Furthermore, the data support the view that solvation of the photoexcited MLCT transition induces $D_3 \rightarrow C_2$ symmetry breaking. Figure 7.5 shows that with and without symmetry breaking the asymptotic values of the anisotropy are equal to 0.1 and -0.06, respectively. This difference in anisotropies is readily measured experimentally and underscores the power of transient absorption anisotropy for elucidating details of electronic structure.[58-60]

216

The decreasing contribution of the activationless ET mechanism found with increasing pump frequency is consistent with the idea suggested by Figure 7.8, which was first proposed in Reference 33. The present measurements use a 22-fold increase in time resolution to more quantitatively distinguish dynamics associated with the two ET mechanisms. The time scale of nuclear motion entering the adiabatic rate formula, τ_{total}, is not fully resolved. However, Figure 7.10 and the fitting parameters in Table 7.1 establish that the activated and activationless mechanisms contribute equally at the nuclear geometry corresponding to excitation at 680 nm. Furthermore, contributions of the activationless mechanism are enhanced by a factor of 3.8 with an 800 cm^{-1} increase in the pump frequency (i.e., excitation at 645 nm versus 680 nm). This sensitivity to the pump frequency is consistent with the 875 cm^{-1} activation energy barrier.[33,34] Overall, the measurements make clear that excitation above the electronic origin of the MLCT transition enhances the interligand electron transfer rate as suggested by Figure 7.8.

7.5. CONCLUSIONS

The present use of nonlinear spectroscopy to distinguish adiabatic and nonadiabatic ET mechanisms is similar to spirit to the large body of theoretical and experimental work examining Frenkel exciton formation in molecular aggregates and pigment complexes in biological light harvesting proteins.[61-69] In molecular aggregates, electronic states localize when heterogeneity in molecular site energies (i.e., diagonal disorder) dominates over intermolecular couplings; non-radiative relaxation then occurs by way of incoherent hopping of excitations between molecular sites. By contrast, delocalized Frenkel exciton states form when intermolecular couplings are larger than the magnitude of energy level fluctuations caused by environmental motion. In this regime, electronic relaxation proceeds through internal conversion between delocalized electronic states. Thus, similar issues govern the appropriate choice of basis states for systems undergoing both energy transfer and electron transfer. For this reason, much of the intuition and techniques developed for the investigation of excited states in molecular aggregates can be mapped to the study of ET adiabaticity.

The present application to the prototypical metal polypyridal complex, $Os^{II}(bpy)_3$, shows that conventional transient absorption spectroscopy readily distinguishes diabatic and adiabatic bases. This approach has advantages over alternative methods of studying ET adiabaticity that alter solvents and/or temperature because the nature of the electronic states is unambiguously probed with transient absorption anisotropy. Altering the solvent, for example, generally impacts solvent reorganization energies and the free energies of the donor and acceptor states (i..e., parameters of k_{na} in Equation 7.1), which complicates experimental isolation of the adiabaticity. One limitation to the model presented in Chapter 7.2 is that it

does not interpolate between nonadiabatic and adiabatic regimes. However, we suggest that intermediate cases can be treated by averaging the optical response over an inhomogeneous distribution of solvent configurations. For example, Reference 33 computes an appropriate distribution for $Os^{II}(bpy)_3$ using molecular dynamics simulations. Given an ensemble of $Os^{II}(bpy)_3$ complexes whose MLCT energies are allowed to fluctuate, the Hamiltonian for each system is readily diagonalized to compute transition dipoles and transient absorption anisotropies. Only the portion of systems with either 2 or 3 nearly degenerate MLCT states would then possess delocalized states with response functions deviating from those given in Chapter 7.2.2. Another potential limitation to our approach is that well-defined response functions are not readily written for complex systems such as dye-sensitized nanoparticles[70-73] and/or (heterogeneous) polymer films.[74-77] Nonetheless, the results obtained here should have broad application for myriad metal polypyridal complexes with potential use in solar energy technologies.[6,7,78-83]

7.6. REFERENCES

(1)   Barbara, P. F.; Meyer, T. J.; Ratner, M. A. *J. Phys. Chem.* 1996, *100*, 13148-13168.

(2)   Gray, H. B.; Winkler, J. R. *Annu. Rev. Biochem.* 1996, *65*, 537-561.

(3)   Isied, S. S., Ed. Electron Transfer Reactions. Inorganic, Organometallic, and Biological Applications; Oxford University Press: Oxford, 1998.

(4)   Huynh, M. H.; Meyer, T. J. *Chem. Rev.* 2007, *107*, 5004-5064.

(5)   Rice, S. A., Ed. *Electron Transfer-From Isolated Molecules to Biomolecules*; John Wiley and Sons: New York, 1999.

(6)   Meyer, T. J. *Acc. Chem. Res.* 1989, *22*, 163-170.

(7)   Alstrum-Acevedo, J. H.; Brennaman, M. K.; Meyer, T. J. *Inorg. Chem.* 2005, *44*, 6802-6827.

(8)   Weaver, M. J.; McManis, G. E.; Jarzeba, W.; Barbara, P. F. *J. Phys. Chem.* 1990, *94*, 1715-1719.

(9)   Hynes, J. T. *J. Phys. Chem.* 1986, *90*, 3701-3706.

(10)   Zusman, L. D. *Chem. Phys.* 1980, *49*, 295-304.

(11)   Sumi, H.; Marcus, R. A. *J. Chem. Phys.* 1985, *84*, 4894-4914.

(12)   Hoffman, B. M.; Ratner, M. A. *Inorg. Chim. Acta* 1996, *243*, 233-238.

(13)   Yan, Y. J.; Sparpaglione, M.; Mukamel, S. *J. Phys. Chem.* 1988, *92*, 4842-4853.

(14)   Ben-Amotz, D.; Harris, C. B. *J. Chem. Phys.* 1987, *86*, 4856-4870.

(15)   Moran, A. M.; Aravindan, P.; Spears, K. G. *J. Phys. Chem. A* 2005, *109*, 1795-1801.

(16)   Moran, A. M.; Spears, K. G. *Chem. Phys. Lett.* 2004, *393*, 397-402.

(17)   Ponnu, A.; Sung, J.; Spears, K. G. *J. Phys. Chem. A* 2006, *110*, 12372-12384.

(18)   Fleming, C. N.; Dattlebaum, D. M.; Thompson, D. W.; Ershov, A. Y.; Meyer, T. J. *J. Am. Chem. Soc.* 2007, *129*, 9622-9630.

(19)   Thompson, D. W.; Fleming, C. N.; Myron, B. D.; Meyer, T. J. *J. Phys. Chem. B* 2007, *111*, 6930-6941.

(20)   Kramers, H. A. *Physica* 1940, *7*, 284.

(21)   Risken, H. *The Fokker-Planck Equation*; Springer: Berlin, 1984.

(22)   Nitzan, A. *Chemical Dynamics in Condensed Phases*; Oxford University Press: New York, 2006.

(23)   Troe, J. *Chem. Phys. Lett.* 1985, *114*, 241-247.

(24)   Schröder, J.; Troe, J. *Chem. Phys. Lett.* 1985, *116*, 453-459.

(25)   Millar, D. P.; Eisenthal, K. B. *J. Chem. Phys.* 1985, *83*, 5076-5083.

(26)   Lee, M.; Holtom, G. R.; Hochstrasser, R. M. *Chem. Phys. Lett.* 1985, *118*, 359-363.

(27)   Rothenberger, G.; Negus, D. K.; Hochstrasser, R. M. *J. Chem. Phys.* 1983, *79*, 5360-5367.

(28)   Kahlow, M. A.; Wlodzimierz, J.; Kang, T. J.; Barbara, P. F. *J. Chem. Phys.* 1989, *90*, 151-158.

(29)   Crosby, G. A.; Demas, J. N. *J. Am. Chem. Soc.* 1971, *93*, 2841-2847.

(30)   Kober, E. M.; Meyer, T. J. *Inorg. Chem.* 1984, *23*, 3877-3886.

(31)   Lumpkin, R. S.; Kober, E. M.; Worl, L. A.; Murtaza, Z.; Meyer, T. J. *J. Phys. Chem.* 1990, *94*, 239-243.

(32)   Cushing, J. P.; Butoi, C.; Kelley, D. F. *J. Phys. Chem. A* 1997, *101*, 7222-7230.

(33)   Shaw, G. B.; Styers-Barnett, D. J.; Gannon, E. Z.; Granger, J. C.; Papanikolas, J. M. *J. Phys. Chem. A* 2004, *108*, 4998-5006.

(34)   Shaw, G. B.; Brown, C. L.; Papanikolas, J. M. *J. Phys. Chem. A* 2002, *106*, 1483-1495.

(35)   Sparpaglione, M.; Mukamel, S. *J. Chem. Phys.* 1988, *88*, 3263-3280.

(36)   Sumi, H. *J. Phys. Soc. Jpn.* 1980, *49*, 1701-1712.

(37)   Sparpaglione, M.; Mukamel, S. *J. Chem. Phys.* 1988, *88*, 4300-4311.

(38)   Damrauer, N. H.; Cerullo, G.; Yeh, A.; Boussie, T. R.; Shank, C. V.; McCusker, J. K. *Science* 1997, *275*, 54-57.

(39)   Yeh, A.; Shank, C. V.; McCusker, J. K. *Science* 2000, *289*, 935-938.

(40)   Horng, M. L.; Gardecki, J. A.; Papazyan, A.; Maroncelli, M. *J. Phys. Chem.* 1995, *99*, 17311-17337.

(41)   Mukamel, S. *Principles of Nonlinear Optical Spectroscopy*; Oxford University Press: New York, 1995.

(42)   Glomm, W. R.; Moses, S. J.; Brennaman, M. K.; Papanikolas, J. M.; Franzen, S. *J. Phys. Chem. B* 2005, *109*, 804-810.

(43)   Womick, J. M.; Miller, S. A.; Moran, A. M. *J. Phys. Chem. B* 2009, *113*, 6630-6639.

(44)   Womick, J. M.; Miller, S. A.; Moran, A. M. *J. Phys. Chem. A* 2009, *113*, 6587-6598.

(45)   Miller, S. A.; Womick, J. M.; Parker, J. F.; Murray, R. W.; Moran, A. M. *J. Phys. Chem. C* 2009, in-press.

(46)   Cowan, M. L.; Ogilvie, J. P.; Miller, R. J. D. *Chem. Phys. Lett.* 2004, *386*, 184-189.

(47)   Goodno, G. D.; Astinov, V.; Miller, R. J. D. *J. Phys. Chem. B* 1999, *103*, 603-607.

(48)   Moran, A. M.; Nome, R. A.; Scherer, N. F. *J. Phys. Chem. A* 2006, *110*, 10925-10928.

(49)   Moran, A. M.; Nome, R. A.; Scherer, N. F. *J. Chem. Phys.* 2007, *127*, 184505:184501-184513.

(50)   Brixner, T.; Mancal, T.; Stiopkin, I. V.; Fleming, G. R. *J. Chem. Phys.* 2004, *121*, 4221-4236.

(51)   Milota, F.; Sperling, J.; Nemeth, A.; Kauffman, L. J. *Chem. Phys.* 2008, *357*, 45-53.

(52)   Lepetit, L.; Chériaux, G.; Joffre, M. *J. Opt. Soc. Am. B* 1995, *12*, 2467-2474.

(53)   Tokunaga, E.; Terasaki, A.; Kobayashi, T. *J. Opt. Soc. Am. B* 1995, *12*, 753-771.

(54)   Gallagher, S. M.; Albrecht, A. W.; Hybl, J. D.; Landin, B. L.; Rajaram, B.; Jonas, D. M. *J. Opt. Soc. Am. B* 1998, *15*, 2338.

(55)   Moran, A. M.; Maddox, J. B.; Hong, J. W.; Kim, J.; Nome, R. A.; Bazan, G. C.; Scherer, N. F. *J. Chem. Phys.* 2006, *124*, 194904:194901-194915.

(56)   Moran, A. M.; Park, S.; Scherer, N. F. *J. Phys. Chem. B* 2006, *110*, 19771-19783.

(57)   Nakayama, T.; Amijima, Y.; Ibuki, K.; Hamanoue, K. *68* 1997, 4364-4371.

(58)   Qian, W.; Jonas, D. M. *J. Chem. Phys.* 2003, *119*, 1611.

(59)   Farrow, D. A.; Smith, E. R.; Qian, W.; Jonas, D. M. *J. Chem. Phys.* 2008, *129*, 174509:174501-174520.

(60)   Parson, W. W. *Modern Optical Spectroscopy*; Springer-Verlag: Berlin, 2007.

(61)   Fidder, H.; Knoester, J.; Wiersma, D. A. *J. Chem. Phys.* 1991, *95*, 7880-7890.

(62)   De Boer, S.; Wiersma, D. A. *Chem. Phys.* 1989, *131*, 135-144.

(63)   Fleming, G. R.; Scholes, G. D. *Nature* 2004, *121*, 4221-4236.

(64)   Scholes, G. D.; Jordanides, X. J.; Fleming, G. R. *J. Phys. Chem. B* 2001, *105*, 1640-1651.

(65)   van Amerongen, H.; Valkunas, L.; van Grondelle, R. *Photosynthetic Excitons*; World Scientific: Singapore, 2000.

(66)   Abramavicius, D.; Mukamel, S. *Chem. Rev.* 2004, *104*, 2073-2098.

(67)   Abramavicius, D.; Palmieri, B.; Voronine, D. V.; Sanda, F.; Mukamel, S. *Chem. Rev.* 2009, *109*, 2350-2408.

(68)   Womick, J. M.; Moran, A. M. *J. Phys. Chem. B* 2009, *113*, 15771-15782.

(69)   Womick, J. M.; Moran, A. M. *J. Phys. Chem. B* 2009, *113*, 15747-15759.

(70)   Asbury, J. B.; Ellingson, R. J.; Ghosh, H. N.; Ferrere, S.; Nozik, A. J.; Lian, T. *J. Phys. Chem. B* 1999, *103*, 3110-3119.

(71)   Ghosh, H. N.; Asbury, J. B.; Lian, T. *J. Phys. Chem. B* 1998, *102*, 6482-6486.

(72)   Asbury, J. B.; Hao, E.; Wang, Y.; Ghosh, H. N.; Lian, T. *J. Phys. Chem. B* 2001, *105*, 4545-4557.

(73)   Asbury, J. B.; Anderson, N. A.; Hao, E.; Ai, X.; Lian, T. *J. Phys. Chem. B* 2003, *107*, 7376-7386.

(74)   Schwartz, B. J. *Annu. Rev. Phys. Chem.* 2003, *54*, 141-172.

(75)   Hoppe, H.; Sariciftci, N. S. *J. Mater. Chem.* 2006, *16*, 45-61.

(76)   Sylvester-Hvid, K. O.; Rettrup, S.; Ratner, M. A. *J. Phys. Chem. B* 2004, *108*, 4296-4307.

(77)   Kraabel, B.; Hummelen, J. C.; Vacar, D.; Moses, D.; Sariciftci, N. S.; Heeger, A. J.; Wudl, F. *J. Chem. Phys.* 1996, *104*, 4267-4273.

(78)   Meylemans, H. A.; Lel, C.-F.; Damraurer, N. H. *Inorg. Chem.* 2008, *47*, 4060-4076.

(79)   Soler, M.; McCusker, J. K. *J. Am. Chem. Soc.* 2008, *130*, 4708-4724.

(80)   Knight, T. E.; Guo, D.; Claude, J. P.; McCusker, J. K. *Inorg. Chem.* 2008, *47*, 7249-7261.

(81)   Esswein, A. J.; Nocera, D. G. *Chem. Rev.* 2007, *107*, 4022-4047.

(82)   Wallin, S.; Davidsson, J.; Modin, J.; Hammarström, L. *J. Phys. Chem. A* 2005, *109*, 4697-4704.

(83)   Lomoth, R.; Häupl, T.; Johansson, O.; Hammarström, L. *Chem. Eur. J.* 2002, *8*, 102.

CHAPTER 8 . UNCOVERING MOLECULE-TiO₂ INTERACTIONS WITH NONLINEAR SPECTROSCOPY

8.1. INTRODUCTION

Knowledge of electronic structure and transport mechanisms in dye-sensitized semiconductors is motivated by their ubiquity in photoelectrochemical cells.[1-3] One vital area of research aims to understand how molecule-semiconductor interactions influence the primary events initiated by light absorption (e.g., electron transfer, nuclear relaxation).[4-13] Pioneering experimental work established <100fs time scales for photoinjection in several dye-sensitized TiO₂ systems.[14,15] The observed dynamics conform (approximately) to the rate theory developed by Marcus and Gerischer decades ago in which photoexcitation of the molecular sensitizer and electron injection are regarded as sequential processes.[16-18] In this model, the rate is determined primarily by the donor-acceptor coupling and the density of states of the semiconductor at the energy of the excited molecular donor (cf., Scheme 2 in Reference 4). Recent quantum dynamics simulations have suggested a more complex picture in which the nature of the photoexcited state depends sensitively on the geometry of the system at the "instant" of photon absorption.[5] Due to geometry heterogeneity, electronic excitations are initially localized on the molecular sensitizers in some members of the ensemble, whereas for others the excitations are delocalized between the molecule and semiconductor surface. When such delocalization takes hold, light absorption and electron injection are not sequential but should be viewed as one in the same process. This behavior

contrasts with that found in systems with weak molecule-semiconductor coupling, where it instead makes sense to invoke photoinduced electron transfer rates.

In this communication, we use femtosecond transient grating (TG) spectroscopy to investigate the nature of electronic states in nanocrystalline TiO_2 films sensitized with two molecular adsorbates, catechol and a Ruthenium complex $[(Ru(bpy)_2(4,4'-(PO_3H_2)_2bpy)]Cl_2$ hereafter denoted as RuCmp. These sensitizers are well-suited to the present study because they span the weak (RuCmp) and strong (catechol) regimes of molecule-TiO_2 coupling due to their respective phosphate and hydroxyl linkers.[4,5,19] Figure 8.1 shows that strong coupling in catechol-TiO_2 gives rise to an optical charge transfer band near 400nm. The charge transfer band signifies that photoexcitation and electron injection are non-sequential in catechol-TiO_2 because the excited state wavefunction is delocalized between species at the instant of photon absorption.[5,19] By contrast, bonding of RuCmp to TiO_2 results in an absorbance line shape that closely resembles the spectrum of the free molecule in solution. In RuCmp-TiO_2, it might therefore be predicted that electron injection into TiO_2 occurs subsequent to light absorption by the molecule (i.e., a sequential process). However, the fraction of molecules for which this is a good approximation is not immediately clear. It is a goal of this work to establish a spectroscopic method sensitive to the RuCmp-TiO_2 sites where wavefunction delocalization is most significant.
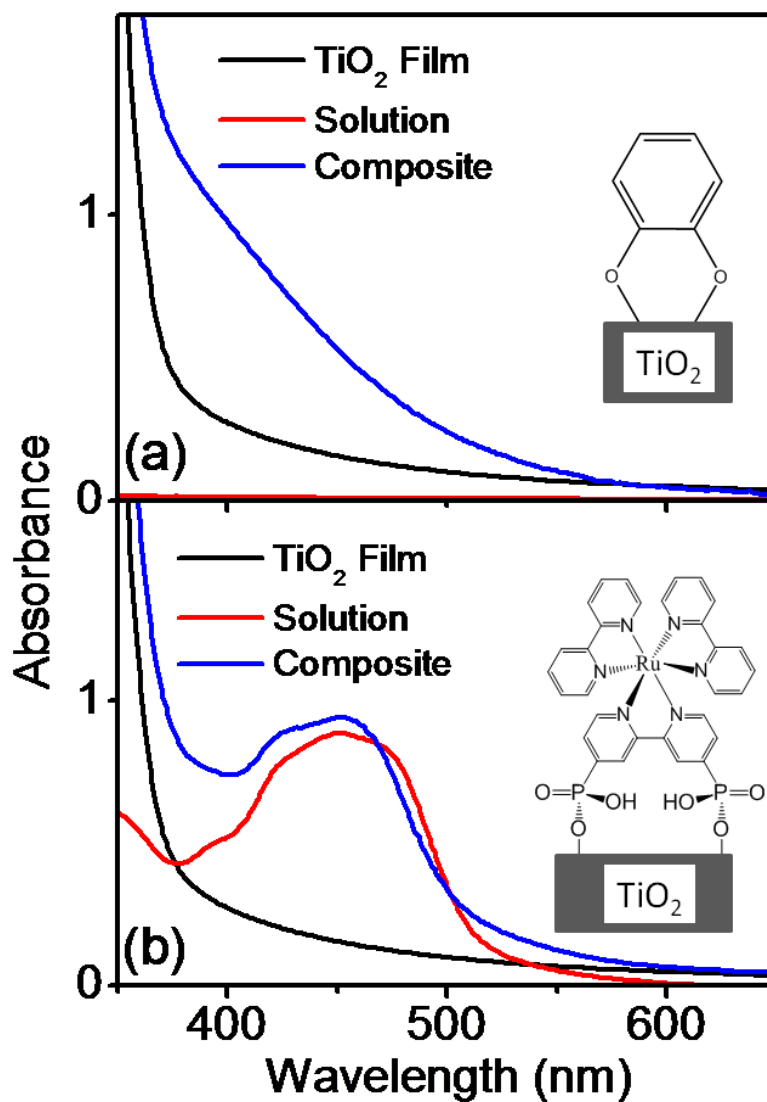
Figure 8.1: (a) Absorbance spectra of catechol in aqueous solution (red) and adsorbed to a TiO$_2$ nanocrystalline film (blue). (b) Absorbance spectra of the ruthenium complex in aqueous solution (red) and adsorbed to a TiO$_2$ nanocrystalline film (blue). The absorbance spectrum of a neat TiO$_2$ film is displayed in both panels (black).

8.2. EXPERIMENTAL METHODS

TiO$_2$ films, which are prepared according to known procedures,[20] cover one side of a

microscope cover slip.   Adsorption of the dye molecules is achieved by soaking the TiO$_2$

films in solutions of the dyes. Both the neat and dye-sensitized TiO_2 films are held in homemade cuvettes containing aqueous solutions during the TG measurements. The TG experiments utilize a diffractive optic based interferometer in which signals are collected under the phase matching condition, $\mathbf{k}_S = -\mathbf{k}_1 + \mathbf{k}_2 + \mathbf{k}_3$.[21] The time coincident 400nm "pump" pulses (E_1 and E_2) are 35-55fs in duration. The 525nm "probe" pulse (E_3) and the reference pulse used for interferometric signal detection are 20fs in duration. All pulses possess 40-90nJ energies and are focused to 120μm FWHM spot sizes. Signal detection by spectral interferometry is achieved using a back-illuminated CCD mounted on a 0.3 meter spectrograph with a 600g/mm grating.[22] Further details involved in the optical experiments and sample preparation are described in Appendix 7.[23]

8.3. RESULTS AND DISCUSSION

Optical nonlinearities associated with three distinct regions of the sample generally contribute to the total TG signal: (i) the "bulk" TiO_2 nanocrystal; (ii) the molecular sensitizer; (iii) the interface between the molecule and TiO_2. Because (iii) is of primary interest here, we deliberately suppress (i) using a tensor element, denoted as ZXZX, for which the response of the TiO_2 film is negligible. As illustrated in the inset of Figure 8.2(a), the two time-coincident 400nm laser pulses used for excitation (E_1 and E_2) possess orthogonal polarizations; the 525nm probe pulse (E_3) and signal (E_S) also have orthogonal polarizations. In our notation, ZXZX signifies that the pulses, E_1 and E_3, have the same polarization. That is, ZXZX is distinct from a second "polarization grating" tensor element, ZXXZ, wherein the E_1 and E_3 pulses have orthogonal polarizations. While ZXZX and

ZXXZ give rise to indistinguishable responses in many isotropic systems, we find that they do not yield identical signal amplitudes in nanocrystalline TiO_2 films. This property of the optical response may originate in the tetragonal symmetry of the anatase crystals.[24,25]

TG signals acquired for the dye-sensitized and neat TiO_2 films are presented in Figure 8.2. The dye-sensitized films exhibit a pulsewidth-limited spike at time-zero followed by an oscillatory response at positive delay. Quantitative analysis is carried out by fitting the signals with the phenomenological equation

$$S(T) = A_0 G(T;\delta) + \theta(T) \int_{-\infty}^{\infty} dt\, G(t;\delta) \left\{ A_1 \sin\left[\omega(t+T)+\Phi\right] \exp\left[\frac{-(t+T)}{\tau_1}\right] + A_2 \right\} \quad (8.1)$$

Here $\theta(T)$ is a Heaviside step function and $G(t;\delta)$ is a Gaussian function with a full width half maximum equal to δ. Fitting parameters are given in Table 8.1. Interestingly, the $142 cm^{-1}$ frequency of the coherence is independent of the molecular sensitizer, suggesting that the vibration is localized in TiO_2. However, vibrational coherences are not observed in the neat TiO_2 films under identical conditions. Using a TG experiment conducted with the ZXXZ tensor element, Figure 8.3 makes clear that the vibrational coherences indeed correspond to TiO_2. In addition, detection of the same $142 cm^{-1}$ resonance using a spontaneous Raman measurement further suggests that the vibrational coherences are associated with the ground electronic states of the composite molecule-TiO_2 systems. It is possible that excited state vibrational coherences contribute to the TG signal provided that the ground and excited state frequencies are identical. Notably, the presence of excited state vibrational coherences (initiated by Franck-Condon coupling) would not detract from the conclusions reached in this work.
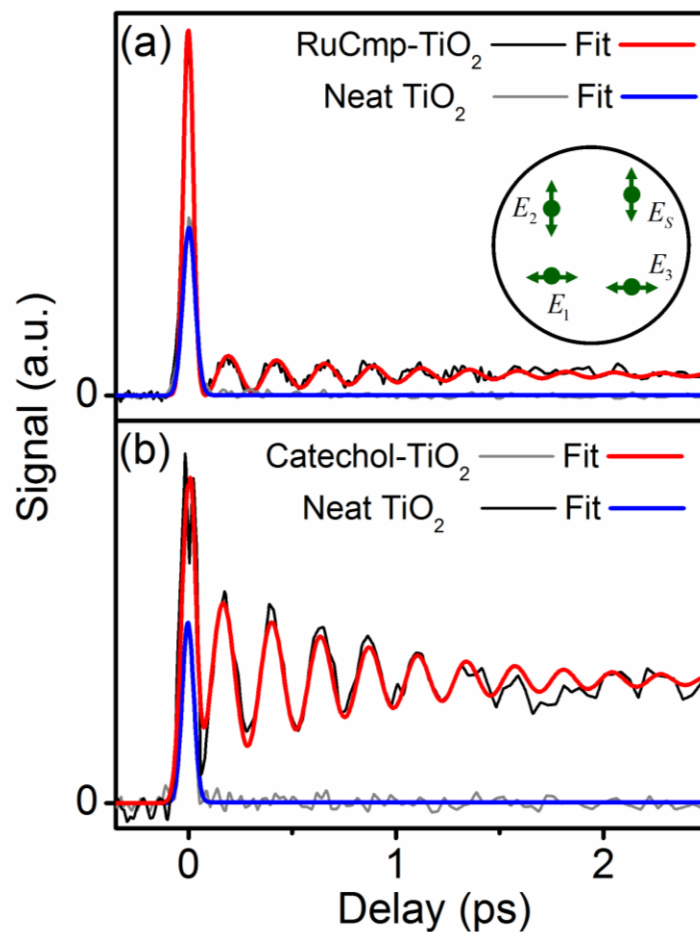
Figure 8.2: Absolute value of TG signals acquired under the ZXZX tensor element with "pump" (E_1 and E_2) and probe (E_3) pulses centered at 400nm and 525nm, respectively. Signals acquired for the molecule-TiO$_2$ composites are fit with a red line, whereas those obtained for the neat TiO$_2$ films are fit with a blue line. All samples including the neat TiO$_2$ films are in aqueous solutions (cf., Appendix A7). The inset of panel (a) illustrates the orientations of the four electric field polarizations involved in the ZXZX tensor element. Fitting components are given in Table 8.1.
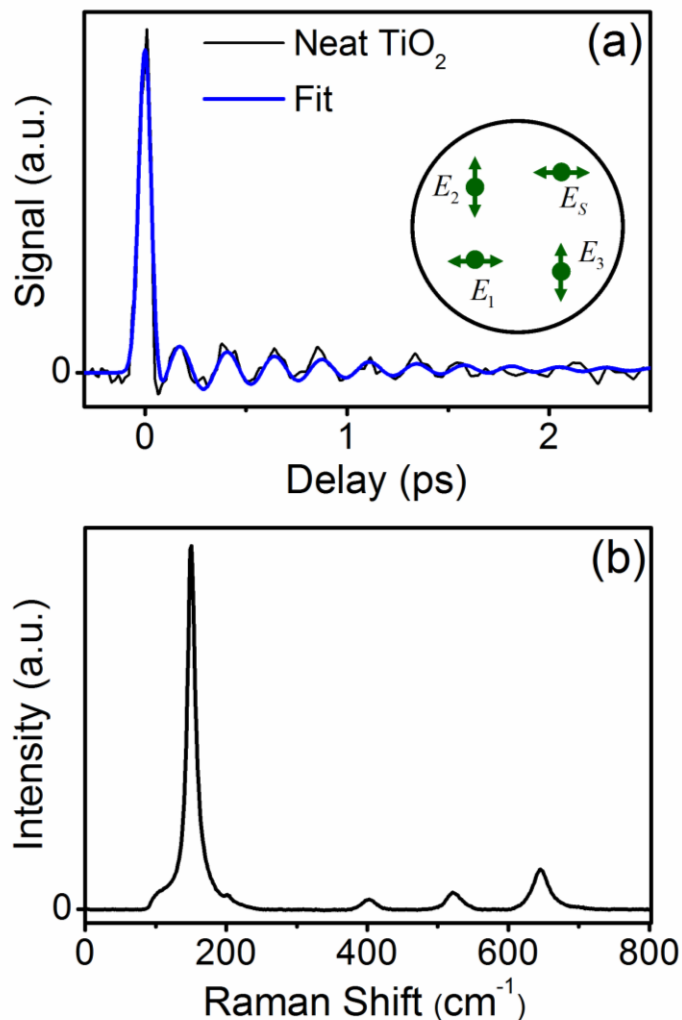
Figure 8.3: Absolute value of TG signals acquired under the ZXXZ tensor element for a neat TiO$_2$ film with "pump" (E_1 and E_2) and probe (E_3) pulses centered at 400nm and 525nm, respectively. The inset illustrates the orientations of the four electric field polarizations involved in the ZXXZ tensor element. Fitting components are given in Table 8.1. (b) Spontaneous Raman spectrum of the same TiO$_2$ film obtained with an excitation wavelength of 633nm. This measurement suggests that the vibrational coherence detected by TG is associated with the ground electronic state.

Table 8.1. Transient grating fitting parameters

Parameter	[a]RuCmp-TiO$_2$	[a]Catechol-TiO$_2$	[b]Neat TiO$_2$
A_0	0.979	0.917	0.987
δ (fs)	55	79	73
A_1	0.011	0.039	0.012
ω_{vib} (cm^{-1})	143	142	142
ϕ (rad.)	2.1	2.6	2.6
τ_1 (fs)	900	820	824
A_2	0.009	0.043	0.001

[a]ZXZX tensor element shown in Figure 8.2.

[b]ZXXZ tensor element shown in Figure 8.3.

Together, the measurements presented in Figures 8.2 and 8.3 suggest that the displacement in the vibrational coordinate is induced directly by photoexcitation of the system, not through a subsequent non-radiative process. For example, the present mechanism contrasts with the sequential process found in perylene-TiO$_2$, where vibrational coherence is induced by a 75fs electron transfer transition subsequent to photoexcitation.[26] Electron transfer induced vibrational coherences have also been observed in a rutile TiO$_2$ substrate sensitized with PbSe nanocrystals.[11] The key physical quantity governing the initiation of the vibrational coherences observed here is depicted in Figure 8.4. As in a resonance Raman experiment, the vibrational amplitude reflects the magnitude of the displacement in potential energy surfaces corresponding to the ground and excited electronic states.[27] What makes our findings particularly interesting is that the nuclear mode is

232

localized in TiO$_2$. Displacement in this mode makes clear that the electronic excitation produces a fairly significant change in the charge distribution within TiO$_2$. In other words, some of the electronic orbitals that participate in the electronic excitation must be delocalized between the two species at the interface.
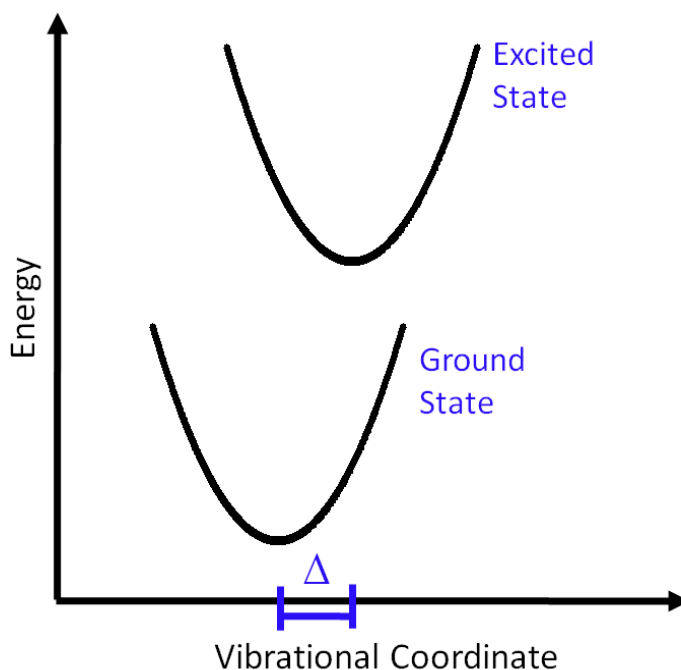
Figure 8.4: The amplitude of the vibrational coherence in the ~142cm^{-1} mode increases with the displacement in the potential energy minima associated with the ground and excited electronic states, Δ. We assign the vibrational motions detected in this work to the ground electronic states of the composite molecule-TiO$_2$ systems.

It is likely that little delocalization of the electronic orbitals occurs in the ground electronic state because the highest occupied molecular orbitals of RuCmp and catechol reside within the bandgap of TiO$_2$.[4,5,19] By contrast, the density of states in TiO$_2$ is much greater at energies corresponding to the lowest unoccupied molecular orbitals of the two sensitizers.[4,5,19] The excited state wavefunctions should therefore readily delocalize between species provided that the molecule-TiO$_2$ coupling is sufficient. Our TG experiments suggest

that charge-redistribution induced by the presence of the radiation (i.e., the transition dipole) gives rise to significant force on the vibrational coordinate. Furthermore, the magnitude of the force exerted on the coordinate, and the corresponding displacement, reflects the "amount" of charge redistribution in its vicinity. Thus, attainment of the size of the displacement (i.e., Huang-Rhys factor) can potentially provide quantitative information regarding delocalization in the excited state wavefunctions. The actual sizes of the displacements have not been obtained in the present study. However, qualitative physical insight can still be derived by comparing the vibrational amplitudes given in Table 8.1.

Strong vibronic coupling is expected in catechol-TiO_2 because its charge transfer absorbance band shows unambiguously that the excited electronic state is delocalized between species;[5,19] photoexcitation can therefore readily displace nuclear coordinates in TiO_2. However, the extent to which such forces are imparted is less clear *a priori* in RuCmp-TiO_2 because weaker molecule-TiO_2 interactions are mediated by the phosphate linker groups. Figure 8.2 shows that similar observations are made in both systems despite this difference in (nominal) coupling strengths. To evaluate the vibrational amplitudes for the two systems on a similar footing, we compare the coefficient representing the spike at time-zero, A_0, to that associated with the vibrational coherence, A_1. The ratios of amplitudes, A_0 / A_1, are 89 and 23 in RuCmp-TiO_2 and catechol-TiO_2, respectively. We hypothesize that the smaller ratio obtained in catechol-TiO_2 reflects its larger displacement, which is consistent with the dominant charge transfer character of its excited state. By the same rationale, we interpret the weaker vibronic coupling strength found in RuCmp-TiO_2 as a signature that the delocalization of electronic orbitals takes hold in a small portion of the ensemble. In other words, our data suggest that light absorption and electron injection are

correctly viewed as a non-sequential process for a relatively small fraction of the RuCmp-TiO$_2$ sites. It should be emphasized that the TG signals are important for reaching this insight, which is not obvious based on inspection of the linear absorbance spectra in Figure 8.1.

The above hypothesis assumes that the coherence spikes (at zero pulse delay) possess similar origins in both samples. Coherence spikes represent quasi-instantaneous nonlinearities (e.g., electronic polarizability) and are well-known in the TG literature.[28,29] Here it is important to note that such spikes do not require resonance enhancement; they are present even in transparent materials.[30] Because of this off-resonance contribution, we suggest that the glass cover slips and TiO$_2$ films (common to all samples) are primarily responsible for the spikes. The offsets in the TG signals measured at long delay times, A_2, reflect the excited state electronic structures of RuCmp-TiO$_2$ and Catechol-TiO$_2$. These long-lived signal components are unrelated to the coherent dynamics of interest. Transient absorption spectra for the two dye-sensitized films are presented in Appendix A7 and in the Supporting Information of Reference 23.

8.4. SUMMARY AND CONLUSIONS

In summary, TG signatures of strong molecule-TiO$_2$ interactions have been established using model systems spanning the weak and strong coupling regimes. We suggest that the amplitudes of photoinduced vibrational coherences are positively correlated with the charge transfer character of the optical transition (i.e., excited state delocalization). Notably, the detection of these vibrational coherences requires special tensor elements, which are not possible in conventional spontaneous Raman spectroscopy. Future work will explore

these physics using additional molecular sensitizers and semiconductors. The rapid signal acquisition afforded by coherent Raman techniques employing both broadband and narrowband pulses will facilitate the study of a wide range of systems.[21]

8.4. REFERENCES

(1)   Concepcion, J. J.; Jurss, J. W.; Brennaman, M. K.; Hoertz, P. G.; Patrocinio, A. O. T.; Iha, N. Y. M.; Templeton, J. L.; Meyer, T. J. *Acc. Chem. Res.* 2009, *42*, 1954-1965.

(2)   Grätzel, M. *Nature* 2001, *414*, 338-344.

(3)   Ardo, S.; Meyer, G. J. *Chem. Soc. Rev.* 2009, *38*, 115-164.

(4)   Anderson, N. A.; Lian, T. *Annu. Rev. Phys. Chem.* 2005, *56*, 491-519.

(5)   Duncan, W. R.; Prezhdo, O. V. *Annu. Rev. Phys. Chem.* 2007, *58*, 143-184.

(6)   Jakubikova, E.; Snoeberger III, R. C.; Batista, V. S.; Martin, R. L.; Batista, E. R. *J. Phys. Chem. A* 2009, *113*, 12532-12540.

(7)   Haque, S. A.; Tachibana, Y.; Willis, R. L.; Moser, J. E.; Grätzel, M.; Klug, D. R.; Durrant, J. R. *J. Phys. Chem. B* 2000, *104*, 538-547.

(8)   Morris-Cohen, A. J.; Frederick, M. T.; Cass, L. C.; Weiss, E. A. *J. Am. Chem. Soc.* 2011, *133*, 10146-10154.

(9)   Nozik, A. J. *Annu. Rev. Phys. Chem.* 2001, *52*, 193-231.

(10)   Pandey, A.; Guyot-Sionnest, P. *J. Phys. Chem. Lett.* 2010, *1*, 45-47.

(11)   Tisdale, W. A.; Williams, K. J.; Timp, B. A.; Norris, D. J.; Aydil, E. S.; Zhu, X.-Y. *Science* 2010, *328*, 1543-1547.

(12)   Morandeira, A.; Boschloo, G.; Hagfeldt, A.; Hammarström, L. *J. Phys. Chem. C* 2008, *112*, 9530–9537.

(13)   Xiong, W.; Laaser, J. E.; Paoprasert, P.; Franking, R. A.; Hamers, R. J.; Gopalan, P.; Zanni, M. T. *J. Am. Chem. Soc.* 2009, *131*, 18040-18041.

(14)   Ghosh, H. N.; Asbury, J. B.; Lian, T. *J. Phys. Chem. B* 1998, *102*, 6482-6486.

(15)   Asbury, J. B.; Hao, E.; Wang, Y.; Ghosh, H. N.; Lian, T. *J. Phys. Chem. B* 2001, *105*, 4545-4557.

(16)   Marcus, R. A. *J. Chem. Phys.* 1965, *43*, 679-701.

(17)   Gerischer, H. *Surf. Sci.* 1969, *18*, 97-122.

(18)   Gerischer, H. *Photochem. Photobiol.* 1972, *16*, 243-260.

(19)   Redfern, P. C.; Zapol, P.; Curtiss, L. A.; Rajh, T.; Thurnauer, M. C. *J. Phys. Chem. B* 2003, *107*, 11419-11427.

(20)   Lee, S.-H. A.; Abrams, N. M.; Hoertz, P. G.; Barber, G. D.; Halaoui, L. I.; Mallouk, T. E. *J. Phys. Chem. B* 2008, *112*, 14415-14421.

(21)   Womick, J. M.; Miller, S. A.; Moran, A. M. *J. Phys. Chem. A* 2009, *113*, 6587-6598.

(22)   Lepetit, L.; Chériaux, G.; Joffre, M. *J. Opt. Soc. Am. B* 1995, *12*, 2467-2474.

(23)   Miller, S. A.; West, B. A.; Curtis, A. C.; Papanikolas, J. M.; Moran, A. M. *J. Chem. Phys.* 2011, *135*, 081101-1-4.

(24)   Cromer, D. T.; Herrington, K. *J. Am. Chem. Soc.* 1955, *77*, 4708-4709.

(25)   Silversmit, G.; Poelman, H.; Fiermans, L.; De Gryse, R. *Solid State Communications* 2001, *119*, 101-104.

(26)   Zimmerman, C.; Willig, F.; Ramakrishna, S.; Burnfeindt, B.; Pettinger, B.; Eichberger, R.; Storck, W. *J. Phys. Chem. B* 2001, *105*, 9245-9253.

(27)   Kelley, A. M. *J. Phys. Chem. A* 1999, *103*, 6891-6903.

(28)   Park, J.-S.; Joo, T. *J. Chem. Phys.* 2004, *120*, 5269-5274.

(29)   Moran, A. M.; Nome, R. A.; Scherer, N. F. *J. Chem. Phys.* 2006, *125*, 031101:031101-031104.

(30)   Vöehringer, P.; Scherer, N. F. *J. Phys. Chem.* 1995, *99*, 2684-2695.

APPENDIX 1 . MATLAB ALGORITHM FOR NUMERICAL CORRECTION OF

THIRD ORDER DISPERSION IN ULTRAFAST PULSES

Below, the Matlab (R2007b) algorithm discussed in Chapter 3.2.4 developed for the numerical correction of third and higher order pulse dispersions in ultrafast pulses is given. Black and blue text represents executable code, while green text represents non-executable labels/descriptions added for clarity. Code shown within sections of dashed lines indicates the use of subroutines.

```
clear;

% OPEN FILES

%Data.dat = Uncompressed data matrix array where columns represent
           %different time delays and rows represent different
           wavelengths

%Time.dat = One dimensional array defining the column time delays of
           %"data.dat" recorded directly from the mechanical stage
           %controlling the pulse delay

%wvln.dat = One dimensional array defining the wavelengths of the rows of
           %"data.dat"

A0=dlmread('.\Data.dat');
Time=dlmread('.\Time.dat');
wvln2=dlmread('.\wvln.dat');



% SOME ADJUSTABLE PARAMETERS
% npts=# of time points to process
% npix=# of pixels in CCD array
% islc1=wavelength to take slice through 2D plot
%
[a,b]=size(A0);
npts=b;  % ***NOT GENERAL***
npix=length(wvln2);

%Change time values to delay relative to absolute time zero. Note
%that "x" represents the mechanical stage time position for time zero

t=1:npts;
delay(t)=Time(t)-x; ***NOT GENERAL***
%The data matrix is now input into the Scorrect subroutine where, after
%processing, the output will be a new "compressed" data matrix.
```

```
[NewDelay,CompressedData] = Scorrect(A0,wvln2,Time);

---------------------------------------------------------------------------------
function [delay2,ReS] = Scorrect(S,wvln,time)
%
%tlow = Lower pulse delay endpoint for the new interpolated
        % pulse delay axis
%thigh = Upper pulse delay endpoint for the new interpolated
        % pulse delay axis
%tpt = Desired number of pulse delay points to be included in
        % the new interpolated pulse delay axis.  Note, this
        % number should not be less than the number of time
        % points in the orignal data matrix or the output data
        % matrix will be incorrectly interpolated.
%
tlow=-1.2;    %***NOT GENERAL***
thigh=5.2;    %***NOT GENERAL***
tpt=130;      %***NOT GENERAL***
tstep=(thigh-tlow)/tpt;

x=1:tpt
y=x-1;

for m=1:tpt
delay2(m)=10^(log10(thigh-tlow+1)/tpt*y(m))+tlow-1;
end
%
kj=1:length(time);
kg=1:tpt;
for k=1:length(wvln);

%The subroutine "delaycal" now creates a one dimensional array based on
%the FROG calibration in an "instantaneously" responding medium that
%describes the wavelength dependent "time zero" of the pulses.

[tzero] = delaycal(k,wvln);
---------------------------------------------------------------------------------
function [tzero] = delaycal(ii,wvln)
%

tzero = %Calibration polynomial describing the wavelength dependent "time
        %zero" of the pulses.  Note that the polynomial is written as a
        %function of wvln(ii).

return;
---------------------------------------------------------------------------------

delay(kj)=-tzero+time(kj);
reslc(kj)=S(k,kj);
g(kj)=isfinite(reslc(kj));
reslcreal=reslc(g(kj));
delayreal=delay(g(kj));

if length(reslcreal)>1
else
```

```matlab
    reslcreal(2)=0;
    delayreal(2)=0.0000001;
end
%reslc(kj)=abs(S(k,kj));
%


reslc2 = interp1(delayreal,reslcreal,delay2);
ReS(k,kg)=reslc2(kg);

end
return;

------------------------------------------------------------------------------
```

APPENDIX 2 . MATLAB ALGORITHM FOR PROCESSING

INTERFEROMETRIC TRANSIENT GRATING SIGNALS

Below is given the general Matlab (R2007b) algorithm developed for the processing of interferometric transient grating signals measured with the experimental apparatus discussed in Chapter 3.6.5. It should be noted that if necessary, the algorithm shown above in Appendix 1 would have already been performed on the data in order to remove high order pulse dispersions. Note that black and blue text represents executable code, while green text represents non-executable labels/descriptions added for clarity. Code shown within sections of dashed lines indicates the use of subroutines.

```
clear;
%
% OPEN FILES

%CompressedData.dat = Compressed interferogram data matrix array where
                     %columns represent different time delays and rows
                     %represent different wavelengths

%Time.dat = One dimensional array defining the column time delays of
           %"CompressedData.dat" recorded either directly from the
           %mechanical stage controlling the pulse delay or from the
           %algorithm shown in Appendix 1.

%wvln.dat = One dimensional array defining the wavelengths of the rows of
           %"CompressedData.dat"

%LOSpec = Measured spectrum of local oscillator pulse

A0=dlmread('.\CompressedData.dat');
wvln=dlmread('.\wvln.dat');
Time=dlmread('.\Time.dat');
lospecA=dlmread('.\LOSpec.dat');

% SOME ADJUSTABLE PARAMETERS
% npts=# of time points to process
% npix=# of pixels in CCD array
% islc1=wavelength to take slice through 2D plot
% window=wavelength window in nm over which to sum
npts=150;  % ***NOT GENERAL***
```

```matlab
npix=1340; % ***NOT GENERAL***


%Change time values to delay relative to zero pulse delay. Note
%that "x" represents the mechanical stage time position for time zero
%Note also that this step is not necessary if "Time.dat" is input from
%the algorithm given in Appendix 1 as the delay axis will have already
been
%calibrated correctly.

 t=1:npts;
 delay(t,1)=Time(t)-x;    % ***NOT GENERAL***

% PROCESS INTERFEROGRAMS AND CORRECT SIGNAL AMPLITUDES FOR LOCAL
OSCILLATOR
% SPECTRUM

% fntrp=new frequency axis with equally spaced points
% z2=complex frequency domain field
% emt=emission time axis
% z1=complex time domain field
%

% CONVERT WAVELENGTH (nm) TO FREQUENCY (rad/fs)
kj=1:npix;
for k=1:npix
    ff(k)=1885/wvln(k);
end

for k=1:npts
     l=1:npix;

        ifsp4(l)=A0(l,k);

%Here the interferograms are input into the subroutine
%"ftsiDataAnalysis5" and processed to yield TG signals

    [fntrp,z2d,emt,z1d,filt]=ftsiDataAnalysis5(ifsp4,ff,phcal);

--------------------------------------------------------------------------------

function [fntrp,z2,time,z1,filt] = ftsiDataAnalysis5(s1,ff,phinit)
%
% INTERPOLATE FOR LINEARITY IN FREQUENCY
%
npix=length(ff);
fntrp(1)=ff(1);
dw=(ff(1)-ff(npix))/(npix-1);
kn=2:npix;
fntrp(kn)=fntrp(1)-(kn-1)*dw;
sp1 = interp1(ff,s1,fntrp);
%
% FOURIER TRANSFORM TO TIME DOMAIN
%
tsp1=ifft(sp1);
```

243

```
kj=1:1340;
time(kj)=-3.141592/dw+2*3.141592*(kj-1)/dw/npix;
%
% SHUFFLE
%
n=length(tsp1);
for k=1:1:n/2
    z1(n/2+k)=tsp1(k);
    z1(k)=tsp1(n/2+k);
end
%
% APODIZATION PARAMETERS. These are determined by plotting emt vs.
%abs(z1d)and centering the apodization function (filt) around the peak on
%the right (the signal peak).  See Figure A2.1
%
kft=1:length(z1);
x0=781;  % ***NOT GENERAL***773
dx=10;   % ***NOT GENERAL***
ifilt=0; % ***NOT GENERAL***
for km=1:n
    filt(km)=1;
    if km<x0-ifilt
     filt(km)=exp(-2.773*((km - x0+ifilt)./dx).^2);
    end
    if km>x0+ifilt
     filt(km)=exp(-2.773*((km - x0-ifilt)./dx).^2);
    end
end
z3(kft)=z1(kft).*filt(kft);
%
% FOURIER TRANSFORM BACK TO FREQUENCY DOMAIN
%
z2=fft(z3);
%
% PARAMETERIZE CONSTANT AND LINEAR TERMS IN SPECTRAL PHASE
%
tau=300;  % ***NOT GENERAL***
absolutephase = 2; % ***NOT GENERAL***
is=-1;
for k=1:n
   z2(k)=z2(k)*exp(-j*(fntrp(k)*tau-absolutephase))*is; % ***NOT
%GENERAL***
   is=is*-1;
end
%
return;

--------------------------------------------------------------------------------

for m=1:npix
        z1d2(m,k)=z1d(m);

        A1(m,k)=z2d(m);/sqrt(lospecA(m)); %%Not General%%

        phA1(m,k) = -atan(imag(z2d(m))/real(z2d(m)));
```

```
        ampA1(m,k)=abs(A1(m,k));

        wvln2(m)=1885/fntrp(m);
    end
    k
end
```

%Here amplA1 represents the absolute value of the TG signal field. In
%order to view only the real and or imaginary projection, the signal phase
%must be used. First, the spectral phase is unwrapped for convenience.
%Here the subroutine "phunwrap" is used to unwrap the spectral phase at
%each pulse delay point.

```
k=1:npts
for m=1:1340
    phunwrapped(m,t)=phunwrap(phA1(m,t));
end
```

```
function [ph2] = phunwrap(ph);

kj=1:length(ph);
ph2=ph(kj);
for ki=2:length(ph)
for li=ki:length(ph)
%
if (ph(ki)-ph(ki-1)  > 2)
   ph2(li)=ph2(li)-3.14159;
end
if (ph(ki)-ph(ki-1) < -2)
   ph2(li)=ph2(li)+3.14159;
end
%
end
end
%
return;
```

%To obtain the real projection (i.e., transient absorption) of the TG
%signal field multiply the cosine of the signal phase by the absolute
%value of the signal.

```
Real = cos(phunwrapped)*ampA1;
```

%To obtain the imaginary projection (i.e., dispersive signal) of the TG
%signal field multiply the sin of the signal phase by the absolute value
%of the signal.

```
Imag = sin(phunwrapped)*ampA1;
```
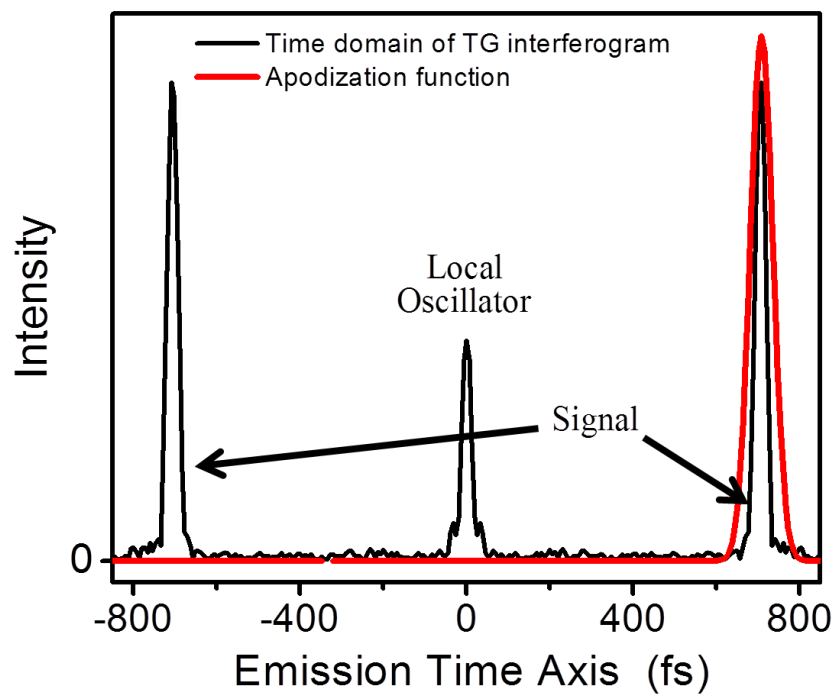
Figure A2.1: Time domain picture of a measured TG interferogram at a single pulse delay. The local oscillator intensity is removed from the measured signal through the use of an apodization function (red) which is centered over the positive signal peak. Following multiplication with the apodization function, the time domain TG signal is Fourier transformed back to the frequency domain.

APPENDIX 3 . SUPPORTING INFORMATION FOR CHAPTER 4:

"FEMTOSECOND RELAXATION DYNAMICS OF Au$_{25}$L$_{18}^{-}$ MONOLAYER-

PROTECTED CLUSTERS"

A3.1. FITS TO TRANSIENT ABSORPTION MEASUREMENTS

This section presents fits to the measurements shown in Figure 4.2(a) of Chapter 4: "Femtosecond Relaxation Dynamics of Au$_{25}$ Monolayer-Protected Clusters".
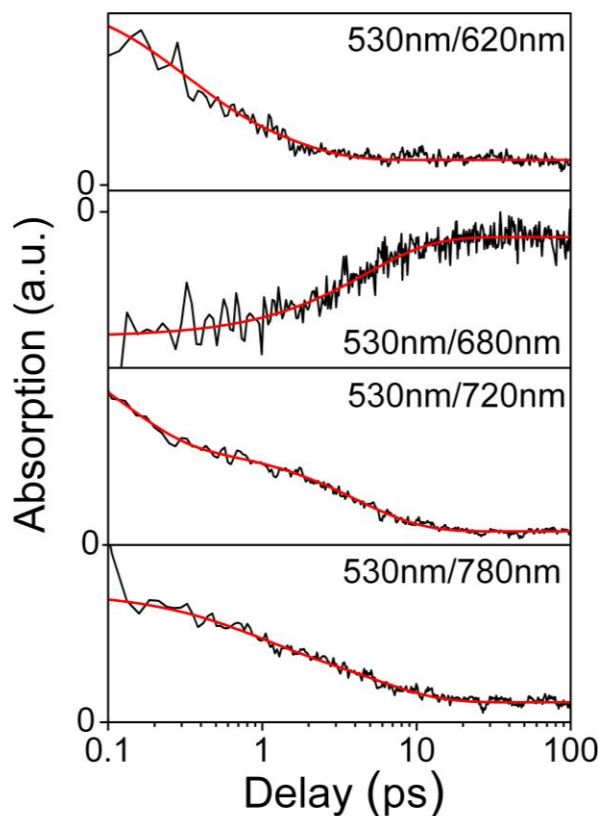
Figure A3.1: Transient absorption signals (black) and fits (red) at selected probe wavelengths following excitation with a 530 nm laser pulse. The pump and probe wavelengths are given in each panel as $\lambda_{pump}/\lambda_{probe}$. Parameters corresponding to the fits are defined by Equation 4.1 and Table 4.1 of Chapter 4.

A3.2. TRANSIENT ABSORPTION MEASUREMENTS WITH PARALLEL AND PERPENDICULAR PUMP AND PROBE POLARIZATIONS

The transient "pump-probe" anisotropy is computed by the standard formula

$$r(T) = \frac{S_{\parallel}(T) - S_{\perp}(T)}{S_{\parallel}(T) + 2S_{\perp}(T)} \tag{A3.1}$$

where $S_{\parallel}(T)$ and $S_{\perp}(T)$ are signals acquired with parallel and perpendicular laser pulse polarizations, respectively.
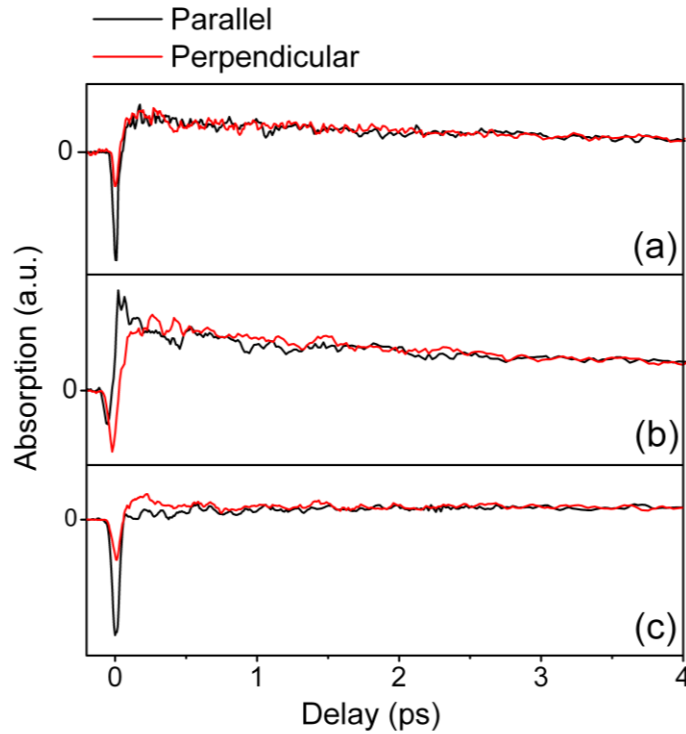
Figure A3.2: Transient absorption measurements corresponding to Figure 4.5 in Chapter 4. Pulse configurations are: (a) 530nm pump/530 nm probe; (b) 530nm pump/720 nm probe; (c) 660nm pump/720 nm probe. Black and red lines respectively represent measurements performed with parallel and perpendicular pump and probe polarizations.

APPENDIX 4 . SUPPORTING INFORMATION FOR CHAPTER 5:

"NONLINEAR OPTICAL SIGNATURES OF CORE AND LIGAND

ELECTRONIC STATES IN $Au_{24}PdL_{18}$"

A4.1. LOW TEMPERATURE ABSORPTION SPECTRA

Absorbance and fluorescence spectra are measured at various temperatures using a 1 mm thick cuvette mounted in a liquid nitrogen cooled cryostat (Optistat-DN). The samples are prepared in dichloromethane with an absorbance of 0.53 at 530 nm in 1 mm path length. A balanced deuterium tungsten lamp (DH-2000-BAL) is used as the light source. Detection is achieved with a back-illuminated CCD array (Princeton Instruments PIXIS 100B) mounted on a 0.3 meter spectrograph.

A4.2. TRANSIENT GRATING FITTING PARAMETERS

This section presents all parameters involved in fits of the transient grating signals shown in Figure 5.3 in Chapter 5. All fits are conducted using Equation 5.1.

$$S(t;w) = \sum_{m=1}^{3} \int_{-\infty}^{t} dt' G(t';w) A_m \exp(-t'/\tau_m) dt' \qquad (A4.1)$$

Equation A4.1 uses a Gaussian instrument response function, $G(t';w)$, to deconvolute the finite instrument response width, w, from the three exponential decay components m. We reiterate that the instrument response width is comparable to the time scale of the process related to τ_1 (i.e., equilibration of electrons in core). Example fits are plotted in Figure 5.2 of the main text.

Table A4.1 Transient grating fitting parameters associated with component $m=1$ of Equation A4.1. These dynamics are assigned to equilibration of electrons in the metal core.

Signal Wavelength (nm)	A_1 (a.u.)	τ_1 (ps)	w (ps)
625	526 $^{+}/_{-}$ 14	0.004 $^{+}/_{-}$ 0.002	0.05
630	381 $^{+}/_{-}$ 10	0.006 $^{+}/_{-}$ 0.003	0.05
640	146 $^{+}/_{-}$ 4	0.011 $^{+}/_{-}$ 0.001	0.05
645	100 $^{+}/_{-}$ 7	0.010 $^{+}/_{-}$ 0.003	0.05
650	81 $^{+}/_{-}$ 2	0.013 $^{+}/_{-}$ 0.001	0.06
660	50 $^{+}/_{-}$ 4	0.014 $^{+}/_{-}$ 0.001	0.10
675	23.5 $^{+}/_{-}$ 0.5	0.026 $^{+}/_{-}$ 0.002	0.11
690	36.5 $^{+}/_{-}$ 0.8	0.014 $^{+}/_{-}$ 0.001	0.15
700	12.4 $^{+}/_{-}$ 0.8	0.028 $^{+}/_{-}$ 0.003	0.14
715	10.6 $^{+}/_{-}$ 0.3	0.027 $^{+}/_{-}$ 0.001	0.15
720	9.7 $^{+}/_{-}$ 0.8	0.032 $^{+}/_{-}$ 0.003	0.15
735	20.7 $^{+}/_{-}$ 0.7	0.014 $^{+}/_{-}$ 0.001	0.15
740	27 $^{+}/_{-}$ 1	0.014 $^{+}/_{-}$ 0.001	0.14
750	7 $^{+}/_{-}$ 2	0.032 $^{+}/_{-}$ 0.005	0.15

Table A4.2. Transient grating fitting parameters associated with component $m = 2$ of Equation A4.1. These dynamics are assigned to core-to-ligand internal conversion.

Signal Wavelength (nm)	A_2 (a.u.)	τ_2 (ps)	w (ps)
625	15.6 $^{+}/_{-}$ 0.4	0.54 $^{+}/_{-}$ 0.03	0.05
630	13.8 $^{+}/_{-}$ 0.4	0.52 $^{+}/_{-}$ 0.03	0.05
640	11.3 $^{+}/_{-}$ 0.4	0.45 $^{+}/_{-}$ 0.02	0.05
645	10.1 $^{+}/_{-}$ 0.5	0.42 $^{+}/_{-}$ 0.03	0.05
650	9.3 $^{+}/_{-}$ 0.6	0.33 $^{+}/_{-}$ 0.03	0.06
660	3.7 $^{+}/_{-}$ 0.3	0.41 $^{+}/_{-}$ 0.05	0.10
675	3.0 $^{+}/_{-}$ 0.2	0.46 $^{+}/_{-}$ 0.04	0.11
690	1.87 $^{+}/_{-}$ 0.04	0.51 $^{+}/_{-}$ 0.04	0.15
700	1.46 $^{+}/_{-}$ 0.03	0.52 $^{+}/_{-}$ 0.04	0.14
715	1.05 $^{+}/_{-}$ 0.03	0.53 $^{+}/_{-}$ 0.05	0.15
720	1.14 $^{+}/_{-}$ 0.04	0.56 $^{+}/_{-}$ 0.06	0.15
735	1.28 $^{+}/_{-}$ 0.08	0.53 $^{+}/_{-}$ 0.06	0.15
740	1.9 $^{+}/_{-}$ 0.1	0.39 $^{+}/_{-}$ 0.04	0.14
750	1.57 $^{+}/_{-}$ 0.07	0.40 $^{+}/_{-}$ 0.04	0.15

Table A4.3 Transient grating fitting parameters associated with component $m=3$ of Equation A4.1. These dynamics are assigned to solvation of the semiring moieties subsequent to internal conversion.

Signal Wavelength (nm)	A_3 (a.u.)	τ_3 (ps)	w (ps)
625	2.5 $^+/_-$ 0.3	18 $^+/_-$ 3	0.05
630	2.2 $^+/_-$ 0.3	18 $^+/_-$ 3	0.05
640	1.8 $^+/_-$ 0.2	24 $^+/_-$ 4	0.05
645	1.5 $^+/_-$ 0.1	21 $^+/_-$ 4	0.05
650	1.3 $^+/_-$ 0.1	28 $^+/_-$ 5	0.06
660	0.53 $^+/_-$ 0.05	31 $^+/_-$ 7	0.10
675	0.51 $^+/_-$ 0.04	31 $^+/_-$ 6	0.11
690	0.41 $^+/_-$ 0.03	34 $^+/_-$ 6	0.15
700	0.33 $^+/_-$ 0.02	35 $^+/_-$ 7	0.14
715	0.24 $^+/_-$ 0.02	33 $^+/_-$ 6	0.15
720	0.27 $^+/_-$ 0.02	31 $^+/_-$ 5	0.15
735	0.25 $^+/_-$ 0.02	31 $^+/_-$ 5	0.15
740	0.39 $^+/_-$ 0.03	25 $^+/_-$ 4	0.14
750	0.39 $^+/_-$ 0.03	23 $^+/_-$ 4	0.15

APPENDIX 5 . SUPPORTING INFORMATION FOR CHAPTER 6: "EXCITED STATE PHOTOPHYSICS IN A LOW BAND GAP POLYMER WITH HIGH PHOTOVOLTAIC EFFICIENCY"

A5.1. ELECTRONIC STRUCTURE CALCULATIONS

Below we describe the procedure by which the molecular geometries of oligomers used in the ZINDO electronic structure calculations are created. All calculations discussed below were conducted using Gaussian 2009 and GaussView version 3.09. In order to reduce computational expense, alkane side chains branching from the indicated atoms (*) were replaced with methyl groups as shown in Figure A5.1. Because the electronic transitions of interest involve the conjugated region of the polymer backbone, removal of these side chains has little effect on the parameters obtained from the calculations.
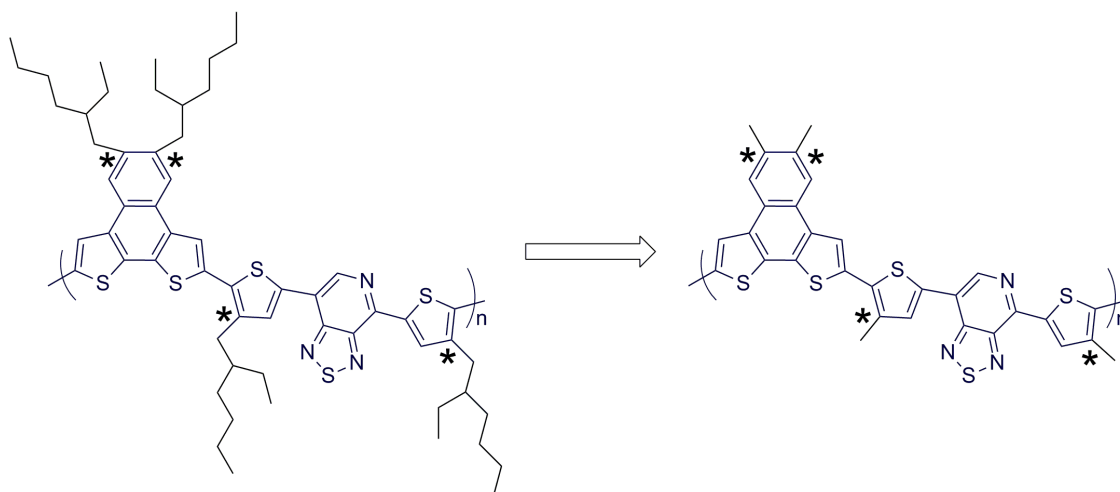

Figure A5.1: The alkane side chains of PNDT-DTPyT branching from the atoms indicated with an asterisk are replaced methyl groups in order to manage computational expense in both the DFT geometry optimization and ZINDO electronic structure calculations. Removal of these aliphatic groups has little effect on the lowest energy electronic transitions.

The equilibrium structure of the monomer in vacuo was computed using a geometry optimization performed at the B3LYP/3-21G level basis set. The charge and spin of the structure were set to zero and singlet, respectively. The optimized geometry of the monomer is shown below in Figure A5.2, which confirms that the monomer adopts a planar geometry. The two carbon atoms labeled with asterisks in Figure A5.2 bond to adjacent repeat units in the oligomers. To estimate the relative orientations of adjacent repeat units, a separate B3LYP/3-21G geometry optimization was performed on the dimer. The results of the geometry optimization are shown below in Figure A5.3, which again indicates that the dimer exhibits a planar geometry.
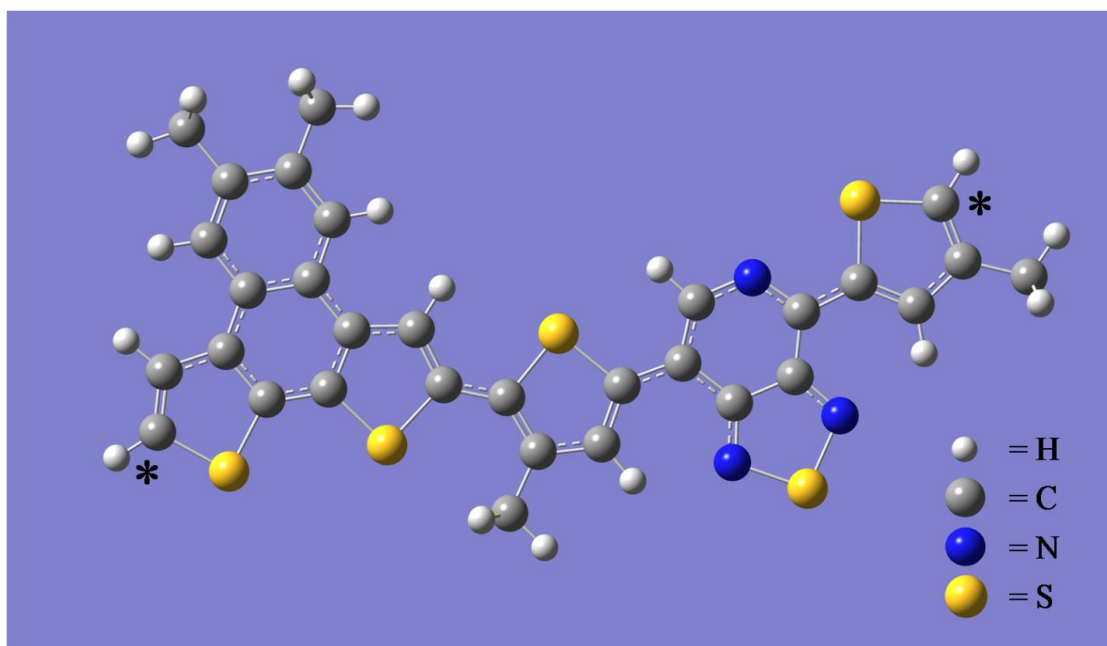

Figure A5.2: Optimized geometry as calculated by Density Functional Theory of the PNDT-DTPyT repeat unit. The two carbon atoms labeled with asterisks indicate where the linkage between units occurs. This geometry is used as input for the ZINDO electronic structure calculations discussed in Chapter 6.1.
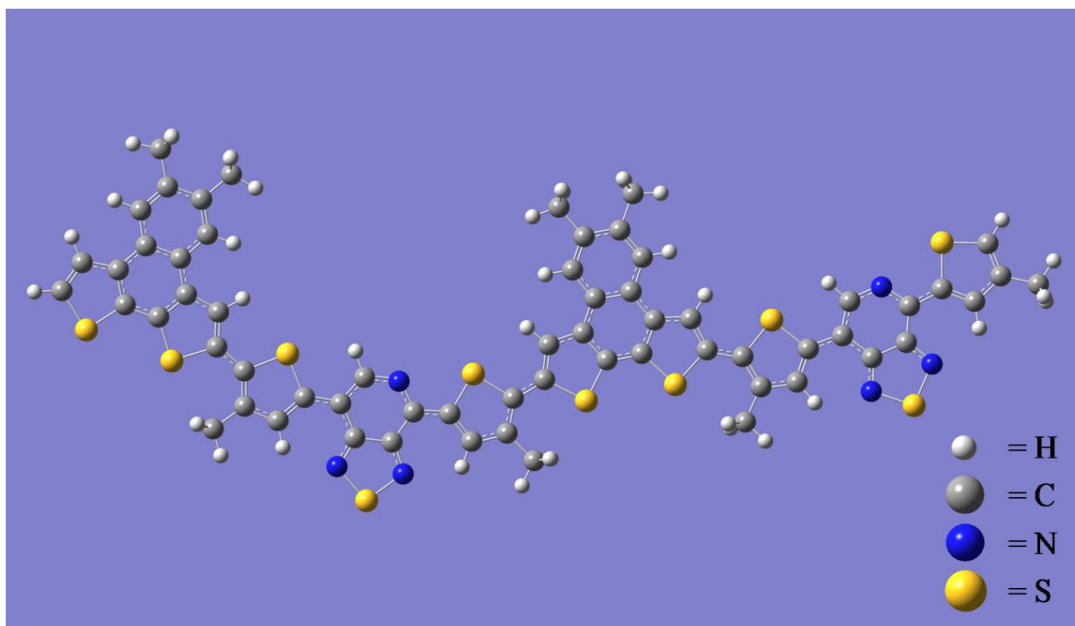
Figure A5.3: Optimized geometry as calculated by Density Functional Theory of the PNDT-DTPyT dimer. This geometry is also used as input for the ZINDO electronic structure calculations discussed in Chapter 6.1.

For oligomers possessing more than two monomer segments, Gaussian input files were created by assuming: (i) each repeat unit possesses the structure of the optimized monomer; (ii) the relative orientations of adjacent units resemble those of the optimized dimer. Under these assumptions, both rotation and translation operations on the coordinates of each repeat unit are required to generate oligomers with arbitrary length. This procedure is described with Equations A5.1 and A5.2

$$[C_{i+1}] = [R][C_i] + [T] \tag{A5.1}$$

$$[Oligomer_i] = \{[C_1], [C_2], [C_3], ... [C_i]\} \tag{A5.2}$$

Here $[R]$ is a matrix that rotates the monomer about an axis normal to the plane of its rings, $[T]$ is a translation vector, $[C_i]$ is a matrix containing all of the Cartesian coordinates of repeat unit, i, and $[C_{i+1}]$ is a matrix containing the Cartesian coordinates of the adjacent repeat

unit. Equation A5.2 indicates that the oligomers are periodic in the geometry of the optimized monomer. For clarity, an example is given below demonstrating how the coordinates (in Å) of the second repeat unit in the dimer, $[C_2]$, are generated starting with the original monomer coordinates, $[C_1]$.

$$[C_2]=[R][C_1]+[T]$$

$$[C_2]=\begin{bmatrix} 0.976 & 0.228 & 2.79 \times 10^{-5} \\ -0.228 & 0.974 & 1.34 \times 10^{-3} \\ 2.79 \times 10^{-4} & -1.31 \times 10^{-3} & 1.00 \end{bmatrix}[C_1]+\begin{bmatrix} 5.15 \\ -17.4 \\ 0.208 \end{bmatrix} \qquad \text{(A5.3)}$$

$$[Oligomer_2]=\{[C_1],\ [C_2]\} \qquad \text{(A5.4)}$$

For oligomers possessing more than two repeat units, the above process is repeated until the desired number of units is reached. In this study, the process is repeated up to the oligomer containing ten repeat units (Oligomer$_{10}$). The resulting structures are shown in Figures A5.4-A5.10.

These structures generated with the above procedure are then used as input geometries for the ZINDO electronic structure calculations. Excitation energies and oscillator strengths associated with the six lowest energy excited states are calculated using the ZINDO method. For each calculation, the transition exhibiting the largest oscillator strength is selected for use in our empirical model. Figure 6.3 of Chapter 6 displays these transition frequencies and oscillator strengths.
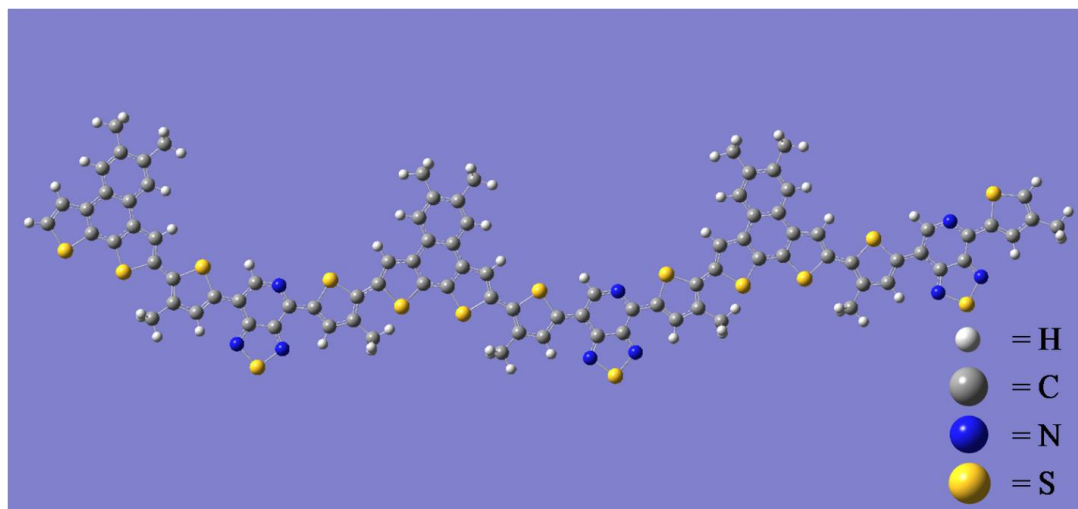
Figure A5.4: Calculated structure of the oligomer of PNDT-DTPyT containing three repeat units. This geometry is used as input in the ZINDO electronic structure calculations discussed in Chapter 6.1. Note that this structure is not a result of a DFT geometry optimization, but is mathematically calculated assuming that the *trans* linkage shown in Figure A5.3 is periodic.

Figure A5.5: Calculated structure of the oligomer of PNDT-DTPyT containing four monomer segments. This geometry is used as input in the ZINDO electronic structure calculations discussed in Chapter 6.1. Note that this structure is not a result of a DFT geometry optimization, but is mathematically calculated assuming that the *trans* linkage shown in Figure A5.3 is periodic.

Figure A5.6: Calculated structure of the oligomer of PNDT-DTPyT containing five monomer segments. This geometry is used as input in the ZINDO electronic structure calculations discussed in Chapter 6.1. Note that this structure is not a result of a DFT geometry optimization, but is mathematically calculated assuming that the *trans* linkage shown in Figure A5.3 is periodic.
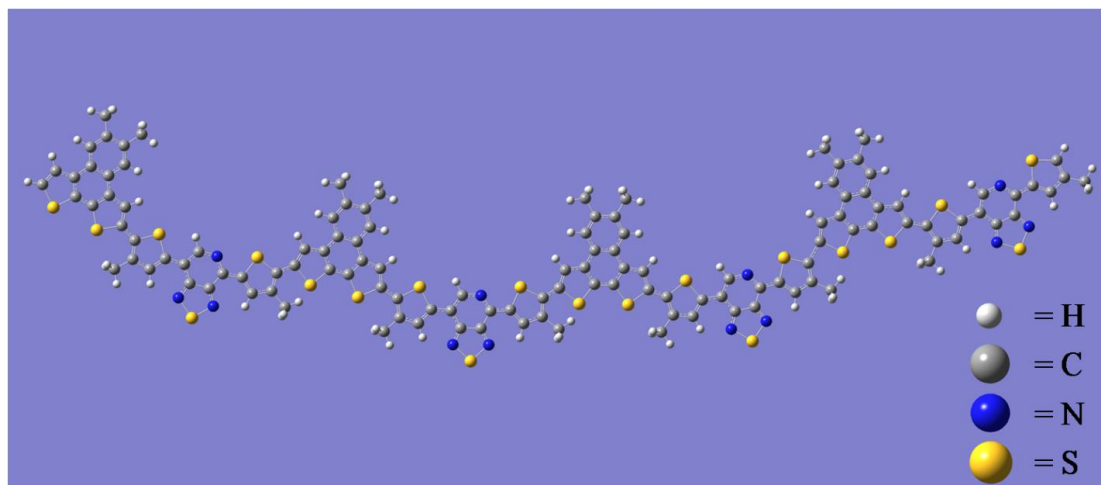

Figure A5.7: Calculated structure of the oligomer of PNDT-DTPyT containing six monomer segments. This geometry is used as input in the ZINDO electronic structure calculations discussed in Chapter 6.1. Note that this structure is not a result of a DFT geometry optimization, but is mathematically calculated assuming that the *trans* linkage shown in Figure A5.3 is periodic.
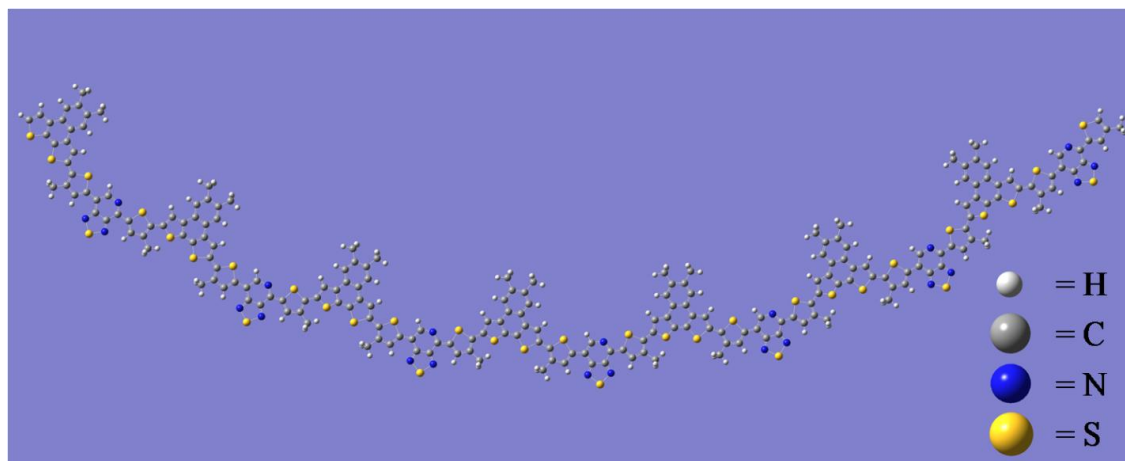
Figure A5.8: Calculated structure of the oligomer of PNDT-DTPyT containing seven repeat units. This geometry is used as input in the ZINDO electronic structure calculations discussed in Chapter 6.1. Note that this structure is not a result of a DFT geometry optimization, but is mathematically calculated assuming that the *trans* linkage shown in Figure A5.3 is periodic.
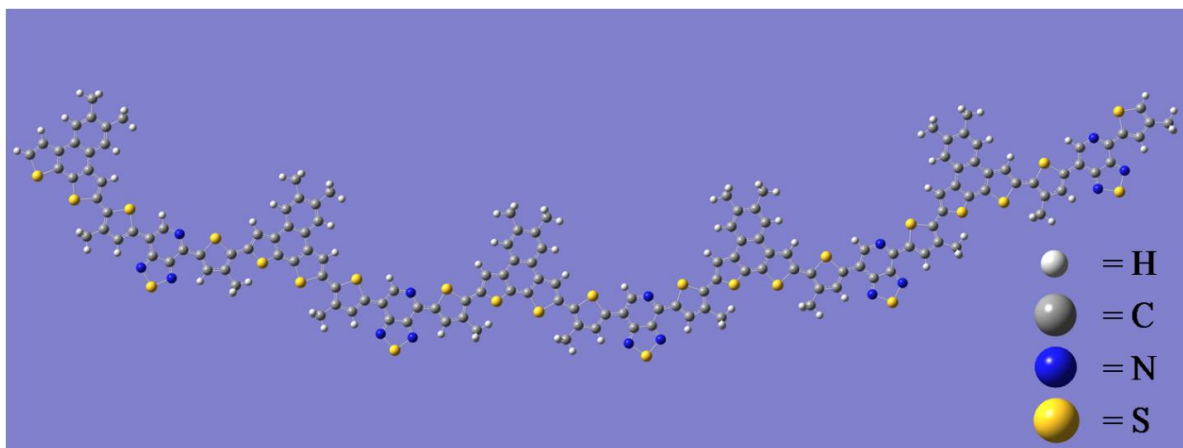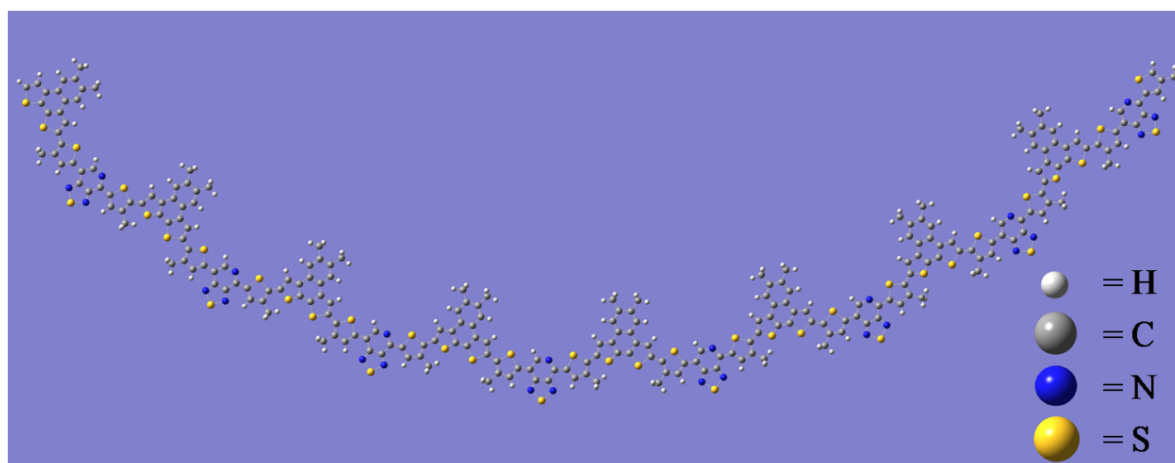

Figure A5.9: Calculated structure of the oligomer of PNDT-DTPyT containing eight repeat units. This geometry is used as input in the ZINDO electronic structure calculations discussed in Chapter 6.1. Note that this structure is not a result of a DFT geometry optimization, but is mathematically calculated assuming that the *trans* linkage shown in Figure A5.3 is periodic.
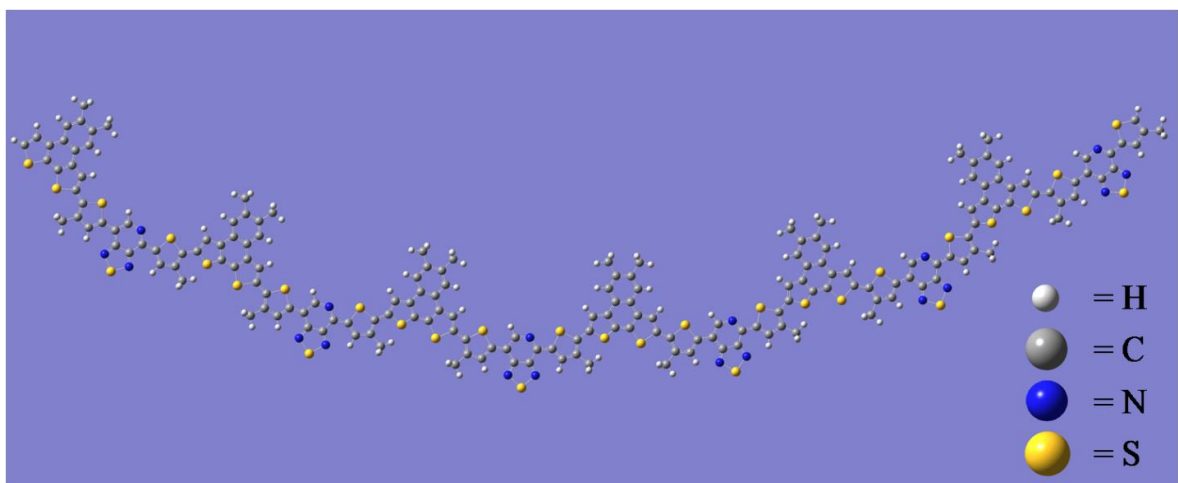
Figure A5.10: Calculated structure of the oligomer of PNDT-DTPyT containing ten repeat units. This geometry is used as input in the ZINDO electronic structure calculations discussed in Chapter 6.1. Note that this structure is not a result of a DFT geometry optimization, but is mathematically calculated assuming that the *trans* linkage shown in Figure A5.3 is periodic.
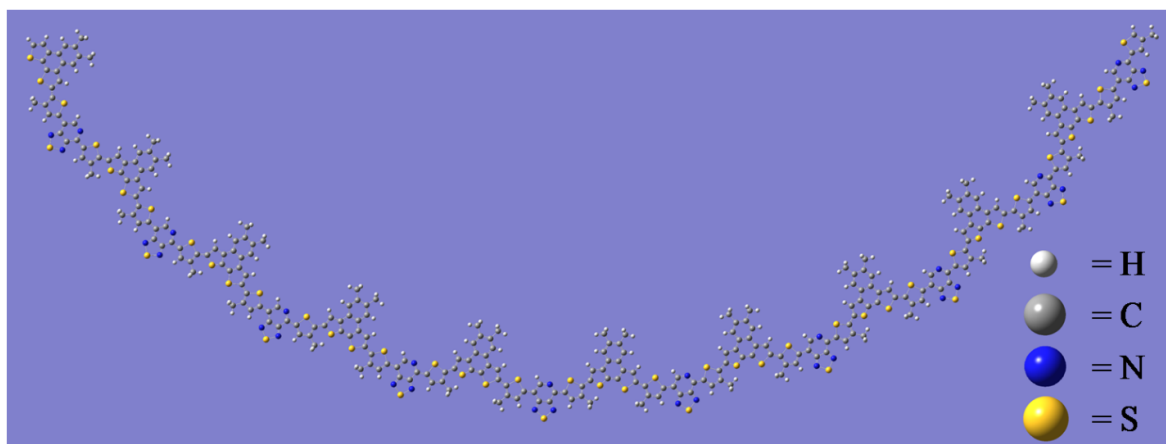
A5.2. DENSITY OF PHOTOEXCITATIONS

In this section, the average distance between photoexcitations at zero pulse delay is approximated. First the fluence (i.e., photons/cm^2) of the pump step in the transient grating experiment is calculated using the beam waist, w_0, the total energy, E_{Pulse}, and frequency of the "pump" pulses, ν. With these parameters, the fluence is obtained using

$$
\begin{aligned}
F &= \frac{E_{Pulse}}{h\nu\pi w_0^2} \\
&= \frac{(2 \text{ x } 10^{-9}\text{J})}{(1.986 \text{ x } 10^{-23}\text{J cm})(16670 \text{ cm}^{-1})\pi(0.006 \text{ cm})^2} \\
&= 5.34 \text{ x } 10^{13} \text{ photons/cm}^2
\end{aligned}
\tag{A5.5}
$$

The extinction coefficient per repeat unit in PNDT-DTPyT is calculated by first dividing the extinction coefficient of the polymer per repeat unit (54,300 M^{-1}cm^{-1}) by the average number of repeat units, 18. The absorption cross section is then obtained as

$$\sigma = 1000\ln(10)\frac{\varepsilon}{N_A}$$

$$= 1000\ln(10)\frac{54300 \text{ M}^{-1}\text{cm}^{-1}}{6.02 \text{ x } 10^{23}\text{mol}^{-1}} \qquad (\text{A5.6})$$

$$= 2.10 \text{ x } 10^{-16} \text{ cm}^2$$

where, N_A, is the Avogadro's constant. Using the absorption cross section and the fluence, the fraction of monomers of photoexcited repeat units is given by

$$\Phi = F\sigma$$

$$= (5.34 \text{ x } 10^{13} \text{ cm}^{-2})(2.10 \text{ x } 10^{-16} \text{ cm}^2) \qquad (\text{A5.7})$$

$$= 0.011$$

Thus, approximately 1 in every 100 repeat units is photoexcited at zero pulse delay. Using this fraction, the average distance between photoexcitations can be estimated using basic polymer chain statistics. Two approximations must be made to perform this calculation. First, it is assumed that the bulk polymer exists as an amorphous melt. Second, as is generally the case with such melts, it is assumed that the polymer chains conform to nearly ideal chain statistics (i.e., as if the polymer was contained in a θ-solvent).[1] The average distance between photoexcitations at zero pulse delay can be approximated as the mean end to end distance of a chain containing N=1600 monomer segments using the following expression[2]

$$R = bN^2$$

$$= (1.82 \text{ nm})(1600)^{\frac{1}{2}} \qquad (\text{A5.8})$$

$$= 72 \text{ nm}$$

where the Kuhn monomer length, b, is equated to the "length" of a repeat unit (cf. Figure A5.2).

A5.3. ABSORBANCE SPECTRUM OF THE PNDT-DTPyT⁺ CATION

Pure NDT-DTPyT in chlorobenzene was spuncast onto a clean glass substrate. A baseline absorption spectrum was taken, and then the substrate was cut into two pieces of similar size. One piece was placed in a sealed 20mL vial with 0.02g Iodine, while the other piece was placed in a sealed 20mL vial with 0.5g Iodine. Absorption spectra of each film were then taken at 30 second, 90 second, 3 minute and 15 minute intervals.

One of the products generated by electron transfer from PNDT-DTPyT to PCBM is the PNDT-DTPyT⁺ cation. The linear absorbance spectrum of this species was investigated by oxidizing a film of pure PNDT-DTPyT in the presence of I_2. Absorbance spectra of a PNDT-DTPyT film acquired after exposure to I_2 for different amounts of time are shown in Figure A5.11. As the exposure time increases, the concentration of the cation, PNDT-DTPyT+, increases. The absorbance increases at frequencies less than 12500cm⁻¹ and greater than 18000cm⁻¹, thereby showing that the cation absorbs in the visible frequency range.
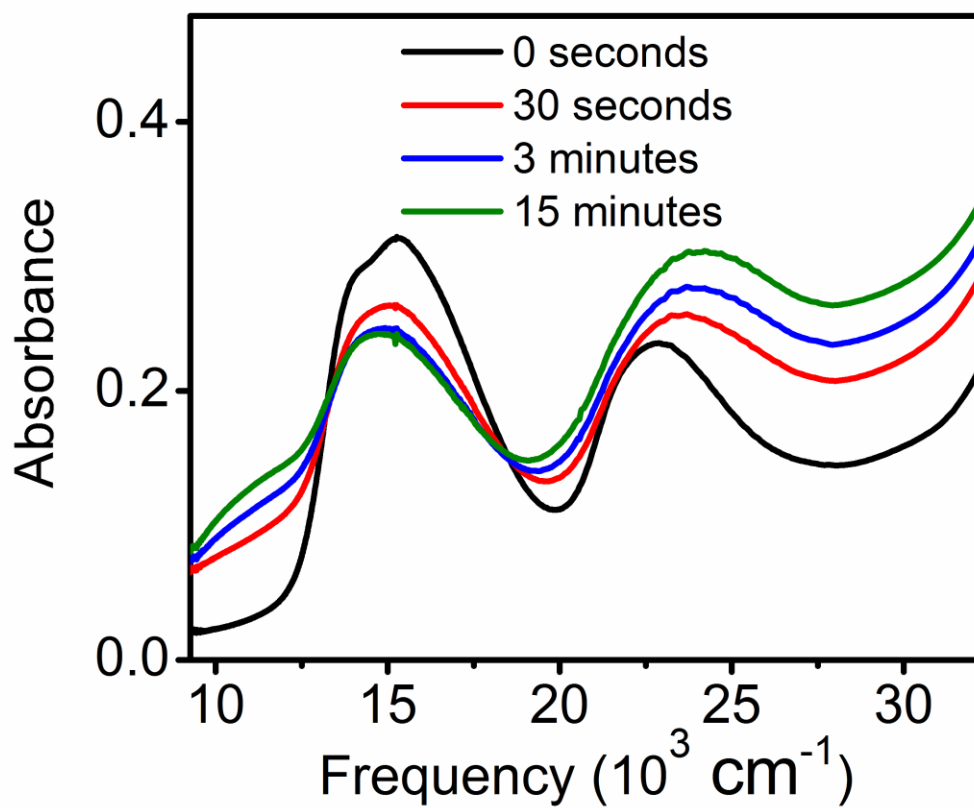
Figure A5.11: Ground state absorbance of thin films of PNDT-DTPyT doped submerged in gaseous I_2 (cf., Chapter 6.3). The concentration of the cation, PNDT-DTPyT$^+$, increases as the exposure time increases. Although the spectrum of the pure cation is not obtained, this series of measurements shows that the cation absorbs in the visible wavelength range. Note that the absorbance increases at frequencies less than 12500cm^{-1} and greater than 18000cm^{-1}. Therefore, the cation, along with the PCBM anion, can contribute to the excited state absorption nonlinearities probed in this work.

A5.4. LOW TEMPERATURE FLUORESCENCE OF PURE POLYMER FILMS
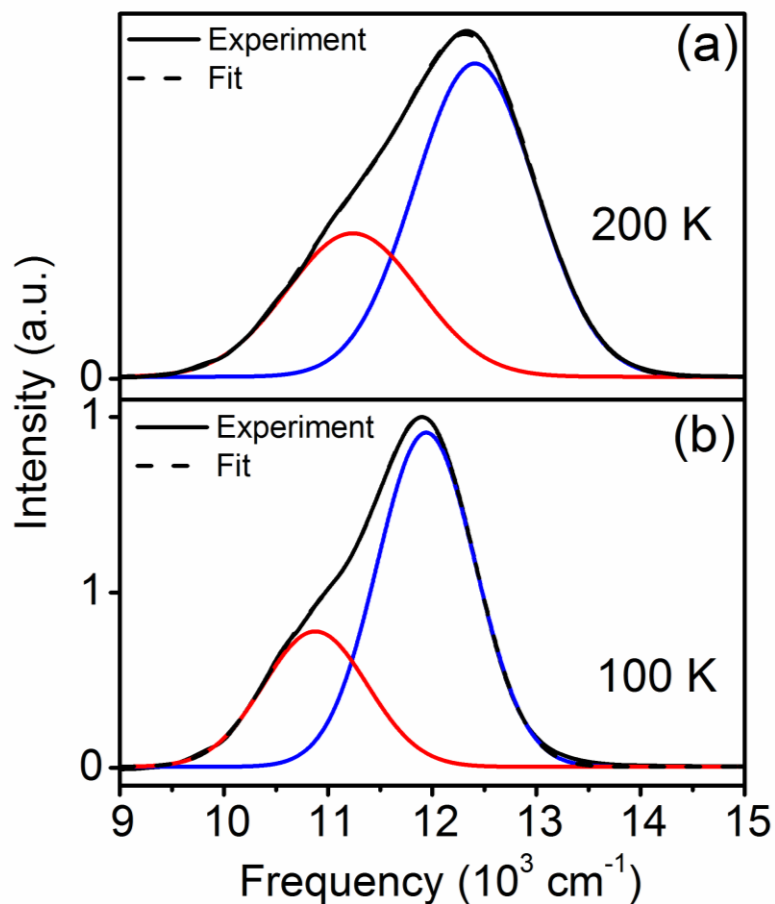
Figure A5.12: Fluorescence spectra are fit at (a) 200K and (b) 100K with a sum of two Gaussian functions. The reorganization energy, $\lambda = \Delta_1^2 / 2k_B T$, is estimated using the line width of the nominal 0-0 transition (i.e., higher energy peak), where Δ_1 is the standard deviation of the function. Fits conducted at 200K and 100K yield $\Delta_1 = 524$ cm^{-1} and $\Delta_1 = 473$ cm^{-1}, respectively.
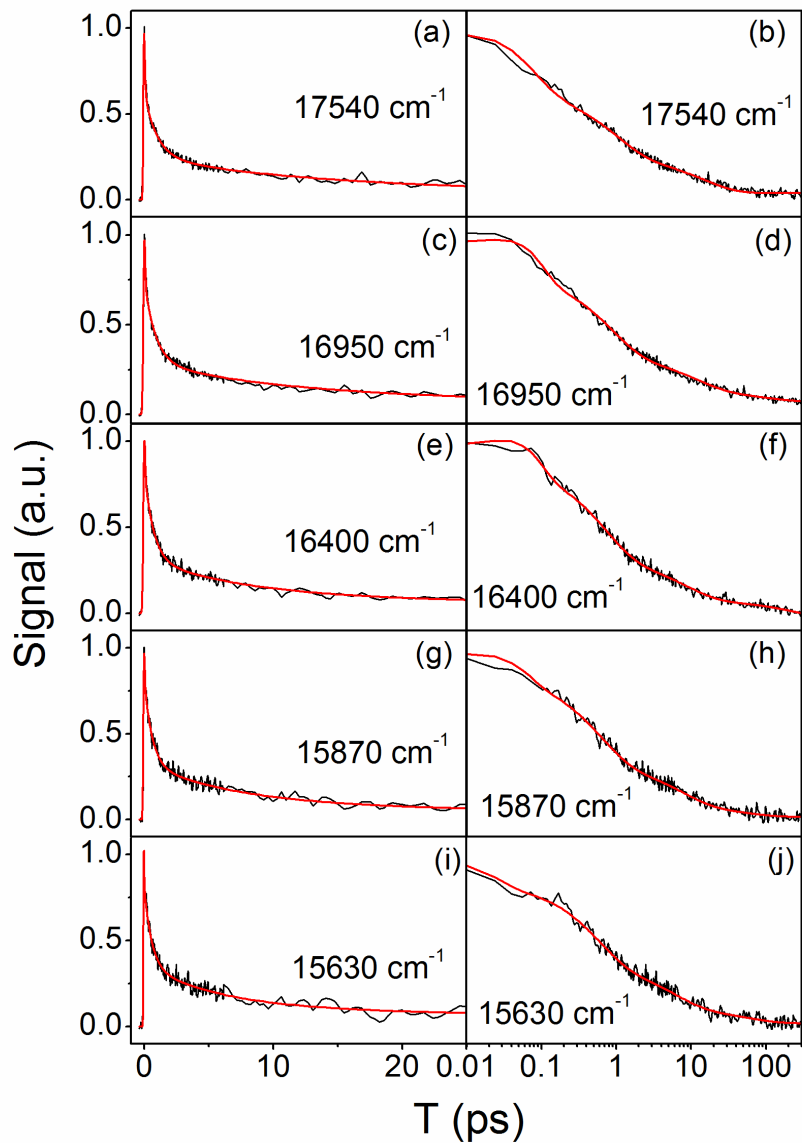
Figure A5.13: Real part of measured transient grating signals (black) and fits (red) for pure PNDT-DTPyT films. Signals are acquired with all fields possessing parallel polarizations, $S_\parallel(T)$, where excitation is achieved with a 20fs pulse centered at 20400cm^{-1}. Time constants are given in Table 6.3 in Chapter 6. Within each row, the same data are plotted on linear and log scales. The detection frequency is given in each panel.
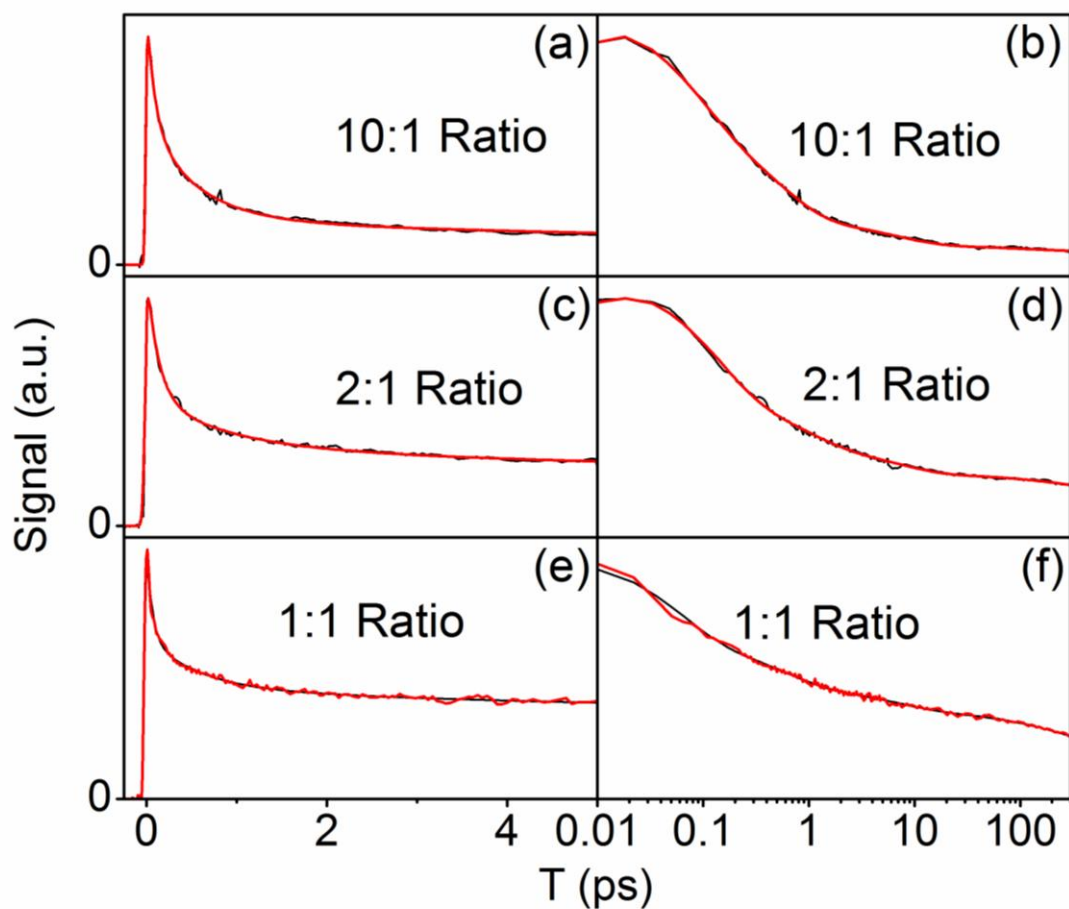
Figure A5.14: Real part of measured transient grating signals (black) and fits (red) obtained using Equation 6.4. Signals are acquired with all field possessing parallel polarizations, $S_{\parallel}(T)$. Time constants are given in Table 6.4 in Chapter 6. Within each row, the same data are plotted on linear and log scales. The weight ratios, PNDT-DTPyT:PCBM, is given in each panel.

A5.6. REFERENCES

(1)   Flory, P. J. *Principles of Polymer Chemistry*; Cornell University Press: Ithaca, 1953.

(2)   Rubinstein, M., Colby, R. H. *Polymer Physics*; Oxford University Press: New York, 2006.

APPENDIX 6 . SUPPORTING INFORMATION FOR CHAPTER 7:

"INVESTIGATING ELECTRON TRANSFER ADIABATICITY WITH

TRANSIENT ABSORPTION ANISOTROPY"

A6.1. EIGENVECTORS FOR MLCT AND BIPYRIDINE RADICAL STATES

The eigenvectors are readily obtained as symmetry adapted linear combinations of local basis states for D_3 point group.

A6.1.1. MLCT States

A_1 symmetry

$$|\varepsilon_1\rangle = \frac{1}{\sqrt{3}}\left[|e1\rangle + |e2\rangle + |e3\rangle\right] \tag{A6.1}$$

E symmetry

$$|\varepsilon_2\rangle = \frac{1}{\sqrt{2}}\left[|e2\rangle - |e3\rangle\right] \tag{A6.2}$$

$$|\varepsilon_3\rangle = \frac{1}{\sqrt{6}}\left[2|e1\rangle - |e2\rangle - |e3\rangle\right] \tag{A6.3}$$

A6.1.2. Bipyridine Radical States

A_1 symmetry

$$|\phi_1\rangle = \frac{1}{\sqrt{3}}\left[|f1\rangle + |f2\rangle + |f3\rangle\right] \tag{A6.4}$$

E symmetry

$$|\phi_2\rangle = \frac{1}{\sqrt{2}}\big[|f2\rangle - |f3\rangle\big] \tag{A6.5}$$

$$|\phi_3\rangle = \frac{1}{\sqrt{6}}\big[2|f1\rangle - |f2\rangle - |f3\rangle\big] \tag{A6.6}$$

A6.2. TRANSITION DIPOLES IN DIABATIC BASIS

This section obtains transition dipoles in the diabatic basis. The work of Hammarström and co-workers informs the present analysis.[1] Assume basis of MLCT transition dipoles aligned to axis joining the metal and ligand.

$$\vec{\mu}_{ge1} = \frac{|\vec{\mu}_{ge1}|}{\sqrt{2}}\big[\hat{x} - \hat{y}\big]$$

$$\vec{\mu}_{ge2} = \frac{|\vec{\mu}_{ge2}|}{\sqrt{2}}\big[-\hat{x} + \hat{z}\big]$$

$$\vec{\mu}_{ge3} = \frac{|\vec{\mu}_{ge3}|}{\sqrt{2}}\big[\hat{y} - \hat{z}\big]$$

where $\qquad |\vec{\mu}_{ge1}| = |\vec{\mu}_{ge2}| = |\vec{\mu}_{ge3}|$

The transition dipoles of the bipyridine radicals are aligned with the long axes of the ligands.

$$\vec{\mu}_{e1,f1} = \frac{|\vec{\mu}_{e1,f1}|}{\sqrt{2}}\big[\hat{x} + \hat{y}\big]$$

$$\vec{\mu}_{e2,f2} = \frac{|\vec{\mu}_{e2,f2}|}{\sqrt{2}}\big[\hat{x} + \hat{z}\big]$$

$$\vec{\mu}_{e3,f3} = \frac{|\vec{\mu}_{e3,f3}|}{\sqrt{2}}\big[\hat{y} + \hat{z}\big]$$

$$\left|\vec{\mu}_{e1,f1}\right|=\left|\vec{\mu}_{e2,f2}\right|=\left|\vec{\mu}_{e3,f3}\right|$$

A6.3. TRANSITION DIPOLES IN ADIABATIC BASIS

For convenience, the coefficients $\left|\vec{\mu}_{gei}\right|/\sqrt{2}$ and $\left|\vec{\mu}_{ei,fi}\right|/\sqrt{2}$ will be set equal to one. Signal pulse energies are not measured in the present anisotropy experiments so the absolute vector lengths are unimportant. In addition, because of all transitions of the same class (e.g., MLCT) have the same transition dipole magnitude in the local basis, the final results can later be expressed in terms of the ratio $\left|\vec{\mu}_{gei}\right|/\left|\vec{\mu}_{ei,fi}\right|$.

 (1) Transitions initiating in the ground state γ

$$\left\langle\gamma\left|\vec{\mu}\right|\varepsilon_1\right\rangle=0 \tag{A6.7}$$

$$\left\langle\gamma\left|\vec{\mu}\right|\varepsilon_2\right\rangle=\frac{1}{\sqrt{2}}[-\hat{x}-\hat{y}+2\hat{z}]=\sqrt{3}\hat{\mu}_{\gamma\varepsilon2} \tag{A6.8}$$

$$\left\langle\gamma\left|\vec{\mu}\right|\varepsilon_3\right\rangle=\frac{1}{\sqrt{6}}[3\hat{x}-3\hat{y}]=\sqrt{3}\hat{\mu}_{\gamma\varepsilon3} \tag{A6.9}$$

where the transition dipoles are expressed as a product of the magnitude and a unit vector. For example, $\left\langle\gamma\left|\vec{\mu}\right|\varepsilon_2\right\rangle$ and $\left\langle\gamma\left|\vec{\mu}\right|\varepsilon_3\right\rangle$ both have a magnitude of $\sqrt{3}$.

(2) Transitions initiating in the ε_2 and ε_3 excited MLCT states.

$$\left\langle\varepsilon_2\left|\vec{\mu}\right|\phi_1\right\rangle=\frac{1}{\sqrt{6}}[\hat{x}-\hat{y}]=\frac{1}{\sqrt{3}}\hat{\mu}_{\varepsilon2,\phi1} \tag{A6.10}$$

$$\left\langle\varepsilon_2\left|\vec{\mu}\right|\phi_2\right\rangle=\frac{1}{2}[\hat{x}+\hat{y}+2\hat{z}]=\sqrt{\frac{3}{2}}\hat{\mu}_{\varepsilon2,\phi2} \tag{A6.11}$$

270

$$\langle \varepsilon_2 | \vec{\mu} | \phi_3 \rangle = \frac{1}{\sqrt{12}} [-\hat{x} + \hat{y}] = \frac{1}{\sqrt{6}} \hat{\mu}_{\varepsilon 2, \phi 3} \tag{A6.12}$$

$$\langle \varepsilon_3 | \vec{\mu} | \phi_1 \rangle = \frac{1}{\sqrt{18}} [\hat{x} + \hat{y} - 2\hat{z}] = \frac{1}{\sqrt{3}} \hat{\mu}_{\varepsilon 3, \phi 1} \tag{A6.13}$$

$$\langle \varepsilon_3 | \vec{\mu} | \phi_2 \rangle = \frac{1}{\sqrt{12}} [-\hat{x} + \hat{y}] = \frac{1}{\sqrt{6}} \hat{\mu}_{\varepsilon 3, \phi 2} \tag{A6.14}$$

$$\langle \varepsilon_3 | \vec{\mu} | \phi_3 \rangle = \frac{1}{6} [5\hat{x} + 5\hat{y} + 2\hat{z}] = \frac{1}{3} \hat{\mu}_{\varepsilon 3, \phi 3} \tag{A6.15}$$

A6.4. ANGLES BETWEEN TRANSITION DIPOLES FOR ADIABATIC BASIS

This section summarizes angles between transition dipoles in the adiabatic basis to facilitate the attainment of the tensor elements in Chapter 7.5. The ε_1 state is neglected because its transition dipole is optically forbidden (Equation A6.7).

A6.4.1 Angles between transition dipoles involved in GSB and ESE

These $\langle \gamma | \vec{\mu} | \varepsilon_2 \rangle$ and $\langle \gamma | \vec{\mu} | \varepsilon_3 \rangle$ dipoles are oriented at a 90 degree angle with respect to each other.

A6.4.2. Angles between transition dipoles involved in ESA

(1) When ESA initiates at the ε_2 state

Pumped\Probed	$\langle \varepsilon_2 | \vec{\mu} | \phi_1 \rangle$	$\langle \varepsilon_2 | \vec{\mu} | \phi_2 \rangle$	$\langle \varepsilon_2 | \vec{\mu} | \phi_3 \rangle$
$\langle \gamma | \vec{\mu} | \varepsilon_2 \rangle$	90°	70.5°	90°

$\langle\gamma|\vec{\mu}|\varepsilon_3\rangle$	0°	90°	0°

(2) When ESA initiates at the ε_3 state

Pumped\Probed	$\langle\varepsilon_3|\vec{\mu}|\phi_1\rangle$	$\langle\varepsilon_3|\vec{\mu}|\phi_2\rangle$	$\langle\varepsilon_3|\vec{\mu}|\phi_3\rangle$
$\langle\gamma|\vec{\mu}|\varepsilon_2\rangle$	0°	90°	70.5°
$\langle\gamma|\vec{\mu}|\varepsilon_3\rangle$	90°	0°	90°

A6.5. NONLINEAR RESPONSE FUNCTION FOR ADIABATIC BASIS

A6.5.1. Ground State Bleach (GSB) Terms in Adiabatic Basis

For $Os^{II}(bpy)_3$, R_3 and R_4 each have 2 diagonal ($a=b$) and 2 cross ($a \neq b$) terms. Equations A6.16 and A6.17 account for these 8 terms. The ε_1 state is neglected because its transition dipole is optically forbidden (Equation A6.7).
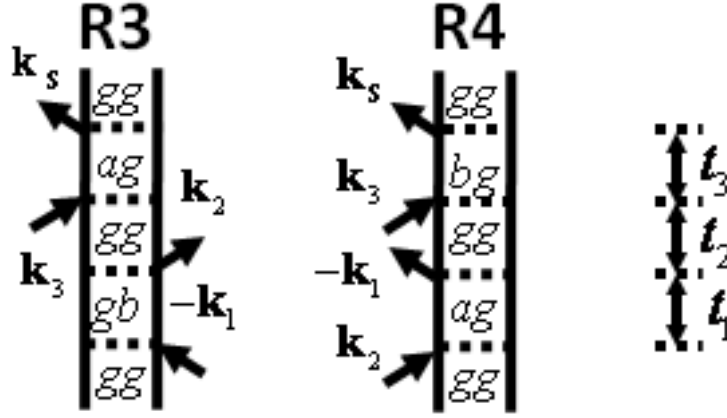
Figure A6.1: Feynman diagrams for R_3 and R_4 terms contributing to the GSB signal component

$$S_{ZZZZ}^{GSB} = \frac{2}{5}\mu_{\gamma\varepsilon 2}^4 + \frac{2}{5}\mu_{\gamma\varepsilon 3}^4 + \frac{4}{15}\mu_{\gamma\varepsilon 2}^2\mu_{\gamma\varepsilon 3}^2 \tag{A6.16}$$

$$S_{ZZXX}^{GSB} = \frac{2}{15}\mu_{\gamma\varepsilon 2}^4 + \frac{2}{15}\mu_{\gamma\varepsilon 3}^4 + \frac{8}{15}\mu_{\gamma\varepsilon 2}^2\mu_{\gamma\varepsilon 3}^2 \tag{A6.17}$$

where $\mu_{\gamma\varepsilon 2}$ is the magnitude of the transition dipole. For example, $\mu_{\gamma\varepsilon 2} = \mu_{\gamma\varepsilon 3} = \sqrt{3}$. The orientational part of the response is evaluated using Equation A6.30.

A6.5.2. Excited State Emission (ESE) Terms in Adiabatic Basis

For $Os^{II}(bpy)_3$, R_1 and R_2 generally each have 2 terms evolving as either populations ($a = b$) or coherences ($a \neq b$) during t_2. Equations A6.18 and A6.19 neglect the cross terms ($a \neq b$) under the assumption of extremely fast dephasing of excited state electronic coherences. Photon echo measurements performed in our lab suggest dephasing occurs in less than 20 fs.
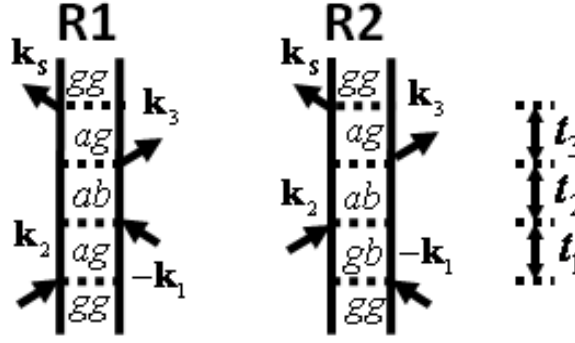
Figure A6.2: Feynman diagrams for R_1 and R_2 terms contributing to the ESE signal component

$$S_{ZZZZ}^{ESE}(T) = M(T)\left[\frac{2}{5}\mu_{\gamma\varepsilon 2}^4 + \frac{2}{5}\mu_{\gamma\varepsilon 3}^4\right] \tag{A6.18}$$

$$S_{ZZXX}^{ESE}(T) = M(T)\left[\frac{2}{15}\mu_{\gamma\varepsilon 2}^4 + \frac{2}{15}\mu_{\gamma\varepsilon 3}^4\right] \tag{A6.19}$$

where $M(T)$ is the solvation correlation function. The solvation correlation function captures red-shifting of ESE outside of the detection window defined by the probe laser spectrum. Measurement of steady-state fluorescence for $Os^{II}(bpy)_3$, show that the ESE terms emit at frequencies low compared to our laser spectra.[2]

A6.5.3. Excited State Absorption (ESA) Terms in Adiabatic Basis

For $Os^{II}(bpy)_3$, R_1* and R_2* generally each have 2 terms evolving as populations ($a = b$) and 2 terms evolving as coherences ($a \neq b$) during t_2. The expressions below neglect the coherent cross terms ($a \neq b$) under the assumption of extremely fast dephasing of excited state electronic coherences.

274

The $\vec{\mu}_{\gamma\varepsilon 1}$ transition dipole is forbidden by symmetry (see Equation A6.7). Furthermore, the energy of the $\varepsilon 1$ state is $3\,J_e$ greater than the energies of the doubly degenerate $\varepsilon 2$ and $\varepsilon 3$ states (Figure 7.6 in Chapter 7). By earlier estimations, $3\,J_e$ is more than $7\,k_B T$.[3,4] For this reason, we assume that interligand electron transfer occurs only between the $\varepsilon 2$ and $\varepsilon 3$ states.
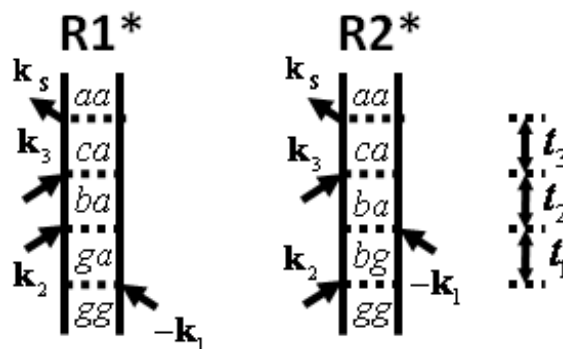

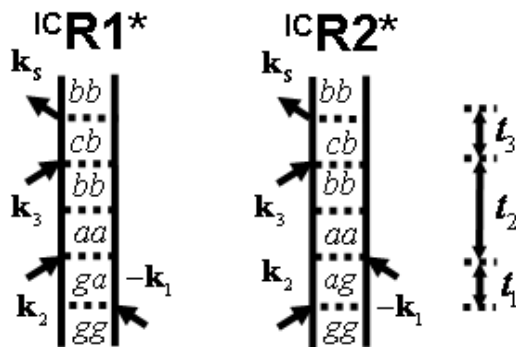**Figure A6.3:** Feynman diagrams for R_1 and R_2 terms contributing to the ESA signal component

Figure A6.4: Feynman diagrams for $^{IC}R_1^*$ and $^{IC}R_2^*$ terms contributing to the ESA signal component

$$S_{ZZZZ}^{ESA}(T) = \mu_{\gamma\varepsilon2}^2 G_{et}(T) \left\{ \frac{2}{15} \mu_{\varepsilon2,\phi1}^2 + \frac{2}{15}\left(1 + 2\cos^2(70.5°)\right)\mu_{\varepsilon2,\phi2}^2 + \frac{2}{15}\mu_{\varepsilon2,\phi3}^2 \right\}$$

$$+ \mu_{\gamma\varepsilon3}^2 G_{et}(T) \left\{ \frac{2}{15}\mu_{\varepsilon3,\phi1}^2 + \frac{2}{5}\mu_{\varepsilon3,\phi2}^2 + \frac{2}{15}\mu_{\varepsilon3,\phi3}^2 \right\}$$

$$+ \mu_{\gamma\varepsilon2}^2 \left[1 - G_{et}(T)\right] \left\{ \frac{2}{5}\mu_{\varepsilon3,\phi1}^2 + \frac{2}{15}\mu_{\varepsilon3,\phi2}^2 + \frac{2}{15}\left(1 + 2\cos^2(70.5°)\right)\mu_{\varepsilon3,\phi3}^2 \right\}$$

$$+ \mu_{\gamma\varepsilon3}^2 \left[1 - G_{et}(T)\right] \left\{ \frac{2}{5}\mu_{\varepsilon2,\phi1}^2 + \frac{2}{15}\mu_{\varepsilon2,\phi2}^2 + \frac{2}{5}\mu_{\varepsilon2,\phi3}^2 \right\}$$

(A6.20)

$$S_{ZZXX}^{ESA}(T) = \mu_{\gamma\varepsilon2}^2 G_{et}(T) \left\{ \frac{4}{15}\mu_{\varepsilon2,\phi1}^2 + \frac{2}{15}\left(2 - \cos^2(70.5°)\right)\mu_{\varepsilon2,\phi2}^2 + \frac{4}{15}\mu_{\varepsilon2,\phi3}^2 \right\}$$

$$+ \mu_{\gamma\varepsilon3}^2 G_{et}(T) \left\{ \frac{4}{15}\mu_{\varepsilon3,\phi1}^2 + \frac{2}{15}\mu_{\varepsilon3,\phi2}^2 + \frac{4}{15}\mu_{\varepsilon3,\phi3}^2 \right\}$$

$$+ \mu_{\gamma\varepsilon2}^2 \left[1 - G_{et}(T)\right] \left\{ \frac{2}{15}\mu_{\varepsilon3,\phi1}^2 + \frac{4}{15}\mu_{\varepsilon3,\phi2}^2 + \frac{2}{15}\left(2 - \cos^2(70.5°)\right)\mu_{\varepsilon3,\phi3}^2 \right\}$$

$$+ \mu_{\gamma\varepsilon3}^2 \left[1 - G_{et}(T)\right] \left\{ \frac{2}{15}\mu_{\varepsilon2,\phi1}^2 + \frac{4}{15}\mu_{\varepsilon2,\phi2}^2 + \frac{2}{15}\mu_{\varepsilon2,\phi3}^2 \right\}$$

(A6.21)

A6.6. NONLINEAR RESPONSE FUNCTION FOR DIABATIC BASIS

A6.6.1. Ground State Bleach (GSB) Terms in Diabatic Basis

For $Os^{II}(bpy)_3$, R_3 and R_4 each sum over three localized MLCT transitions. Equations A6.22 and A6.23 account for these 6 terms.
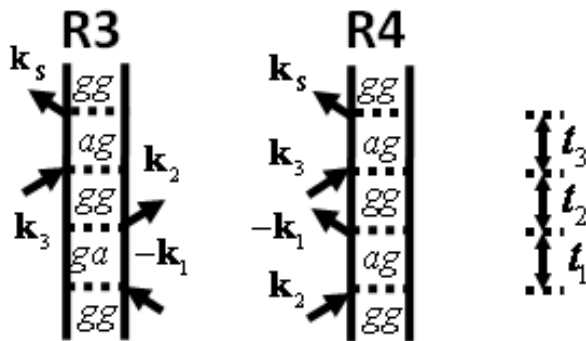
Figure A6.5: Feynman diagrams for R_3 and R_4 terms contributing to the GSB signal component

$$S_{ZZZZ}^{GSB} = \frac{6}{5}\mu_{eg}^4 \tag{A6.22}$$

$$S_{ZZXX}^{GSB} = \frac{2}{5}\mu_{eg}^4 \tag{A6.23}$$

where $\mu_{eg} = \left|\vec{\mu}_{ge1}\right| = \left|\vec{\mu}_{ge2}\right| = \left|\vec{\mu}_{ge3}\right|$

A6.6.2. Excited State Emission (ESE) Terms in Diabatic Basis

For $Os^{II}(bpy)_3$, R_1 and R_2 each sum over three localized MLCT transitions. Equations A6.24 and A6.25 account for these 6 terms.
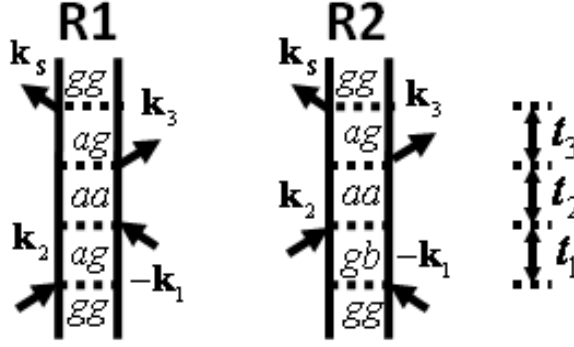
Figure A6.6: Feynman diagrams for R_1 and R_2 terms contributing to the ESE signal component

$$S_{ZZZZ}^{ESE}(T) = \frac{6}{5}\mu_{eg}^4 M(T) \qquad (A6.24)$$

$$S_{ZZXX}^{ESE}(T) = \frac{2}{5}\mu_{eg}^4 M(T) \qquad (A6.25)$$

where $M(T)$ is the solvation correlation function. The solvation correlation function captures red-shifting of ESE outside of the detection window defined by the probe laser spectrum. Measurement of steady-state fluorescence for $Os^{II}(bpy)_3$, show that the ESE terms emit at frequencies low compared to our laser spectra.[2]

A6.6.3. Excited State Absorption (ESA) Terms in Nonadiabatic Basis

For $Os^{II}(bpy)_3$, R_1* and R_2* each sum over three localized MLCT states a, where the summation over c is restricted to bipyridine radical ESA localized on the same ligand as MLCT transition. As interligand electron transfer occurs, the terms in Figure A6.7 decay concomitant with growth of the terms in Figure A6.8. With D_3 symmetry, the $\vec{\mu}_{bc}$ transition

dipole (Figure A6.8) is oriented at 60° with respect to the pumped $\vec{\mu}_{ab}$ dipole following a
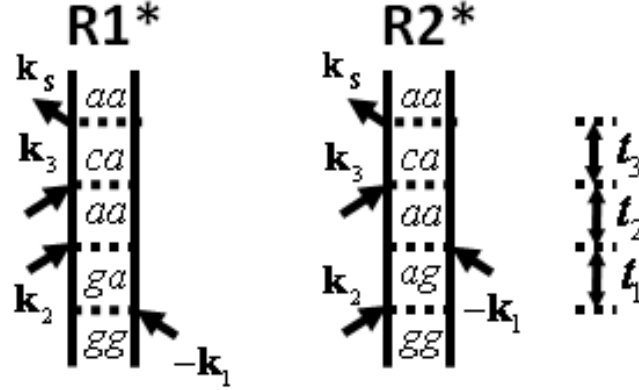
single electron transfer event.

Figure A6.7: Feynman diagrams for R₁* and R₂* terms contributing to the ESA signal component
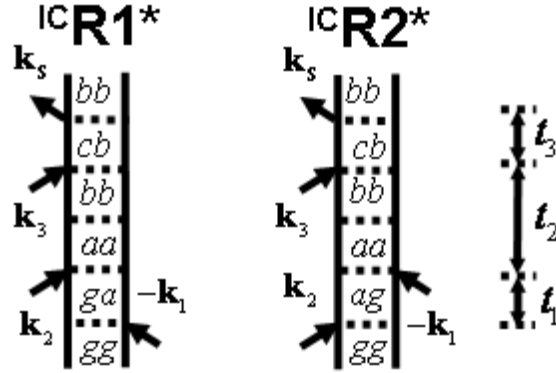
Figure A6.8: Feynman diagrams for ^{IC}R₁* and ^{IC}R2* terms contributing to the ESA signal component

$$S_{ZZZZ}^{ESA}(T) = \mu_{eg}^2 \mu_{fe}^2 \left\{ \frac{2}{5} G_{et}(T) + \frac{3}{5} (1 - G_{et}(T)) \right\} \qquad (A6.26)$$

$$S_{ZZXX}^{ESA}(T) = \mu_{eg}^2 \mu_{fe}^2 \left\{ \frac{4}{5} G_{et}(T) + \frac{7}{10} (1 - G_{et}(T)) \right\} \qquad (A6.27)$$

where $\mu_{fe} = \left| \vec{\mu}_{e1,f1} \right| = \left| \vec{\mu}_{e2,f2} \right| = \left| \vec{\mu}_{e3,f3} \right|$.

Equations A6.26 and A6.27 describe the experimental data at $T=0$ but yield an anisotropy

deviating from measured values at $T>1$ ps. We therefore postulate that solvation reduces the

D_3 symmetry of the ground state to C_2 symmetry in the excited state. Furthermore, the relative orientation between pumped and probed transition dipoles is taken to change from from 60° with D_3 symmetry to 45° with C_2 symmetry. Equations A6.28 and A6.29 assume that the dipoles rotate by 15° on the time scale governed by the solvation correlation function $M(T)$.

$$S_{ZZZZ}^{ESA}(T) = \mu_{eg}^2 \mu_{fe}^2 \left\{ \frac{2}{5} G_{et}(T) + \left(1 - G_{et}(T)\right)\left[\frac{3}{5} M(T) + \frac{4}{5}\left(1 - M(T)\right) \right] \right\} \qquad (A6.28)$$

$$S_{ZZXX}^{ESA}(T) = \mu_{eg}^2 \mu_{fe}^2 \left\{ \frac{4}{5} G_{et}(T) + \left(1 - G_{et}(T)\right)\left[\frac{7}{10} M(T) + \frac{3}{5}\left(1 - M(T)\right) \right] \right\} \qquad (A6.29)$$

A6.7. ORIENTATIONAL PART OF RESPONSE FUNCTION

This section presents the formula used to compute the orientational parts of the nonlinear response functions. The indices α, β, γ, χ and respectively correspond to the fields E_1, E_2, E_3 and E_S. For convenience, this orientational factor absorbs the four transition dipole magnitudes as[5,6]

$$
\begin{aligned}
\left\langle \chi_{gh} \gamma_{ef} \beta_{cd} \alpha_{ab} \right\rangle &= \mu_{ab}\mu_{cd}\mu_{ef}\mu_{gh} \Big[\left\langle \cos\theta_{ab,cd} \cos\theta_{ef,gh} \right\rangle \\
&\times \left(4\cos\theta_{\alpha\beta}\cos\theta_{\gamma\chi} - \cos\theta_{\alpha\gamma}\cos\theta_{\beta\chi} - \cos\theta_{\alpha\chi}\cos\theta_{\beta\gamma} \right) \\
&+ \left\langle \cos\theta_{ab,ef}\cos\theta_{cd,gh} \right\rangle \left(4\cos\theta_{\alpha\gamma}\cos\theta_{\beta\chi} - \cos\theta_{\alpha\beta}\cos\theta_{\gamma\chi} \right. \\
&\left. - \cos\theta_{\alpha\chi}\cos\theta_{\beta\gamma} \right) + \left\langle \cos\theta_{ab,gh}\cos\theta_{cd,ef} \right\rangle \left(4\cos\theta_{\alpha\chi}\cos\theta_{\beta\gamma} \right. \\
&\left. - \cos\theta_{\alpha\beta}\cos\theta_{\gamma\chi} - \cos\theta_{\alpha\gamma}\cos\theta_{\beta\chi} \right) \Big]
\end{aligned}
\qquad (A6.30)
$$

A6.8. MEASURED TENSOR ELEMENTS USED TO COMPUTE ANISOTROPIES IN FIGURE 7.11

This section presents the real part of transient grating signal fields used to calculate the anisotropies shown in Figure 7.11 of Chapter 7.
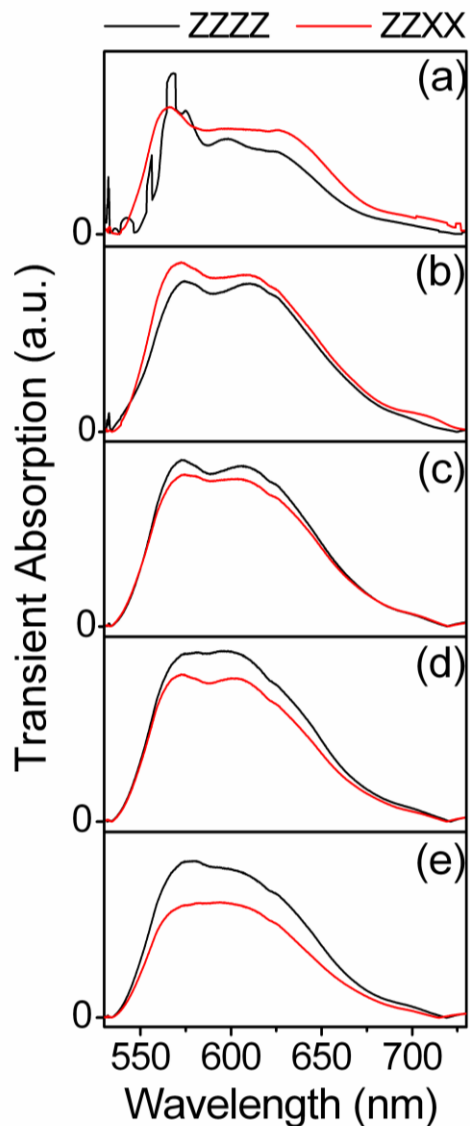

Figure A6.9: Transient absorption signals obtained as the real part of transient grating signal fields at pulse delay, T : (a) 0.10 ps; (b) 0.25 ps; (c) 0.45 ps; (d) 0.75 ps; (e) 3.0 ps. These data are used to calculate the anisotropies shown in Figure 7.11.

A6.9. REFERENCES

(1)   Wallin, S.; Davidsson, J.; Modin, J.; Hammarström, L. J. Phys. Chem. A 2005, 109, 4697.

(2)   Glomm, W. R.; Moses, S. J.; Brennaman, M. K.; Papanikolas, J. M.; Franzen, S. J. Phys. Chem. B 2005, 109, 804.

(3)   Shaw, G. B.; Brown, C. L.; Papanikolas, J. M. J. Phys. Chem. A 2002, 106, 1483.

(4)   Shaw, G. B.; Styers-Barnett, D. J.; Gannon, E. Z.; Granger, J. C.; Papanikolas, J. M. J. Phys. Chem. A 2004, 108, 4998.

(5)   Dreyer, J.; Moran, A. M.; Mukamel, S. Bull. Korean Chem. Soc. 2003, 24, 1091.

(6)   Hochstrasser, R. M. Chem. Phys. 2001, 266, 273.

APPENDIX 7 . SUPPORTING INFORMATION FOR CHAPTER 8: "UNCOVERING MOLECULE-TiO₂ INTERACTIONS WITH NONLINEAR SPECTROSCOPY"

A7.1. SAMPLE PREPARATION.

TiO₂ nanoparticle surface: TiO₂ slides consisting of ~10μm thick films of TiO₂ nanoparticles (10-20nm in diameter) were prepared by the following procedures. Quartz microscope slides with 1mm thicknesses were thoroughly cleaned by sonication in the following sequence of solutions (for 5 minutes each): aqueous NaOH at pH 12.5; acetone; ethanol; a second solution of ethanol. A nanocrystalline TiO₂ paste was prepared as described previously by Mallouk et. al. except that an autoclave temperature of 190°C was utilized instead of 230°C in order to increase film transparency.[1] The autoclaved TiO₂ paste was subsequently diluted with de-ionized water to achieve the desired transparency. The paste was spread onto the clean microscope slides using two pieces of scotch tape (4 layers per side) to achieve a homogeneous thickness of ~10μm. The slides were sintered in a bench top muffle furnace (Thermoscientific Thermolyne) by increasing the furnace temperature from 25°C to 450°C at 5°C per minute. The slides were then baked at 450°C for 30 minutes before cooling them back to 25°C at 10°C per minute. The resulting films have optical densities of 0.3 at 400nm.

[(Ru(bpy)₂(4,4'-(PO₃H₂)₂bpy)]Cl2 / TiO₂ Composite: $[(Ru(bpy)_2(4,4'-(PO_3H_2)_2bpy)]^{2+}$ sensitized TiO₂ films were prepared by soaking the previously prepared TiO₂ slides in an aqueous solution of $2x10^{-3}$ M $[(Ru(bpy)_2(4,4'-(PO_3H_2)_2bpy)]Cl_2$ and 0.1 M HClO₄ for 45 minutes. While soaking, the dye adhered to the TiO₂ surface resulting in a deep red-orange

color. The dye-sensitized films were gently rinsed with approximately 50mL of deionized water and then soaked in a dilute aqueous solution of HCl (pH=5) for 1 hour to remove excess dye. In order to quench long-lived photoexcitations (confirmed by the emission of TG signals at negative pulse delay), TG experiments were performed with the films immersed in a solution of 80 mM triethanolamine and 0.1 M LiClO$_4$ (pH= 6.7). The origin of these long-lived excitations is still under investigation. For the present investigation, it is only important that the system equilibrates in the 1ms interval between shots of our laser system. The final optical densities of the films were 0.75 at 400nm.

Catechol / TiO$_2$ composite: TiO$_2$ films sensitized with catechol were prepared in an manner analogous to the [(Ru(bpy)$_2$(4,4'-(PO$_3$H$_2$)$_2$bpy)]$^{2+}$ films. The TiO$_2$ films were soaked for 45 minutes in a solution of 1×10^{-3} M catechol in acetonitrile. While soaking, the dye adhered to the TiO$_2$ surface, resulting in a deep orange color. The dye-sensitized films were rinsed with approximately 50 mL of acetonitrile and then soaked for one hour in a weakly acidic solution of hydrochloric acid in acetonitrile (pH=5). TG experiments were performed with the films immersed in dilute aqueous solutions of HCl (pH =5). The optical densities of the films were 1.0 at 400 nm.

A7.2. SAMPLE HOLDER FOR NEAT AND DYE-SENSITIZED TiO$_2$ FILMS

All TG experiments reported in Chapter 8 were conducted with the samples immersed in solutions. The presence of the solution enables the quenching of long lived photoexcitations (in the [(Ru(bpy)$_2$(4,4'-(PO$_3$H$_2$)$_2$bpy)]$^{2+}$ experiments) in addition to

suppressing sample degradation by dissipating thermal energy from the film surface. In this section, we describe a home-made cuvette used to immerse the sampled in solutions during the TG experiments. As shown in Figure A7.1, two metallic washers (~1 mm thick) are sandwiched between two 3x1" (~1mm thick) borosilicate microscope slides. Both washers are situated at the ends of the glass slides in order to leave empty space for the sample between them. At this point, the slides are held together by binder clips. In order to create a water tight cavity for the sample to rest in, the bottom and sides of the two microscope slides are bonded together with waterproof epoxy and left to set overnight. After the epoxy cures, the binder clips are removed and the sample holder is ready for use.

Figure A7.1: Home-made cuvette used to contain dye-sensitized films during transient grating experiments.

When performing TG experiments, we insert the microscope slide covered with the dye sensitized TiO_2 film into the home-made cuvette; the cuvette is also filled with the appropriate solution. The thickness of the washers is such that the spacing between the two glass surfaces is just thick enough for the microscope slide to fit snugly (cf., Figure A7.2). Throughout the experiment, the entire sample container is oscillated with a linear actuator to suppress photodamage.
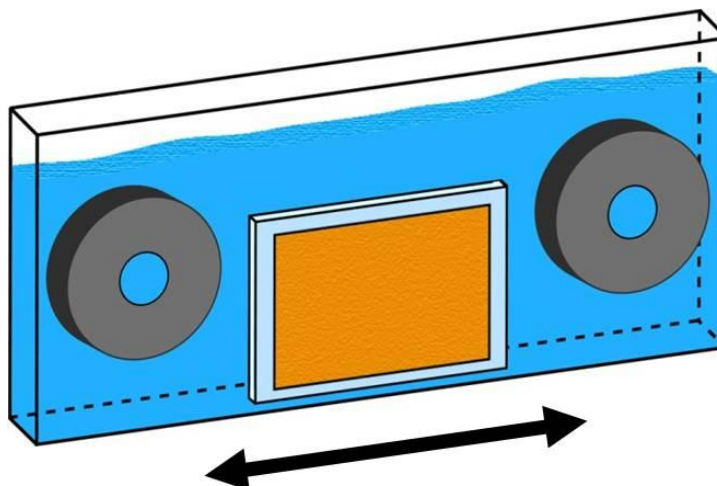
Figure A7.2: Dye sensitized TiO$_2$ films are held in a home-made cuvette during transient grating experiments and oscillated in the plane of the film with a linear actuator to suppress sample degradation.

A7.3. REFERENCES

(1)   Lee, S.-H. A.; Abrams, N. M.; Hoertz, P. G.; Barber, G. D.; Halaoui, L. I.; Mallouk, T. E. *J. Phys. Chem. B.* 2008, *112*, 14415-14421.